THE UNIVERSITY OF HULL

Wake Hydrodynamics Downstream from a Horizontal Axis Turbine Under Current Flow and Waves

Being a Thesis submitted for the Degree of Doctor of Philosophy in the University of Hull

by

Laura-Beth Jordan (BSc, Hull)

March 2018

Abstract

Due to concerns over the potential impacts of climate change on the environment, there is a growing interest in developing renewable forms of energy. Tidal streams are a potential source of renewable energy that can be harnessed for electricity generation using tidal stream turbines. However, due to the technology being a relatively new development, with limited testing and commercial applications, the flow dynamics and environmental impact of such devices is still poorly understood.

This research investigates the flow dynamics downstream from a horizontal axis tidal stream turbine device using a physical modelling experiment in the Total Environment Simulator laboratory flume, using a channel which measured 11m long, 1.6m wide and 0.6m deep. Detailed flow measurements were collected using a two-camera submersible Particle Image Velocimetry (PIV) system to quantify the three-dimensional flow velocities and turbulence downstream from the model tidal turbine device. A wide range of rotor positions and flow conditions were tested, including current flow and combined wave-current flows. The data collected will be used to validate numerical models developed by project partners, which will assist with developing full-scale operational tidal stream turbines.

The presence of the tidal stream turbine within the channel had a significant impact on the flow downstream. A significant velocity deficit was observed in the wake of the turbine. This was particularly skewed, owing to the turbine rotation, to the right hand side of the centreline, where the deficit was greater than the left hand side. Subjecting the turbine to wave-current flow reduced this deficit considerably, with the shortest wake length occurring under the troughs of waves. Positioning the turbine closer to the bed resulted in a substantial increase in shear stress, with vertical and horizontal asymmetry observed in the wake of the turbine and horizontal asymmetry observed in the resulting scour below the turbine.

The work outlines the impact of these variables on seafloor scour and integrity, and highlights and discusses the optimisation of turbine efficiency with minimal wake and seafloor scour impacts.

Acknowledgements

This thesis would not have been possible without the help and support from many people. Firstly, I must thank my supervisors, Dr Stuart McLelland and Professor Dan Parsons for their help and continued support throughout the duration of this work. They provided opportunities for me to improve and grow as a researcher, and their valuable advice and knowledge was always there when it was needed. Without them I would not have reached this stage, so I am truly grateful to them both.

Thanks must also go to the Geography and Geology Experimental Officer, Brendan Murphy. Without his tireless help with setting up and running the experiments at the Total Environment Simulator, this research would not have been possible. Brendan also provided much needed help and support during the data processing and write-up stages, for which I am very grateful.

I benefitted greatly from the support and advice from other colleagues within the School of Environment Sciences, including but not limited to, Steve Simmons, Hannah Williams, Wietse van de Lageweg, Chris Hackney, Kim Rosewell, Mark Anderson and Mike Dennett.

I would also like to thank my fellow PhD students, namely Leiping Ye, Jess Moloney, Bas Bodewes, Chloe Morris and Rita Santos. In particular, they provided support while I was working long, tiresome hours in the office during the data processing and writing up stages.

I have also benefitted from the support of my friends, Kirsten Palmer and Francesca Rodgers, who provided me with moral support throughout all stages of the PhD process, and were both good housemates for a while.

Particular mention goes to my mum and dad, for always believing in me and providing me with the greatest amount of support. Thanks go to Charlie, who spent many hours listening to me ramble on whilst trying to figure things out and gave me his unconditional love. Thanks also go to my brother, sister-in-law, and young nephew Oliver, who provided me with much needed entertainment when it was needed the most. I have been very fortunate to have received continuous encouragement and support from my family and friends, particularly through the final, most difficult months. Without them, I would not have got this far, so I would like to thank them all.

Laura-Beth Jordan

March 2018.

Table of Contents

Table of Figures

Table of Tables

Chapter 1

Introduction

1.1 Climate change

Climate change is defined as the long-term, large scale change in the global weather patterns and temperatures (Met Office, 2017), and is often attributed to human activity which changes the composition of the atmosphere (United Nations, 1992). Although there was previously considerable debate and speculation about climate change, it has now become widely accepted by the majority of scientists that climate change caused by anthropogenic activities exists (IPCC, 2014; Cook *et al.*, 2016). Although climate change has been occurring for centuries, for the last 60-70 years, the measured changes have been unmistakeable, with clear observations of changes in the sea level and temperature and atmospheric temperature (IPCC, 2014). It is now understood that human activity, particularly power generation from burning fossil fuels, which releases greenhouse gases, has led to global climatic change (IPCC, 2014).

Although greenhouse gases can be natural, anthropogenic greenhouse gas emissions have increased significantly since the industrial revolution in the 18th century, and are continuing to increase (figure 1.1; IPCC, 2014). The increase in economic and population growth have led to the increase in emissions of carbon dioxide, methane and nitrous oxide (United Nations, 1992; IPCC, 2014).

Climate change impacts both natural and human systems across the planet. There are impacts on precipitation and melting snow and ice which impact hydrological systems and water resources (Stroeve *et al.,* 2007; IPCC, 2014). Climate change also affects species across terrestrial, freshwater and marine environments, causing changes in abundance and migration, amongst other changes (Johnston *et al.*, 2013; IPCC, 2014). There are also impacts in a number of regions on crops, leading to reduced crop yields. (IPCC, 2014). In Europe, there have been observed impacts on glaciers, snow, ice and permafrost; wildfires; marine ecosystems; and health and economics (IPCC, 2014). Continued emission of greenhouse gases will lead to further climate change (IPCC, 2014).

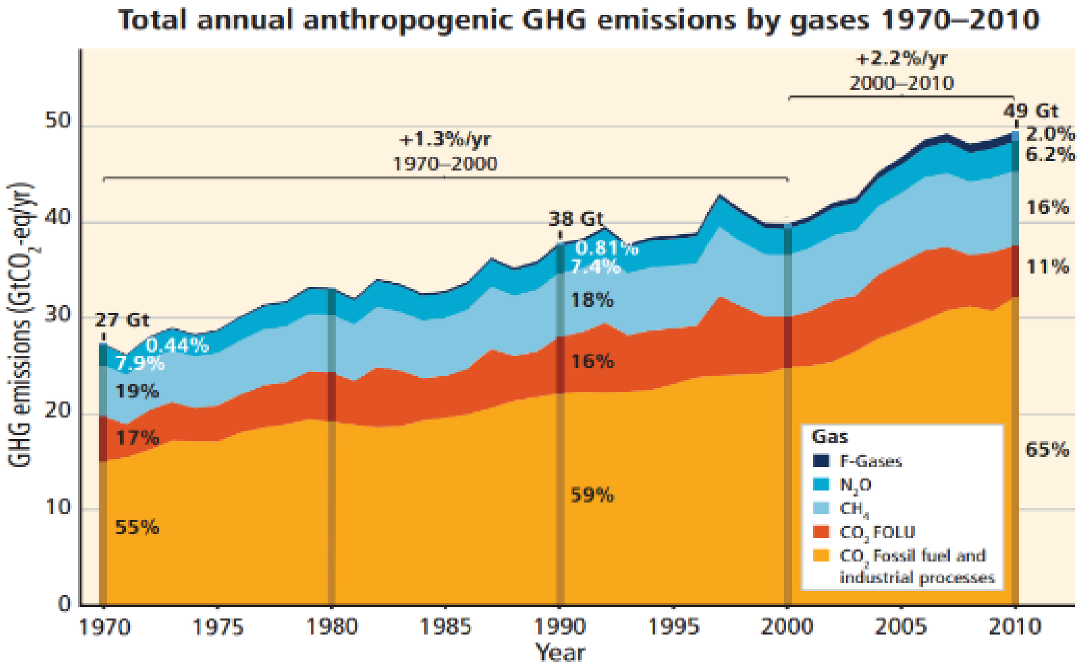

Figure 1.1: Total annual anthropogenic greenhouse gas emissions (gigatonne of CO_2 *equivalent per year,* $GtCO_2$*-eq/year) between 1970 and 2010. (Edited from IPCC, 2014, figure 1.6, pg. 5).*

1.2 The state of the art in tidal renewables

There has been a shift in the last 30 years, which has seen a significant reduction in the use of coal for electricity production. More recently, in the last 20 years, there has been a significant increase in the uptake and use of renewable energy for electricity production (figure 1.2). There is a European

Union target to achieve 20% of energy consumption from renewable sources by 2020 (European Union, 2009; European Commission, 2017). Renewable energy sources include solar, hydro, wind, wave, bioenergy, tidal and geothermal. Each source of renewable energy will be considered in more detail in chapter 2. However, the focus of this research is on tidal power generation.

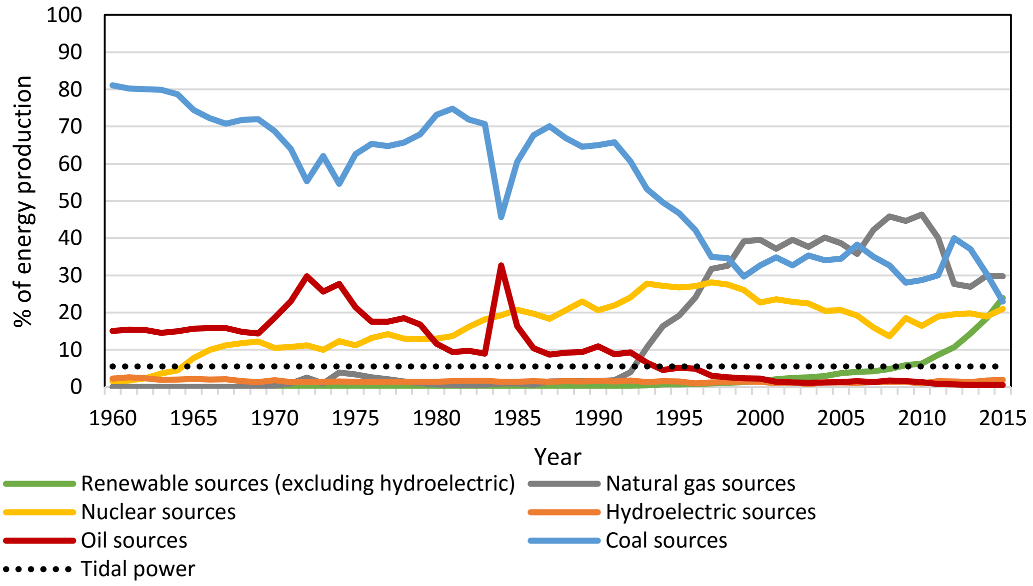

Figure 1.2: Electricity production sources as percentage of total energy production in the United Kingdom. Data source: The World Bank (2017). Black dashed line represents the potentially extractable resource of tidal power around the United Kingdom (Black and Veatch Ltd, 2005).

There is the potential to generate a significant amount of electricity from tidal energy in the United Kingdom (McCall *et al.*, 2007; Burrows *et al.*, 2009) with two different approaches to extracting energy from the tides: tidal barrages and tidal stream turbines. This thesis will focus on tidal stream turbines, which make use of tidal flows, whilst tidal barrages use the tidal range (Elliott, 2012). There are two main types of tidal stream turbines: horizontal axis and vertical axis. The research presented herein uses a model horizontal axis turbine (figure 1.3). Horizontal axis turbines will be discussed briefly below, but the different types of devices will be discussed further in chapter 2.

There is a wide range of horizontal axis turbine devices which have been proposed and developed, but they all have many similarities in their design (figure 1.4). Each element (A-G) is briefly described below.

Composite turbine blades (A) typically use an aerofoil design (Bir *et al.,* 2011). Commercial turbine designs are typically either two-bladed or three-bladed, with the length of the blade varying by turbine design. The main gearbox (B) is used to match the rotational speed of the blades to that which is suitable for electricity generation and energy conversion. The nacelle and pitch control gearboxes (C) connect the blades to the drive shaft, and control the blade pitch and angle of attack. The generator (D) connects to the main gearbox (B) and convert rotation into electricity, while the electronics (D) control the voltage and current that is supplied to the shore. The yaw thruster (E) rotates the turbine on a pivot at the top of the structure to allow the turbine to operate in both the tidal floods and tidal ebbs. The support structure (F) connects the turbine to the bed using a mounting base (G) (Walker, 2014).

Figure 1.3: Model three-bladed horizontal axis tidal stream turbine used during experiments.

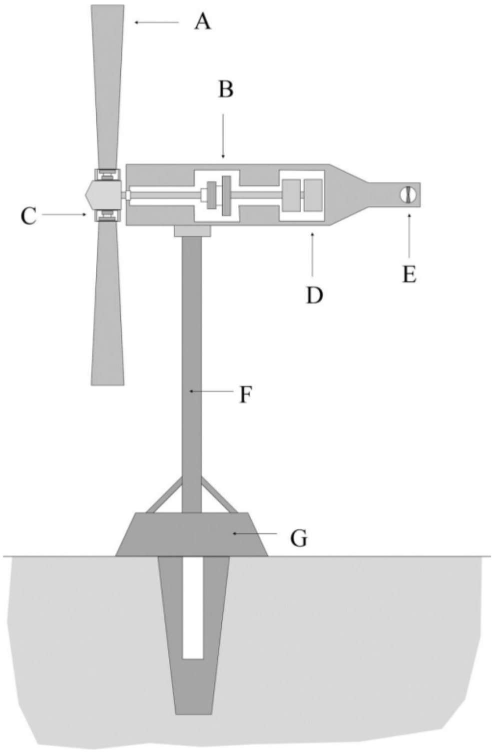

Figure 1.4: Schematic diagram of a tidal stream turbine (Walker, 2014, pg. 20).

The uptake of the technology which harnesses tidal energy is limited, with only a small number of demonstrator sites currently operational in the United Kingdom (RenewableUK, 2002). This may be related to the uncertainties in the potential environmental impacts of tidal stream turbines on the bed of the ocean and/or estuaries. There is the potential for adverse impacts on sediment on the bed due to erosion and scour, as well as potential habitat and other environmental impacts. Despite these concerns, there is a lack of laboratory and field data which attempts to understand the potential environmental impacts of tidal stream turbines.

1.3 Project aims

The physical modelling and experimental programme described herein were undertaken as part of the “Interactions of flow, tidal stream turbines and local sediment bed under combined waves and tidal conditions” (INSTRON) project funded by the Engineering and Physical Sciences Research Council (EPSRC).

The INSTRON project aimed to investigate the processes surrounding the interactions between tidal stream turbines, flow and sediment, and to improve the prediction methods that can be used for full scale planning and design, as well as monitoring the environmental impacts of tidal stream turbines (EPSRC, 2017). It is important to understand tidal stream turbine flow dynamics and how the turbines interact with the surrounding environment.

1.4 Research objectives

The general aim of this research is to understand the wake development and bed interaction downstream from horizontal axis tidal stream turbines, and to contribute to the current knowledge surrounding tidal stream turbine flow dynamics. The specific research objectives are:

1. To improve the understanding of how the wake of a tidal stream turbine (TST) develops
2. To improve the understanding of how the wake of a TST is affected by the distance of the rotor from the bounding surface
3. To identify how the wake of a TST is modified by waves

1.5 Synopsis

This thesis presents an experimental study designed to quantify the changes to the flow-field in the near-field of a tidal stream turbine, with a particular focus on the parameters that are of importance to the influence of tidal stream turbines on environmental processes, such as velocity deficit and shear stress. The remainder of this thesis will be divided into seven chapters. A brief description of each of these chapters is given below.

Chapter 2 consists of a detailed and comprehensive overall literature review, which looks at the current state of the field of tidal renewable energy. The development of tidal stream turbine devices and the current research within the area is discussed. An overview of the current state of the research on the flow dynamics of tidal stream turbines is also provided. Following this, an overview of the existing research and findings regarding the environmental impacts which are associated with tidal stream turbines is also provided.

Chapter 3 details the overall methods used to conduct the experimental modelling used within this research. It will focus primarily on the experimental setup and will describe the horizontal axis tidal stream turbine and flume facility which were used during this research. The data collection methods used during this research will be described and considered. The processing and analysis of the collected data will also be discussed.

Chapter 4 presents the results of one phase of the experimental modelling, which focussed on the initial wake development, and will address the first research objective.

Chapter 5 focuses on addressing the second research objective, and will look at the wake interaction with the bounding surface, and will present the results from the second phase of the experimental modelling.

Chapter 6 presents the results of the final phase of the experimental modelling, and will address the final research objective. This chapter will focus upon the modification of the tidal stream turbine wake under waves.

Chapter 7 provides overall discussions and findings from the research conducted, and the primary results obtained during the research. Details of further work and research ideas which have arisen as a result of this research are identified.

Chapter 2

Background and Justification

2.1 A brief background of renewable energy

Due to concerns over climate change, and the potentially irreversible effects of these changes, alongside a growing energy demand, there is a perceived need to generate power using technologies that have the potential to generate less environmental damage such as renewable energy sources (Johansson *et al.*, 1993; Barber, 2014). However, there are difficulties in defining what constitutes a renewable energy source, as there is no single agreed definition of renewable energy. For example, Sørensen (2004) defined renewable energy as “energy flows, which are replenished at the same rate as they are “used”” (p. 16) and “the usage of any energy storage reservoir which is being “refilled” at rates comparable to that of extraction” whilst Twidell and Weir (1986) defined renewable energy as “energy obtained from the continuous or repetitive currents of energy recurring in the natural environment” (quoted in Boyle *et al.*, 2012, p. 14). Whilst both of these definitions have a similar basis to one another, the lack of a clear and consistent definition can lead to difficulties and inconsistencies when considering renewable energy. A working definition of a renewable energy source that will be used throughout this thesis is: a naturally occurring and continuously replenished form of energy.

Renewable energy can be split into a number of different subsections, separated by the source of the energy being harnessed. The main types of renewable energy include tidal, wind, wave, hydroelectric and solar power, as well as bioenergy and geothermal (Boyle *et al.*, 2012). However, this research will focus primarily on tidal energy. There are two different approaches to utilising tidal power: tidal barrages (or tidal lagoons), and tidal stream turbines. Each type will be discussed in further detail on pages 13-14 under ‘Tidal power devices’.

There appears to be a future for renewable energy in electricity generation, but the extent to which it will and can be used is currently under debate. Turner (1999) believed that renewable energy technologies should be developed and implemented very rapidly, whilst Sørensen (2004) recognised that renewable energy sources must take over non-renewable sources at some stage, but the timings were not certain.

2.1.1 UK tidal stream resource

The tide is controlled by the gravitational forces of the Sun and the Moon. The tide has both daily and monthly variations. Each day, the tide rises (floods) and falls (ebbs).

Each month, spring and neap tides occur, alternating approximately every 7 days. Spring tide occurs twice a month when the Sun, Moon and Earth form a line, leading to the tidal force due to the sun reinforcing the tidal force due to the moon, causing the tidal range to be at its maximum. Neap tide occurs twice a month, between spring tides, when the Sun and Moon are at right angles to each other, and the solar tidal force partially cancels the tidal force of the Moon, causing the tidal range to be at its minimum (Hicks, 2006).

The Moon and the Sun are both tide generating forces, and each can be represented by a cosine curve, with M_2 and S_2 being the tidal constituent (or cosine curve) for each tide-generating force. M_2 is the principal lunar semidiurnal constituent, and occurs every 12.42 solar hours. S_2 is the principal solar semidiurnal constituent, and occurs every 12 solar hours (Sinha and Pingree, 1997; Hicks, 2006).

There is a potential to generate around 20% of the UK's electricity requirements through wave and tidal energy (RenewableUK, 2016), with the tidal resource able to provide around 5-6% of the UK's electricity requirements (Black and Veatch Ltd, 2005; Walkington and Burrows, 2009). Figure 2.1 shows a map of the average annual tidal energy resource for the UK. The areas of the UK with the greatest tidal resource are the Pentland Firth and the Channel Islands (Black and Veatch Ltd, 2005; ABP Marine Environmental Research Limited, 2008). It has been identified that much of the UK's tidal energy resource is found at depths greater than 40m, with approximately 63% of the UK's tidal energy resource being found at depths in excess of 40m (Black and Veatch Ltd, 2005).

A significant proportion of the UK's tidal energy resource is expected to be harnessed in areas with spring tide velocity ranges of between 2.5 ms^{-1} and 4.5 ms^{-1} (Black and Veatch Ltd, 2005). The average neap tide velocities are typically 50% of the spring tide velocity (Black and Veatch Ltd, 2005). The optimum tidal current speed is around 2-2.5ms^{-1} (Fujita Research, 2000). Speeds in this range are typically obtained during spring tides, as neap tide speeds are substantially slower. Speeds within this range limit the stress placed on the tidal stream turbines, whilst still ensuring that the energy extraction is economical (Fujita Research, 2000). The greatest current speeds are typically in areas of headlands, constricted or inter-island channels, as well as open sea sites (Black and Veatch Ltd, 2005; Walkington and Burrows, 2009). A number of these sites can have complex flows, but can still represent a significant tidal current resource (Black and Veatch Ltd, 2005). However, there is still some debate surrounding the placement of tidal stream turbines near headlands. Edmunds *et al.* (2014) noted that placing a closely spaced row of turbines led to a positive blockage effect, and therefore a higher power output from the turbines. Frid *et al.* (2012) and Neill *et al.* (2012), however, suggested that the presence of tidal stream turbines too close to a headland could affect the sandbanks and morphodynamics of the headland as well as the ability of the sandbanks to dissipate and refract waves.

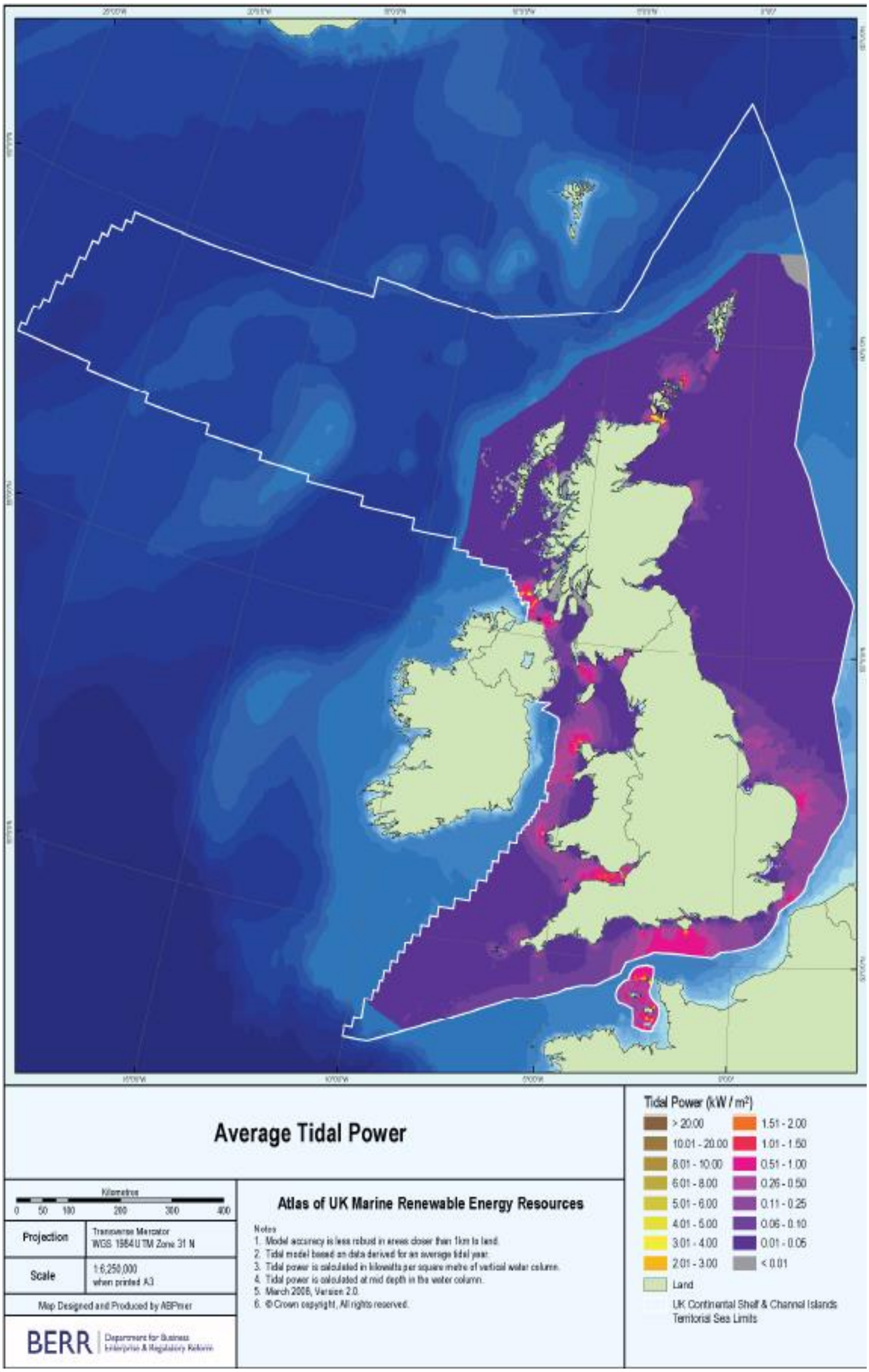

Notes
1. Model accuracy is less robust in areas closer than 1km to land.
2. Tidal model based on data derived for an average tidal year.
3. Tidal power is calculated in kilowatts per square metre of vertical water column.
4. Tidal power is calculated at mid depth in the water column.
5. March 2008, Version 2.0.
6. © Crown copyright, All rights reserved.

Figure 2.1: Map showing the average UK annual tidal power (ABP Marine Environmental Research Limited, 2008).

2.1.2 Tidal power devices

Tidal power has been harnessed for centuries in the form of mills, but is becoming of greater interest for generating electrical power, particular using tidal stream turbines (Hardisty, 2009). Charlier and Justus (1993) suggested that effective extraction of electricity from tides required tidal barrages or dams but these potentially have large environmental impacts, such as altering discharge, water quality, and sediment transport dynamics, as well as having a detrimental effect on aquatic organisms (O Rourke *et al.*, 2010). Hardisty (2009) suggests that there should be more focus on tidal power generation with a smaller environmental impact, including tidal stream turbines. The main difference between tidal barrages and tidal stream turbines is that tidal barrages (or tidal lagoons) use the tidal range (the vertical difference in the heights between the low tide and the following high tide), whilst tidal stream turbines use the tidal current as the tide floods and ebbs (Tedds *et al.*, 2014).

Tidal barrages are the traditional method of deriving power from the tides. Barrages capture the potential energy of the water by trapping tidal water behind a barrage at high tide, then releasing the water as the tide ebbs (Kerr, 2007; Elliott, 2012). During the release, water passes through a turbine, generating electricity, similar to a hydroelectric dam (Elliott, 2012). Tidal lagoons usually refer to smaller containment structures that function in the same way as a tidal barrage (Elliott, 2012). Tidal lagoons typically occupy a subsection of the channel, whereas tidal barrages are constructed using a barrier that spans the full channel, leading to lagoons typically having less impacts on the channel than barrages (Xia *et al.*, 2010).

Tidal stream turbines use the horizontal movement of the tides, rather than the vertical movement of the tide (Elliott, 2012). Tidal stream turbines are very similar to wind turbines, but differ in their potential energy extraction due to water being 800 times denser than air, meaning that a water flow speed of 1 ms^{-1} has a similar energy density to a wind flow speed of 9 ms^{-1}, and therefore the tidal turbines can be smaller than the wind turbines (Coiro *et al.,* 2006; Kerr, 2007; Elliott, 2012; Barber, 2014). Tidal stream turbines can take the form of horizontal or vertical axis turbines, with each having its own advantages and disadvantages, which will be explained in the following sections (Kerr, 2007; Hardisty, 2009; Elliott, 2012). However, the tidal power device and technology used would depend upon the individual circumstances of each potential site.

2.1.3 Benefits of tidal stream turbines

Tidal power provides a predictable sources of renewable energy (Pelc and Fujita, 2002; Bahaj and Myers, 2003; Plew and Stevens, 2003; Hardisty, 2009); and when they are located off-shore, tidal stream turbines are also likely to have fewer environmental impacts than other forms of renewable energy (Osborne, 1998; Pelc and Fujita, 2002). Fraenkel (2002) identified that sea-based renewable energy technologies have less constraints than land-based renewable energy technologies, due to there being less impact and conflict. Tedds *et al.* (2014) noted that tidal stream turbines allow water to pass straight through, and therefore have a minimal impact upon the marine and tidal environment. Their relatively low tip speed, relative to wind turbines or propellers, would also make them less of a threat to marine life (Fraenkel, 2002). It was suggested that tidal barrages would negatively affect marine life to a higher degree than tidal stream turbines due to the differences in location, as well as the tidal barrage affecting the entire width of the estuary, and the tidal stream turbines only affecting a portion of the tidal stream (O Rourke *et al.,* 2010). The tidal stream turbines are less visually impacting than tidal barrages due to them usually being fully submerged (Fraenkel, 2002; Tedds *et al.*, 2014). Tidal stream turbines therefore appear to be a positive form of future renewable energy technology. However, the impacts of both tidal barrages and tidal stream turbines are site specific, and therefore understanding the environmental impacts of tidal power devices is still an area which requires research and assessment (O Rourke *et al.*, 2010).

2.1.4 Tidal stream turbine designs

Numerous designs and configurations of tidal stream turbine designs have been proposed and considered (Hardisty, 2009). Many designs are based upon those of wind turbines, and are engineered from well-known concepts (Fraenkel, 2006). Fraenkel (2002) and Amin and Xiao (2013) identified two different tidal turbine configurations that can be used: horizontal axis (or axial flow) turbines, and vertical axis (or Darrieus) turbines. More details and some examples of these configurations are given below. However, as with wind turbines, the horizontal axis turbine seems to be the most popular, feasible and efficient design (Fraenkel, 2002; Bahaj *et al.,* 2007a, Bahaj *et al.*, 2007b; Amin and Xiao, 2013).

2.1.4.1 Horizontal axis

Horizontal axis turbines are similar to horizontal axis wind turbines (Bir *et al.* 2011). The rotational axis of a horizontal axis turbine is parallel to the flow direction. Due to the current advances that have been made with wind turbine technology, Bir *et al.* (2011) suggest that horizontal axis tidal stream turbines are a promising technology. A number of different prototypes of tidal stream turbines, particularly horizontal axis turbines, have been proposed and developed (Hardisty, 2009; Bir *et al.,* 2011), including the Clean Current turbine, the Marine Current Turbines' SeaGen turbine and the Lunar Energy Rotech tidal turbine (Hardisty, 2009; Clean Current, 2014; Lunar Energy, 2014a; Marine Current Turbines, 2014a). There is a consensus that the optimal shape of the tidal stream turbine blades are hydrofoils, with an increase twist and blade width towards the hub (Andrews and Jelley, 2007 in Hardisty, 2009; Hardisty, 2009). This shape is optimal because the angle of the flow decreases near the hub as the blade is moving slower, and therefore the twist and blade width which increase towards the hub maintain an optimal angle of attack and generate lift for optimal turbine efficiency (Andrews and Jelley, 2007 in Hardisty, 2009). Whilst a lot of research has been done into horizontal axis tidal stream turbines, more research is still needed, particularly in terms of their operation and interactions with the environment in which they are sited.

The Marine Current Turbines' SeaGen Turbine (shown in figure 2.2) uses two twin-blade turbines. The blades are able to be pitched at 180 degrees and can operate in bi-directional flows. It differs from some other tidal stream turbines (such as the Clean Current Tidal Turbine and the Lunar Rotech Tidal Turbine) in that the rotors are positioned higher in the water column (the top third) as tidal currents are stronger (Marine Current Turbines, 2014c). The SeaGen Turbine, with rotors that are 16m in diameter, has a generating capacity of 1.2MW (O Rourke *et al.*, 2010).

The Lunar Rotech Tidal Turbine (shown in figure 2.3) is a bi-directional horizontal axis turbine which can be deployed in tidal depths in excess of 40m, allowing it to make use of a large energy source (Black and Veatch Ltd, 2005; Lunar Energy, 2014a). The Lunar Rotech Tidal Turbine has a generating capacity of 1 MW and is 11.5m in diameter with a duct which is 19.2m in length and 15m in diameter (O Rourke *et al.*, 2010). The Lunar Rotech Tidal Turbine uses a venturi shaped duct system and a gravity foundation (O Rourke *et al.,* 2010; Lunar Energy, 2014a). The venturi duct makes use of the venturi effect, which occurs when the flow rate of a fluid increases as it passes through a constriction in a tube (Barber, 2005). Figure 2.4 shows the results of a computation fluid dynamics (CFD) analysis which shows the change in the speed at which the water passes through the ducted Lunar Rotech Tidal Turbine. The change in colour (green to red) shown in figure 2.4 shows that the duct accelerates the flow, thereby increasing the power available and energy captured by the device (Lunar Energy, 2014b).

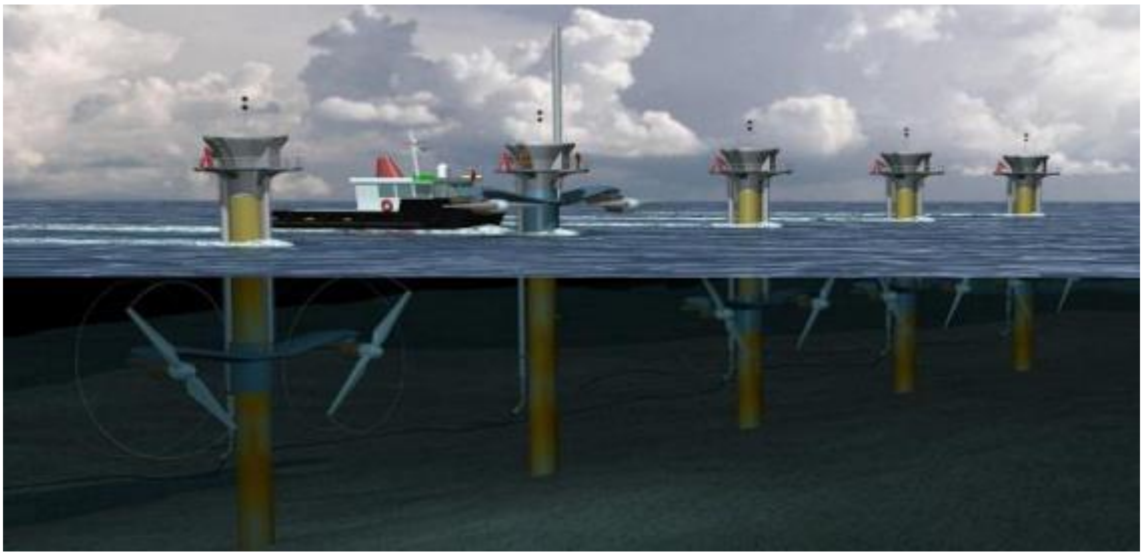

Figure 2.2: Artist's impression of Marine Current Turbines' SeaGen array (Marine Current Turbines, 2014b).

Figure 2.3: Lunar Rotech Tidal Turbine (Lunar Energy, 2014a).

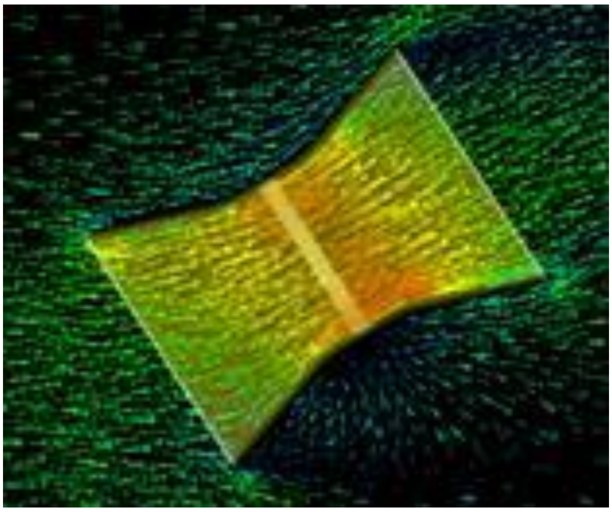

Figure 2.4: Computational Fluid Dynamics (CFD) analysis result showing flow through Lunar Rotech Tidal Turbine as a result of the venturi duct in a Lunar Rotech Tidal Turbine. Green indicates a slower flow speed, whilst red indicates a faster flow speed (Lunar Energy, 2014b).

2.1.4.2 Vertical axis

Vertical axis turbines differ from horizontal axis turbines in that the rotational axis is perpendicular to the flow direction, as seen in figure 2.5 (a) and (b). Some designs of vertical axis tidal turbines have existing prototypes which have been built and tested at a commercial level (Hardisty, 2009; Khalid et al., 2013). This includes a prototype of Neptune Proteus, a cross-flow vertical axis tidal turbine (Hardisty, 2009). Other vertical axis turbine designs such as the Blue Energy ocean turbine have started to be developed and tested (Hardisty, 2009; Blue Energy Canada, 2014).

The Blue Energy Canada vertical axis turbine, shown in figure 2.5 (a) and (b), is based upon the concept of a Darrieus wind turbine. It consists of four fixed hydrofoil blades which generate hydrodynamic lift. This is a result of Bernoulli's principle, which works in a similar manner to the venturi effect. The Bernoulli principle states that the pressure within a fluid decreases as the velocity of the moving fluid increases. The converse also applies, in that as the velocity of the fluid decreases, the pressure within the fluid increases. It is this Bernoulli’s principle which can lead to hydrodynamic lift and lead to the blades of the tidal stream turbine moving faster than the surrounding water speed (Barber, 2005; U.S. Department of Transportation, 2009). The turbine is bi-directional and can therefore operate as the tide both ebbs and floods. The turbine rotor is fully submerged but the machinery room which houses the generator and electronic controls is situated above the water surface (Blue Energy Canada, 2014). However, as with horizontal axis tidal stream turbines, vertical axis tidal stream turbines are a developing technology, and the environmental impacts, as well as the engineering aspects of the turbines, require further research.

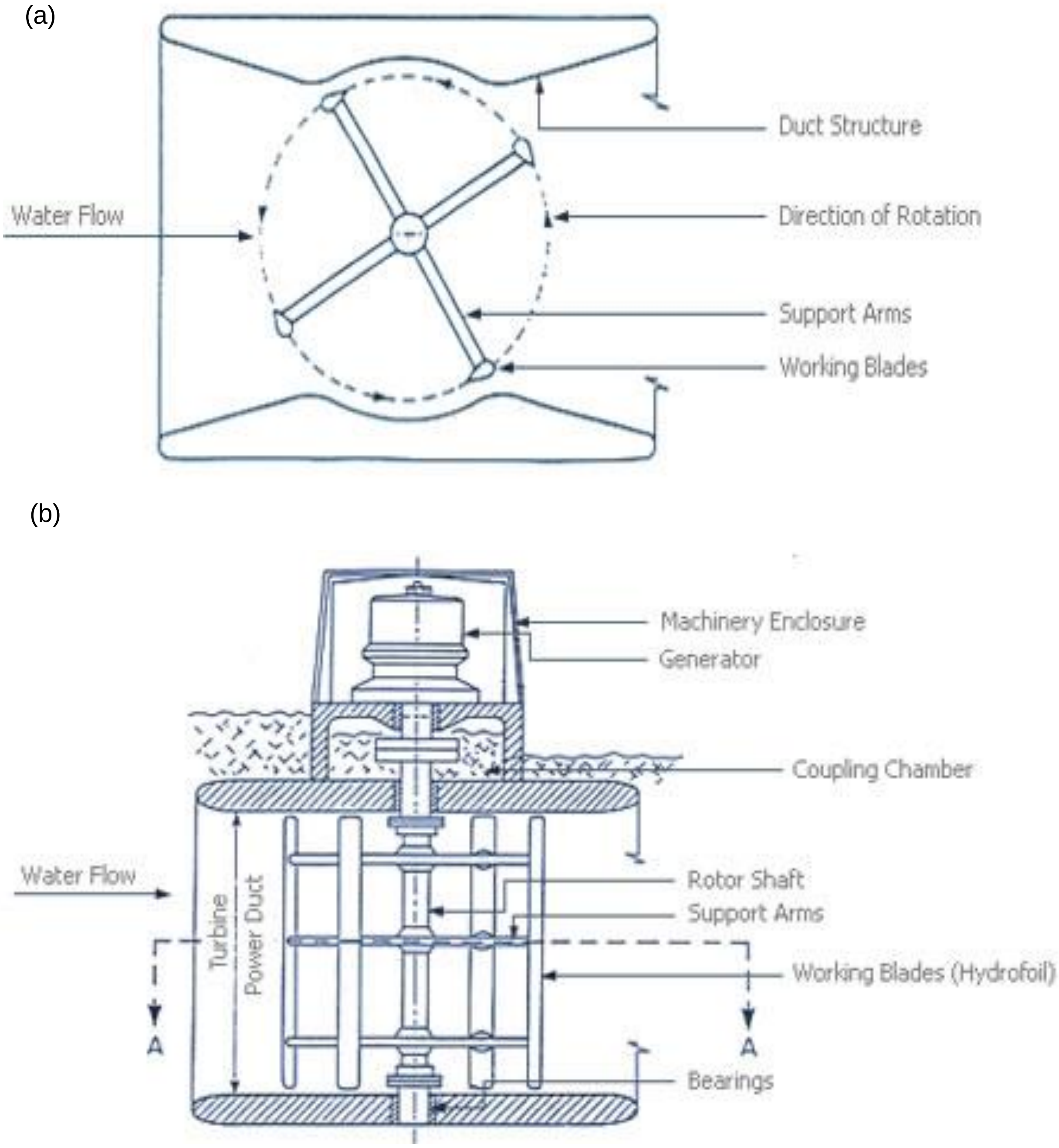

Figure 2.5 (a): Top view of the Blue Energy Canada turbine and (b) Blue Energy Canada turbine (Blue Energy Canada, 2014).

2.2 Flow dynamics and characteristics downstream of horizontal axis tidal stream turbines

It is important to understand tidal stream flows to be able to determine how the presence of tidal stream turbines can affect the flow dynamics.

2.2.1 Bi-directional

The flow in tidal stream channels fluctuate in a predictable and periodic nature diurnally due to being controlled by the tides (Hardisty, 2009; Khan *et al.,* 2009). Tidal streams are bi-directional, rather than uni-directional (Fraenkel, 2002; Khan *et al.*, 2009; Turnock *et al.*, 2011) due to the tidal streams being controlled by the tides which ebb and flood. This feature will allow tidal stream turbines to extract energy during both the flood and ebb tides (Khan *et al.*, 2009), and will also affect the location and direction of a tidal stream turbine with respect to the flow (Turnock *et al.*, 2011). However, the ebb and flood flows are asymmetric and do not flow in exactly opposite directions (Lu and Lueck, 1999). The bi-directionality of tidal stream channels leads to more complex erosional and depositional features and characteristics (Fagherazzi *et al.*, 2004) which need to be considered when assessing the effect of placing turbines within a tidal stream channel. Alongside these bi-directional characteristics of tidal stream channels, there will also be other variations such as vertical differences in velocities within channels.

2.2.2 Vertical velocity differences

The flow within a tidal channel as well as the vertical velocity differences varies depending on the distance from the shore as well as the topography of the tidal stream channel (Khan *et al.*, 2009). However, it is the vertical velocity differences that tends to have a more significant influence on the placement of tidal stream turbines and the effects that the turbines have on the flow of the tidal stream channel. As height above the channel bed increases, the speed of the current and water flow within the tidal stream channel increases rapidly (Stacey *et al.,* 1999; Hardisty, 2009). This is likely to be due to a reduction in shear stress and friction as the distance above the bed increases. Shear stress is discussed in more detail below. The energy flux (change) at the water surface of a tidal stream channel is higher than that at the bed of the channel as the energy flux is dependent upon the density of the fluid, the cross-sectional area, and the cubed velocity of the fluid (Khan *et al.,* 2009).

2.2.3 Shear stress

Shear stress in its broadest sense is the stress which acts tangentially to an area (Bansal, 2010). In the case of tidal stream channels, the shear stress is the frictional force exerted on the bed by the flowing water (Ji, 2008). Water in a tidal stream responds to the stress which is applied to it by flowing, and the rate of flow and changes to a given flow are dependent upon the magnitude of the stress which is applied to the fluid (Hardisty, 2009). The shear stress of the flow within a tidal stream channel is applied to the sediment on the bed of the channel, with the amount of shear stress being dependent upon both the flow of the water as well as the type of sediment on the channel bed (Hardisty, 2009). When the force in shear stress becomes greater than the friction and gravitational forces that are acting on the sediment in the channel bed, sediment entrainment occurs and leads to the onset of sediment transport.

2.2.4 Cavitation

Cavitation is the appearance of vapour cavities (or bubbles) within a liquid, including flowing water (Franc and Michel, 2005). Cavitation can occur on a turbine blade when the local pressure level falls to or below the pressure level of the ambient water vapour pressure (Batten *et al.,* 2006; Wang *et al.*, 2007). Cavitation can occur below a certain level before it causes a significant loss in the performance of a tidal stream turbine (Batten *et al.,* 2006). The cavitation can, however, lead to flow instabilities, vibrations, and damage to the turbine (Escaler *et al.,* 2006; Wang *et al.,* 2007).

2.2.5 Wake of a turbine

The presence of a tidal stream turbine within a channel impacts upon the flow dynamics around the turbine. A wake is typically characterised by a reduction in the velocity of the flow both upstream and downstream of the turbine, and an accelerated flow either side of the tidal stream device (McCombes *et al.*, 2011).

Figure 2.6 shows, in a basic form, the wake behind a solid object. It can be seen from figure 2.6 that a wake consists of a near field wake and a far field wake. The wake behind a tidal stream turbine has a similar basis to the wake behind a solid object, with the addition of helical vortices, which are shed from the rotating blades of the turbine. However, vortices can still develop downstream of a solid object such as a cylinder. At the downstream boundary of a cylinder, vortices (also known as eddies) begin to develop and grow, forming an oscillatory wake in the flow downstream of the cylinder (Rapaport and Clementi, 1986).

Figure 2.7 shows how the water flow varies around different shaped objects. It indicates that as water flows around an object, the boundary layer between the water and the object becomes detached, and vortices begin to form, which are then transported downstream in the wake (Andrews and Jelley, 2007 in Hardisty, 2009). Figure 2.7 shows that the shape of an object influences the amount of disruption that occurs to the water flow and the vortices that are produced, with a cylinder having less impact than a plate, but a hydrofoil having an even lower impact and effect upon the flow. The size and development of the vortices can be limited by the distance from the bounding surfaces such as the channel bed and the free surface (Stacey *et al.,* 1999).

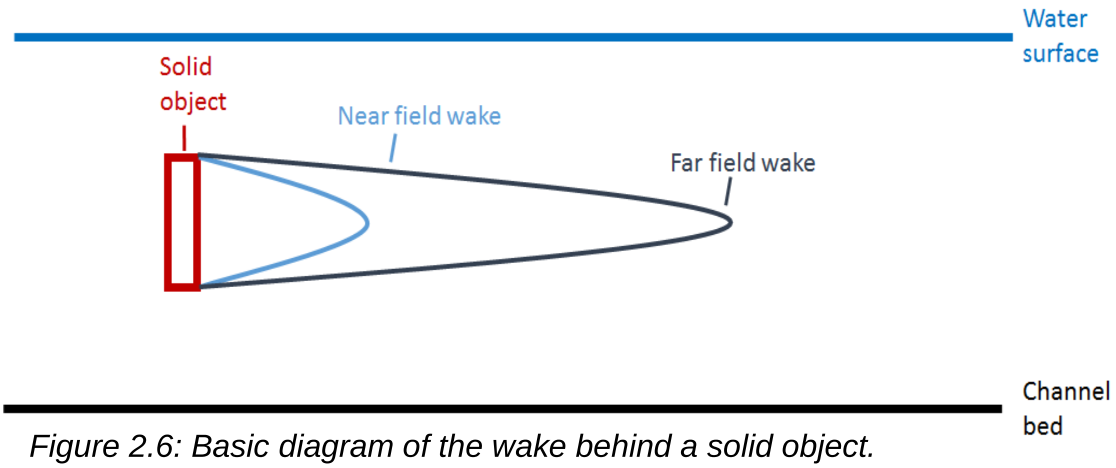

Figure 2.6: Basic diagram of the wake behind a solid object.

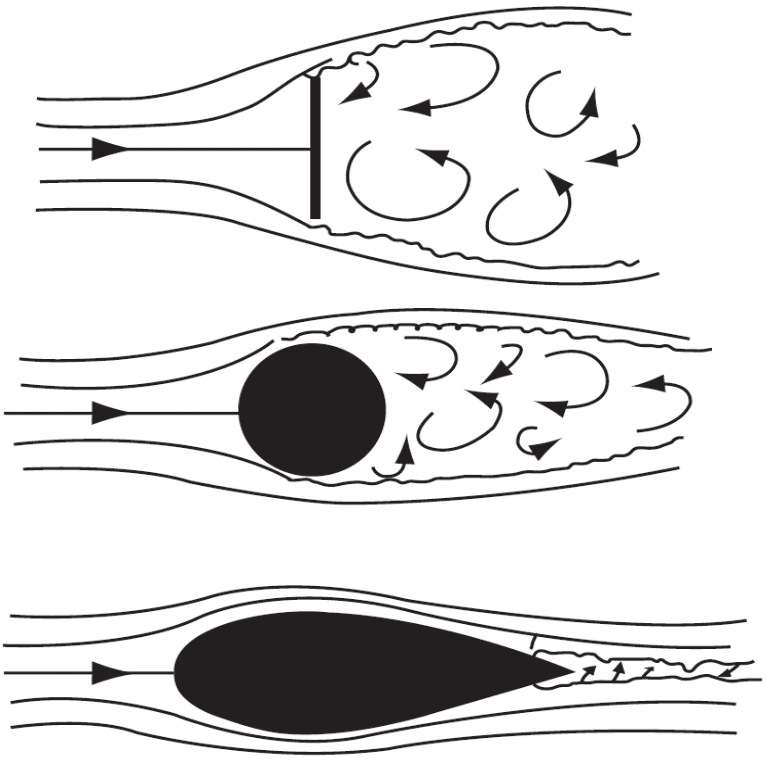

Figure 2.7: Diagram showing how the water flow varies around different shaped objects. The top image is a plate, middle image is a cylinder, and the bottom image is a hydrofoil (Hardisty, 2009).

2.2.5.1 Wake behind a porous object (e.g. rotor)

Tidal stream turbines cause a wake to be created downstream in a similar manner to how cylinders and other solid objects do. These wakes are characterised by hub and tip vortices, a velocity deficit, as well as an increase in turbulence intensity (Neary *et al*., 2013). The wake behind a tidal stream turbine, like that of a solid object, typically takes the general form of a gradually expanding cone shaped area (Myers *et al.*, 2008; Myers and Bahaj, 2010). Figure 2.8 shows the vorticity field of an expanding turbine wake. It can be seen that the wake of the turbine develops and grows downstream of the turbine, with the vortices becoming less well defined as distance downstream increases. There are a number of factors which affect the structure and development of the wake of a tidal stream turbine, as shown in figure 2.9. The wake of a turbine features a near field and a far field section, which will be discussed in more detail below.

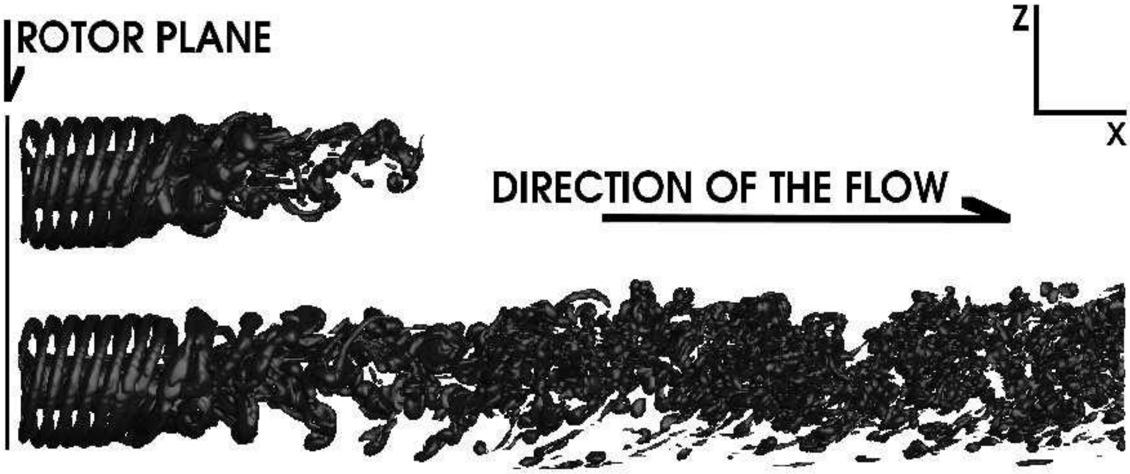

Figure 2.8: Side view of the vorticity field of a turbine wake. The top image shows the early stages of the wake development (after 42 seconds) and the bottom image shows the wake development after 189 seconds (Vybulkova et al., 2013).

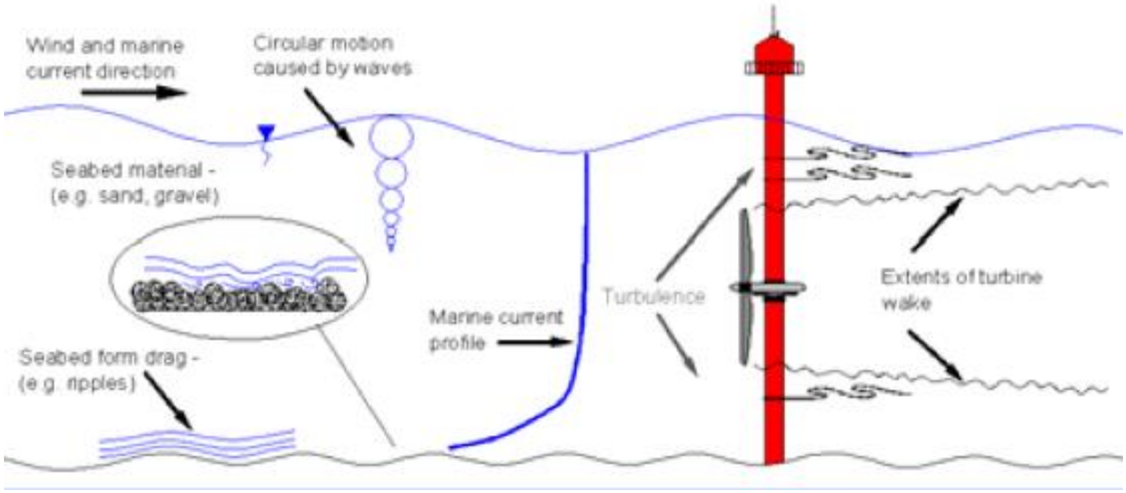

Figure 2.9: Some of the factors affecting the wake of a tidal stream turbine and the device performance (Bahaj et al., 2007c).

2.2.5.2 Near field wake

The exact extent of the near field area of the wake is not well defined, with it having been defined as anywhere between 0 and 7 rotor diameters downstream of the turbine (Bahaj *et al.*, 2007c; Tedds *et al.,* 2014). The near wake typically consists of the momentum and velocity from the flow being harnessed by the turbine which, combined with the mass of the water staying constant, leads to wake expansion (Bahaj *et al.*, 2007c, McCombes *et al.*, 2011). The turbine will generate electricity by converting the energy from the flow into a mechanical motion. In doing so, vortices (or eddies) are shed from the turbine, particularly the blade tips. Circulation of tip vortices limits the rate of expansion of the flow of the turbine wake into the faster moving free-stream flow (Bahaj *et al.,* 2007c). Further downstream, the turbulence from the free-stream flow causes the vortices to break down (Bahaj *et al.,* 2007c), which leads to the far wake and its associated characteristics.

2.2.5.3 Far field wake

The far field wake behind a tidal stream turbine consists of the transition between flow conditions which were established in the near field wake and the re-development of the flow to the condition which it was in upstream of the tidal stream turbine. The far field wake consists of two main mechanisms which drive the changes which occur: convection and turbulent mixing (Bahaj *et al.,* 2007c).

Turbulent mixing causes the wake to re-energise and regain velocity that was lost as a result of energy being extracted from the tidal stream. This mixing causes the vortices which were shed from the turbine to break up. The breaking up of vortices and an increase in velocity occurs until the velocity returns to that which existed upstream of the turbine (Bahaj *et al.,* 2007c). This process can also be seen in the velocity profiles of a tidal stream, such as those shown in figure 2.10 below.

2.2.6 Velocity profiles for a tidal stream channel

Velocity profiles which show the vertical velocity in a channel can be used to determine the impacts that a tidal stream turbine may have on the flow in a tidal stream channel. Figure 2.10 shows the vertical velocity profiles for a model tidal stream turbine at various distances both upstream and downstream of a tidal stream turbine. The model tidal stream turbine had a hub height of 0.425m and a rotor diameter of 0.5m (Neary *et al.*, 2013). It can be seen from figure 2.10 that the turbine causes changes in the velocity of the flow. There is a noticeable decrease in the velocity in the near wake of the turbine compared to the velocity upstream of the turbine. This is most significant around the hub of the rotor (at 0.425m). However, in the far wake of the turbine, the flow recovers much of its velocity. There are discrepancies seen in the velocities measured by the two different measurement instruments (acoustic Doppler profiler (ADP) and acoustic Doppler velocimeter (ADV)) due to the manner in which the instruments operate. ADP collects flow velocities over the entire depth of the water column, whilst ADV provides single point measurements (Nortek AS, 2017). Neary *et al.* (2013) determined the differences were due to errors in the ADP measurements, due to the nature of the flow near the turbine. However, the overall trend seem in the data is consistent between data collection methods.

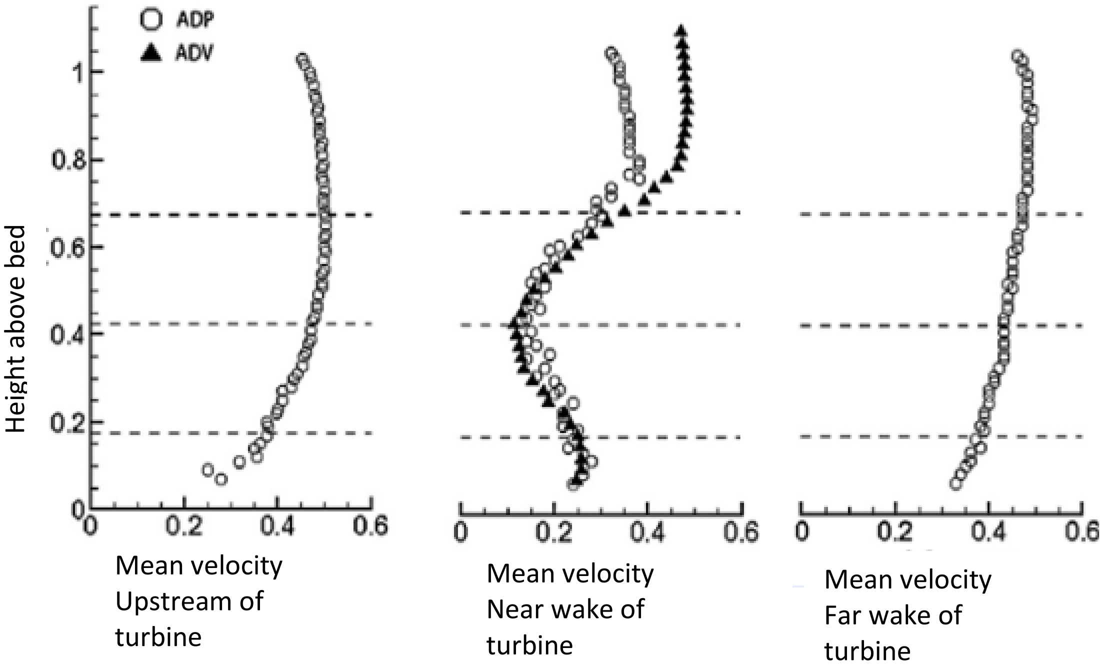

Figure 2.10: Vertical stream-wise mean velocity profiles for a tidal stream turbine (Image taken and edited from Neary et al., 2013). Measurements are shown for acoustic Doppler profiler (ADP) and acoustic Doppler velocimetry (ADV).

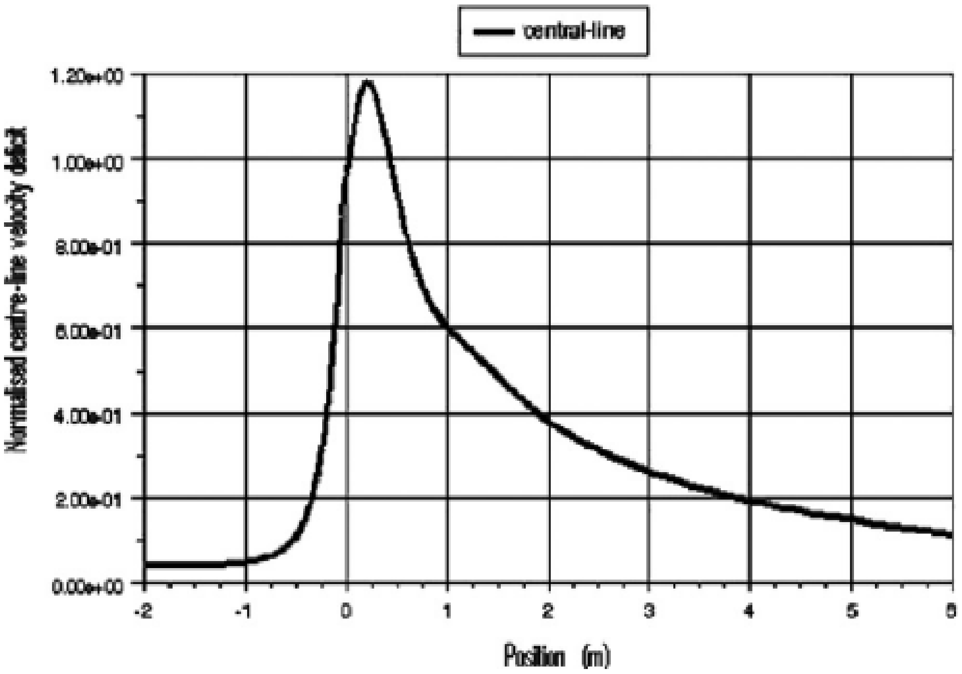

Figure 2.11: Recovery of reduced velocity (velocity deficit) as downstream distance (position) increases (Sun et al., 2008).

Figure 2.11 shows how the velocity deficit develops through the wake of a tidal stream device. The velocity deficit is a reduction in the velocity of the flow within a tidal stream channel. It can be seen from figure 2.11 that the velocity deficit occurs immediately downstream of the device, and then gradually recovers as the distance downstream increases (Sun *et al.*, 2008). Figure 2.11 shows that the majority of the velocity deficit has recovered by 6m downstream of the tidal stream device, which in this situation has a diameter of 0.5m. Therefore, the majority of the velocity recovery in this situation is within 12 rotor diameters downstream of the turbine. Neary *et al.* (2013) identified that the majority of the flow recovery from the wake of the turbine occurs within 10 rotor diameters downstream of the turbine, which does agree with the findings of Sun *et al.* (2008). The research conducted by Neary *et al.* (2013) and Sun *et al.* (2008) had depths of 1.15m and 1m respectively, and rotor diameters of 0.5m, leading to the depth to diameter ratio being similar in both cases. However, Sun *et al.* (2008) primarily used numerical modelling, whilst Neary *et al.* (2013) used physical modelling. Although Sun *et al.* (2008) did not specifically state the flow velocity used, it was deduced to be approximately 0.7 metres per second (ms^{-1}), whereas Neary *et al.* (2013) used a flow velocity of $0.4ms^{-1}$.

2.2.7 Transient velocities and flow

Tidal streams consist of transient and residual flows. The transient flows and velocities refer to the instantaneous flows which fluctuates with time, and the residual flow refers to the net or mean flow which occurs over one or a number of tidal cycles (Nihoul and Ronday, 1975; Fluid Mechanics Ltd, 2014; Iglesias *et al.,* 2014). Tidal stream turbines are likely to affect the transient and residual flows, with the residual flow being modified over a large area, whereas the transient flow is affected within the vicinity of the tidal stream turbine (Ramos *et al.*, 2014). The transient flow is affected both upstream and downstream of the tidal stream turbine which is characterised by a weakening or reduction in the flow velocity (Ramos *et al.*, 2014). However, at both sides of the turbine, the transient flow is intensified and the velocity increases. However, this change is to a lesser extent than the change downstream of the turbine (Ramos *et al.*, 2014).

2.3 Environmental impacts of tidal power and tidal stream turbines

There is a lack of understanding of the environmental impacts of tidal stream turbines (Boehlert and Gill, 2010; Malki *et al.*, 2014). For example, Shields *et al.* (2011) suggest that the ecological impacts of removing kinetic energy from the marine environment is poorly understood, whilst Boehlert and Gill (2010) and Ahmadian *et al.* (2012) identified the importance of understanding the spatial and temporal environmental impacts of tidal power.

Pelc and Fujita (2002) recognised that tidal turbines are likely to be the most environmentally friendly form of tidal power, whilst Osborne (1998) in Pelc and Fujita (2002) suggested that tidal turbines have less environmental impacts than other forms of tidal power as they do not block the channel, and have no impact on fish migration or the hydrology. Charlier and Justus (1993) believed that tidal power plants have little environmental impact. However, they continued to discuss that there was evidence of the relocation of some sand banks, and the disappearance of some fish species.

2.3.1 Impact on sediment

Whilst it is sometimes thought that tidal stream turbines have minimal environmental impact, it has been suggested that there will be impacts upon sediment transport dynamics. Neill *et al.* (2009) recognised that extracting energy from a tidal system can have a significant effect on the sediment dynamics of the stream, both in the immediate vicinity of the turbine, as well as further downstream from the turbine. The presence of tidal stream turbines too close to a headland could lead to increased erosion of the headland sandbanks as well as affecting the wave dissipation and refraction and therefore coastal protection that the sandbanks present (Neill *et al.*, 2012). The presence of a tidal stream turbine is likely to cause sea bed scour around the turbine (Rambabu *et al.*, 2003; Cada *et al.*, 2007; Chen and Lam, 2014; Hill *et al.*, 2014; Hill *et al.,* 2016). There are a number of factors which could influence the degree of sea bed scour from a tidal stream turbine, including, but not limited to: turbine structure and design, height of the turbine above the bed and water velocity (Cada *et al.*, 2007; Polagye *et al.*, 2010). The changes in velocity as a result of the tidal stream turbine being present could lead to either increasing scour (in the case of increases in velocity) or increasing deposition (in the case of decreases in velocity) (Polagye, 2009). Increasing the distance between the sea bed and the turbine shaft and blades should avoid severe impacts occurring to the bed sediment (Wang *et al.*, 2007; Chen and Lam, 2014). An increase in the water velocity would lead to an increase in the lift and drag forces which drive scour, and therefore lead to an increase in sea bed scour (Rambabu *et al.*, 2003). However, much more research into the impact of tidal stream turbines is needed to fully understand the interactions and effects that occur.

2.3.2 Impact on suspended sediment

Suspended sediment is the sediment load which is carried within the water column (United States Environmental Protection Agency, 2012). For the sediment to remain suspended, the velocity of the upward currents and eddies must be equal to or greater than the velocity at which the particle falls through the water column (known as the particle fall velocity) (Bagnold, 1966; Rijn, 1984).

Ahmadian *et al.* (2012) used a 2D numerical model to predict the impact of tidal stream turbines on the suspended sediment concentrations within a channel. Ahmadian *et al.* (2012) used an array that consisted of 2000 turbines each with a diameter of 10m, occupying an area of 7.2km^2, with a turbine spacing of 50m in all directions. The results show that the suspended sediment concentrations were noticeably affected within 15km of the turbine array. The levels of suspended sediment were predicted to substantially decrease upstream and downstream of the turbine array, as well as within the array (Ahmadian *et al.*, 2012). However, the 2D hydro-environmental model was designed to simulate tidal stream turbines, and may be lacking in accuracy due to it not using a 3D physical model with physical turbines and primary physical modelling data.

Ahmadian *et al.* (2012) did not directly explain why the suspended sediment concentration decreased around the tidal stream turbine array. However, it was noted that the installation of a tidal stream turbine may increase the levels of suspended sediment within the stream. This is a result of sediment being released into the water column during installation (Cada *et al.*, 2007; Faber, Maunsell and Metoc PLC, 2007). These effects will be limited in extent and duration due to the tidal stream being a high energy and dynamic environment which has continual changes to the levels of suspended sediment (Faber, Maunsell and Metoc PLC, 2007). However, Cada *et al.* (2007) indicated that site-specific studies would be required in order to understand the potential impacts upon suspended sediment as a result of constructing and operating tidal stream turbines at a given site.

2.3.3 Noise/acoustic impacts

Another potential environmental impact that needs to be considered is the acoustic/noise impacts of the tidal stream turbines. The noise produced by a tidal stream turbine will be affected by a number of factors including blade design, water depth, water velocity and bathymetry, and is therefore site and device specific (Lloyd *et al.*, 2011). However, there is some disagreement surrounding the levels of acoustic impacts of tidal stream turbines.

Li and Çalişal (2010) noted that turbines generate noise when they are rotating, which has been determined to be an important environmental impact of tidal stream turbines that needs to be considered. They also noted that tidal turbines generate noise in two areas: hydrodynamic noise and mechanical noise. Mechanical noise is produced from the gearbox and bearings within the turbine (Li and Çalişal, 2010). Hydrodynamic noise is generated from the fluctuating hydrodynamic lift acting on the turbine blades. The categories used to determine the different types of noise emitted from a tidal stream turbine vary, and Lloyd *et al.* (2011) separated them into the categories of self-noise (which includes vortex shedding from wake instabilities), interaction noise (which includes cavitation) and hydroelastic noise (which was characterised as being similar in tone and vibration to vortex shedding). Wang *et al.* (2007) recognised that the noise from tidal stream turbines shedding vortices from the blades would impact marine life. There was further concern about cavitation of the turbines increasing the noise levels which are radiated from the turbine, particularly where multiple turbines are concerned (Wang *et al.*, 2007; Vybulkova, 2013).

The construction and installation processes, as well as the decommissioning of tidal stream turbines, are also likely to have noise/acoustic impacts. The noise and vibration that occurs during construction activities such as drilling may disturb fish, birds and marine mammals, potentially leading to avoidance of the area (ABP Marine Environmental Research, 2005; Faber, Maunsell and Metoc PLC, 2007).

The actual impacts of the noise and acoustic levels that tidal stream turbines may produce is also under dispute. Parvin [undated] (*pers. comm.* cited in Fraenkel (2006)) carried out underwater acoustic measurements which indicated that current technology, specifically the Marine Current Turbine Ltd Seaflow project, would not produce noise at levels and frequencies which would impact marine fauna. However, Li and Çalişal (2010) indicated that marine mammals which communicate within the turbine noise frequency bands are likely to be impacted by the tidal turbines. The foregoing review indicates that there is a lack of consistency on the noise levels expected to be produced by tidal stream turbines, and the potential impacts that these noise levels may have upon the environment.

2.3.4 Impact on marine fauna

There is a lack of evidence and research surrounding the impacts that tidal stream turbines may have on marine fauna. Guerin *et al.* (2014) recognised the importance of understanding the potential environmental impacts of marine renewable energy devices, including tidal stream turbines, particularly on fish species.

Hammar *et al.* (2013) noted that the effects of turbines on fish are mostly unknown. There is limited information about the interaction of tidal stream turbines and marine fauna, but it has been suggested that marine mammals, fish, and diving birds may be able to see or hear the device and therefore either avoid the area entirely, or take action at close range to avoid contact and collision with the tidal stream turbine (Wilson *et al.*, 2006). Hammar *et al.* (2013) partially agreed with Charlier and Justus (1993), identifying that whilst no fish directly collided with the turbines, some fish appeared to divert around areas where turbines were present. Hammar *et al.* (2013) focussed their research on vertical axis turbines during daylight hours, and indicated that fish appear to avoid the near-field area of the turbines, and that turbine farms with multiple turbines may have larger and more restrictive effects on the fish movements. Viehman (2012) agreed with Hammar *et al.* (2013) by determining that fish appeared to avoid the turbine during daylight hours. However, Viehman (2012) expanded this by identifying that fish interacted with turbines much more during the night than during the day, with this effect being greater in smaller fish.

Hammar *et al.* (2013) furthered their research by indicating that the colour of the turbines could be a contributing factor to the effects that they have on the fish.

Tidal stream turbine farms may have cumulative environmental and ecological impacts, particularly with regards to local habitat changes (Polagye *et al.*, 2010). Nash *et al*. (2014) used a numerical model to identify potential changes to the tidal range in an estuary as a result of the introduction of a tidal turbine array. This found that the overall tidal range was reduced due to the extraction of energy by the turbines, with the reduction becoming more significant as the density of the turbines in the array was increased. The presence of a turbine array caused blockage effects, which led to time lags in the water flow, and delays at which high tide and low tide occurred (Nash *et al.*, 2014). It was determined that the change to the tidal range and timing as a result of the installation of a tidal turbine array would affect the intertidal zone. The intertidal zone is the area which is dry during low tide, but underwater during high tide. Changes to the tidal range affect the water levels in the inter-tidal zone. It was determined that up to 25% of intertidal zones could become permanently wet, and up to 7% could become permanently dry as a result of the tidal turbine arrays, potentially leading to damage to ecosystems and the loss of habitats in these areas (Nash *et al.* 2014).

However, the validity of the results by Nash *et al.* (2014) are somewhat debateable due to the findings being based on numerical modelling, rather than physical modelling. Kregting *et al.* (2016) determined, through collecting benthic community data at the location of the SeaGen development in Northern Ireland, that in the far field area, tidal turbine arrays in high flow environments are unlikely to have a significant effect on marine life on the seabed. Kregting *et al.* (2016) did not, however, specifically define the extent of the far field area.

It has been identified that there are many potential factors which may influence and affect the impact that tidal stream turbines have on marine and tidal fauna. However, there still appears to be a lack of coherent and thorough research into the impact of horizontal axis tidal stream turbines on marine and tidal fauna, particularly the differences between daylight and night-time hours.

Chapter 3

Experimental Programme

3.1 Introduction

The experimental work described herein aimed to measure the flow-field around a model tidal stream turbine and to provide sufficient detail to establish several parameters of importance to environmental modelling. In particular, the variation of bed shear stress due to the proximity of the turbine and wake to the channel bed, and the effect of waves on this. The intention of this work is to address how reducing the height of the turbine above the bed affects the wake and sediment transport (addressed in chapters 4 and 5), and how waves at the free-surface affect the wake and sediment transport through a wave cycle (addressed in chapter 6).

Figure 3.1 shows the predicted differences in turbine performance when the rotor is positioned at various heights above the bed under a range of flow conditions. Under current only conditions, it is expected that the turbine performance increases with distance from both the water surface and the bed. Although the effects of the water surface and the channel bed on the turbine performance will differ in extent and rate, they can both affect the performance of the turbine, and therefore the optimal vertical position of a turbine under current only conditions is at mid-depth. Where mid-depth is will depend on the tidal height. As the water depth will change with the tidal ebbs and floods, consideration needs to be given to these water depth changes to find the optimal vertical position of a turbine under tidal conditions.

Under combined current and waves, it is expected that there will be a significant drop in turbine performance near the water surface due to the presence of waves affecting the water speed and turbine operation (figure 3.1). As with turbines operating under current only conditions, turbines operating under combined current and wave conditions are expected to have an increase in performance further away from the bed and water surface.

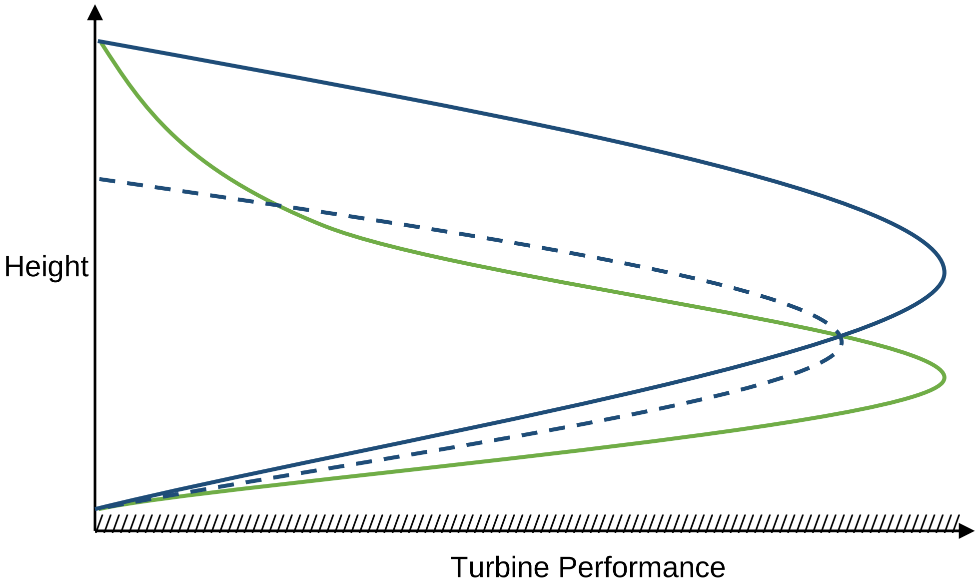

Figure 3.1: Diagram showing the predicted turbine performance under differing flow conditions and turbine heights. Channel bed is indicated by //////. Solid blue line shows performance under current only conditions at high tide. Dashed blue line shows performance under current only conditions at low tide. Green line shows performance under combined current and waves. Diagram is not to scale and is designed to be a representative estimate only.

This chapter describes the experimental work undertaken for this research. The experimental facility which was used for the study is introduced and then described in detail. The measures which were taken to ensure a steady, uniform flow are described, and the measurements to quantify the plain channel flow characteristics are also detailed. This chapter then explains the flow measurement techniques that were used for this research, and describes the set of experiments that were carried out to address the research objectives identified in chapter 1. The research described herein uses a 0.2m diameter three-bladed horizontal axis turbine, designed by the University of Strathclyde. The rotor will be described in more detail in section 3.3.

3.2 Experimental facility/channel

The experimental study used the University of Hull's Total Environment Simulator (TES) recirculating flume. The TES is 16m long and 6m wide with a maximum water depth of 1.6m. The experimental flume was designed by Armfield Ltd. It features two recirculating pumps sited below the flume, and each pump is capable of recirculating up to 500 litres of water per second. The upstream end of the flume features 8 wave paddles, manufactured by HR Wallingford, which can be controlled either together or individually and are capable of producing a range of wave sizes and frequencies, depending on the user specifications, up to a height of 0.5m. The inlet and outlet of the flume both consist of a 3m deep end tank. The inlet can have baffle plates (with various porosities and grid layouts (e.g. honeycomb)) installed to assist with flow uniformity. The downstream end can be fitted with weirs to alter the water depth within the flume.

The experiments had a bulk Reynolds number (Re) of ~1.7×10^5 indicating turbulent flow. This is similar to the experimental modelling carried out by Rose *et al.* (2011) (cited in Tedds *et al.*, 2014) which had a Reynolds number of 1.2×10^5. However, experimental modelling carried out by Myers and Bahaj (2009) and Mycek *et al.* (2011) (cited in Tedds *et al.*, 2014) had slightly greater Reynolds numbers of 3.2×10^5 and 3.5×10^5 respectively, whilst CFD modelling carried out by Harrison *et al.* (2009) had a slightly lower Reynolds number ($Re = 1.1 \times 10^5$) compared to the research presented herein.

The experiments described herein had a Froude number of 0.13 indicating subcritical flow. Consul (2011) investigated the effect of variations in Froude number from 0.082 and 0.131 on the power and thrust of a tidal turbine and determined that within this range, the Froude number had very little impact on the power and thrust of the turbine. Whelan *et al.* (2009) and Stallard *et al.* (2015) all conducted experiments which had a Froude number of 0.2. Although it is higher than the Froude number of the experiments described herein, it still indicates subcritical flow.

Assuming a 1:100th scale, applying Froude scaling, this equates to a 20m diameter turbine in a water depth of 60m, with a mean flow speed of 3.2m/s. A water depth of 60m is viable, and found in the Pentland Firth and Orkney waters (The Scottish Government, 2011). The Reynolds number at full scale would be 1.7×10^8. As long as Froude scaling is applied, and the Reynolds numbers remain in the same classification (turbulent flow), the discrepancies in Reynolds number is acceptable (Myers and Bahaj, 2010).

Research by other authors has used similar flow speeds and turbine diameters. For example, Stallard *et al.* (2013) conducted experiments at 1:70th scaling, which represented a 19m diameter turbine in a water depth of 31.5m and a mean flow velocity of 3.76m/s,

A test channel was constructed within the TES for the purpose of this study. The test channel had a length of 11m and a width of 1.6m. At this channel width, any sidewall effects on the Tidal Stream Turbine (detailed below) used in the experiments would be minimised, and it also enabled the Particle Image Velocimetry (PIV) system, detailed below, to be set up in an area of still water outside the main channel. A working flow depth of 0.6m was used during all of the experiments described herein. This water depth ensured that the rotor was sufficiently far from the water surface. Figure 3.2 shows a basic schematic diagram of the layout of the flume. Figure 3.3 shows a more detailed schematic diagram of the flume, and is scaled to show the relative locations of the equipment. Flow conditioning, shown in figure 3.4, was used immediately downstream from the inlet to ensure uniform flow. The flow conditioning consisted of a number of short plastic tubes aligned lengthways along the channel. The tubes were encased in a metal grid structure to ensure their location remained fixed.

Experiments were conducted over a number of channel surfaces. The first type of surface used in the experiments was a smooth surface which was constructed from varnished marine plywood boards. The second surface used was also constructed from marine plywood boards, which were then coated with sand that was fixed using a thin coat of varnish to maintain the surface roughness. The sand had a median grain size (D_{50}) of 425µm, with grain sizes ranging between 120µm and 1180µm. The grain size distribution curve is shown in figure 3.5. The roughened bed surface created a rough boundary layer. Experiments were also run with an area of mobile bed inset into the roughened fixed bed. This inset measured approximately 1.15m long and 0.72m wide. The sediment within this inset was the same as that used to create the rough boundary (D_{50} =425µm). The inset of mobile bed allowed the investigation of the sediment transport threshold by observing the sand deformation in this zone. Assuming a typical full-scale turbine diameter of 20m (Walker, 2014), the experiments described herein used a 0.2m diameter turbine which would approximate to a scale of 1:100. If the sediment was scaled to the same degree, it would represent sediment with D_{50} of 4.25cm (42.5mm). Sediment with a D_{50}

of 42.5mm is classified as pebbles (Farrell *et al.*¸ 2012). Using a smaller sediment size in the experiments presented herein could have caused the sediment to be affected by electrochemical cohesive forces (Sutherland and Soulsby, 2010). The sediment bed used (D_{50} = 425µm) did not move under the imposed flow conditions, and sediment entrainment was only initiated when the rotor caused the bed shear stress to increase above the entrainment threshold. The entrainment threshold is the point at which particles of all sizes within the sediment are transported (Kramer, 1935 in Dey, 2011), or particle motion is observed at any location along the sediment bed (Vanoni, 1964; Dey, 2011). During the experiments described herein, a technique similar to the latter method was used, as the sediment entrainment was determined based on the observed sediment motion.

Experiments were undertaken across a range of flow conditions. This included flow only, waves only, and combined wave and flow conditions. The plain channel profile under flow only conditions is shown in figure 3.6. The mean stream-wise velocity in the plain channel was 0.32m/s. During the wave only and combined wave and tidal flow, a series of data were collected using 8 wave gauges in order to monitor the waves that were present within the channel. The locations of these wave gauges within the channel are shown in figure 3.3.

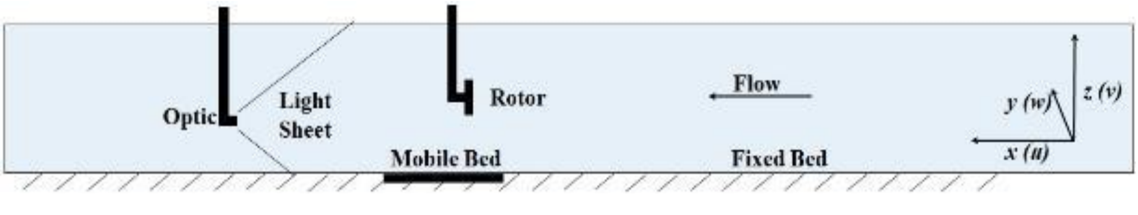

Figure 3.2: Basic schematic diagram of the flume set-up. Flow direction is from right to left. (Not to scale).

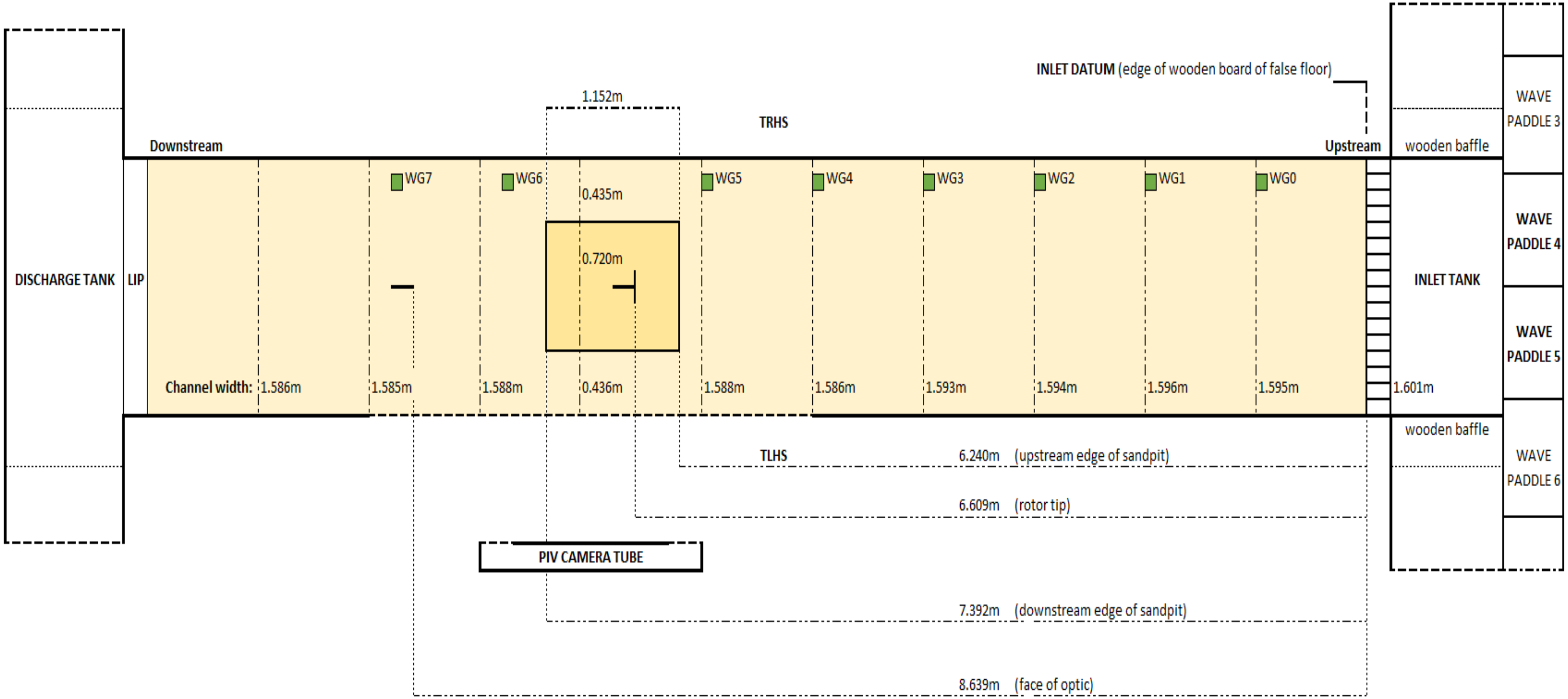

Figure 3.3: Flume schematic with measurements showing the channel set-up within the larger flume facility. The locations of the wave gauges (WG) are also shown. Flow direction is from right to left.

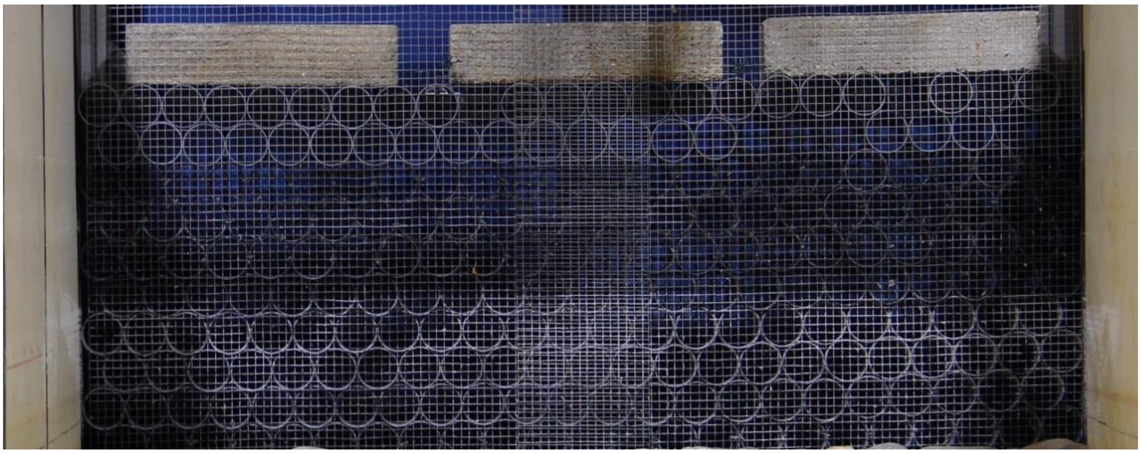

Figure 3.4: Flow conditioning device at the channel inlet, constructed using short plastic tubes aligned lengthways, contained within a metal grid structure.

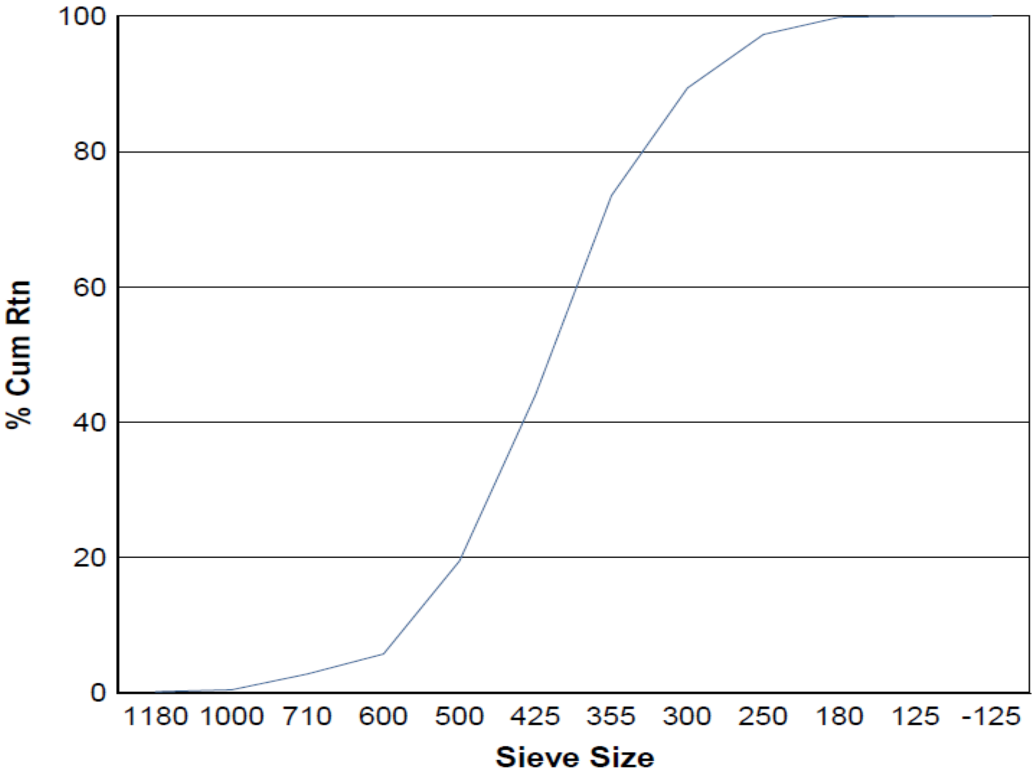

Figure 3.5: Grain size distribution curve for CH30 sand (Sibelco UK, personal communication, 2014).

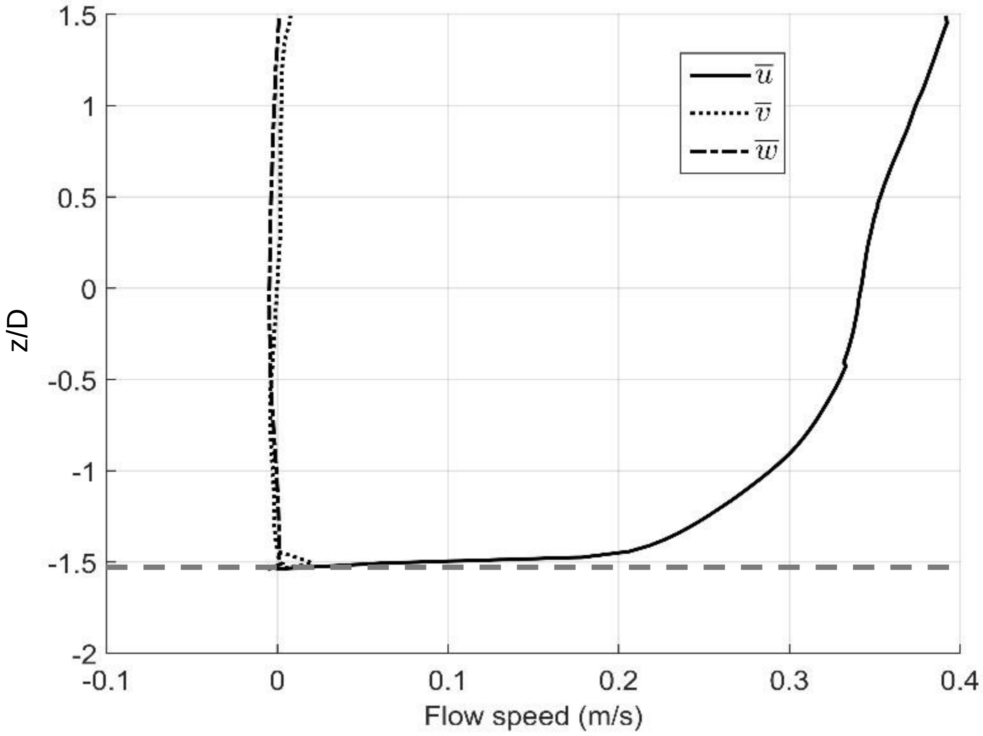

Figure 3.6: Mean of the velocity components $\overline{u}, \overline{v}$ *and* $\overline{w}$ *for the plain channel. Location of channel bed indicated by dashed grey line. The scale on the y axis is normalised to rotor diameters (0.2m).*

3.3 Turbine models

The experiments used two three-bladed, horizontal axis model Tidal Stream Turbines (TST), which were designed at the University of Strathclyde (L. Vybulkova, personal communication, 03 February 2014). The first rotor (shown in figure 3.7 (a)) is unshrouded with a 0.2m diameter and three blades with a NACA 63415 aerofoil shape and a polynomial twist of 17.6 degrees from root to tip. The turbine is assumed to be a constant-speed device with a constant blade pitch of 5 degrees. The second rotor (shown in figure 3.7 (b)) is unshrouded with a 0.2m diameter and three blades with a NACA 0012 aerofoil shape and a polynomial twist of 13 degrees from root to tip. The turbine is assumed to be a constant-speed device with a constant blade pitch of 4 degrees. In the experimental setup described herein, the blockage from the turbine was 3.2%. The rotor rotated in a clockwise direction, if viewed from upstream. The measurements taken in the experiments described herein used the second rotor. The second rotor was chosen for the experiments described herein as its design led to it having a greater impact on the flow than the first turbine design. The turbine design used (NACA 0012 aerofoil shape) was similar to that investigated in numerical modelling by Vybulkova (2013). This allowed comparative work to be carried out as part of the INSTRON project, although the comparison is not considered within this thesis.

The TST rotor was mounted on an 8mm shaft, which was attached to a 32mm diameter housing for a 25W DC motor. The motor was controlled by software which ensured that the TST rotated at a specified speed, which enabled the rotor to be operated at a set tip speed ratio (TSR). Data on rotation speed were collected by the ESCON Studio computer software so that the TSR could be determined. The motor housing was attached to a 68mm x 6mm solid fin supported from above. This allowed the height of the rotor within the water column to be controlled. Figure 3.7 (c) shows rotor 2 attached to the housing described, and mounted 200mm above the mobile bed inset. When in use for measurements, the rotor was positioned in the centre of the channel at ~6.6m downstream from the inlet (Figure 3.3). The height of the rotor above the bed was changed depending on the individual experimental requirements, as detailed later in this section.

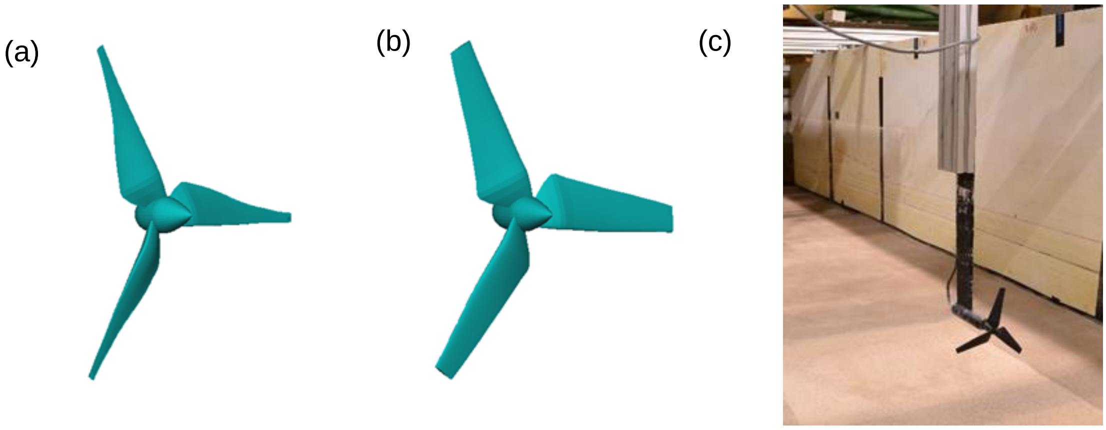

Figure 3.7: (a) CAD image of rotor 1 with a NACA 63415 aerofoil shape (b) CAD image of rotor 2 with a NACA 0012 aerofoil shape (c) rotor 2 mounted on housing and solid fin, positioned in the centre of the channel above the section of mobile bed.

3.3.1. Rotor data analysis

As the raw rotor data was in revolutions per minute (RPM), this needed to be converted into the tip speed ratio, taking account of the free-stream velocity in the channel.

The tip speed ratio (TSR) is calculated using the following equation:

$$TSR = \frac{R\Omega}{V_{\infty}} \quad \text{Equation 1}$$

where Ω is the rotational speed in radians per second, R is the rotor radius in metres and V_∞ is the free-stream velocity in metres per second (Coiro *et al*., 2006). In the experiments described herein, Ω is between 14.75 and 15.66 radians per second and V_∞ is between 0.29 and 0.33 ms^{-1}, measured at the vertical centre of the turbine at each rotor height.

Initial analysis of the rotor data showed variations in TSR during the experiments. Figure 3.8 shows the results of this analysis. The tip speed ratio was calculated using the velocity at the vertical centre of the rotor. The tip speed ratios presented could have had less variation if they were calculated using the average velocity over the swept area of the rotor. The optimal tip speed ratio was 5.5, as this corresponds to the maximum for the power curve for the flow velocity, as shown in figure 3.9. During the experiments, the average TSR varied between ~4.9 and ~5.9, depending on the rotor height, with the optimum average TSR (5.5) occurring when the rotor was positioned at 180mm above the bed. Figure 3.9 shows the band of operating tip speed ratios during the experiments described herein. The power co-efficient (C_P) remained close to the optimum within the operating tip speed ratio range. Using momentum theory, the power co-efficient can be derived using:

$$C_P = 4a[1-a]^2 \qquad \text{Equation 2}$$

where a is the axial induction factor (Hansen *et al.*, 2000; Manwell *et al.*, 2003). The axial induction factor is:

$$a = \frac{U_1 - U_2}{U_1} \qquad \text{Equation 3}$$

where U_1 is the inflow, free-stream velocity, and U_2 is the velocity at the rotor plane (Manwell *et al.*, 2003).

The rotor thrust is shown in figure 3.10. The original thrust curve was not available, and therefore the thrust coefficient (C_T) is calculated using Momentum Theory. Buhl (2005) and Manwell *et al.* (2003) determined that the thrust coefficient can be derived using:

$$C_T = 4a(1 - a) \qquad \text{Equation 4}$$

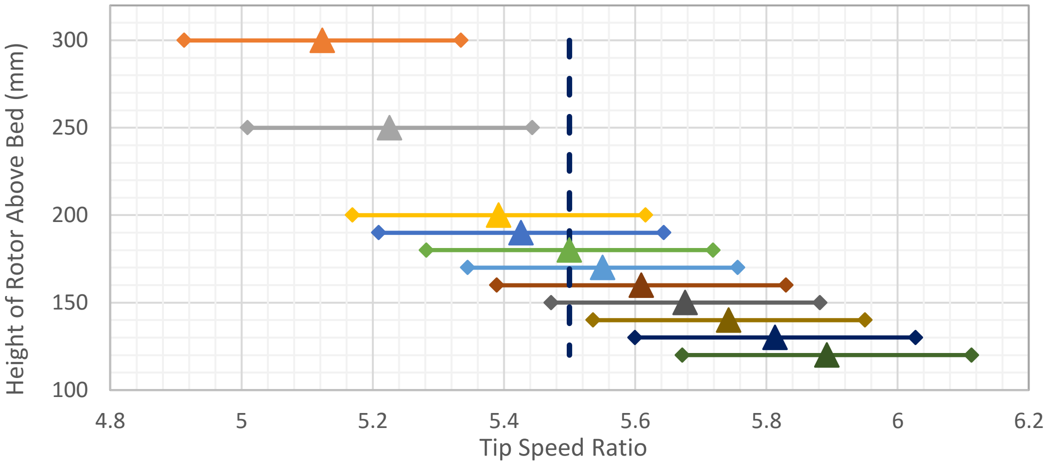

Figure 3.8: Tip speed ratios for rotor 2 at various heights above the channel bed (triangle markers), derived by using the average velocity across the entire rotor diameter. The TSR variability (standard deviation) at each height is also shown (diamond markers). The optimal TSR of 5.5 (representing the maximum for the power curve) is also shown by the vertical dashed line.

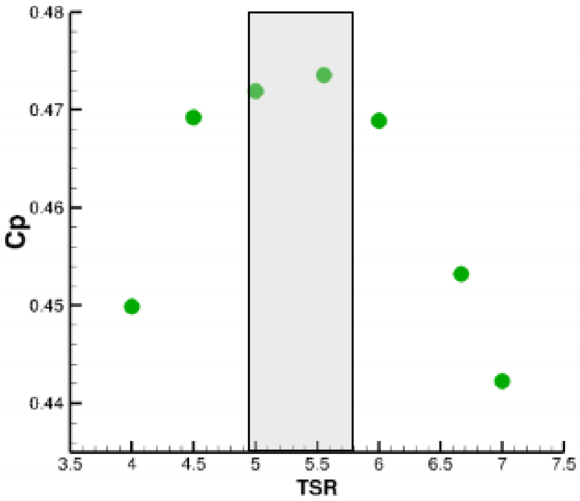

Figure 3.9: Power curve for rotor showing optimal tip speed ratio of 5.5. Grey banding shows the tip speed ratios during the experiments described herein (edited from L Vybulkova, personal communication, 22 June 2016).

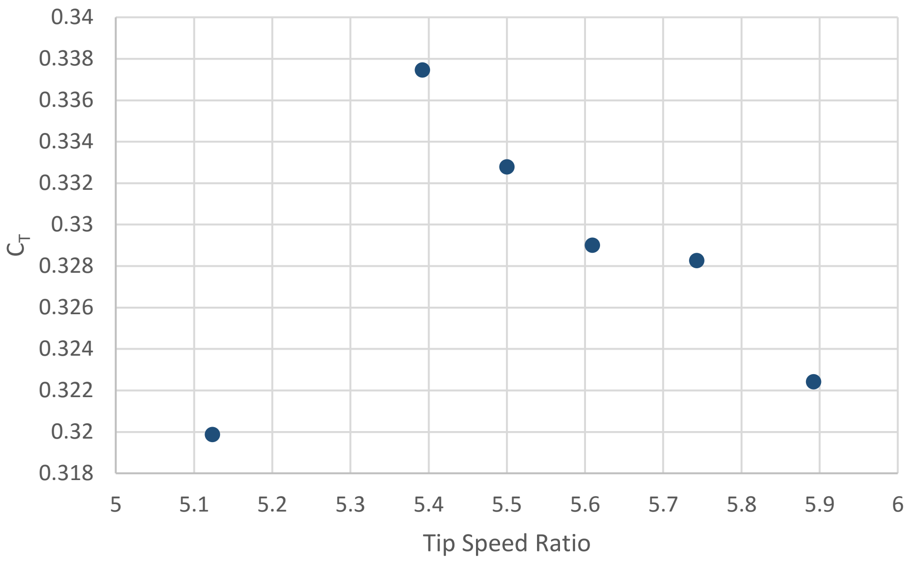

Figure 3.10: Thrust curve for rotor at tip speed ratios used during experiment described herein.

3.4. Particle Image Velocimetry System

3.4.1. Principles of PIV

PIV is a non-intrusive form of velocity measurement, which measures instantaneous fields of scalars and vectors of the velocity field (Adrian, 1991; Adrian, 1997; Prasad, 2000; Dantec Dynamics, 2014a). PIV works by recording the position of seeding particles over time, and uses the displacement of the seeding particles over time in order to calculate the velocity of the fluid (Prasad, 2000; Adrian and Westerweel, 2011).

Alternative measurement techniques, such as acoustic Doppler velocimetry (ADV) could have been used. Prior to the full data collection, ADV and PIV were compared for accuracy and practicality. ADV and PIV were found to have a high level of agreement between measurements (Moshin *et al.,* 2011). However, unlike PIV, ADV probes may partially obstruct the flow of the fluid, potentially affecting the measured velocity, although ADV probes are designed to restrict the obstruction as much as possible (Lohrmann *et al.*, 1994). PIV has another advantage over ADV, in that it provides velocity measurements over a plane, rather than point measurements, as is the case for ADV (Brossard *et al.,* 2009; Sulaiman *et al.*, 2013).

Figure 3.11 shows the typical setup of PIV systems. PIV systems can take the form of two-dimensional (2D) systems, stereo two-dimensional three-component (2D3C) systems, and tomographic three-dimensional three-component PIV (3D3C) systems (Brossard *et al.*, 2009; Dantec Dynamics, 2014a). Figure 3.11 shows the typical setup of a 2D PIV system, whilst the main differences that can be noted between a 2D and a 3D PIV system are that a 2D system comprises of a single camera and measures two velocity components, whereas a 2D3C system comprises of multiple cameras and measures three velocity components (Dantec Dynamics, 2014b; Dantec Dynamics, 2014c). Regardless of whether the PIV system is 2D, 2D3C or 3D3C, it will still typically consist of a laser with a pulsed light sheet, seeding particles within the fluid, and imaging optics (cameras). As well as these components, a PIV system will also comprise of a target area within the fluid, as well as a computer for data storage and analysis (Adrian, 1997; Prasad, 2000; Adrian and Westerweel, 2011; Dantec Dynamics, 2014b). The research described herein uses a 2D3C PIV system, as described above.

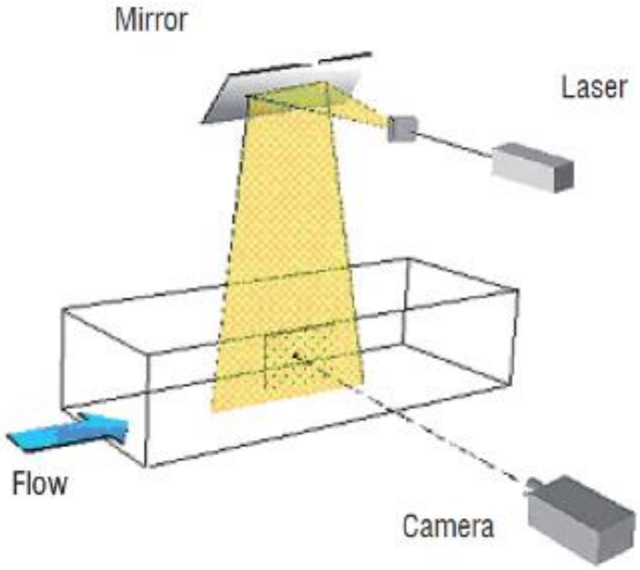

Figure 3.11: Typical set-up of a two dimensional PIV system (Brossard et al., 2009).

3.4.2. PIV system

A stereoscopic two camera, three-component, submersible, double-pulse laser Particle Image Velocimetry (PIV) system, manufactured by Dantec Dynamics, was used. The Nd:YAG laser was mounted on a Rexroth frame above the channel. The laser produces green light at a wavelength of 532nm and has a maximum output of 1000mJ. The laser optic was positioned ~2m downstream of the TST. The data were collected using two SpeedSense 1040 4 megapixel digital cameras mounted on a traverse system and encased in submersible housing. Mounting the cameras on the traverse system allowed the cameras to be positioned across a range of stream-wise, cross-stream and vertical positions. The submersible housing consisted of mirrors in either end to enable the cameras to view upstream and downstream positions within the channel looking through a clear Perspex channel wall. The layout and set-up of the PIV system is shown in figure 3.12. The flow was seeded using Plascoat Talisman 20, a copolymer coating powder with a specific gravity of 0.99g/cm^3. The powder was wet-sieved to refine the size of the seeding to be between 106µm and 212µm.

3.4.2.1 PIV Computer System

The PIV system was controlled and operated using two Dell Precision T5500 Workstation computers (shown in figure 3.12). Each computer had the same components and specifications, as detailed in table 3.1.

Table 3.1: PIV workstation computer specifications

Component	**Specification**
Hard Drives	Hard Disk Drive (HDD) = 1TB Seagate
	Solid State Drive (SSD) = 900GB Crucial
Motherboard	Main board = Dell Inc 0CRH6C
Central Processing Units (CPUs)	Main CPU = Intel Xeon E5620 2.4GHz
	Riser CPU = Intel Xeon E5620 2.4GHz
Random Access Memory (RAM)	Main board = 48GB (6x8GB DDR3-1333)
	Riser = 24GB (3x8GB DDR3-1333)
Operating System	Windows 7 Professional 64-bit

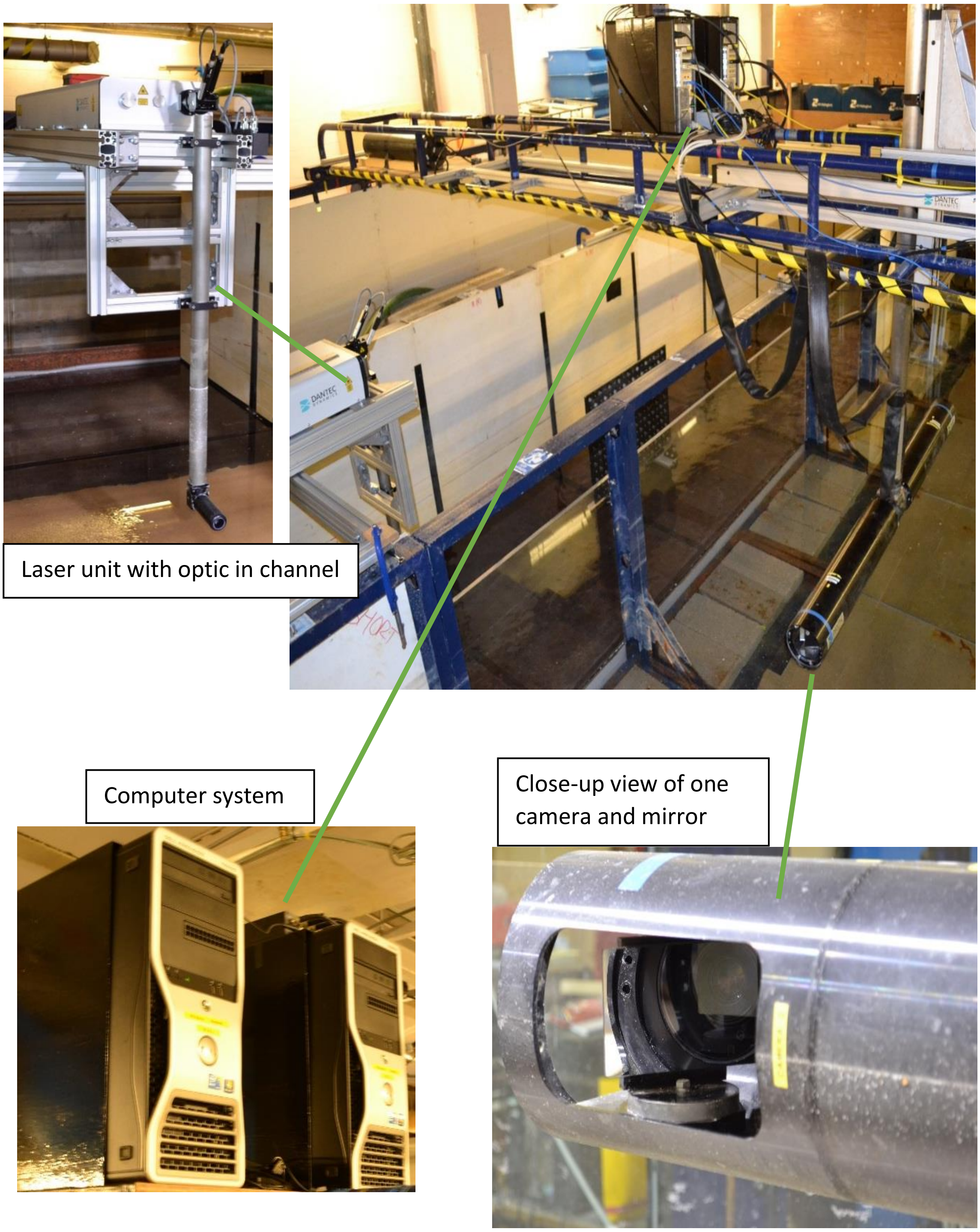

Figure 3.12: PIV system. Top right image shows an overview of the PIV system, and the inset images show close up views of the laser unit and optic, the computer systems and a close up view of one of the two 4MP cameras.

3.4.3. PIV system calibration

A 3D calibration, acquired using a multi-level target, was obtained so that the two camera images could be combined to derive 3D vectors of the flow. Figures 3.13 and 3.14 show the multi-level target used to obtain this 3D calibration. Figure 3.13 shows a close up view of this calibration target, whilst figure 3.14 shows the target location within the channel in postion for the calibration. The calibration was valid for all camera positions since the optics remained submerged and there were no changes in image refraction.

The calibration target was a multi-level dot matrix target (shown in figure 3.13) measuring 800mm by 600mm. It had a zero marker diameter of 7mm, an axis marker diameter of 5mm and main marker diameter of 5mm. The distance between the markers was 45mm and the distance between the two levels was 8mm.

In order to calibrate the PIV system, the calibration target was positioned in the centre of the channel, with the front of the multi-level target facing the PIV cameras. The side edge of the target was in line with the laser. The experimental flume was then filled with water to a depth of 0.6m. A single image of the calibration target was obtained for each camera. A Direct Linear Transform (DLT) imaging model fit, explained below and shown in figure 3.15, was generated for each camera in the Dantec Dynamics PIV software. The calibration target could then be removed to allow the rotor to be positioned within the channel. The calibration remained valid for all PIV measurements as the laser unit and cameras were always moved by equal amounts in the same cross-stream direction.

Figure 3.13: Multi-level target used to obtain a 3D calibration for the PIV system.

Figure 3.14: Calibration target within the channel. The PIV optic can be seen in the lower of the image, with the multi-level target visible upstream.

Table 3.2: Direct Linear Transformation imaging model fit numeric values

Camera 1			
A_{11}	**A_{12}**	**A_{13}**	**A_{14}**
-5.04936E+000	9.40687E-002	-2.01905E+000	1.15946E+003
A_{21}	**A_{22}**	**A_{23}**	**A_{24}**
-1.76228E-001	5.41108E+000	5.81209E-001	8.63159E+002
A_{31}	**A_{32}**	**A_{33}**	**A_{34}**
-2.14834E-004	-1.74757E-005	4.34205E-004	1.00000E+000
Camera 2			
A_{11}	**A_{12}**	**A_{13}**	**A_{14}**
-4.64337E+000	-5.65422E-002	3.08560E+000	1.16019E+003
A_{21}	**A_{22}**	**A_{23}**	**A_{24}**
2.12694E-001	5.49688E+000	5.14507E-001	8.64458E+002
A_{31}	**A_{32}**	**A_{33}**	**A_{34}**
2.09913E-004	-788319E-006	4.15132E-004	1.00000E+000

The calibration used a Direct Linear Transform (DLT) imaging model fit. This is derived from geometrical optics and is based on physics. It cannot describe non-linear phenomena such as the image distortion which occurs when measuring from air into water (Dantec Dynamics, 2016a). However, this was not an issue in the experiments during this study, as the PIV cameras were fully submerged in water. A DLT matrix can be described as follows:

$$\begin{bmatrix} k_x \\ k_y \\ k_0 \end{bmatrix} = \begin{bmatrix} A_{11} & A_{12} & A_{13} & A_{14} \\ A_{21} & A_{22} & A_{23} & A_{24} \\ A_{31} & A_{32} & A_{33} & A_{34} \end{bmatrix} \begin{bmatrix} \mathrm{X} \\ \mathrm{Y} \\ \mathrm{Z} \\ 1 \end{bmatrix} \qquad \text{Equation 5}$$

$$x = \frac{k_x}{k_0}, \qquad y = \frac{k_y}{k_0}$$

where X, Y, Z (uppercase) represent the object coorinates (in millimeters) and x, y (lowercase) represent the corresponding image co-ordinates (in pixels) (Dantec Dynamics, 2016a). *A* and *k* were not defined by Dantec Dynamics. Each of the two cameras requires a separate DLT calibration as each camera observes the light sheet from a different viewpoint to the other. The numeric view of the DLT for one camera is shown in table 3.2 and an image of the DLT over the calibration image (one camera only) is shown in figure 3.15.

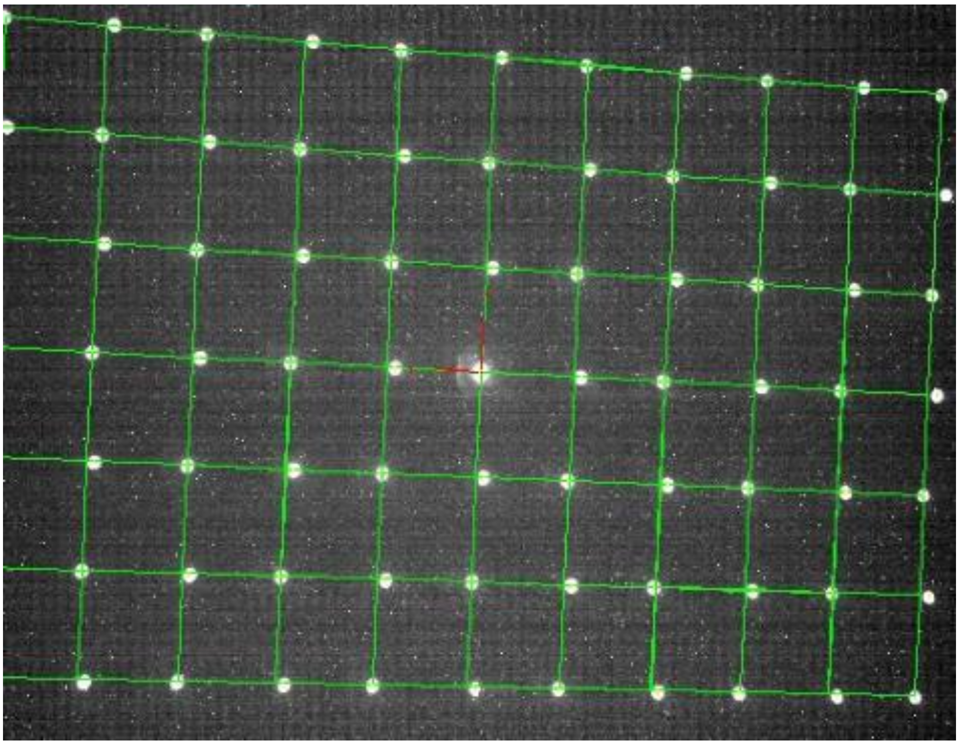

Figure 3.15: DLT over camera 1 PIV calibration image. This calibration was used during the experiments described herein.

Data was collected in such a manner that allowed the computation of three component velocity vectors in a two dimensional plane (i.e. a light sheet). This was achieved by combining data from the two PIV cameras using the above calibration. As each of the cameras views the light sheet from a different angle, the out-of-plane motion will be viewed different from each camera. It is this difference that can be exploited to infer the third velocity component and is due to the Scheimpflug condition (Dantec Dynamics, 2016b). Figure 3.16 shows this difference. The displacement is shown by the blue vector, and the green and red vectors show what it looks like from camera 1 and camera 2 respectively, when projected onto the light sheet or object plane (Dantec Dynamics, 2016b).

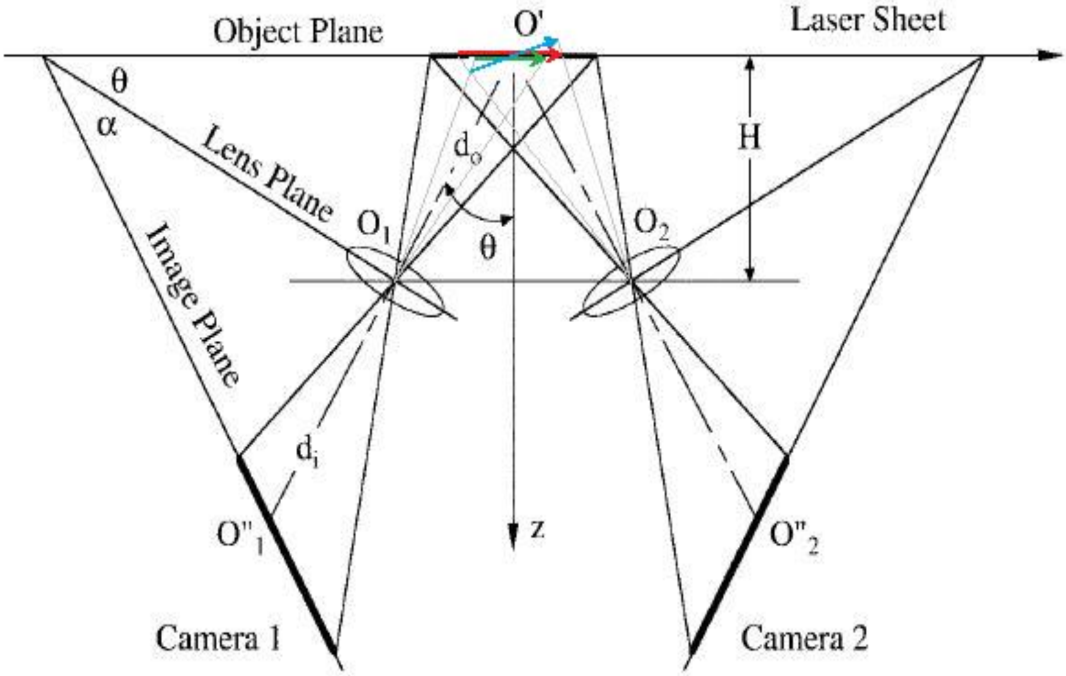

Figure 3.16: Illustration of the Scheimpflug condition for two PIV cameras. (Dantec Dynamics, 2016b).

3.4.4. PIV errors

PIV as a method of fluid velocity data collection is subject to a number of inherent sources of error. These include the use of the wrong particle seeding or inadequately seeded fluid, incorrect experimental conditions and setup, as well as improper use of processing algorithms (Huang *et al.*, 1997). Errors were minimised as far as possible during this research. Test data were collected to determine the quality of the data, the concentration of seeding within the flow and the calibration data prior to the full experimental programme being carried out. As the seeding powder had a size of 106µm and 212µm, this equated to an average particle size of 3.25 pixels, and an average of 17 particles per 32x32 pixel interrogation area. An interrogation area is a sub-window of the overall measured flow-field which is used to split up the analysis. There is overlap between each interrogation area. A seeding density of 10-20 particles for a 32x32 pixel interrogation area window size has been used by other researchers (e.g. Willert and Gharib, 1991). It has been determined that a seeding density of >5 particles per interrogation area, with each particle occupying between 3 and 6 pixels improves the effectiveness of the interpolation (Keane and Adrian, 1992; Hardy *et al.*, 2005). The seeding densities in the research described herein satisfy these conditions. The PIV images and camera calibration were deemed to be of an acceptable quality and reasonable accuracy, as the reprojection errors were approximately 0.8 pixels (camera 1) and 0.6 pixels (camera 2). This equates to approximately 0.15mm and 0.11mm for camera 1 and camera 2 respectively, and is within the acceptable region specified by Dantec Dynamics (2016b).

The potential errors in the PIV data collected were minimised as far as possible. Adaptive PIV, explained in more detail below, was used for the majority of the data processing to provide a higher quality data analysis. All reasonable steps were taken to achieve the highest quality data collection and analysis, and therefore errors in the velocities measured were minimised.

3.5 PIV data collection and analysis

The research described herein uses a 2-dimensional-3-component PIV system. The two cameras in the PIV system were operated in double frame mode, which resulted in a pair of images being recorded each time the camera was activated. When the double-pulsed laser was activated, the first pulse triggered the first frame to be captured, whilst the second frame was captured when the second laser pulse was fired. For the majority of the data collection, 5350 double frame images were captured for each camera. The images had a grid size of 2320 x 1726 pixels. A frequency of 50Hz was used for most data collection, with a set of high frequency (96Hz) measurements also taken in the area closest to the rotor. When a frequency of 50Hz was used, PIV data were collected for 107 seconds at each position. This was the maximum period of data collection possible due to the Random Access Memory (RAM) configuration available in the PIV system. When a frequency of 96Hz was used, PIV data were collected for 55 seconds at each position. Depending on the individual experiment series being run (detailed further in this section), either three or nine different camera positions were used for data collection, as shown in figure 3.17. The horizontal distance between the positions was ~290mm and the vertical distance between the positions was ~175mm. There was an overlap between each position to ensure that the flow field was fully captured, as shown in figure 3.17. The entire flow field could not be captured with four camera positions, and therefore three horizontal and three vertical locations were needed, equating to a total of nine camera positions. The positions of the images were such that the horizontal overlap between each position was the same, and the vertical overlap between each position was the same.

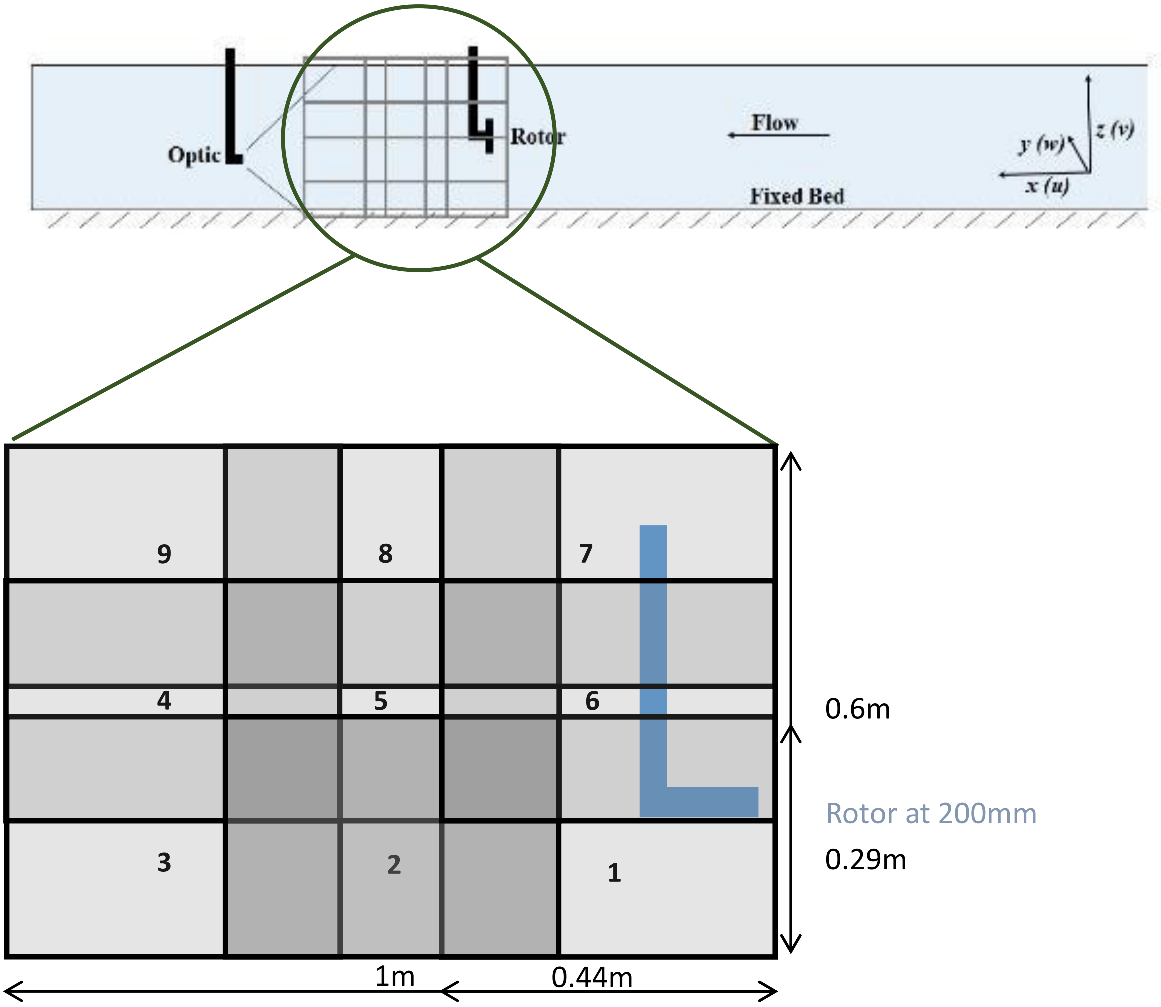

Figure 3.17: Basic schematic diagram of the flume set-up showing the location of the overlapping PIV image capture positions. Flow direction is from right to left. Inset: overlapping PIV slices. Thick black lines indicate the nine (numbered) slices. Darker filled areas indicate areas of overlap. (Not to scale).

3.5.1. PIV data analysis

The collected PIV data were initially processed using Dantec Dynamics' Dynamic Studio v4. The majority of the analysis of this data made use of adaptive PIV and adaptive correlation algorithms. The adaptive PIV algorithm will typically use a grid spacing of 16x16, and a minimum interrogation area size of 16x16 and a maximum interrogation area size of 32x32. This equates to a grid spacing of approximately 3x3mm.These grid spacing and interrogation area sizes were chosen based on preliminary test results. These were carried out in order to determine the grid spacing and interrogation area sizes which was most appropriate for the data collected, as well as for the processing time available. The processing time for the previously specified adaptive PIV grid spacing and interrogation area sizes is approximately twelve hours per 5350 images with a size of 2320x1726px (totalling approximately twenty four hours per slice of data collected) using a quad-core 3.60GHz desktop PC.

The adaptive correlation will typically use a grid size of 32x32. This equated to a grid spacing of approximately 6x6mm. Adaptive PIV will be used for the majority of the data processing as it produces higher quality results than adaptive correlation (Theunissen *et al.* 2007; Wieneke and Pfeiffer, 2010). This is achieved as the adaptive PIV algorithm adjusts the size of the interrogation area in relation to the seeding densities and flow magnitude and gradients within that area. However, adaptive correlation was used for some analysis since it is a much faster method of processing the data. Therefore, it can be used as an initial analysis prior to further, more detailed analysis being carried out. The processing time for the previously specified adaptive correlation grid spacing is approximately thirty minutes per 5350 images with a size of 2320x1726px (totalling approximately one hour per slice of data collected) using a quad-core 3.60GHz desktop PC.

Following the adaptive PIV and adaptive correlation analysis being carried out, the data will be further analysed using stereo PIV in order to combine the data from the two cameras to provide three-component data. Vector statistics can then be derived from this information in order to determine the mean flow characteristics at each position. For the PIV data collected with a flow consisting of waves, the vector statistics will be produced selectively using conditional sampling in order to separate the various stages of the waves (i.e. the wave crests and wave troughs) passing the rotor. The vector statistics will be further processed in data visualisation software Golden Software Surfer v11, to produce contour and flow maps.

3.5.1.1. Estimating Shear Stress

The vector statistics produced by analysing the PIV data can also be further analysed in order to calculate the bed shear stress within the channel. Shear stress is an important component to consider when linking flow conditions to sediment transport (Biron *et al*, 2004). It is key in explaining the force acting upon sediment particles (Sulaiman *et al.,* 2013). When bed shear stress exceeds the critical shear stress level, sediment transport occurs (Luque, 1974; Wu *et al.*, 2010). It is, however, difficult to accurately estimate this variable. Due to this, there are a number of different methods for estimating bed shear stress (Biron *et al.,* 2004). These estimates include Law of the Wall, Reynolds stress, and turbulent kinetic energy (TKE) (Biron *et al.,* 2004; Pope *et al.*, 2006). The accuracies of the various methods varies considerably depending upon the environment and conditions in which they are used, such as varying boundary layers and in simple or complex flow fields (Biron *et al.,* 2004).

Law of the wall

The law of the wall approach is related to the von Karmet-Parndtl equation. Therefore, law of the wall can be defined as:

$$\frac{u}{u_*} = \frac{1}{\kappa} \, ln\left(\frac{z}{z_0}\right) \qquad \text{Equation 6}$$

where u is the velocity at height z above the bed, u_* is the friction or shear velocity, z_0 is the roughness length and κ ($\approx$0.4) is the von Karmen constant (Biron *et al.,* 2004; Sime, 2007). The shear velocity (u_*) can be defined as:

$$u_* = (\tau_0/\rho)^{0.5} \qquad \text{Equation 7}$$

where ρ is the density of the fluid (Biron *et al.,* 2004).

The relationship between u_* and bed shear stress τ_0 is defined thus as:

$$\tau_0 = \rho {u_*}^2 \qquad \text{Equation 8}$$

where ρ is the density of the fluid (Pope *et al.* 2006). Although the law of the wall is a commonly used method of estimating shear stress, its validity in complex flow fields is uncertain (Biron *et al,* 2004; Pope *et al.,* 2006).

Reynolds stress

Shear stress derived from Reynolds stress can be defined as:

$$\tau_0 = \rho(-u'w') \qquad \text{Equation 9}$$

where *u'* and *w'* represent the standard deviation of the stream-wise (*u)* and vertical (*w*) velocity components respectively (Pope *et al.,* 2006). The Reynold stress method may be unsuitable in some situations such as those which include meandering or rotating flows (Kim *et al.*, 2000).

The friction or shear velocity (u_*) cannot be measured directly as it is a derived quantity (Pope *et al.*, 2006). However, for fully turbulent flow, a direct estimation of u_* can be derived using:

$$u_* = -\overline{u'w'} \qquad \text{Equation 10}$$

where *u'* and *w'* denote the standard deviation of the stream-wise (*u*) and vertical (*w*) velocity components respectively (Kim et al., 2000).

Turbulent kinetic energy

Turbulent kinetic energy, k, is defined as:

$$k = \frac{1}{2}\,(\overline{u'^2} + \overline{v'^2} + \overline{w'^2}) \qquad \text{Equation 11}$$

where *u', v'* and *w'* denote the standard deviation of the stream-wise (*u*), cross-stream (*v*) and vertical (*w*) velocity components respectively. The ratio of TKE to shear stress is constant, and the TKE represents the product of the absolute intensity of velocity fluctuations and variances from the mean velocity (Pope *et al.*, 2006). The ratio of TKE to shear stress has been determined to be constant. Therefore, the relationship between shear stress and TKE can be defined as:

$$\tau_0 = C_1 k \qquad \text{Equation 12}$$

where C_1 is the constant. Previous studies such as Stapleton and Huntley (1995), Thompson *et al.* (2003) and Pope *et al.* (2006) have used a C_1 value of ~0.19.

No single method of estimating shear stress can be identified as perfect, and each one has advantages and disadvantages. However, the turbulent kinetic energy approach has been identified as one of the most reliable and consistent methods of estimating shear stress (Kim *et al.,* 2000; Thompson *et al.,* 2003). This research will mainly use turbulent kinetic energy as an estimator of shear stress, but the other methods of estimating shear stress will be considered and compared.

3.5.2. Measurement programme

A series of different measurements were collected in order to address the research objectives specified in chapter 1. These examined wake development and asymmetry, wake interaction and wake modification by waves. More information about these measurements is provided in the following sections within this chapter.

Data was collected in a number of different flow conditions for the rotor housing without the turbine blades in place. This data allowed any effects that the rotor housing has on the flow to be determined and accounted for. However, preliminary analysis of the results indicates that the vertical extents of the wake are in line with the blade tips, which indicates that the housing has little, if any, impact on the turbine wake.

3.5.2.1. Wake development and asymmetry

A series of measurements were taken to capture the full flow field and attempt to identify any asymmetry in the turbine wake. Table 3.3 shows the locations of the slices which were taken on either side of the rotor centreline. The location of these slices relative to the channel can be seen in figure 3.18. In all cases, the rotor was located at 120mm (0.6D) above the channel bed. This distance above the bed was determined to be the height at which the rotor led to sediment transport being initiated, as detailed in chapter 5.

Table 3.3: Details of the slices taken to investigate wake development and asymmetry

Measurement position	**Number of slices**
1D to left hand side of centreline	3
0.5D to left hand side of centreline	3
Centreline	3
0.5D to right hand side of centreline	3
1D to right hand side of centreline	3

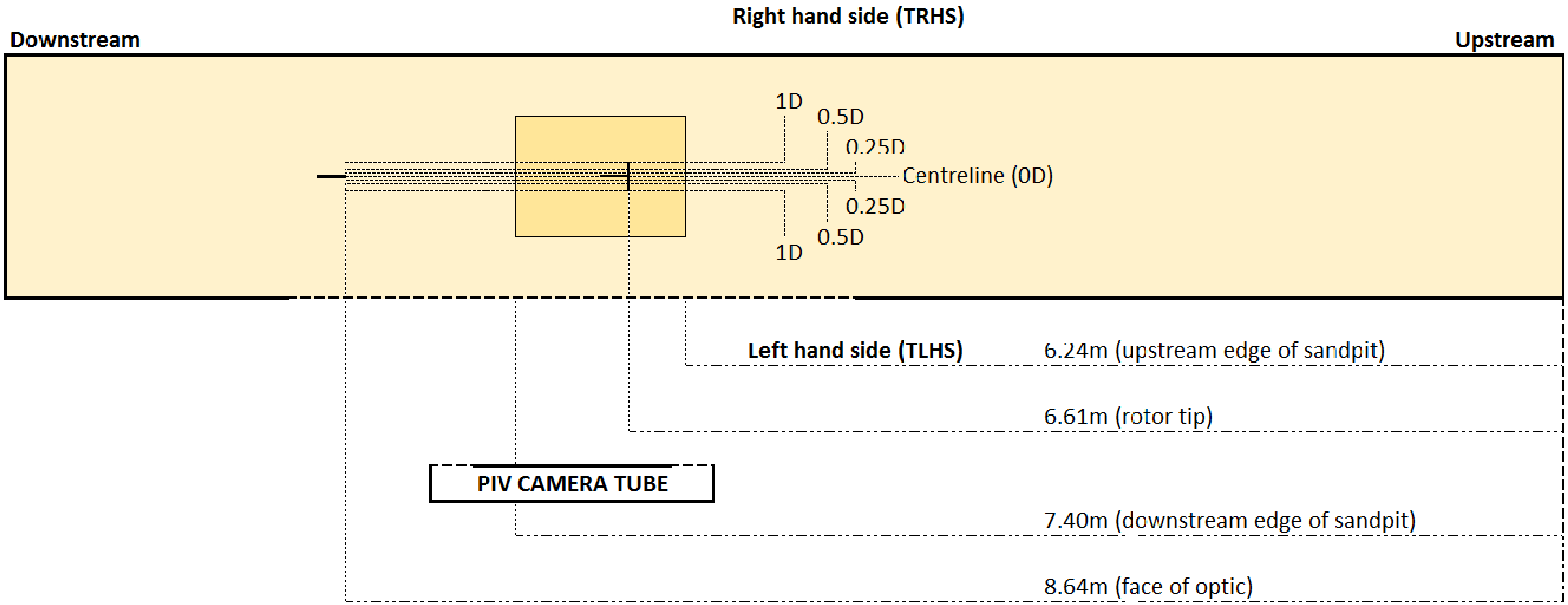

Figure 3.18: Flume schematic showing the locations where PIV data were collected during the wake asymmetry experiments. Flow direction is from right to left.

3.5.2.2. Wake interaction with bed and distance to bounding surface

Measurements were taken with the rotor at a number of different heights within the water column, as detailed in table 3.4, with the highest being with the rotor at 300mm above the bed, and the lowest being 120mm above the bed. The height above the bed is measured from the centre of the rotor, rather than the tip of the blades.

Under standard flow only conditions, when the rotor was at 300mm and 200mm above the bed, 9 slices of data were collected for each rotor height. When the rotor was between 180mm and 120mm above the channel bed, a total of 3 slices of data were collected for each rotor height. At these rotor heights, three PIV slices close to the channel bed were deemed sufficient to capture the full wake flow field.

Table 3.4: Details of the slices taken for each of the rotor heights

Rotor Height Above Bed (mm)	**Slices on the centreline**
300	9
200	9
180	3
160	3
140	3
120	3

3.5.2.3. Wake modification by waves

When the flow conditions included waves, six different wave scenarios were used, with varying wave frequencies and wave heights. The waves were generated using wave paddles at the upstream end of the flume. Two wave paddles which covered the width of the channel generated regular waves, parallel to the channel sides, at a user controlled size and frequency. At the downstream end of the channel, a wave dissipation board was installed to break up the waves and minimise any wave reflection. The wave sizes and frequencies chosen ranged from small 1Hz 6cm waves, to 1Hz 10cm waves, with two scenarios with a wave height of 10cm and frequencies of 1Hz and 1.5Hz. These three wave scenarios were run over a fixed bed.

Table 3.5 details the locations of the slices of data that were collected for each wave scenario with a fixed bed in place. In all cases, the rotor was positioned at 200mm above the channel bed. This allowed a comparison to a range of different scenarios that were carried out with the same rotor position above the bed as part of the INSTRON project. This additional data is not presented in this thesis. In all of the different flow conditions, data were also captured for the plain channel (i.e. without the rotor and housing in place) in order to allow the influence of the rotor on the flow to be determined. In these experiments, there was no rotor and no housing, and data was captured along the channel bed on the centreline plane of the rotor. However, the plain channel data is not presented in this thesis.

Table 3.5: Details of the slices taken with wave-current flow over a fixed bed with the rotor at 200mm above the bed.

Wave frequency and height	**Flow**	**Slices on the centreline**
None – flow only	Yes	9
1Hz 6cm	Yes	9
1Hz 10cm	Yes	9
1.5Hz 10cm	Yes	9

3.6 Wave gauge data collection and analysis

In order to quantify the waves which were generated during the experiments, data were collected using 8 wave gauges, manufactured by HR Wallingford, situated at approximately 1 metre intervals down the length of the channel. There were 6 wave gauges positioned upstream of the TST and 2 wave gauges positioned downstream of the TST. They were positioned approximately 10cm from the right hand side wall in order to minimise the impact that they had on the flow and turbine wake. As the waves were generated as regular waves, it was deemed that they would be symmetrical across the width of the channel. Figure 3.19 shows a number of the wave gauges situated within the channel, as well as a close up view of the wave gauge which was situated furthest downstream close to the laser optic. Data were collected from the wave gauges during each run which consisted of waves. The data collection software (TracerDAQ) was externally triggered by the PIV system. This allowed the wave gauge data collection to be exactly coincident with the PIV data collection, allowing cross referencing between the data. Wave gauge calibration data were collected at the start and end of each day.

Figure 3.19: Left image: Wave gauges situated along the right hand side of the channel. Right image: Close up of furthest downstream wave gauge, positioned close to the laser optic.

3.6.1. Wave gauge data calibration

The raw data collected from the 8 wave gauges was in millivolts. This data needed to be calibrated in order for the data to be converted from millivolts to metres. At the start and end of each day, calibration data was collected for 2 minutes at three different wave gauge heights. This calibration data could then be used to determine the intercept and slope in order for a regression equation to be applied. The regression equation is:

$$Y = mx + c \qquad \text{Equation 13}$$

where Y refers to the dependent variable (in this case it refers to the depth/wave height), m is the gradient of the regression line, c is the intercept and x is the independent variable (in this case, the raw voltage measured by the wave gauges). For the data collected during the research described herein, the linearity of the slope was between 1.000 and 0.998.

3.6.2. Wave gauge data analysis

Once the value of the calibration coefficients had been determined, equation 13 could be applied to the raw wave gauge data. This enabled the raw data of millivolts to be converted into metres, and therefore the wave height could be determined. The wave heights measured throughout the entire measurement period could then be processed as required. This included finding the maximum wave height, the average wave height, and the minimum wave height, amongst other measurements and outputs.

The wave gauge data were used to determine when the wave crests and wave troughs occurred. Peaks and troughs in wave heights indicated a wave crest or wave trough was present. The time stamp from the wave gauge data was then matched to the time stamp on the PIV data to enable the wave crests and wave troughs to be separated within the PIV data to allow conditional sampling of the data.

Wave gauges 5 and 6 (shown in figure 3.3) were the primary wave gauges used for the conditional sampling. At the point at which a wave trough was recorded passing wave gauge 5, a time lag was elapsed according to the speed at which the wave was moving down the channel, and the distance the wave crest had to travel to reach the first PIV measurement position (as shown in figure 3.17). The accuracy of the speed and timing of the wave was verified using the data at wave gauge 6. Therefore, for each of the 9 PIV positions, the wave trough was positioned approximately in the horizontal centre of the measurement window. This process was carried out for all measurement positions (as shown in figures 3.17 and 3.20), adjusting the time lag depending on the distance of the PIV measurement position from wave gauge 5. Each flow map comprised of the 9 different PIV positions overlapped and combined. Therefore, each flow map shows the majority of the flow field under a wave trough, rather than only a small part of the flow field being under a wave trough. The same process was applied for wave crests.

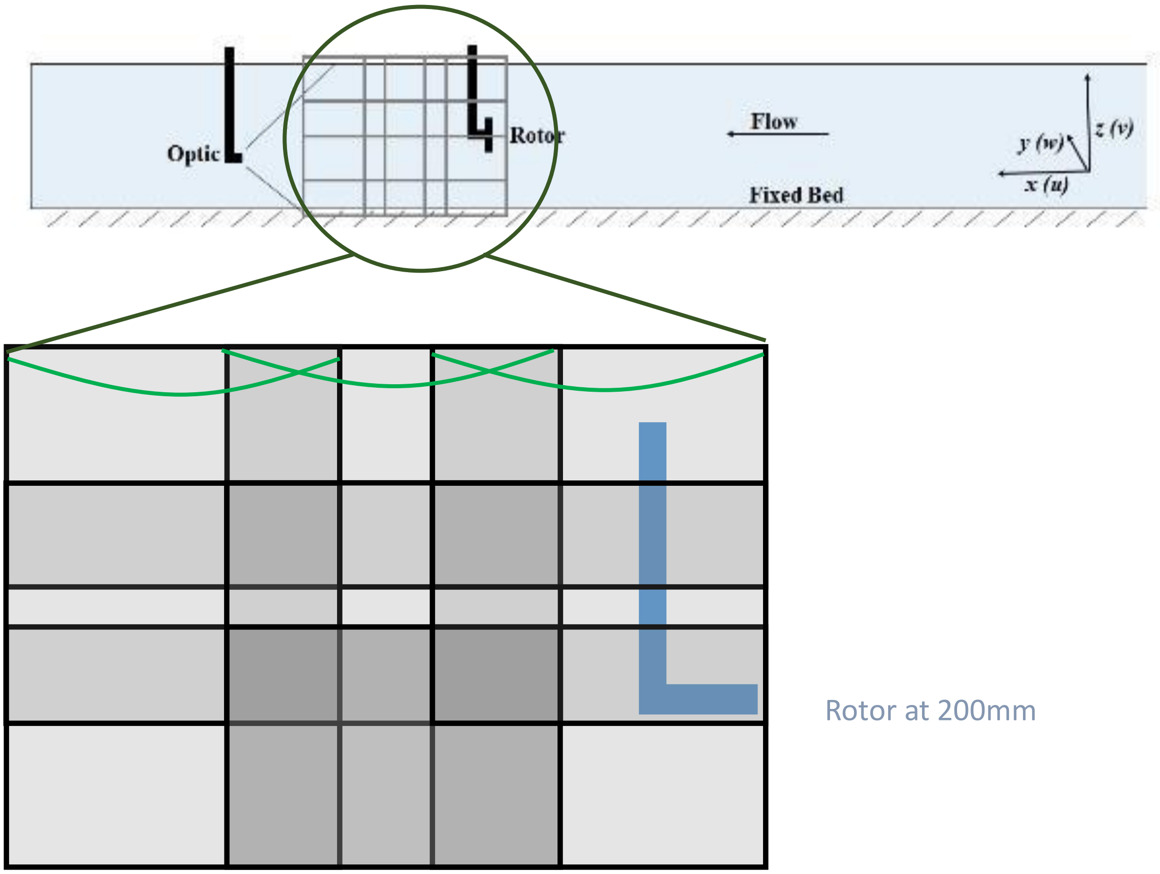

Figure 3.20: Basic schematic diagram of the flume set-up showing the location of the overlapping PIV image capture positions and position of waves. Flow direction is from right to left. Inset: overlapping PIV slices. Thick black lines indicate the nine slices. Darker filled areas indicate areas of overlap. Green lines indicate approximate position of wave troughs within measurement windows (Not to scale).

3.7 Summary

This chapter has detailed the experimental programme used to collect and analyse the data used in this thesis. The facilities and instrumentation used in this thesis have been described and explained. A number of different flow conditions were produced in the Total Environment Simulator experimental flume, and the velocities were measured using Particle Image Velocimetry. In the cases where waves were generated, wave data was collected using wave gauges. The Particle Image Velocimetry data was analysed to determine the flow field downstream from the tidal stream turbine.

Chapter 4

Wake Development and Asymmetry

How does the wake downstream from a tidal stream turbine develop?

This chapter presents the results of an experimental investigation to evaluate how the wake downstream of a tidal turbine develops and will examine the cross-channel asymmetry in the wake.

4.1 Introduction

To date, there is a lack of laboratory data and numerical modelling which identifies and characterises the development of flow asymmetry in the wake of tidal stream turbines. There are some limited data covering wake asymmetry behind other objects. One example is hydrofoils, where wake asymmetry was identified by Ellenrieder and Pothos (2008). However, Ellenrieder and Pothos (2008) focussed more on vertical wake deflection and asymmetry, rather than cross-channel wake asymmetry (i.e. asymmetry to the left and right of the centreline, rather than above and below the centreline). The asymmetry of wind turbine wakes has also been studied (e.g. Tescione *et al.,* 2014), but there are differences between the fluid dynamics of wind and water, as well as between the dynamics of different turbine structures. Therefore, there is a need to identify and understand the development of flow asymmetry behind tidal stream turbines, due to the potential impact which it may have upon future large scale developments, particularly in tidal stream turbine farms.

4.2 Methodology

This chapter will use experimental data collected during a series of experiments in which a 0.2m diameter tidal stream turbine was positioned at 120mm above the channel bed, and measurements were taken on the centreline, as well as up to 1 rotor diameter either side of the centreline (as described in Chapter 3). This chapter will look at the flow velocity deficit in the wake, as well as the flow direction, to understand wake development and growth downstream from the rotor. This chapter will also look at the cross-stream asymmetry that is present in the turbine wake.

Results are presented for the stream-wise velocity (*u*), vertical velocity (*w*), cross-stream velocity (*v*) velocity components for the centreline as well as 0.5D and 1D either side of the centreline. Results are also presented for the shear stress, using turbulent kinetic energy (*k*) of the flow (see equation 11) and the Reynolds stress (*u'w')* (see equation 9), which can be used as a method of estimating shear stress (Biron *et al.,* 2004; Pope *et al.*, 2006). In order to account for asymmetrical onset flow within the channel, velocity values are normalised using the plain channel data for the centreline and the data from 1D either side of the centreline for the left hand side and right hand side of the channel. It was determined that 1D either side of the centreline was sufficiently far from the wake zone to allow this data to be representative of the plain channel.

The stream-wise velocity will be used to identify the wake extent and asymmetry based on the velocity deficit. Cross-stream and vertical velocities will be used to understand wake interaction with the surrounding flow and the internal wake structure. The estimators of shear stress (turbulent kinetic energy and Reynolds stress) will be used to identify the turbulent structures and to understand wake recovery.

4.3 Results

On the centreline, the wake extends to the blade tips (1 rotor diameter), both horizontally and vertically, with the greatest velocity deficit occurring close to the rotor (figure 4.1 (b) and figure 4.2 (a) to (c)). Along the entire length of the measured wake area, the wake appears to interact with the channel bed.

At 0.5D from the centreline, there is a significant difference in the wake length at either side of the centreline (figures 4.1 (a) and (c)). The wake of the TST is significantly longer towards the left hand side of the TST, with a slower wake recovery (figures 4.2 (a) to (c)). The difference in velocity is greatest closest to the rotor, between 1 and 2 rotor diameters downstream (figures 4.1 (a) to (c), 4.2 (a) to (c) and 4.3). The flow on the left hand side of the channel is ~12% greater along the vertical rotor centreline than on the right hand side of the channel. As distance downstream from the rotor increases, the differences between the right hand side and the left hand side of the channel become more pronounced. The boundaries of the wake are less well defined on the left hand side of the channel due to the wake interacting with the channel bed. The interaction between the wake of the TST and the flow above the channel bed on the left hand side of the channel begins at approximately 1 rotor diameter downstream of the TST and the interaction increases with distance downstream.

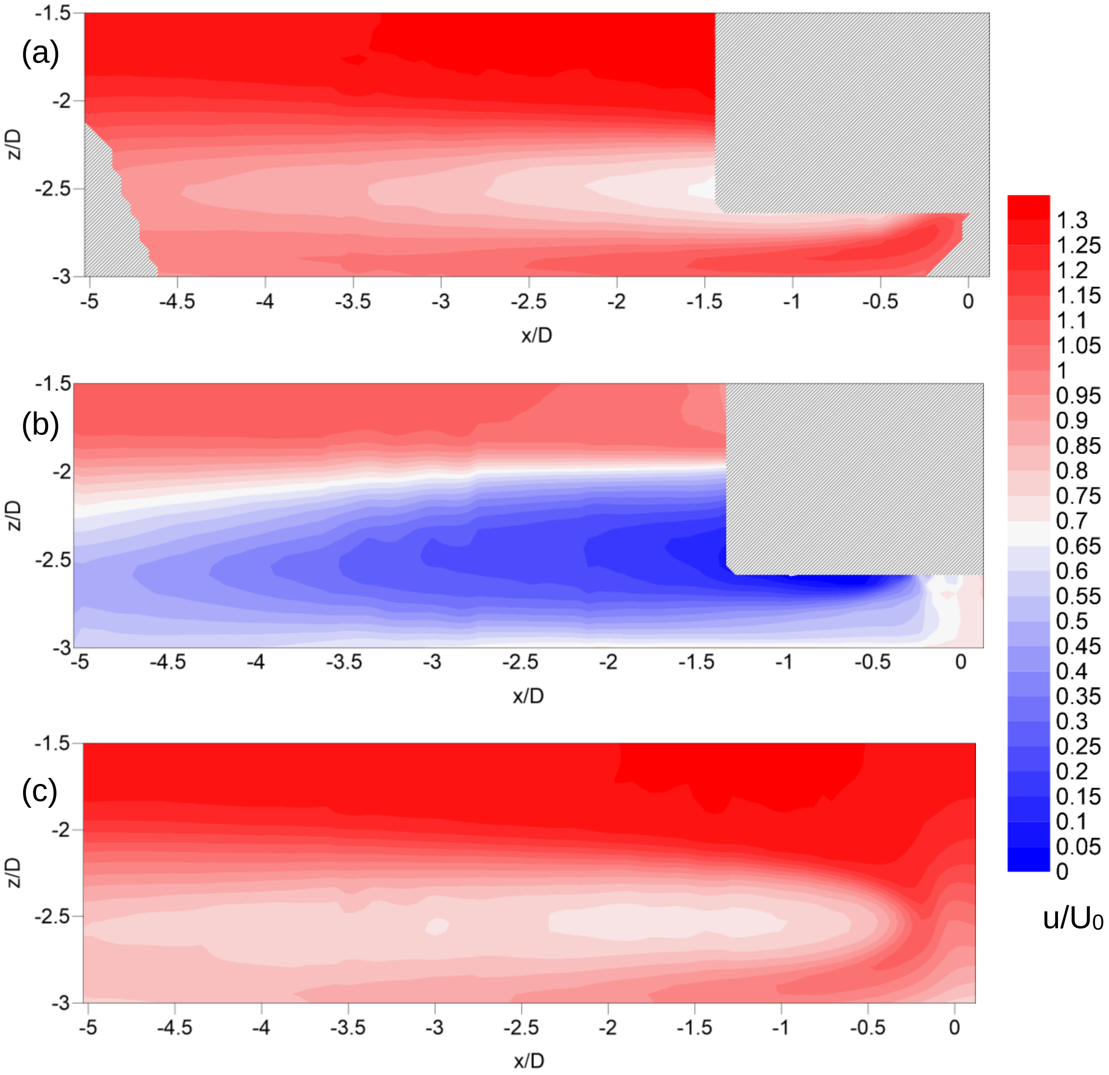

Figure 4.1: Flow structure maps for normalised stream-wise (u) velocity component for (a) 0.5D to the right hand side of the centreline (b) centreline (c) 0.5D to the left hand side of the centreline. Normalising velocities: right hand side = $0.26ms^{-1}$, centreline = $0.29ms^{-1}$, left hand side = $0.27ms^{-1}$. Scales on the axes are normalised to rotor diameters (200mm). Areas covered by upward diagonal line shading indicate areas where data could not be collected as the camera image was obstructed by the rotor and housing or the channel support structure.

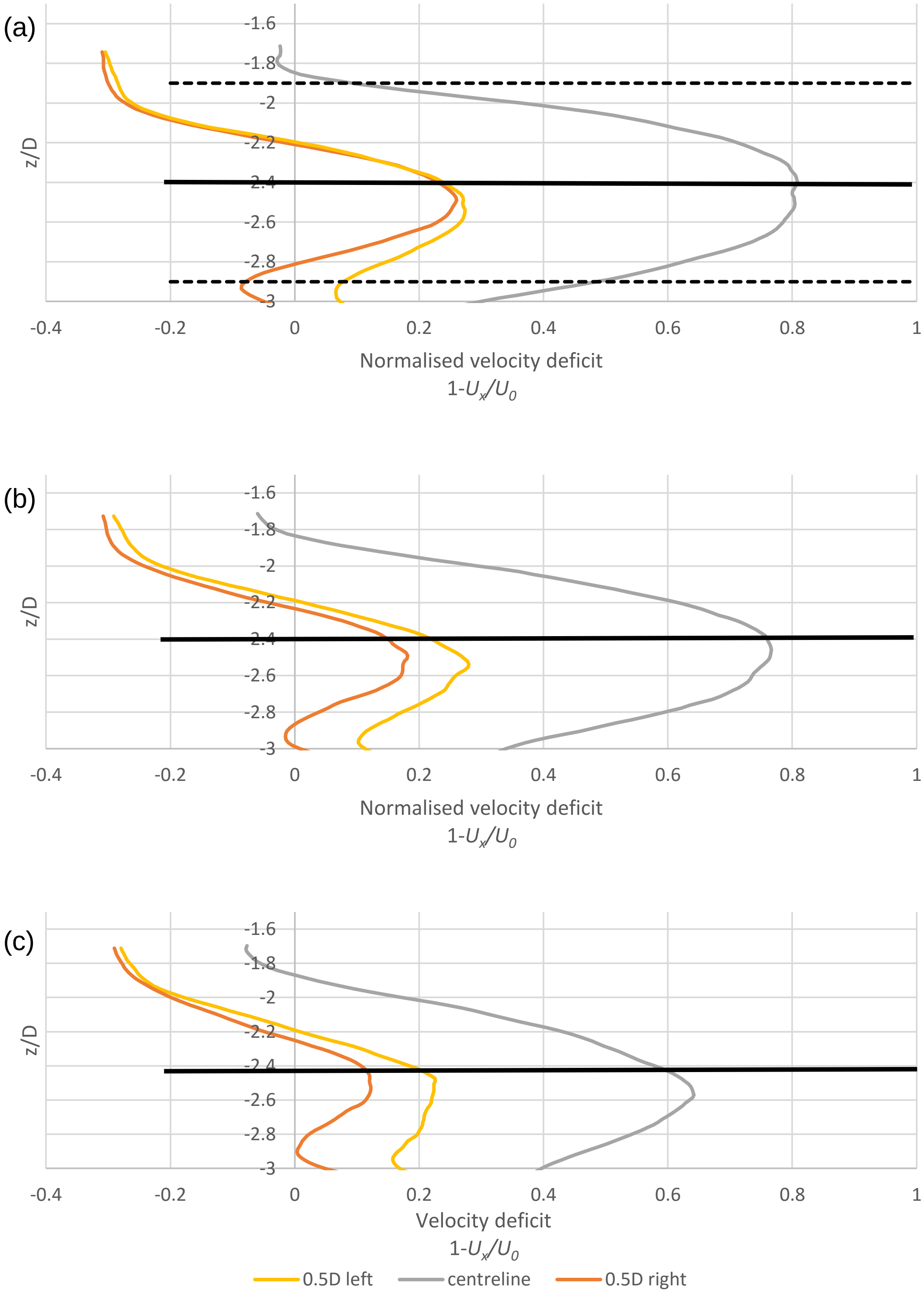

Figure 4.2: Normalised velocity deficit profiles at all measurement positions at (a) 2 rotor diameters downstream from the turbine (b) 3 rotor diameters downstream from the turbine and (c) 4 rotor diameters downstream from the turbine. Scales on the y-axes are normalised to rotor diameters (200mm). Y-axis origin is water surface. Solid black line indicates rotor centreline. Dashed black lines indicate blade tips.

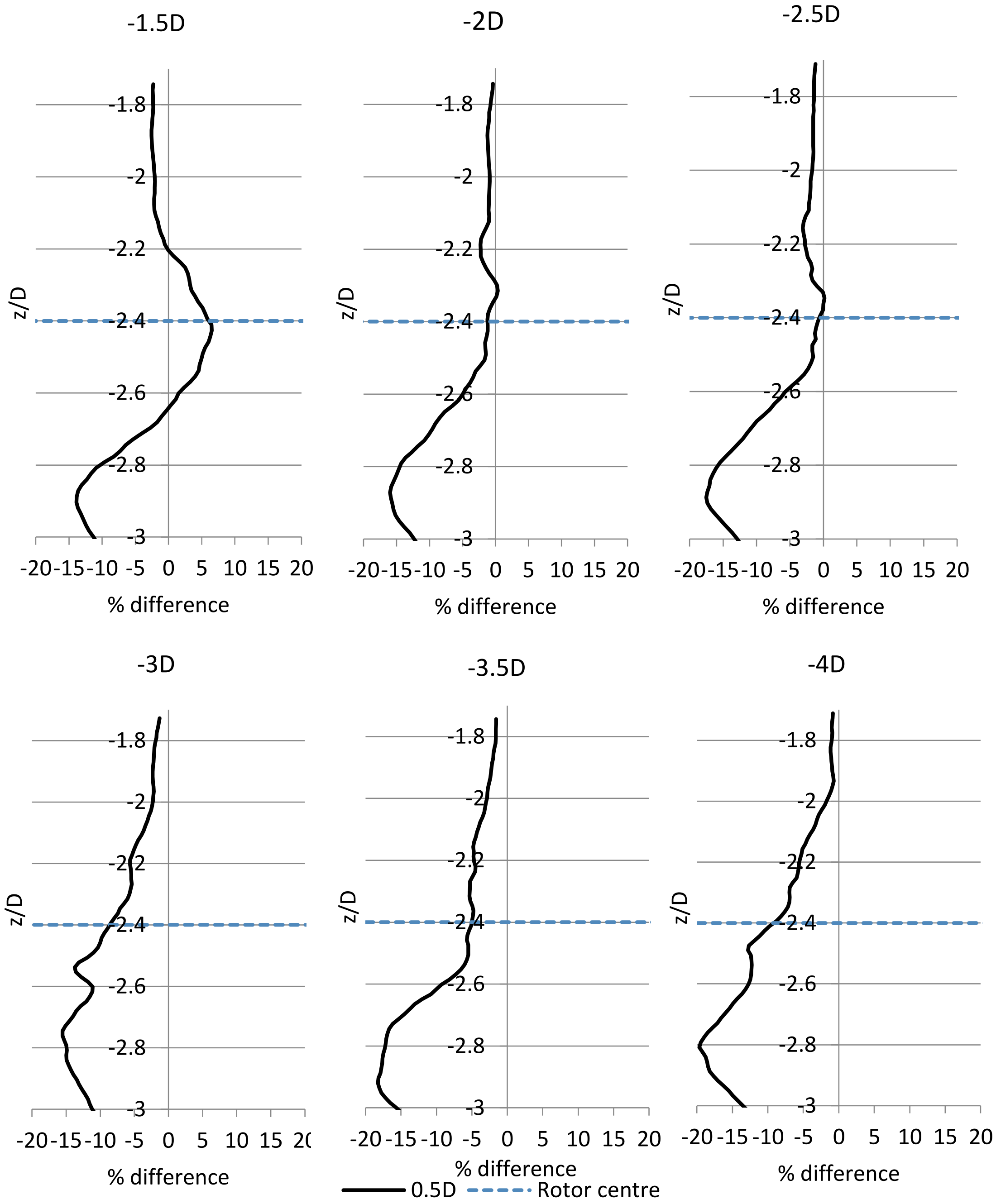

Figure 4.3: Plots showing the percentage difference in the normalised stream-wise velocity (u) between the left hand side of the centreline and the right hand side of the centreline at 0.5D from the centreline. These are taken at (from top left to bottom right) 1.5D, 2D, 2.5D, 3D, 3.5D and 4D downstream of the rotor. A value greater than 0% indicates left hand side is greater than right hand side.

On the centreline (figure 4.4 (b)), there is an area of upwelling immediately beneath the rotor. Further downstream, there is downwelling below the wake and upwelling above the wake. At 0.5D off the centreline (figures 4.4 (a) and (c)), there are clear differences in the direction of the vertical flow. On the left hand side of the centreline, there is upwelling above the wake and downwelling below the wake. On the right hand side of the centreline, there is strong upwelling in the wake area, with an area of downwelling above and below the wake.

On the centreline (figure 4.5 (b)), immediately downstream, there is positive negative cross stream flow above and below the wake, and positive cross-stream flow within the wake. From approximately 2 rotor diameters downstream, there is positive cross-stream flow on the edge of the wake, and negative cross-stream flow within the centre of the wake. There are noticeable differences in the cross-stream velocity on the right hand side and the left hand side of the centreline. At 0.5D from the centreline (figures 4.5 (a) and (c)), there is a strong negative cross-stream flow below and immediately downstream of the rotor on the right hand side of the centreline, and strong positive cross-stream flow below and immediately downstream of the rotor on the left hand side of the centreline. Further downstream, there is positive cross-stream flow on the right hand side of the centreline and negative cross-stream flow on the left hand side of the centreline.

Close to the rotor (approximately 1.5 rotor diameters downstream), on the centreline, areas of upwelling correspond to areas of positive cross-stream flow, and areas of downwelling correspond to areas of negative cross-stream flow.

At 0.5D from the centreline, areas of upwelling occur in approximately the same location as areas of negative cross-stream flow and areas of downwelling occur in the same location as areas of negative cross-stream flow.

On the centreline, there is an increase in the turbulent kinetic energy (k) immediately downstream of the rotor (figure 4.6 (b)). There are two separate regions of increased magnitude of k which develop, with the lower of the two regions having a much smaller increase in k than the upper region. There is interaction between the lower region of k and the channel bed. At 0.5D from the centreline, there is a greater increase in the magnitude of k on the left hand side of the centreline compared to the right hand side, particularly beyond 2 rotor diameters downstream from the rotor (figures 4.6 (a) and (c) and 4.7). The increase in the magnitude of k occurs over a larger area on the left hand side of the centreline than on the right hand side of the centreline. By 3 rotor diameters downstream, the turbulent kinetic energy (TKE) on the left hand side of the centreline is approximately 100% greater than the TKE on the right hand side of the centreline above the wake, and approximately 60% greater within the wake.

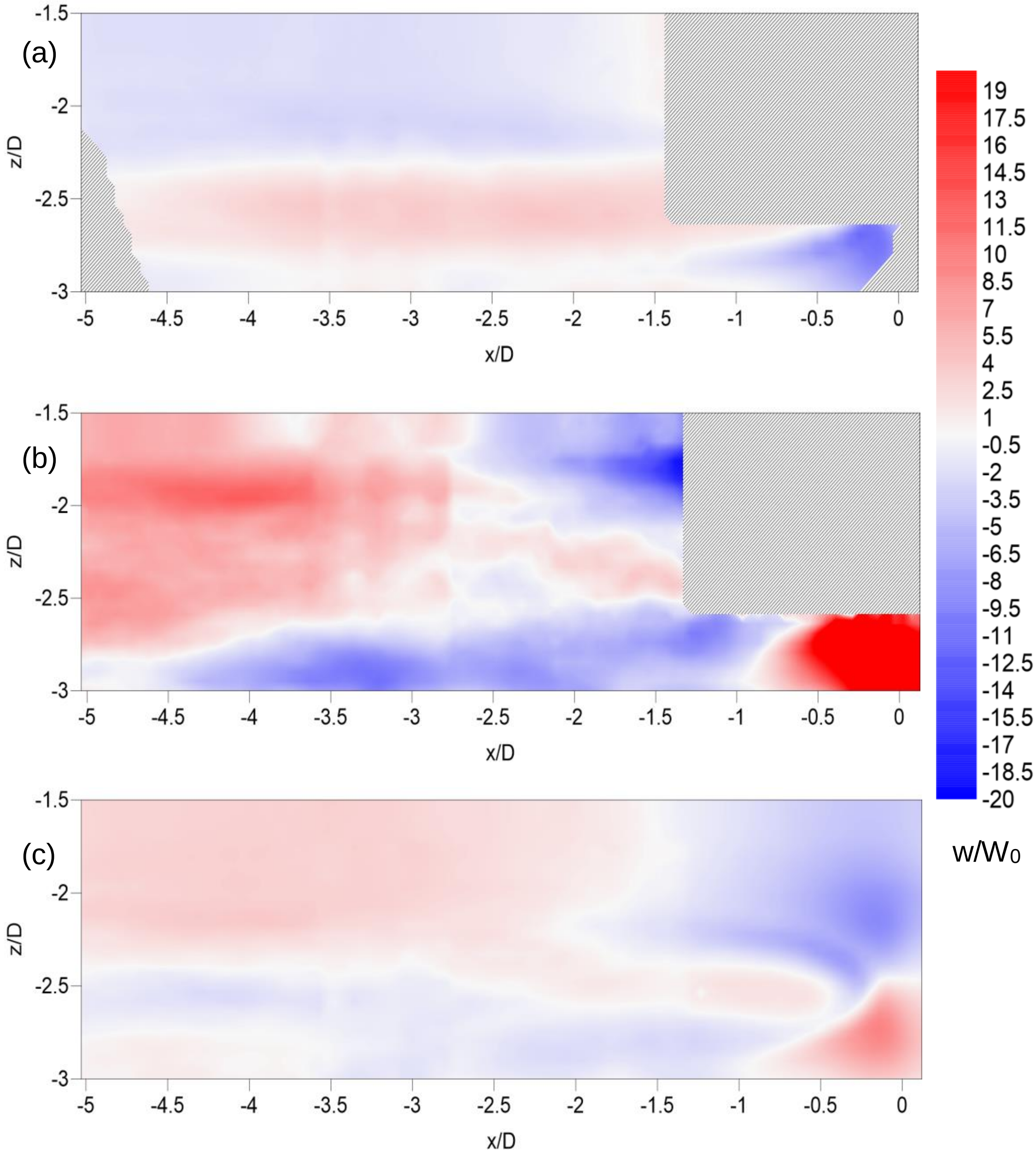

Figure 4.4: Flow structure maps for normalised vertical (w) velocity component for (a) 0.5D to the right hand side of the centreline (b) centreline (c) 0.5 to the left hand side of the centreline. Normalising velocities: right hand side = 0.002ms^{-1}, centreline = -0.0009ms^{-1}, left hand side = -0.002ms^{-1}. Scales on the axes are normalised to rotor diameters (200mm). Areas covered by upward diagonal line shading indicate areas where data could not be collected as the camera image was obstructed by the rotor and housing or the channel support structure.

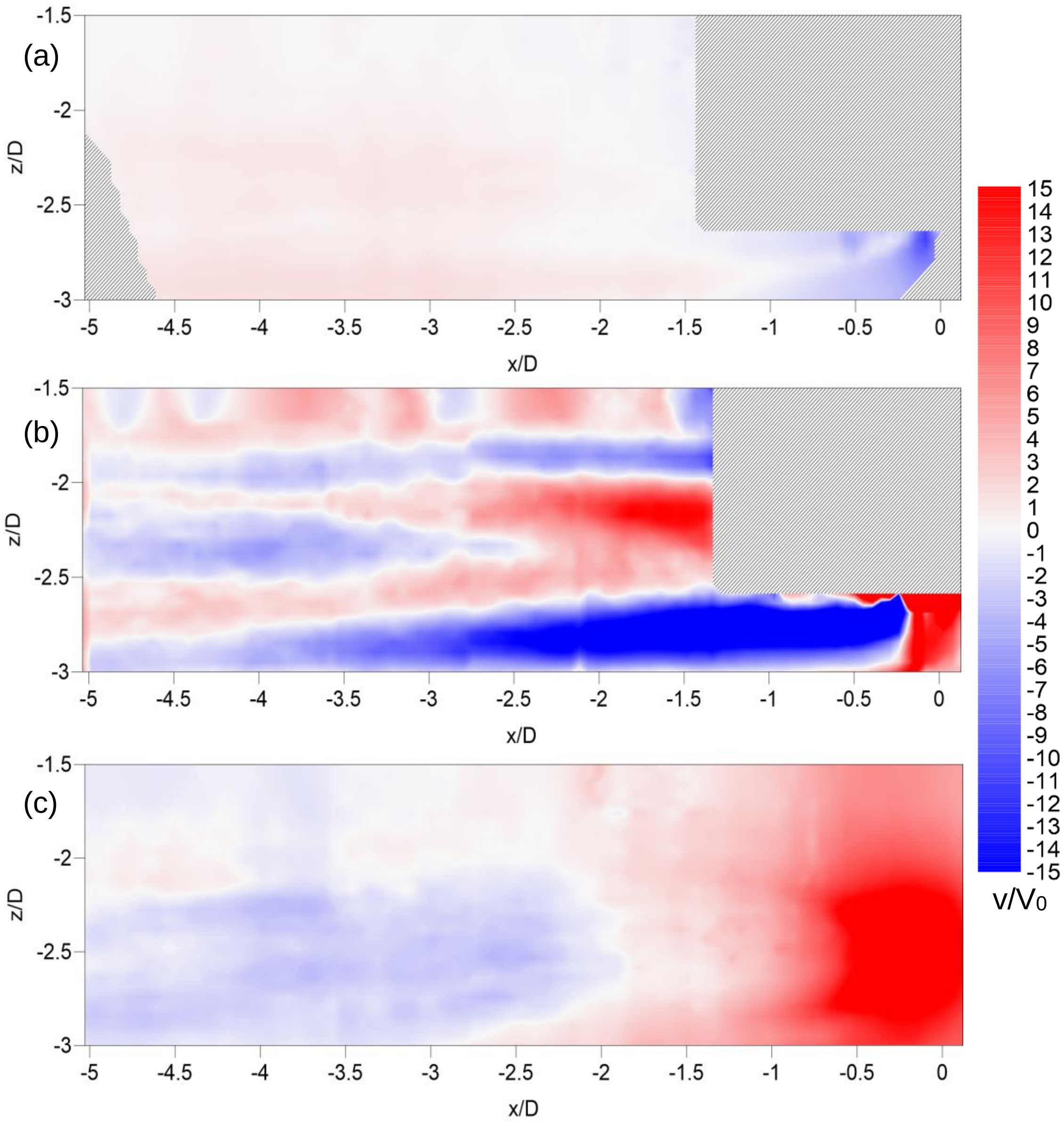

Figure 4.5: Flow structure maps for normalised cross-stream (v) velocity component for (a) 0.5D to the right hand side of the centreline (b) centreline (c) 0.5D to the left hand side of the centreline. Normalising velocities: right hand side = -0.007ms^{-1}, centreline = -0.0013ms^{-1}, left hand side = -0.002ms^{-1}. Scales on the axes are normalised to rotor diameters (200mm). Areas covered by upward diagonal line shading indicate areas where data could not be collected as the camera image was obstructed by the rotor and housing or the channel support structure.

On the centreline, the increase in Reynolds stress is concentrated around the wake area that is in line with the rotor blade tips (figure 4.8 (b)). There are two separate regions of increased Reynolds stress which develop, with the lower of the two regions having a smaller increase in Reynolds stress than the upper region. At 0.5D from the centreline, there is a greater increase in the Reynolds stress on the left hand side of the centreline compared to the left hand side of the centreline (figures 4.8 (a) and (c) and 4.9). The increase in the Reynolds stress occurs over a larger area on the left hand side of the centreline than on the right hand side of the centreline. By 3 rotor diameters downstream, the Reynolds stress is approximately 60% greater at the vertical centre of the rotor on the left hand side compared to the right hand side of the centreline.

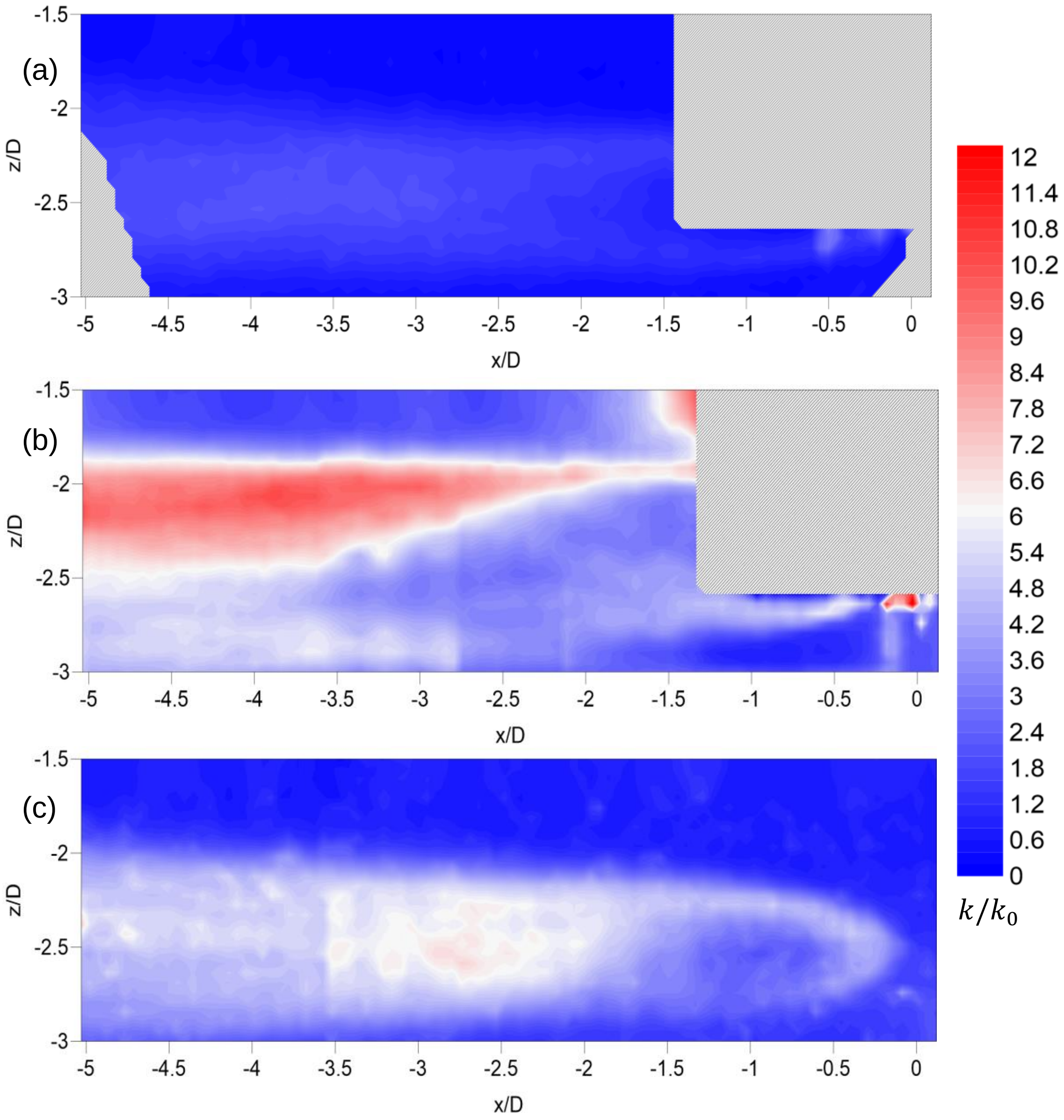

Figure 4.6: Flow structure maps for normalised turbulent kinetic energy (k) velocity component for (a) 0.5D to the right hand side of the centreline (b) centreline (c) 0.5D to the left hand side of the centreline. Normalising k values: right hand side = -0.0012m^2s^{-2}, centreline = -0.0003m^2s^{-2}, left hand side = -0.0005m^2s^{-2}. Scales on the axes are normalised to rotor diameters (200mm). Areas covered by upward diagonal line shading indicate areas where data could not be collected as the camera image was obstructed by the rotor and housing or the channel support structure.

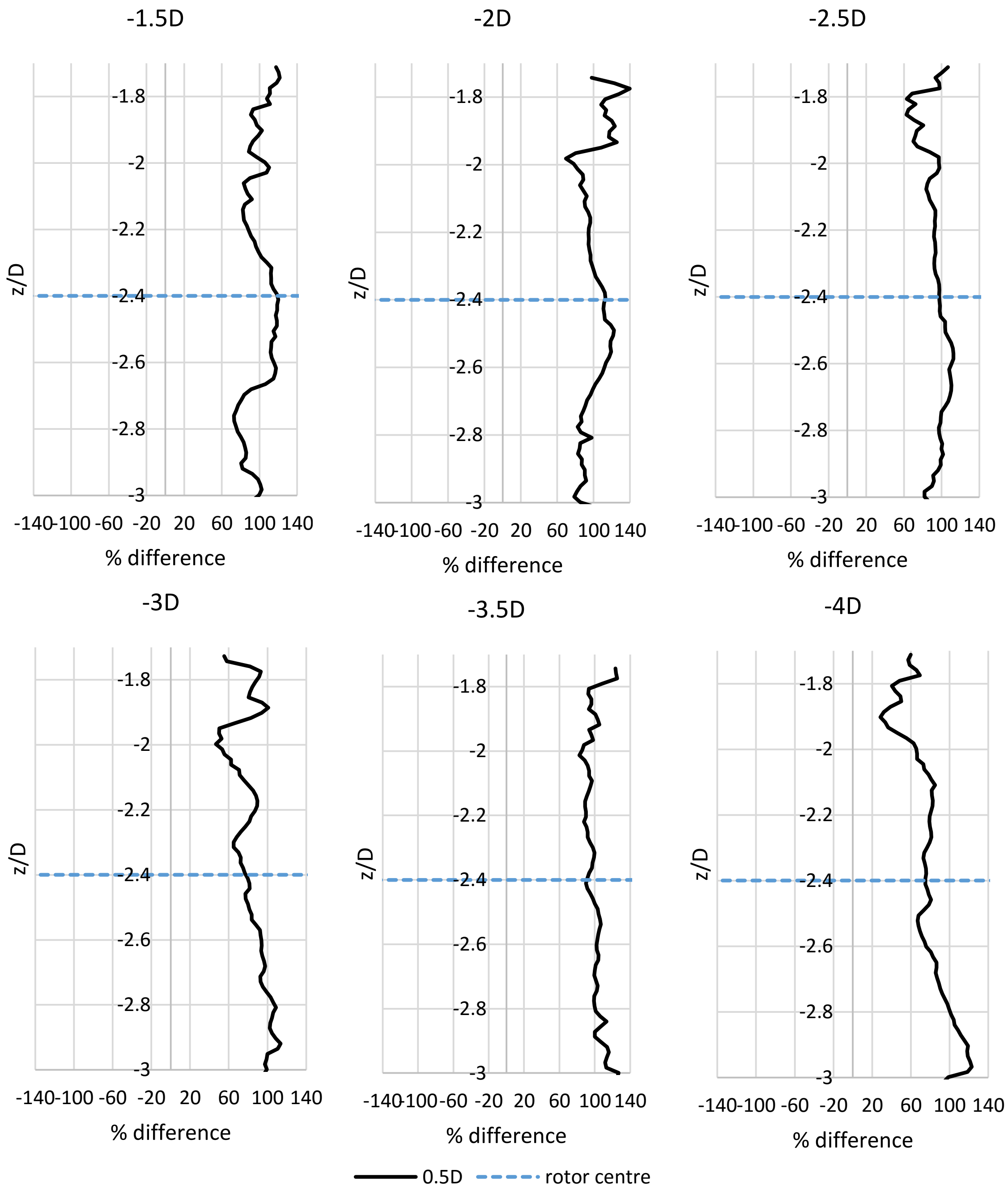

Figure 4.7: Plots showing the percentage difference in normalised turbulent kinetic energy between the left hand side of the centreline and the right hand side of the centreline at 0.5D from the centreline. These are taken at (from top left to bottom right) 1.5D, 2D, 2.5D, 3D, 3.5D and 4D downstream of the rotor. A value greater than 0% indicates left hand side is greater than right hand side.

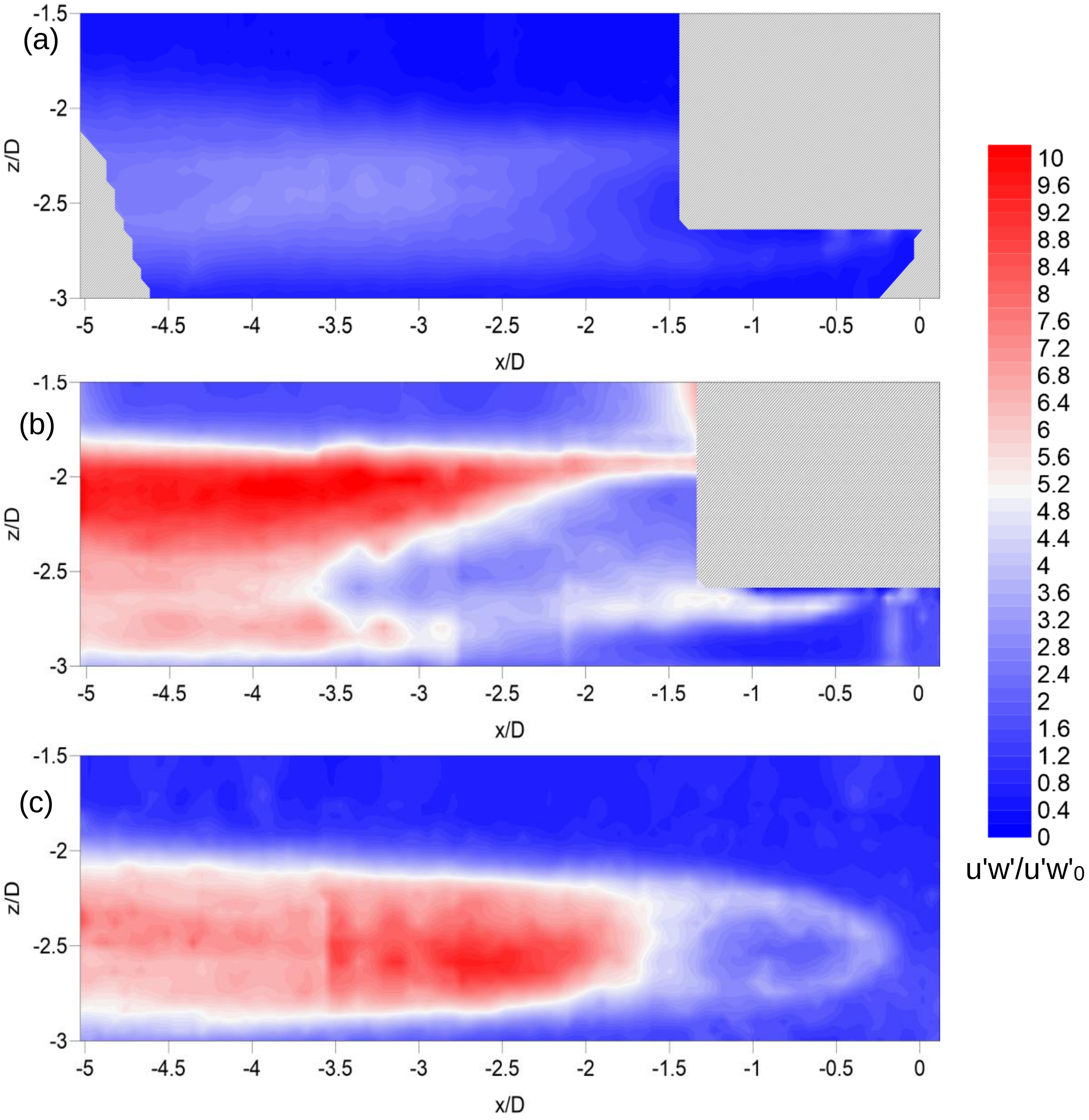

Figure 4.8: Flow structure maps for normalised Reynolds stress (u'w') for (a) 0.5D to the right hand side of the centreline (b) centreline (c) 0.5D to the right hand side of the centreline. Normalising values: right hand side = -0.0004m²s⁻², centreline = -0.0002m²s⁻², left hand side = -0.0002m²s⁻². Scales on the axes are normalised to rotor diameters (200mm). Areas covered by upward diagonal line shading indicate areas where data could not be collected as the camera image was obstructed by the rotor and housing or the channel support structure.

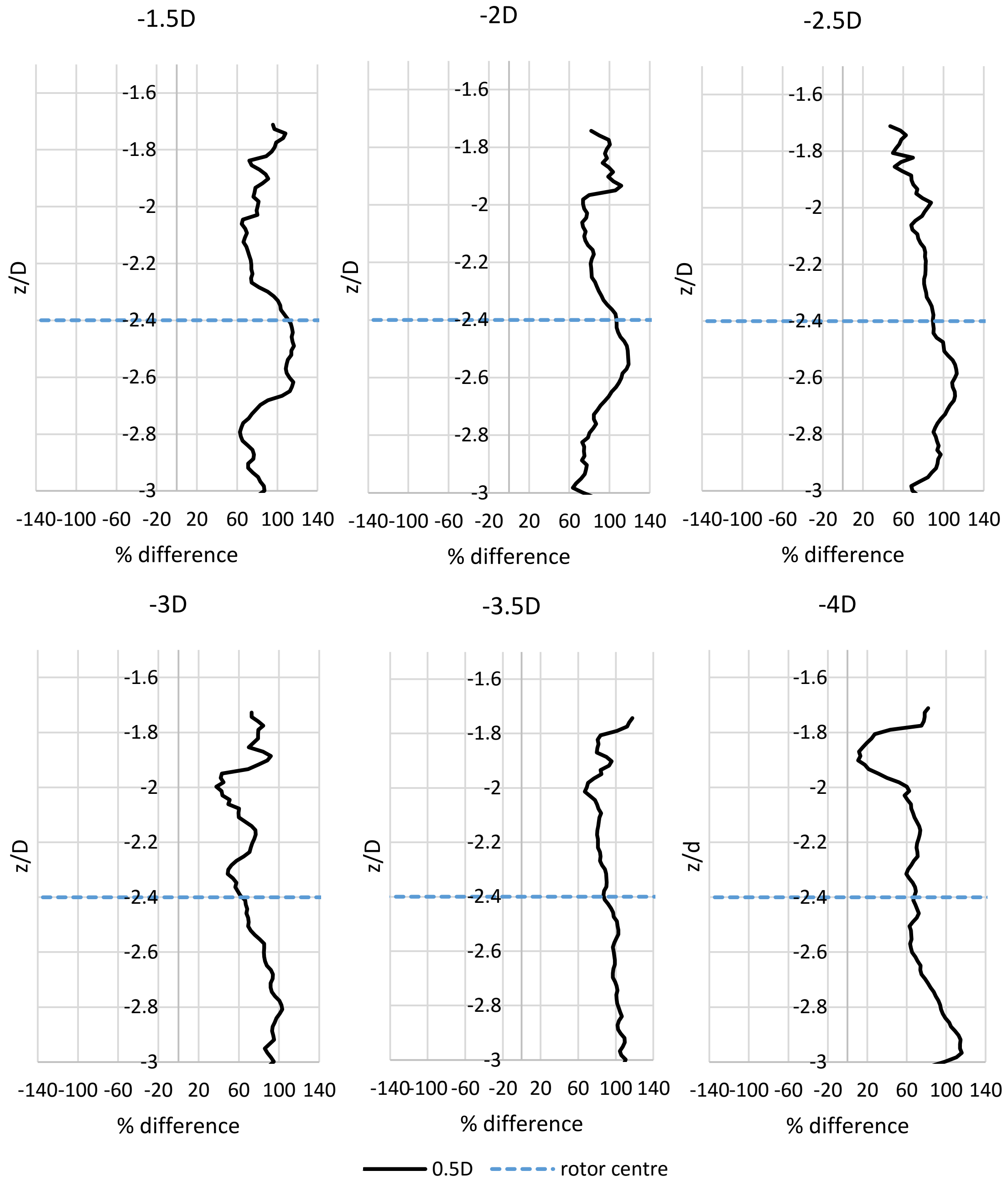

Figure 4.9: Plots showing the percentage difference in normalised Reynolds stress (u'w') between the left hand side of the centreline and the right hand side of the centreline at 0.5D from the centreline. These are taken at (from top left to bottom right) 1.5D, 2D, 2.5D, 3D, 3.5D and 4D downstream of the rotor. A value greater than 0% indicates left hand side is greater than right hand side.

4.4 Discussion

Significant differences can be seen between the wake on the left hand side and the right hand side of the rotor centreline. The wake appears to be more inclined towards the left hand side of the channel, where the wake is extended and the velocity deficit is greater. The wake length is shorter on the right hand side of the centreline where there is greater vertical motion with upwelling and downwelling. The upwelling and downwelling from above and below the wake assist with wake recovery by drawing faster moving free-stream flow into the slower moving flow of the turbine wake. The differences observed are evident close to the rotor, but also further downstream. Although some research suggests that the wake should become more symmetric as the near-field distance downstream increases (Thomas and Liu, 2004; Tescione *et al.*, 2014), this is not the case in these experimental results.

The lack of wake symmetry further downstream suggests that the asymmetry would be transported in the wake beyond this near-field region, and not simply localized to the rotor (Tescione *et al.,* 2014). The asymmetry could therefore partially be a result of deflection of the flow during the turbine rotation, in a similar manner to the Magnus Effect (Briggs, 1959; Tescione *et al*., 2014). However, further analysis of the data and the vortex shedding would need to be performed in order to determine whether or not this is the case. The asymmetry observed could also be related to the re-circulating flume in which the data were collected having a non-uniform lateral distribution of the flow (Myers and Bahaj, 2012). The possibility of a non-uniform onset flow was minimised as far as possible in the experiments described herein as a result of flow conditioning being used at the inlet. The plain channel profile (figure 3.6) shows very little cross-stream flow on the centreline. This potential issue was also further reduced by normalising the data collected at 0.5D from either side of the centreline with the data from 1D either side of the centreline. It was deemed that 1D from the centreline was sufficiently far from the rotor to enable the data to be representative of the plain channel. The cross-stream asymmetry, as observed in the results presented herein, is unlikely to be a result of free-surface and bed proximity, as is the case with vertical asymmetry (Stallard *et al.,* 2013, Stallard *et al.*, 2015; Tedds *et al.*, 2014), which is discussed in more detail in chapter 5.

Although research into the wake asymmetry of horizontal axis tidal stream turbines is limited, some numerical modelling has previously been carried out by Vybulkova (2013) in which a similar wake asymmetry was observed. Vybulkova (2013) noted that the asymmetry which was observed was related to the direction of rotation of the tidal stream turbine. Those results may partially explain the observations seen in the results herein. There are two counter rotating vortices within the wake. The vortices within the centre of the wake rotate in the opposite direction to the turbine, as shown in figure 4.10. However, on the outer edge of the wake, the flow rotates in the same direction as the turbine. The wake asymmetry could therefore be related to the counter-rotating vortices and the interaction between vortices which are shed from the rotor blade tips (Tescione *et al.,* 2014).

Similar asymmetrical results have been seen in the wake of wind turbines. Although there are differences in the fluid dynamics between air and water, the observations seen in wind turbines can still be considered when investigating tidal stream turbine wakes. Ryan *et al.* (2016) observed asymmetry in the vortex structure within the wake of a vertical axis wind turbine. The asymmetry was linked to the tip speed ratio of the turbine, particularly in the near wake of the turbine. However, the increased tip speed ratio aided flow recovery downstream due to greater mixing with the free-stream flow (Ryan *et al.*, 2016). Tescione *et al.* (2014) observed similar results with wind turbines to those presented herein, as their results showed a cross-stream asymmetry in the wake which did not become more symmetric downstream. Lebrón *et al*. (2009) also observed asymmetry in the turbine wake, but attributed some of this to the blockage and the velocity gradient of the boundary layer. It is unlikely that blockage had a significant impact on the results presented herein, as the blockage ratio was approximately 3.2%, which is similar to that used in research by other authors (e.g. Olczak *et al.*, 2015). The blockage ratio can affect turbine performance and wake velocity deficit and length, and is derived from the diameter of the turbine and the area of the channel (Creciun, 2013).

The asymmetry in the wake of a tidal stream turbine needs to be considered when designing large scale developments and tidal farms. Although this aspect has not been studied in depth for tidal stream turbines, the asymmetry in the wake of an array of wind turbines has been studied. As indicated above, the wake of a tidal stream turbine and a wind turbine hold similar characteristics. Therefore, the findings of research into wind turbine arrays can be used to provide some information on the likely interactions between tidal stream turbine arrays and wake asymmetry. Bartl *et al*. (2012) determined that when wind turbines were placed in an array, the wake becomes more symmetric behind the second turbine compared to the first turbine in the array. The cross-stream asymmetry can also be linked to the cumulative effect of all turbines within an array rotating in the same direction (Lebrón *et al.*, 2009).

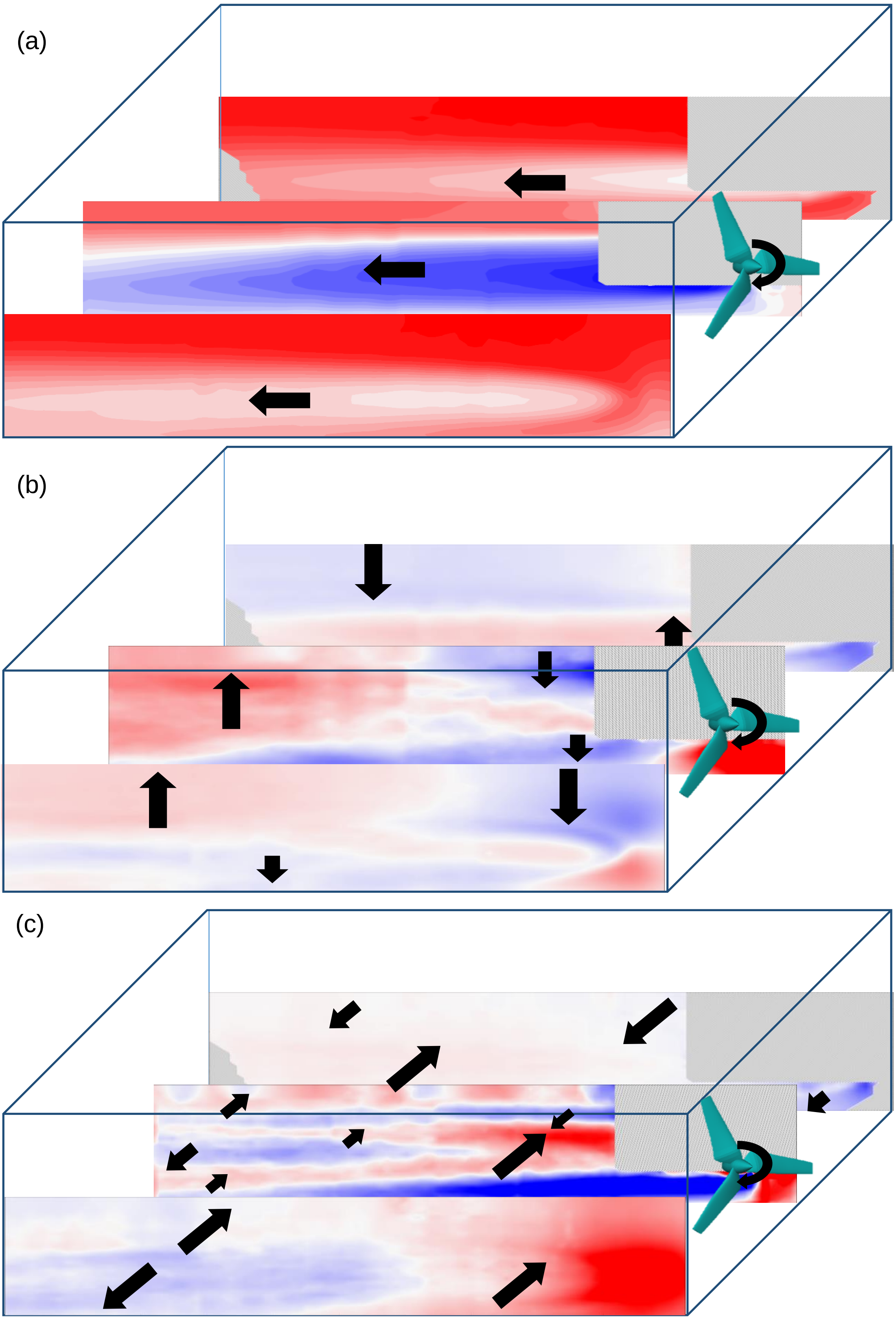

Figure 4.10: Diagrams incorporating flow maps to show flow direction when rotor is positioned at 120mm above the channel bed (a) stream-wise flow (b) vertical flow (c) cross-stream flow.

It is important to consider the implications that turbine wake asymmetry can have when designing tidal turbines and placing them within channels and/or in arrays. Both vertical and cross-stream asymmetry can affect the sediment transport beneath the rotor and routed through arrays, and therefore the proximity of the turbines to the channel bed and each other should be considered in the design of turbines and arrays. It has also been identified, by reviewing the research by other authors, that the cross-stream asymmetry in the turbine wake can also be affected by other turbines within an array, and this should be a consideration when developing tidal turbine arrays.

4.5 Conclusions

Detailed flow maps of the stream-wise, vertical and cross-stream velocity components for the centreline and 0.5D to the left-hand side and the right hand side of the centreline have been presented. The TKE and Reynolds stress ($u'w'$), which can be used to estimate shear stress, have also been presented for the same measurement locations. Figures showing the percentage difference between the left hand side and right hand side of the centreline have also been presented for the stream-wise velocity component as well as the TKE. There is clear asymmetry in the turbine wake, which extends through the measured extent of the wake length. The asymmetry is greater towards the left hand side of the centreline. The results presented herein demonstrate the importance of considering wake asymmetry, which could have implications, particularly for large scale developments and arrays of tidal stream turbines.

Further research should consider the effect of the tip speed ratio on wake asymmetry and flow recovery lengths. The proximity of the turbine to the bounding surface may affect the wake asymmetry, and this should therefore be a consideration of further research.

Chapter 5

Wake Interaction

How does the wake of a tidal stream turbine interact with the bed surface?

This chapter presents the results of an experimental investigation which aims to evaluate how moving a tidal stream turbine closer to the bed affects the flow field downstream from the tidal stream turbine. This chapter will also investigate how the wake of a tidal stream turbine develops downstream from the rotor and how it interacts with the bed surface below the rotor.

5.1 Introduction

It has already been determined that the wake of a tidal stream turbine is characterised by an area of decreased velocity downstream from the turbine, with accelerated flow in the surrounding areas (Bahaj *et al.,* 2007c; Sun *et al.*, 2008; Myers and Bahaj, 2010). When a tidal stream turbine is located close to a bounding surface (i.e. the bed or the water surface), the accelerated flow between the turbine and bounding surface is restricted, resulting in the loss of vertical wake symmetry (Bahaj *et al.* 2007c; Myers and Bahaj, 2010). These effects have previously been studied to an extent using actuator disks. For example, Myers and Bahaj (2010) determined that closer proximity of a device to the channel bed caused greater lateral motion and therefore a longer wake as a result of the flow below the device being restricted. However, actuator disks are known to fail in fully replicating the shedding of vortices from the blade tips or the swirl as a result of turbine rotation, which are particularly important in the near wake (Batten *et al.,* 2013). Olczak *et al.* (2015) used a numerical model tidal stream turbine and identified that the depth to diameter ratio affected the transition of the near wake to the far wake. Decreasing the depth to diameter ratio (and therefore the blockage ratio) led to the depth average moving closer to the rotor plane. However, there is a need to experimentally investigate the effect of the height of the turbine above the channel bed on the turbine wake using small scale tidal stream turbines The results and research presented within this chapter will build upon those from Chapter 4 which examined wake development.

5.2 Methodology

This chapter will use experimental data collected during a series of experiments in which a 0.2m diameter tidal stream turbine was positioned at various distances from a roughened bed surface (as described in Chapter 3). It will look at the shape and length of a TST wake and how the wake and flow recovery varies as the distance of the TST from the channel bed is varied. The interaction of the TST wake with the channel bed will be considered, along with the effect that the TST proximity to the bed has on shear stress. There is a need to experimentally investigate these impacts and to determine the implications for full scale, operational turbines.

The rotational speed of the rotor was kept constant during the data collection for consistency. However, due to the changes in rotor height and the nature of the plain channel profile, this led to a change in the tip speed ratio (TSR) of the rotor, as shown in figure 5.1. When the rotor was positioned at 300mm above the bed, the TSR was 5.12. This increased to 5.42 when the rotor was positioned at 200mm above the bed. The optimal tip speed ratio of 5.5, corresponding to the maximum of the power curve, occurred when the rotor was at 180mm above the channel bed. The TSR further increased to 5.6, 5.67 and

5.74 as the rotor was lowered to 160mm, 140mm and 120mm respectively. Some variation in tip speed ratio could be attributed to the tip speed ratio being calculated using the flow speed at the vertical centre of the turbine (as explained in section 3.3.1). However, due to the velocity profile of the channel, this would not account for all of the variation seen in figure 5.1. The change in TSR can impact the wake downstream from the TST. Higher tip speed ratios have been shown to lead to greater velocity deficit in the wake of wind turbines (Parker and Leftwich, 2016). The wake recovery is dependent upon the TSR as the power extracted from the flow by the TST is a function of the TSR (Whelan *et al.,* 2009; Chamorro *et al.,* 2013), leading to an increase in wake length at greater tip speed ratios (Chamorro *et al.*, 2013). Wake expansion is also greater with increasing tip speed ratio downstream from wind turbines (Grant *et al.*, 2000; Vermeer *et al.* 2003). However, as the overall difference in the tip speed ratios during this study is minimal (±0.38), it is unlikely that the wake downstream from the TST will be significantly affected.

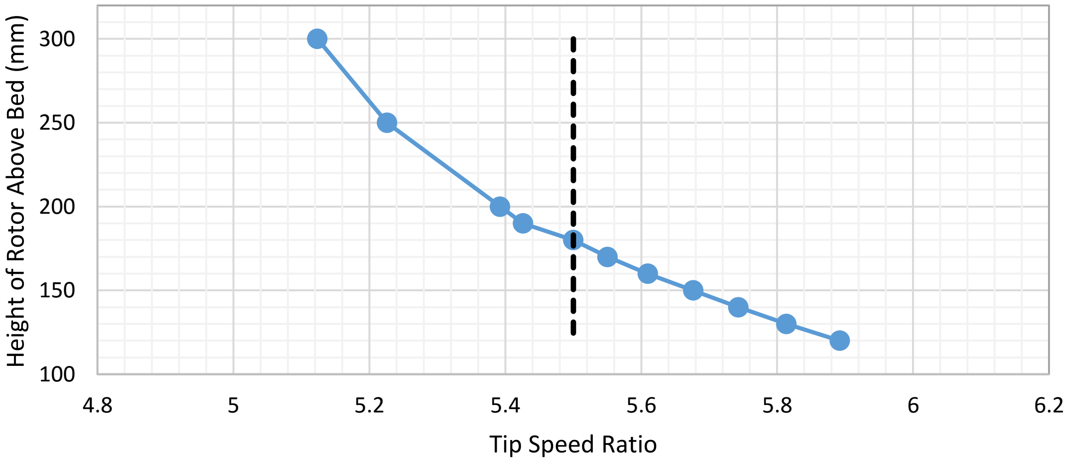

Figure 5.1: Tip speed ratios for the rotor at various heights above the channel bed, derived by using the average velocity across the entire rotor diameter. The optimal TSR of 5.5 (representing the maximum for the power curve) is also shown by the vertical dashed line.

Results are presented for the stream-wise (*u*), vertical (*w*) and cross-stream (*v*) velocity components for rotor heights of 300mm, 200mm, 180mm, 160mm, 140mm and 120mm above the bed, as well as the standard deviation of the stream-wise, vertical and cross-stream components. Results are also presented for the bed shear stress, using turbulent kinetic energy (TKE) of the flow (see equation 11) and the Reynolds shear stress (see equation 9), which can be used as a method of estimating shear stress (Biron *et al.,* 2004; Pope *et al.*, 2006). The turbulence intensity (u'/U_0) is also presented, along with the normalised shear velocity. The normalised shear velocity is:

$$u_*/u_{*0} \qquad \text{Equation 14}$$

where u_* represents the shear velocity with the rotor present, and u_{*0} represents the shear velocity of the plain channel. An asymmetry measure for the stream-wise velocity is also given. This is derived from:

$$\frac{u_{+z}}{u_{-z}} \qquad \text{Equation 15}$$

where u_{+z} and u_{-z} represent the stream-wise velocities above and below the rotor respectively.

The stream-wise velocity will be used to identify the wake extent and asymmetry based on the velocity deficit. Cross-stream and vertical velocities will be used to understand wake interaction with the surrounding flow and the internal wake structure. The turbulence intensities and estimators of shear stress will be used to identify the turbulent structures and to understand wake recovery.

When the rotor was positioned at 300mm and 200mm above the channel bed, data were collected for the full vertical height of the channel (3 rotor diameters). When the rotor was positioned at 180mm to 120mm above the channel bed, data were only collected at ~1.5 rotor diameters above the channel bed as this area sufficiently captured the key dynamics of the wake flow field downstream from the rotor.

5.3 Results

There is a clear symmetry in the stream-wise velocity of the wake of the TST when the rotor is between 300mm and 180mm above the bed (figures 5.2 (a) to 5.2(c)). At these heights, the wake is well developed and characterised by a zone of decreased flow velocity that extends beyond 5 rotor diameters downstream and close to the rotor has a vertical width of approximately 1 rotor diameter (figures 5.3 (a) and (b)). There is a clear separation between the wake of the rotor and the flow above the channel bed. Close to the rotor (2 rotor diameters downstream), the velocity at the vertical centre of the wake is ~18% of the free-stream velocity (figure 5.3 (a)). The greatest velocity deficit at this location occurs when the rotor is positioned at 300mm above the bed. Between 1 and 2 rotor diameters downstream, the flow recovery rate is similar at all rotor heights.

The wake starts to become asymmetric as the rotor is lowered to 160mm (figures 5.4 (a) to (d)). When the rotor is lowered to 160mm above the bed (figure 5.2 (d)), the wake becomes slightly asymmetric from approximately 3 rotor diameters downstream (figure 5.3 (c)). At this downstream location, the velocity deficit at the vertical centre of the wake is between ~35% and ~45% of the free-stream velocity, with the greatest deficit occurring when the rotor is close to the channel bed.

The asymmetry in the wake at 140mm and 120mm above the bed is evident. The wake is more inclined towards the channel bed. When the rotor is at 140mm above the bed, the downstream edge of the wake is approximately 0.2 rotor diameters closer to the bed than when the rotor is at 300mm above the bed (figure 5.3 (d)), and at 5 rotor diameters downstream, the asymmetry measure (figure 5.4 (d)) at the rotor blade tip increases from 1.13 when the rotor is at 300mm above the bed to 1.34 when the rotor is 140mm above the bed. When the rotor is at 140mm above the bed, the interaction between the wake and the channel bed is clearly evident at approximately 3 rotor diameters downstream (figures 5.2 (e) and 5.2 (f)). When the rotor is lowered to 120mm above the bed, the interaction is evident immediately downstream from the TST. At both 140mm and 120mm above the bed, the asymmetry in the wake becomes much more pronounced (asymmetry measure of 1.4 and 1.53 at 140mm and 120mm respectively (figure 5.4 (d)) with an inclination towards the bed, as shown by the asymmetry measure values greater than 1. At this downstream location, flow at the vertical centre of the wake has recovered to between ~48% and ~58% of the free-stream velocity, with the fastest recovery occurring in the higher rotor positions.

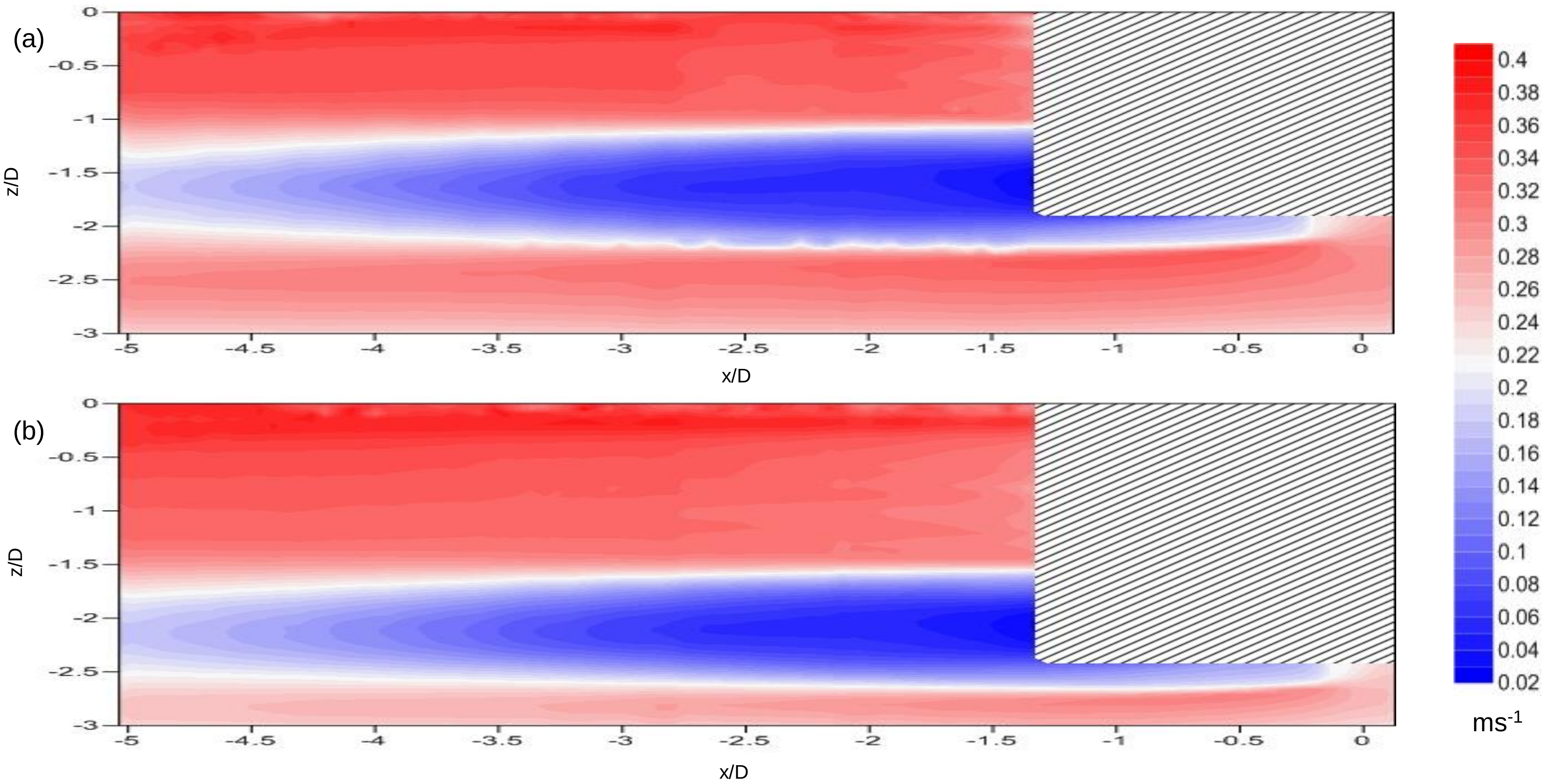

Figure 5.2: Flow structure maps for the stream-wise velocity component for the rotor positioned at (a) 300mm above the bed and (b) 200mm above the bed. Flow direction is from right to left. Scales on the axes are normalised to rotor diameters (200mm). Areas covered by diagonal shading indicate areas where no data could be collected.

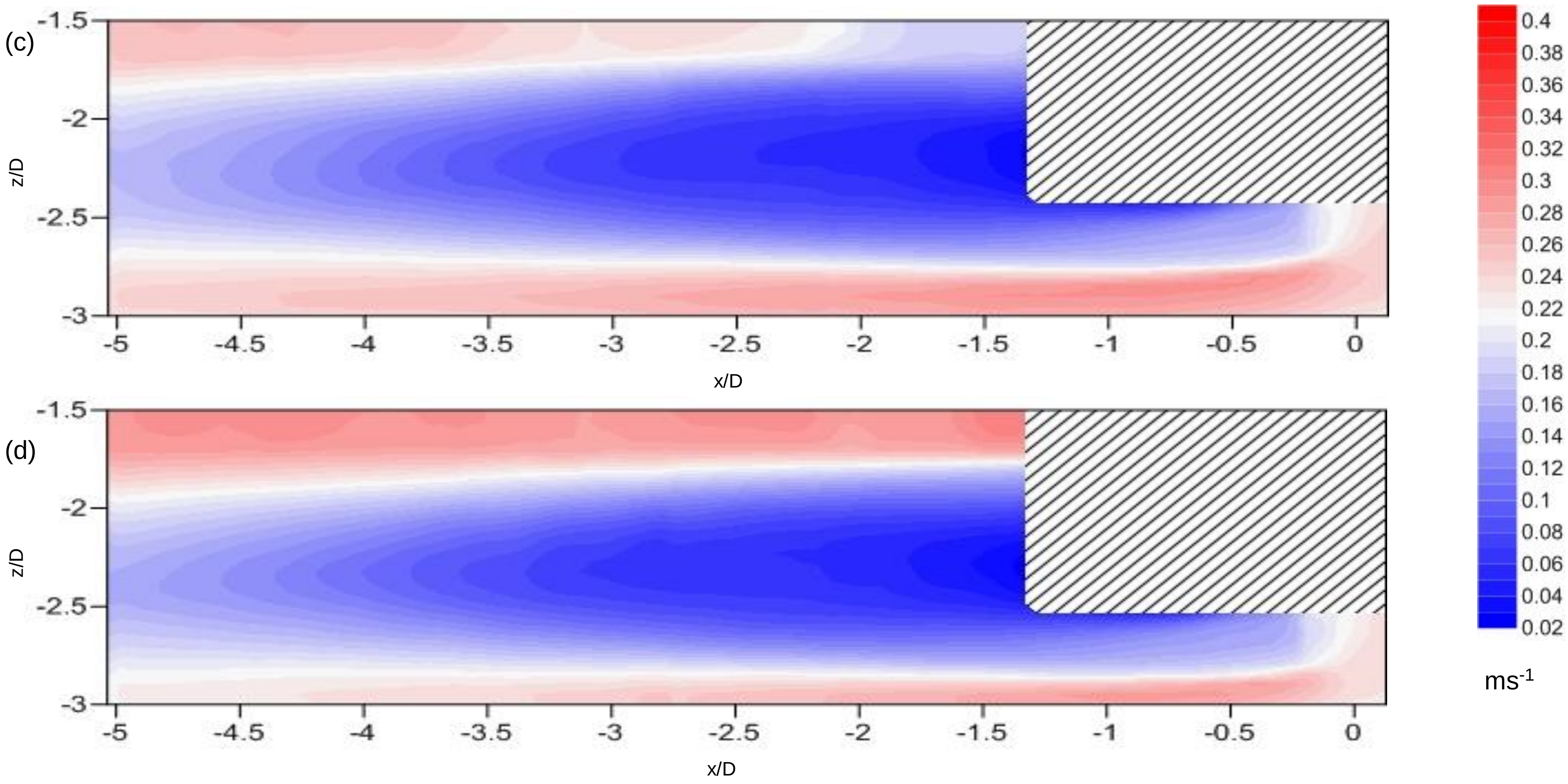

Figure 5.2: Flow structure maps for the stream-wise velocity component for the rotor positioned at (c) 180mm above the bed (d) 160mm above the bed. Flow direction is from right to left. Scales on the axes are normalised to rotor diameters (200mm). Areas covered by diagonal shading indicate areas where no data could be collected.

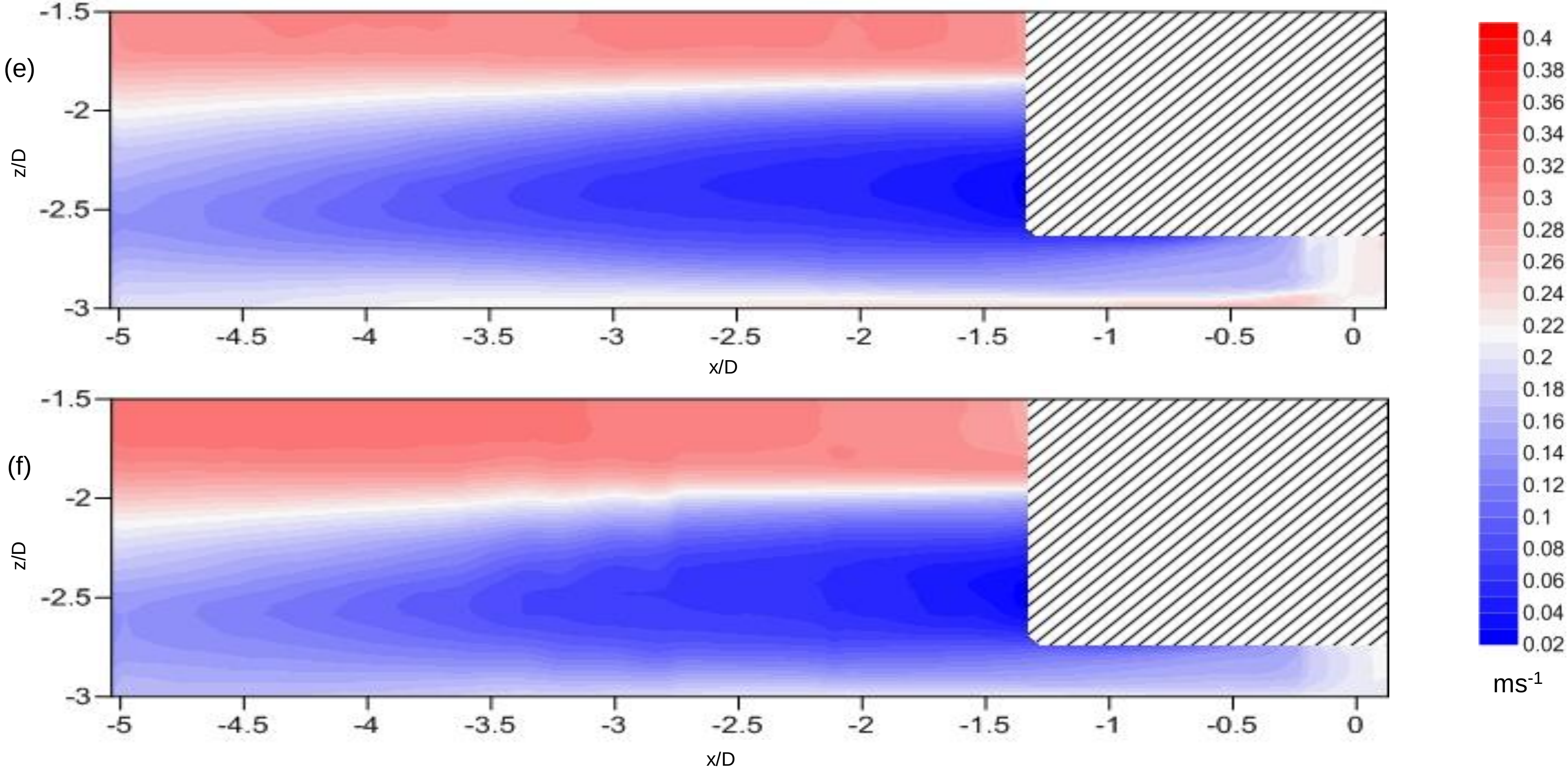

Figure 5.2: Flow structure maps for the stream-wise velocity component for the rotor positioned at (e) 140mm above the bed (f) 120mm above the bed. Flow direction is from right to left. Scales on the axes are normalised to rotor diameters (200mm). Areas covered by diagonal shading indicate areas where no data could be collected.

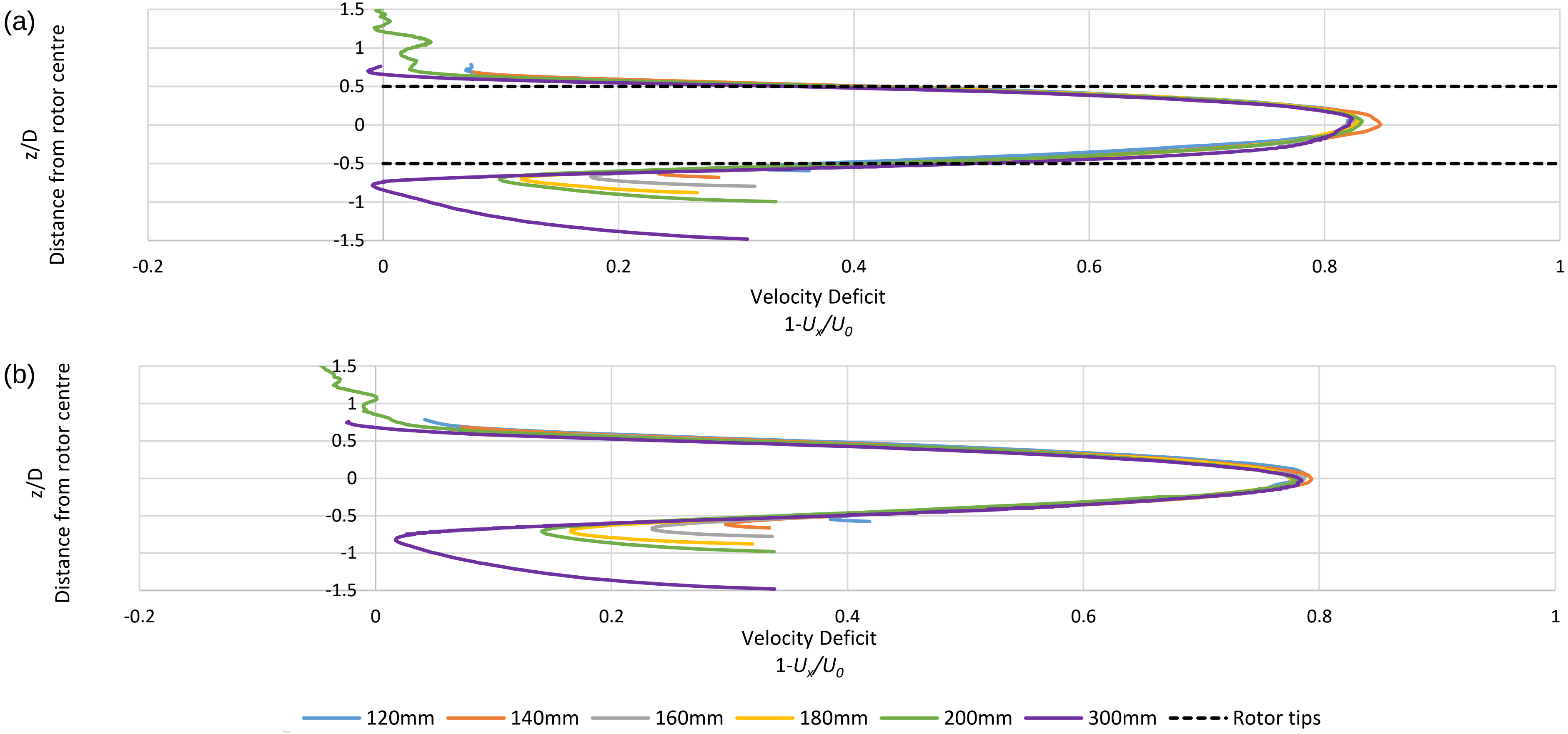

Figure 5.3: Velocity deficit profiles for the rotor positioned at 120mm, 140mm, 160mm, 180mm, 200mm and 300mm above the channel bed at (a) 2 rotor diameters downstream from the turbine (b) 3 rotor diameters downstream from the turbine. Scales on the y-axes are normalised to rotor diameters (200mm).

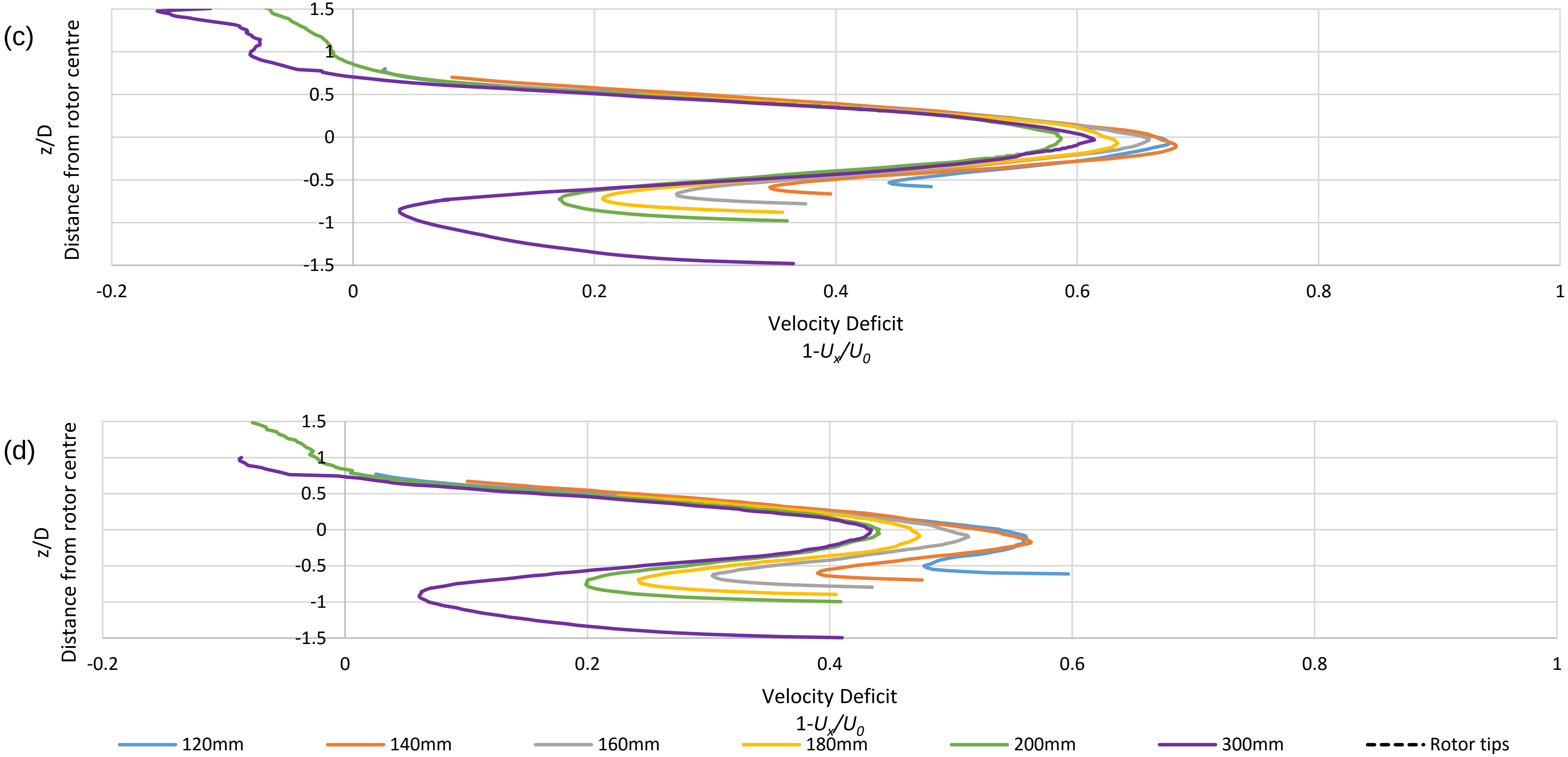

Figure 5.3: Velocity deficit profiles for the rotor positioned at 120mm, 140mm, 160mm, 180mm, 200mm and 300mm above the channel bed at (c) 4 rotor diameters downstream from the turbine and (d) 5 rotor diameters downstream from the turbine. Scales on the y-axes are normalised to rotor diameters (200mm).

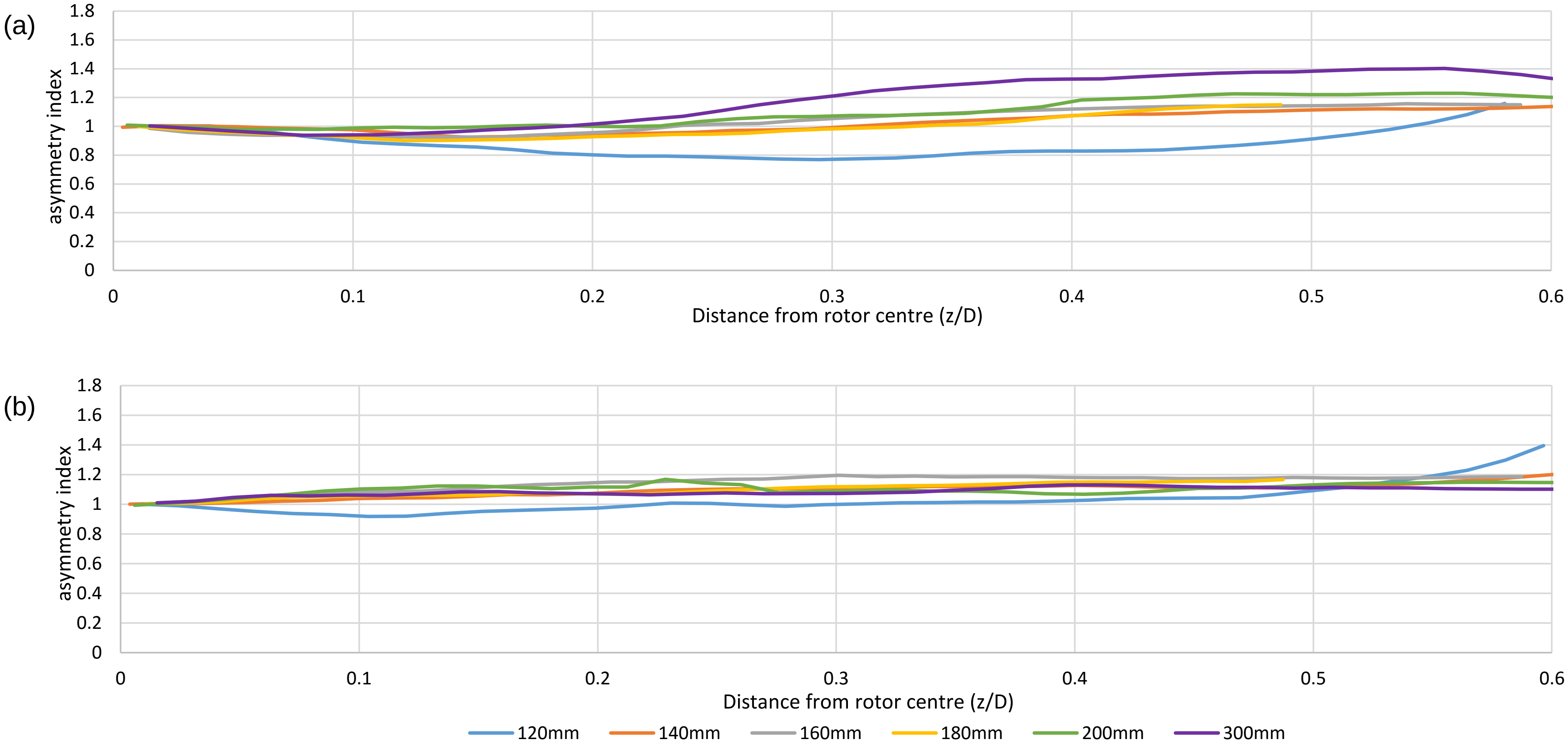

Figure 5.4: Asymmetry measure for the rotor positioned at 120mm, 140mm, 160mm, 180mm, 200mm and 300mm above the channel bed at (a) 2 rotor diameter downstream from the turbine (b) 3 rotor diameters downstream from the turbine. Scales on the x-axes are normalised to rotor diameters (200mm). Value <1 means stream-wise velocity is greater closer to the bed. Value >1 means stream-wise velocity is greater closer to water surface.

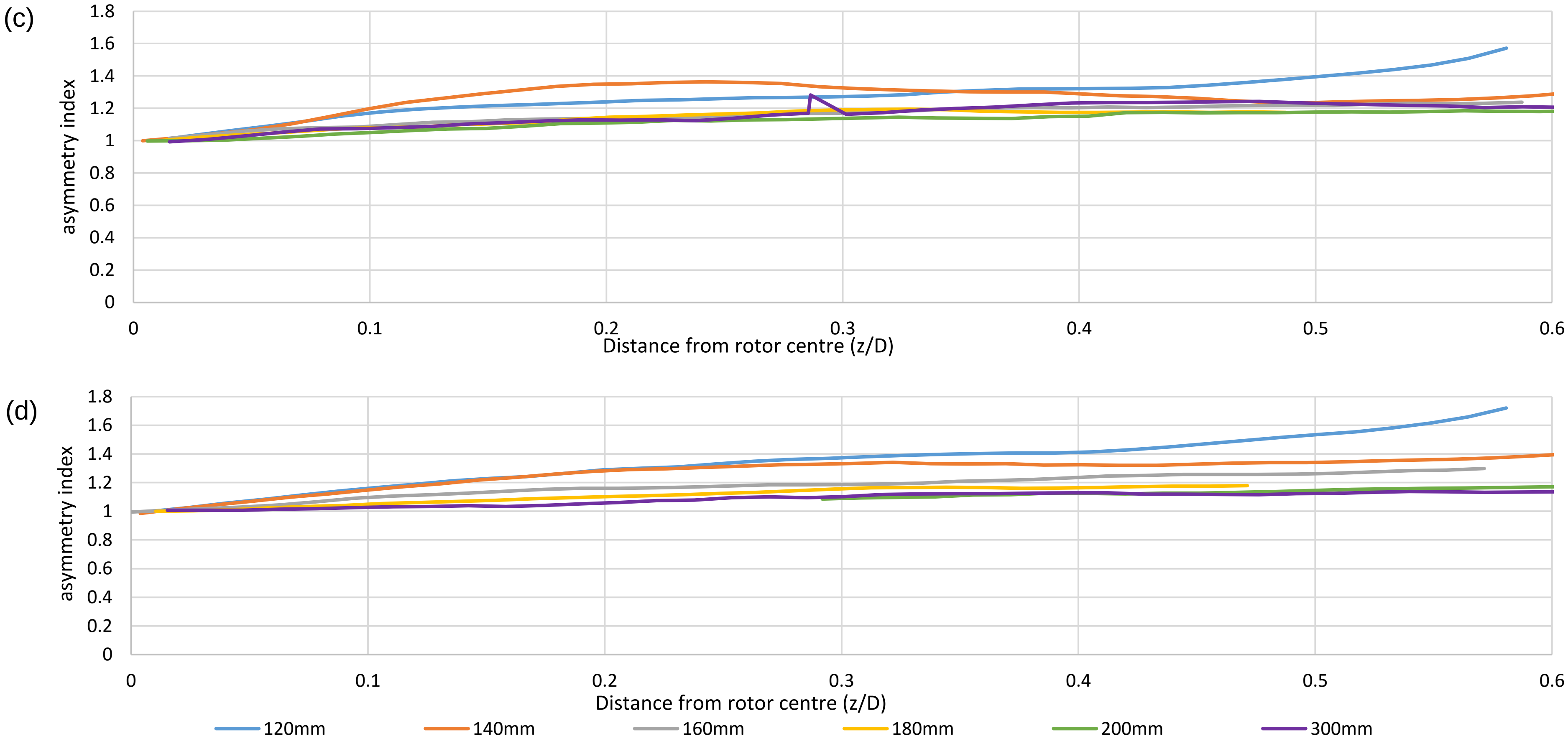

Figure 5.4: Asymmetry measure for the rotor positioned at 120mm, 140mm, 160mm, 180mm, 200mm and 300mm above the channel bed at (c) 4 rotor diameters downstream from the turbine and (d) 5 rotor diameters downstream from the turbine. Scales on the x-axes are normalised to rotor diameters (200mm). Value <1 means stream-wise velocity is greater closer to the bed. Value >1 means stream-wise velocity is greater closer to water surface.

There is a similar pattern in the vertical velocity (*w*) at all rotor heights (figures 5.5 (a) to 5.5 (f)). Immediately beneath the rotor, there is an area of downwelling, which extends from the rotor tip to approximately one rotor diameter downstream. This area of downwelling decreases in size and extent as the rotor is positioned closer to the bed. Immediately behind the rotor is an area of upwelling. Further downstream, there is upwelling below the TST wake and downwelling above the TST wake. The area of upwelling is approximately two rotor diameters in height when the rotor is positioned at 300mm above the bed (figure 5.5 (a)), and decreases in size down to approximately 0.25 rotor diameters in height as the rotor is lowered. The extent of the upwelling is greatest when the rotor is furthest from the bed, and decreases as the rotor is positioned closer to the bed. When the rotor is positioned at 300mm above the bed, this area of upwelling occupies approximately 31% of the total measured flow area, and when the rotor is positioned at 120mm above the bed (figure 5.5 (f)), this area of upwelling occupies approximately 15% of the total measured flow area.

There are significant areas of strong positive cross-stream flow (*v*) at the upper and lower boundaries of the wake close to the rotor (shown in figures 5.6 (a) to (f)). Within the central area of the wake, there is an area of negative cross-stream flow, with an area of positive cross-stream flow that develops in the centre of the wake at approximately 3 rotor diameters downstream. This area of positive cross-stream flow is greatest in magnitude and size when the rotor is positioned at 300mm and 120mm above the channel bed (figures 5.6 (a) and (f)). At these rotor heights, the area of positive cross-stream flow has a maximum height of approximately 0.5 rotor diameters. Beneath the wake, there is an area of negative cross-stream flow. There appears to be no discernible impact on the magnitude of the cross-stream flow as a result of lowering the rotor closer to the bed. However, the size of the areas of strong negative cross-stream flow within the centre of the wake and below the wake, as well as the positive cross-stream flow at the upper and lower boundaries of the wake is significantly reduced when the rotor is closer to the bed. The area of negative cross-stream flow below the wake is most drastically reduced in size as a result of moving the rotor closer to the bed. When the rotor is positioned at 120mm above the bed, this area of negative cross-stream flow is almost negligible, accounting for less than 1% of the total measured flow area. When the rotor is positioned at 300mm above the bed, this area of negative cross-stream flow accounts for approximately 28% of the total measured flow area.

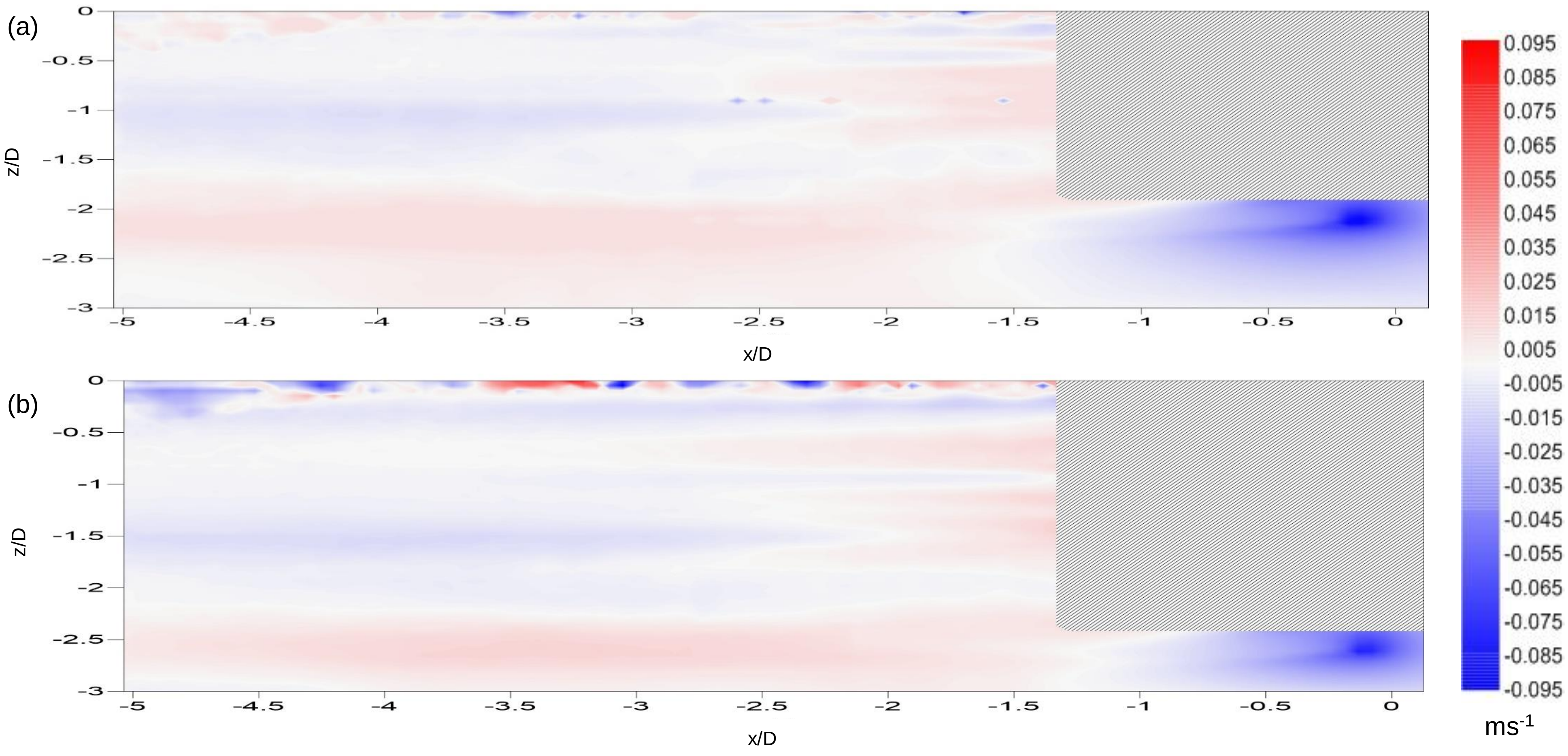

Figure 5.5: Flow structure maps for the vertical velocity component for the rotor positioned at (a) 300mm above the bed and (b) 200mm above the bed. Flow direction is from right to left. Scales on the axes are normalised to rotor diameters (200mm). Areas covered by diagonal shading indicate areas where no data could be collected.

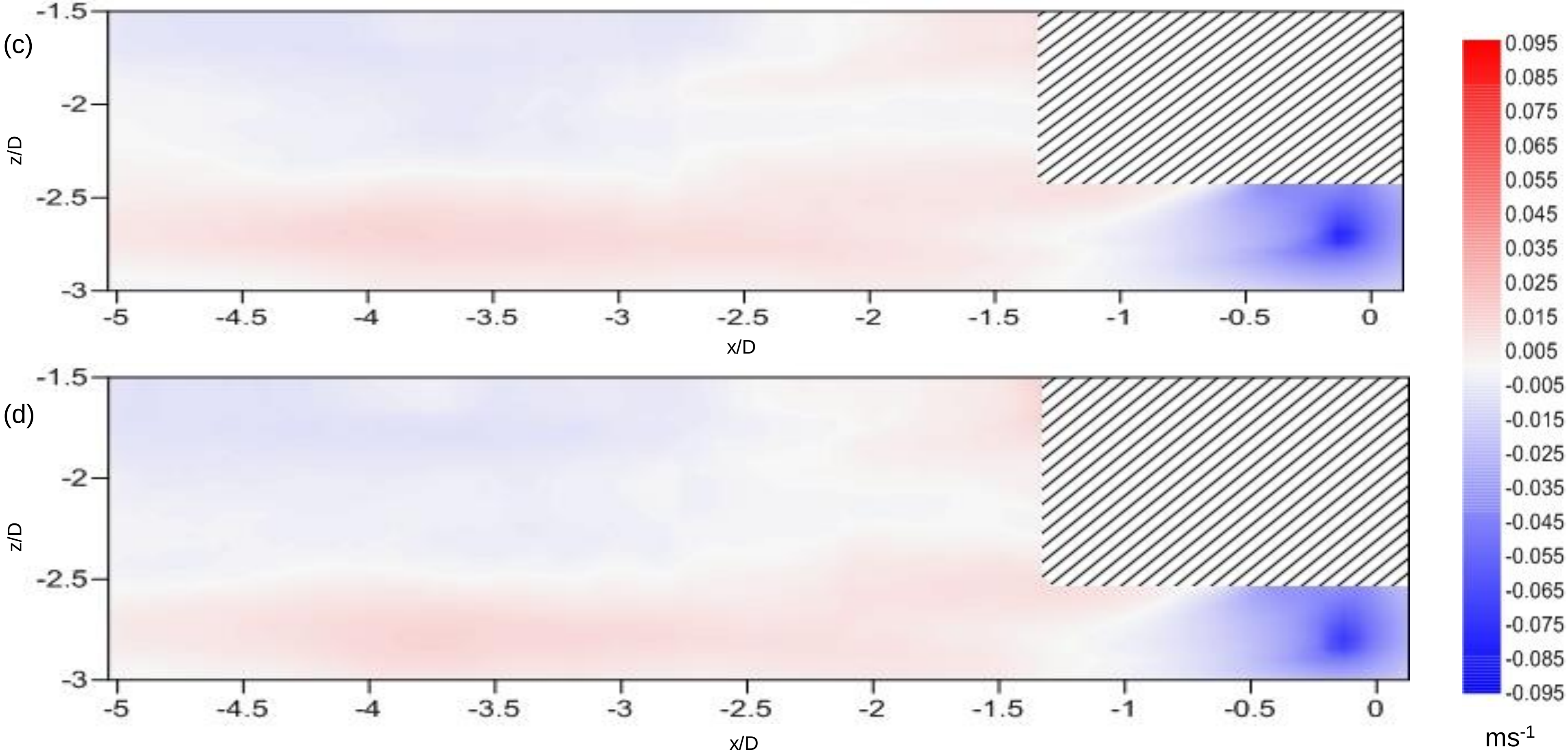

Figure 5.5: Flow structure maps for the vertical velocity component for the rotor positioned at (c) 180mm above the bed (d) 160mm above the bed. Flow direction is from right to left. Scales on the axes are normalised to rotor diameters (200mm). Areas covered by diagonal shading indicate areas where no data could be collected.

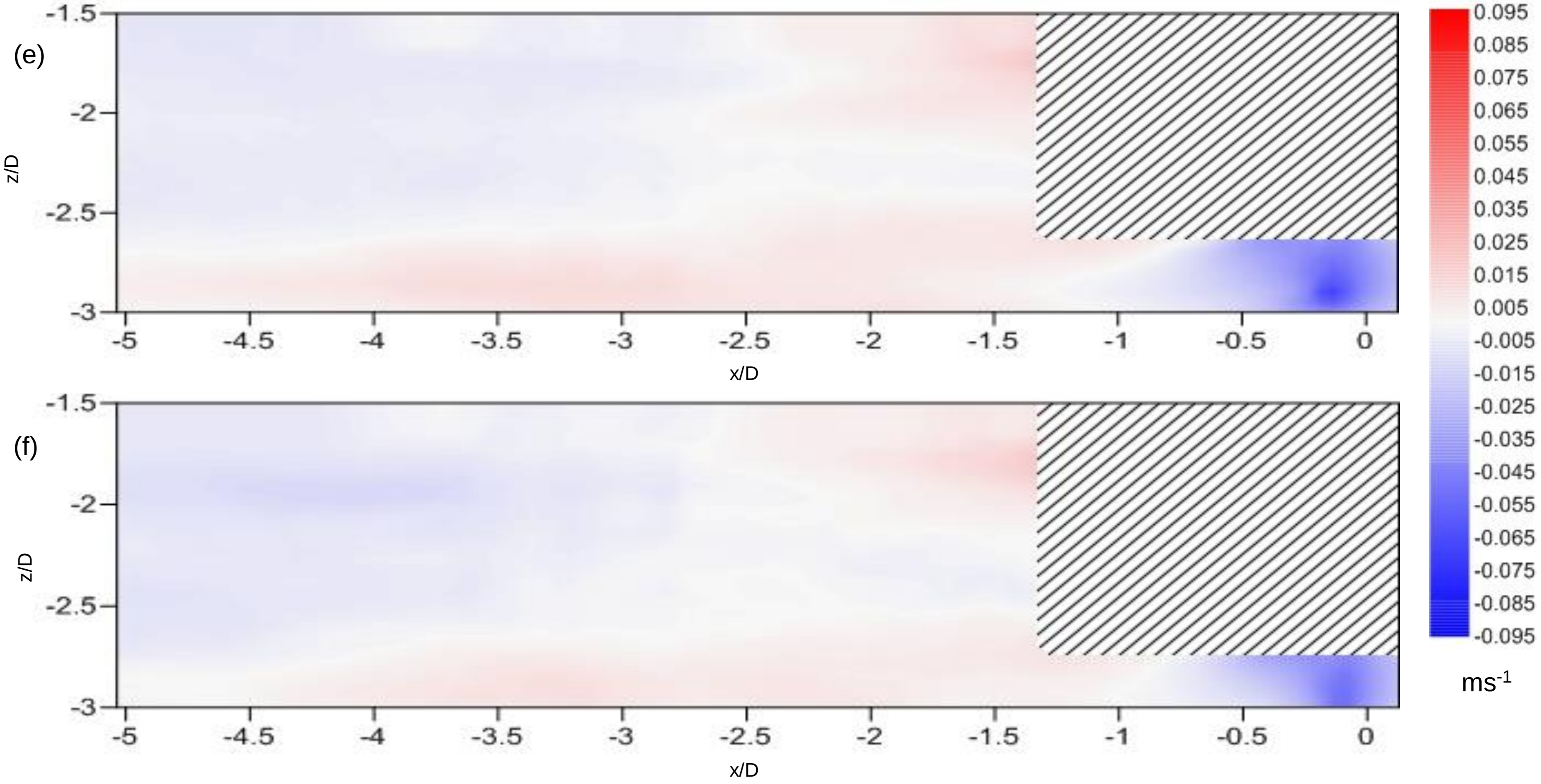

Figure 5.5: Flow structure maps for the vertical velocity component for the rotor positioned at (e) 140mm above the bed (f) 120mm above the bed. Flow direction is from right to left. Scales on the axes are normalised to rotor diameters (200mm). Areas covered by diagonal shading indicate areas where no data could be collected.

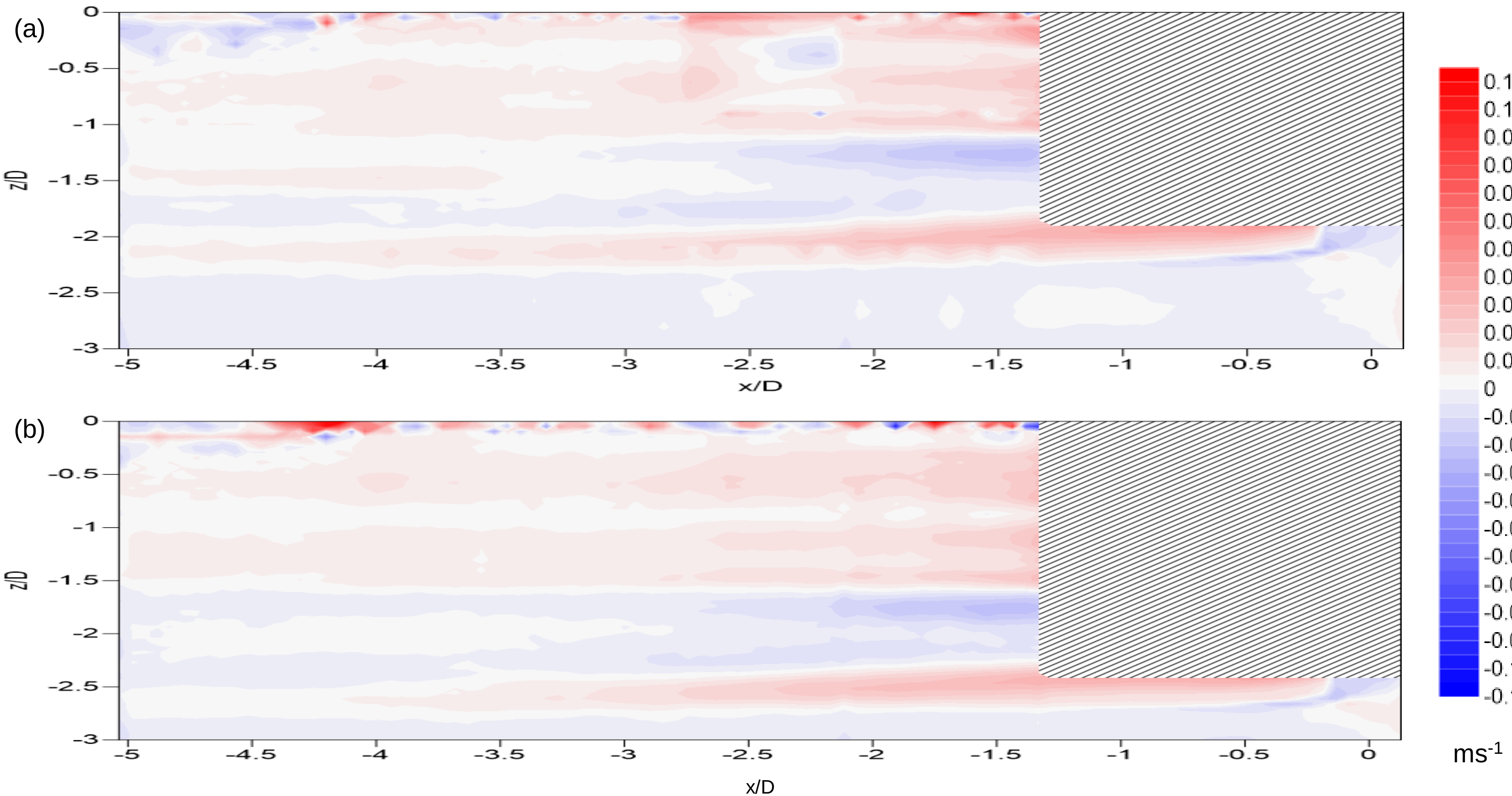

Figure 5.6: Flow structure maps for the cross-stream velocity component for the rotor positioned at (a) 300mm above the bed and (b) 200mm above the bed. Flow direction is from right to left. Scales on the axes are normalised to rotor diameters (200mm). Areas covered by diagonal shading indicate areas where no data could be collected.

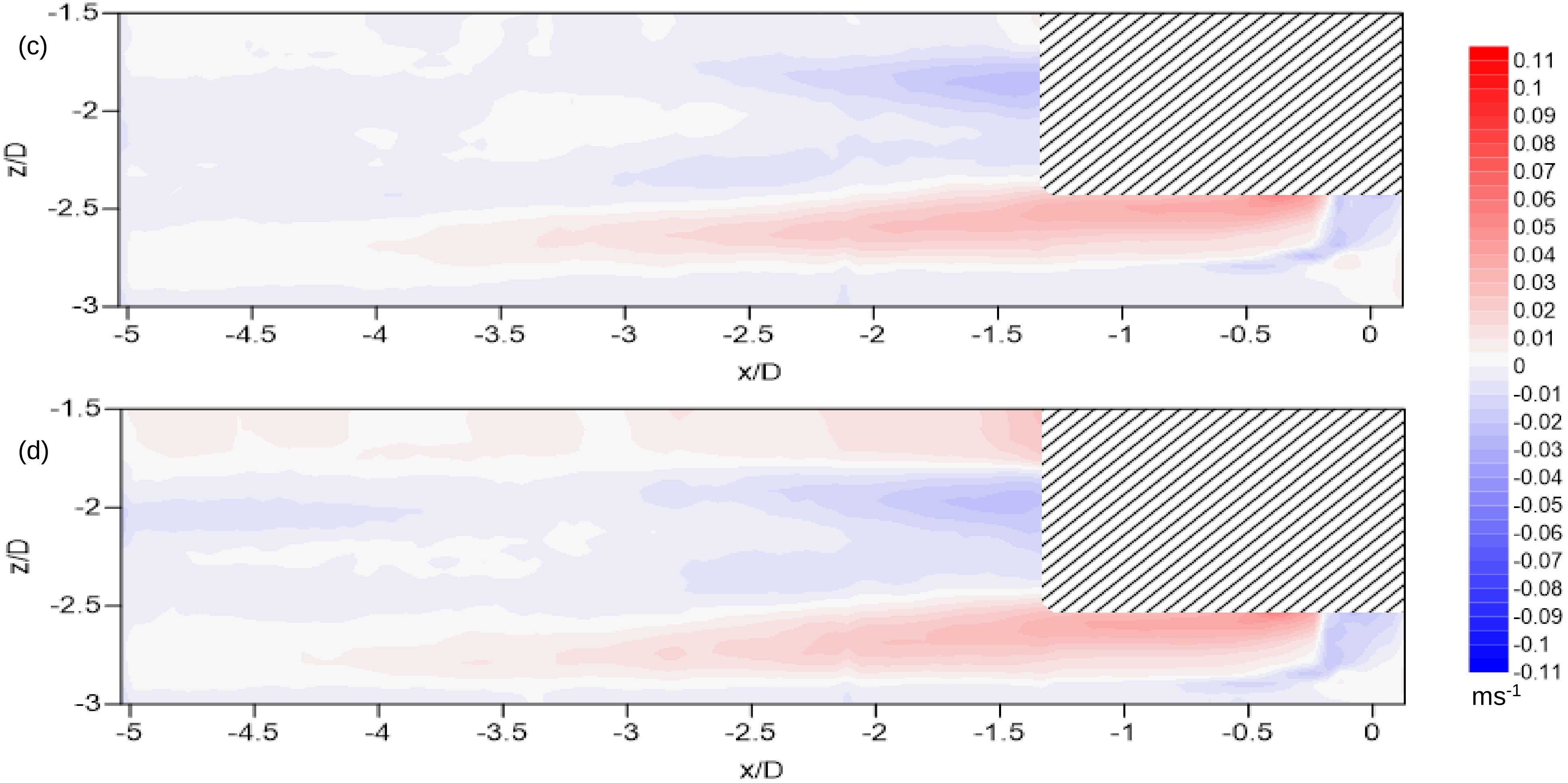

Figure 5.6: Flow structure maps for the cross-stream velocity component for the rotor positioned at (c) 180mm above the bed (d) 160mm above the bed. Flow direction is from right to left. Scales on the axes are normalised to rotor diameters (200mm). Areas covered by diagonal shading indicate areas where no data could be collected.

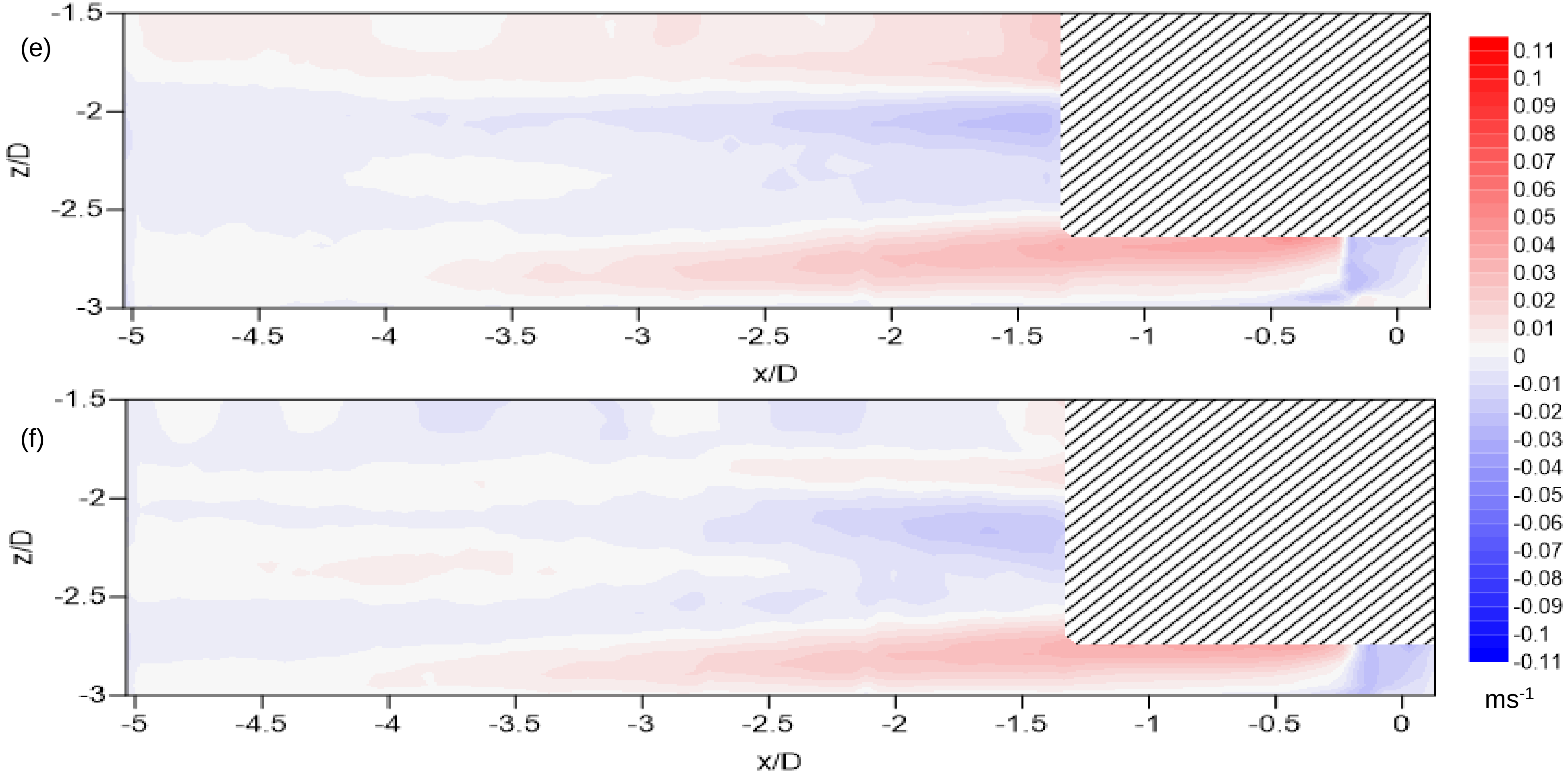

Figure 5.6: Flow structure maps for the cross-stream velocity component for the rotor positioned at (e) 140mm above the bed (f) 120mm above the bed. Flow direction is from right to left. Scales on the axes are normalised to rotor diameters (200mm). Areas covered by diagonal shading indicate areas where no data could be collected.

There are two distinct areas of increased standard deviation of the stream-wise velocity (u') and turbulence intensity (u'/U_0) downstream of the rotor that are aligned with the tips of the rotor blades (0.5D above and below the rotor centreline) (shown in figures 5.7 (a) to (f) and 5.8 (a) to (d) respectively). As the rotor is lowered closer to the bed, particularly beyond 180mm, the lower of these two regions becomes less pronounced. There is reduced turbulence in line with the lower blade tips when the rotor is positioned closer to the channel bed. When the rotor is positioned at 140mm and 120mm above the channel bed, there is a clear interaction between the wake of the rotor and the channel bed.

When the rotor is positioned at 300mm (figure 5.9 (a)) and 200mm (figure 5.9 (b)) above the bed, there is an area of increased standard deviation of the vertical velocity (w') beneath and downstream of the rotor, particularly within the extents of the blade tips, with decreases in the standard deviation of the vertical velocity outside of the main wake area. The increase in the standard deviation of the vertical velocity continues downstream of the rotor (as shown in figures 5.10 (a) to (d)) in a clearly defined zone that is evidently separate from the channel bed. When the rotor is lowered, there is still an area of increased vertical turbulence, but it is less pronounced than when the rotor is positioned at 300mm and 200mm above the channel bed. As the rotor is lowered, the upper half of the wake has a much greater increase in the standard deviation of the vertical velocity than the lower half of the wake (as shown in figures 5.9 (c) to (f) and 5.10 (a) to (d)).

There is a distinct area of increased standard deviation in the cross-stream flow (v') aligned with the upper and lower blade tips (figures 5.11 (a) to (f)). In this region, the standard deviation of the cross-stream flow is approximately three times greater than that of the free-stream flow. When the rotor is positioned at 300mm (figure 5.11 (a)) and 200mm (figure 5.11 (b)) above the bed, there is an obvious zone of minimal standard deviation in the cross-stream velocity below the rotor and wake. When the rotor is lowered closer to the bed (figures 5.11 (c) to (f)), there is an obvious convergence between the flow in the wake of the turbine and the channel bed, with no clear separation zone or boundary. At these lower rotor positions, the standard deviation in the cross-stream velocity is greater on the upper side of the separation zone compared to the lower side of the separation zone.

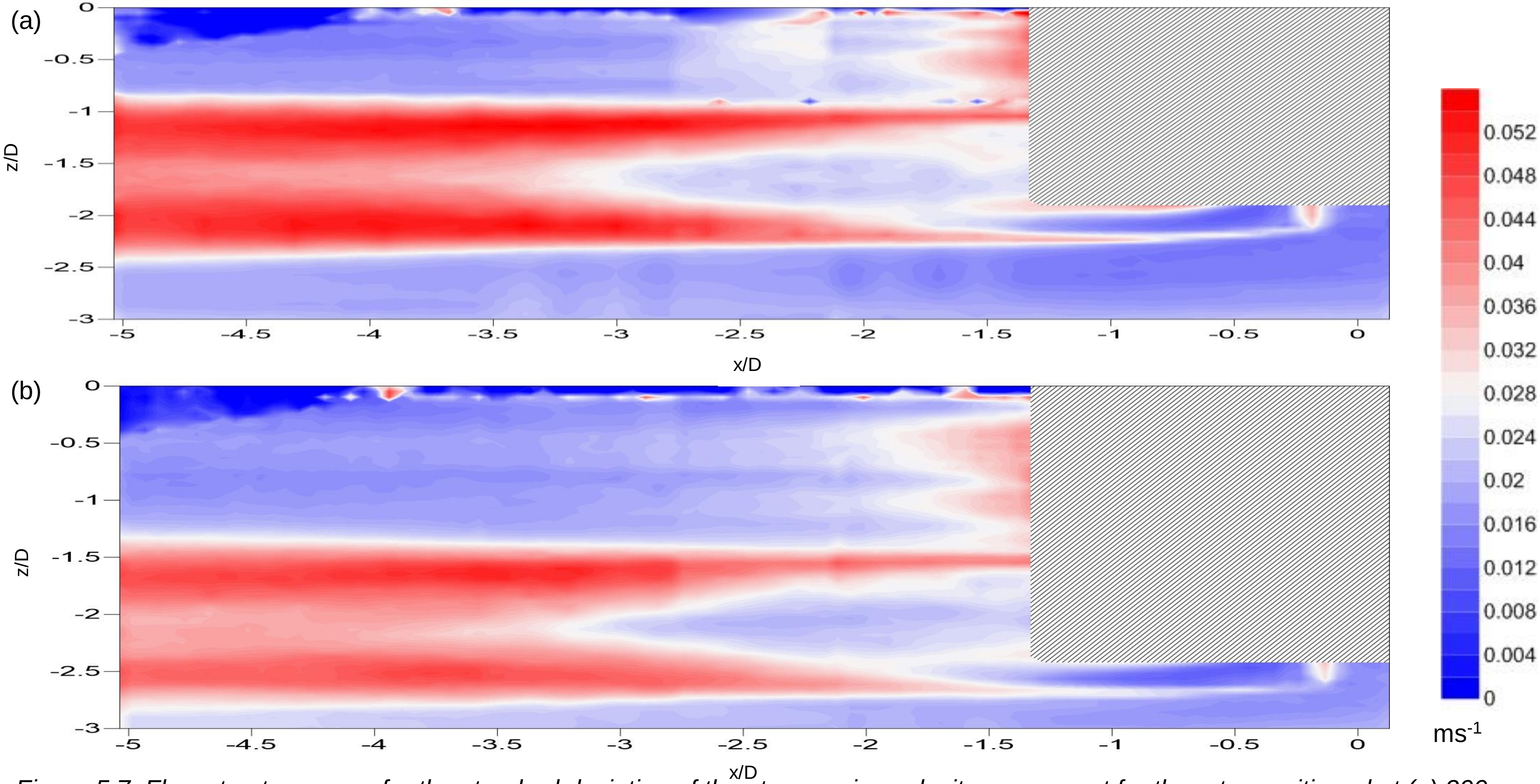

Figure 5.7: Flow structure maps for the standard deviation of the stream-wise velocity component for the rotor positioned at (a) 300mm above the bed (b) 200mm above the bed. Flow direction is from right to left. Scales on the axes are normalised to rotor diameters (200mm). Areas covered by diagonal shading indicate areas where no data could be collected.

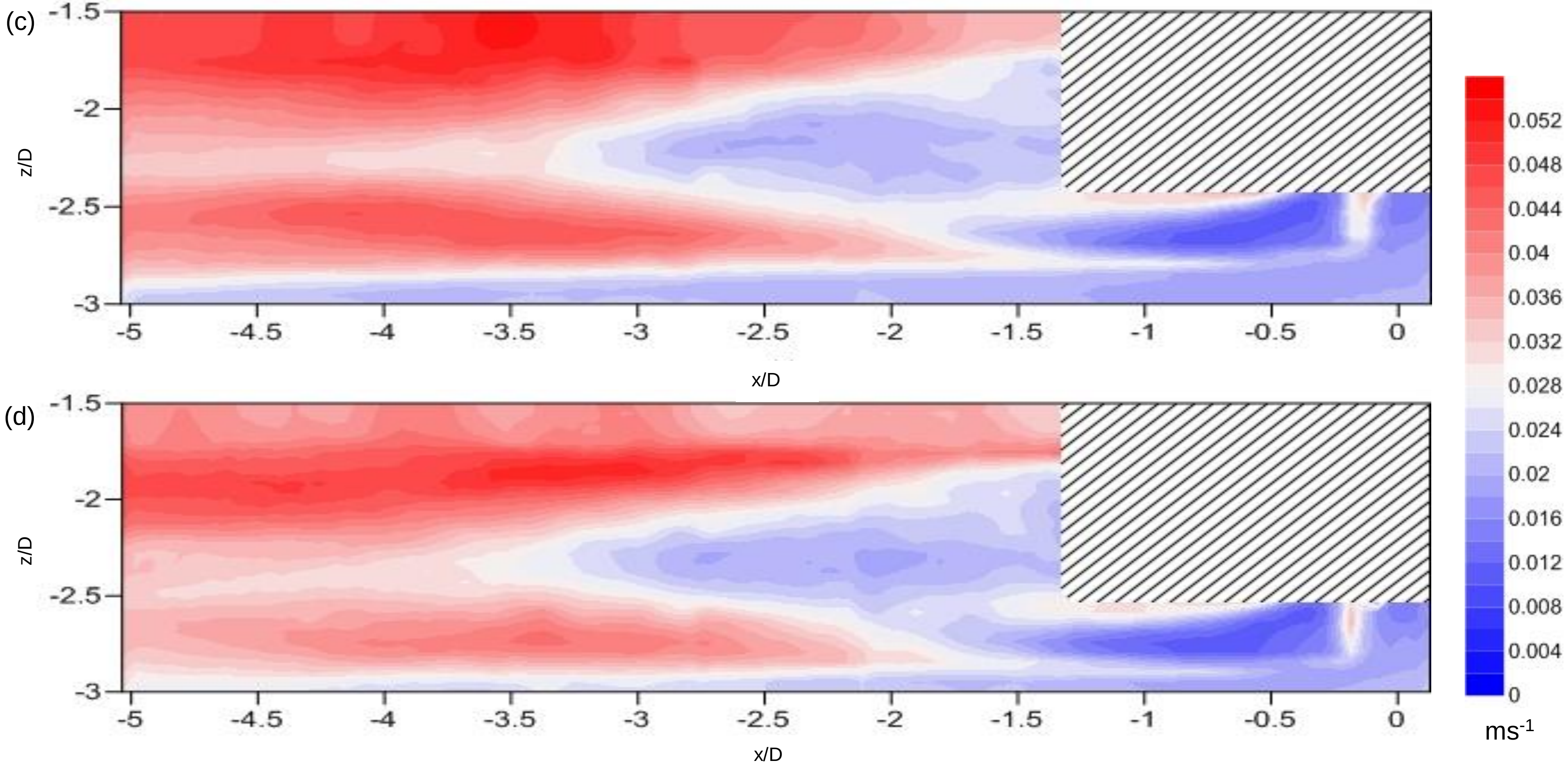

Figure 5.7: Flow structure maps for the standard deviation of the stream-wise velocity component for the rotor positioned at (c) 180mm above the bed (d) 160mm above the bed. Flow direction is from right to left. Scales on the axes are normalised to rotor diameters (200mm). Areas covered by diagonal shading indicate areas where no data could be collected.

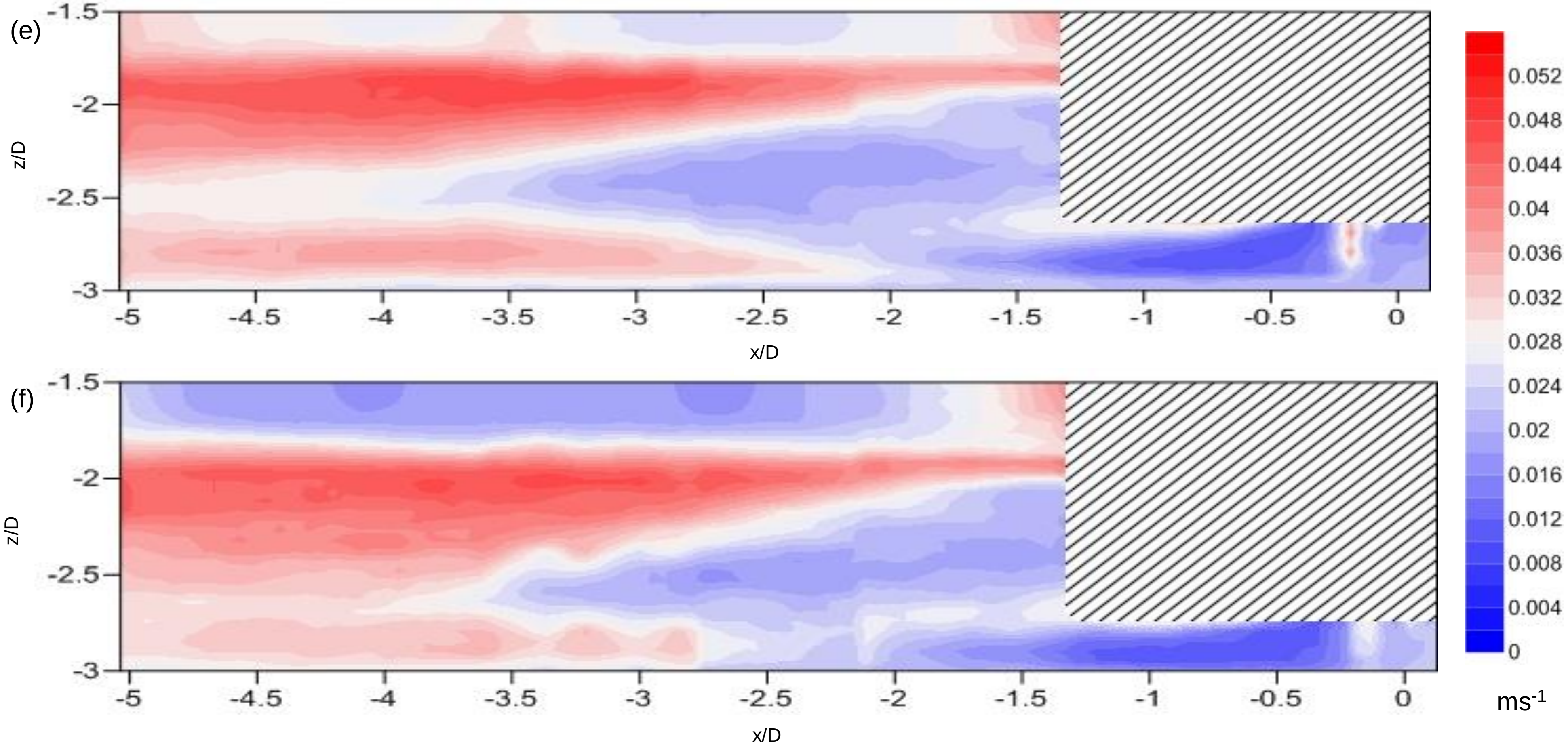

Figure 5.7: Flow structure maps for the standard deviation of the stream-wise velocity component for the rotor positioned at (e) 140mm above the bed (f) 120mm above the bed. Flow direction is from right to left. Scales on the axes are normalised to rotor diameters (200mm). Areas covered by diagonal shading indicate areas where no data could be collected.

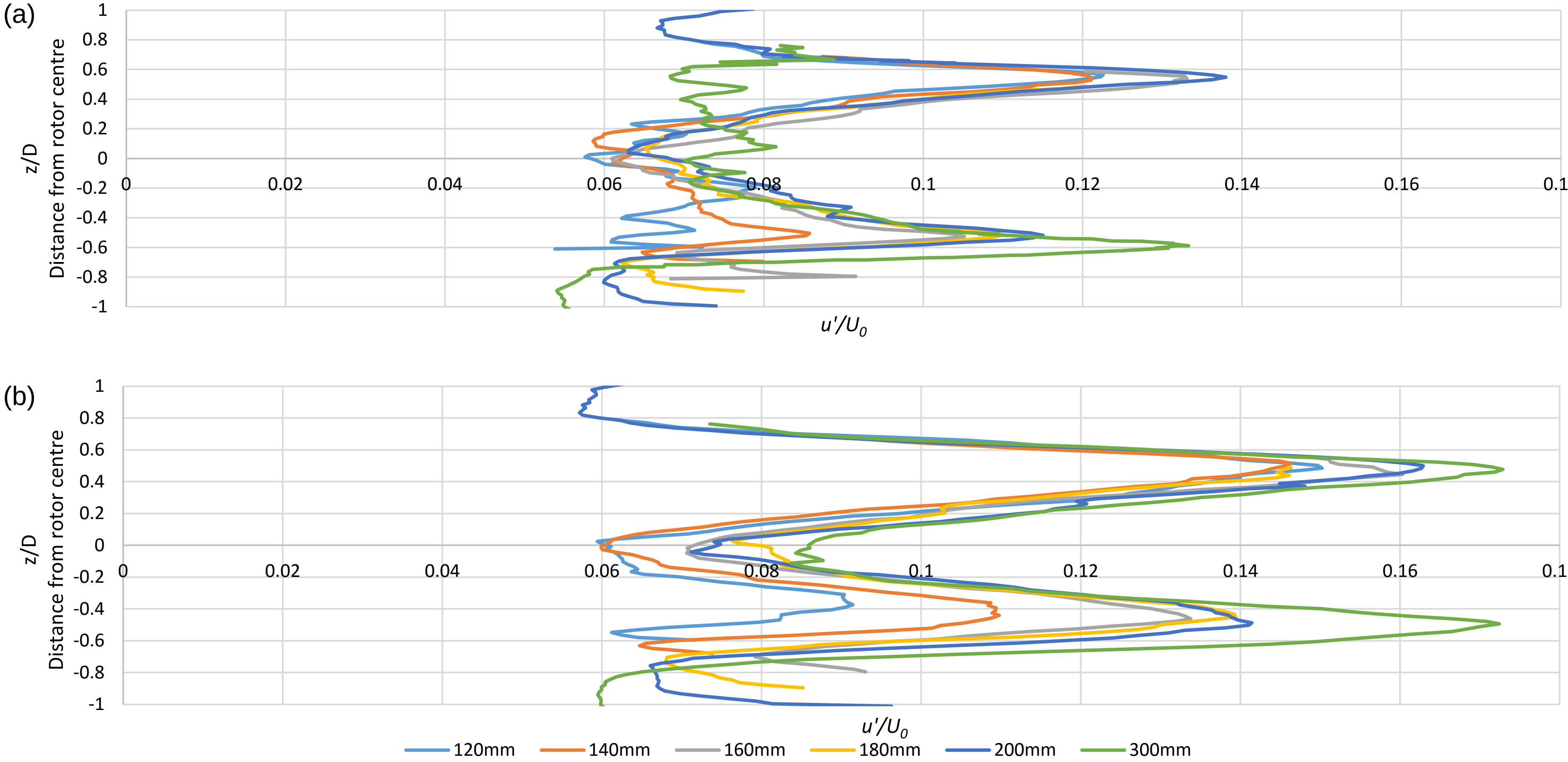

Figure 5.8: Charts showing the vertical profile of the turbulence intensity (u'/U_0) with the rotor positioned at 120mm, 140mm, 160mm, 180mm, 200mm and 300mm above the channel bed at (a) 2 rotor diameter (b) 3 rotor diameters downstream from the turbine. Scales on the y-axes are normalised to rotor diameters (200mm).

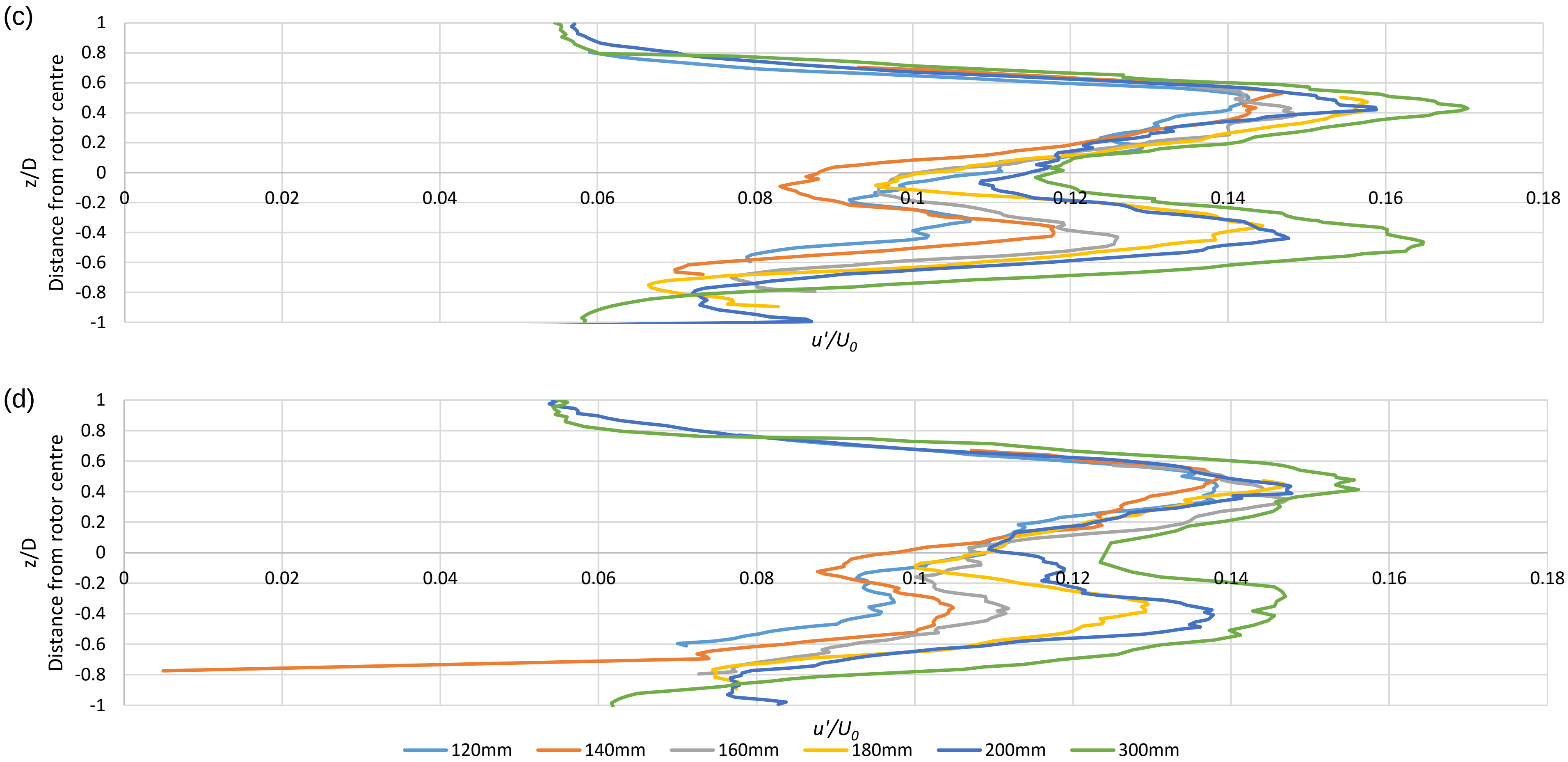

Figure 5.8: Charts showing the vertical profile of the turbulence intensity (u'/U_0) with the rotor positioned at 120mm, 140mm, 160mm, 180mm, 200mm and 300mm above the channel bed at (c) 4 rotor diameters and (d) 5 rotor diameters downstream from the turbine. Scales on the y-axes are normalised to rotor diameters (200mm).

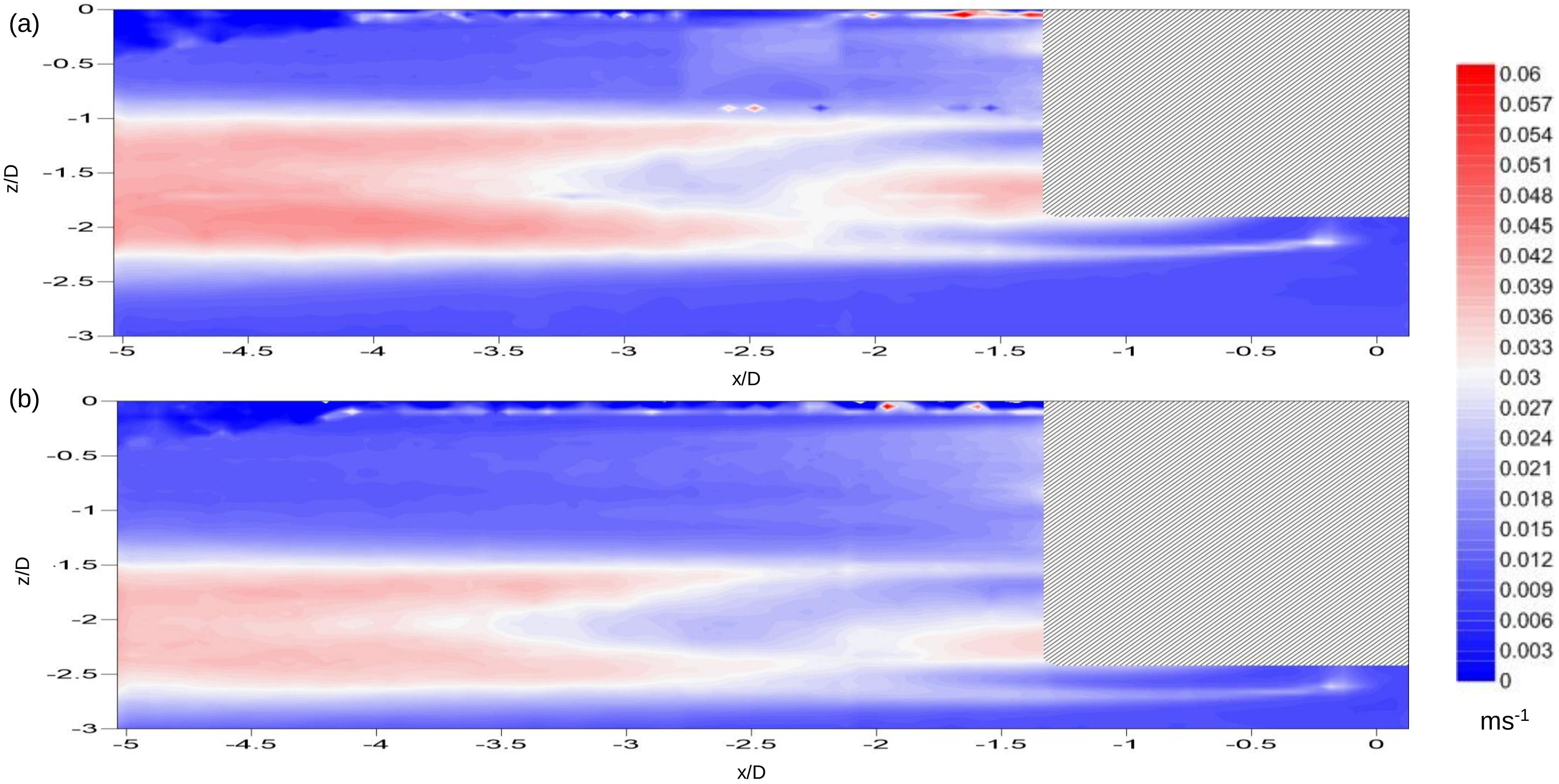

Figure 5.9: Flow structure maps for the standard deviation of the vertical velocity component for the rotor positioned at (a) 300mm above the bed (b) 200mm above the bed. Flow direction is from right to left. Scales on the axes are normalised to rotor diameters (200mm). Areas covered by diagonal shading indicate areas where no data could be collected.

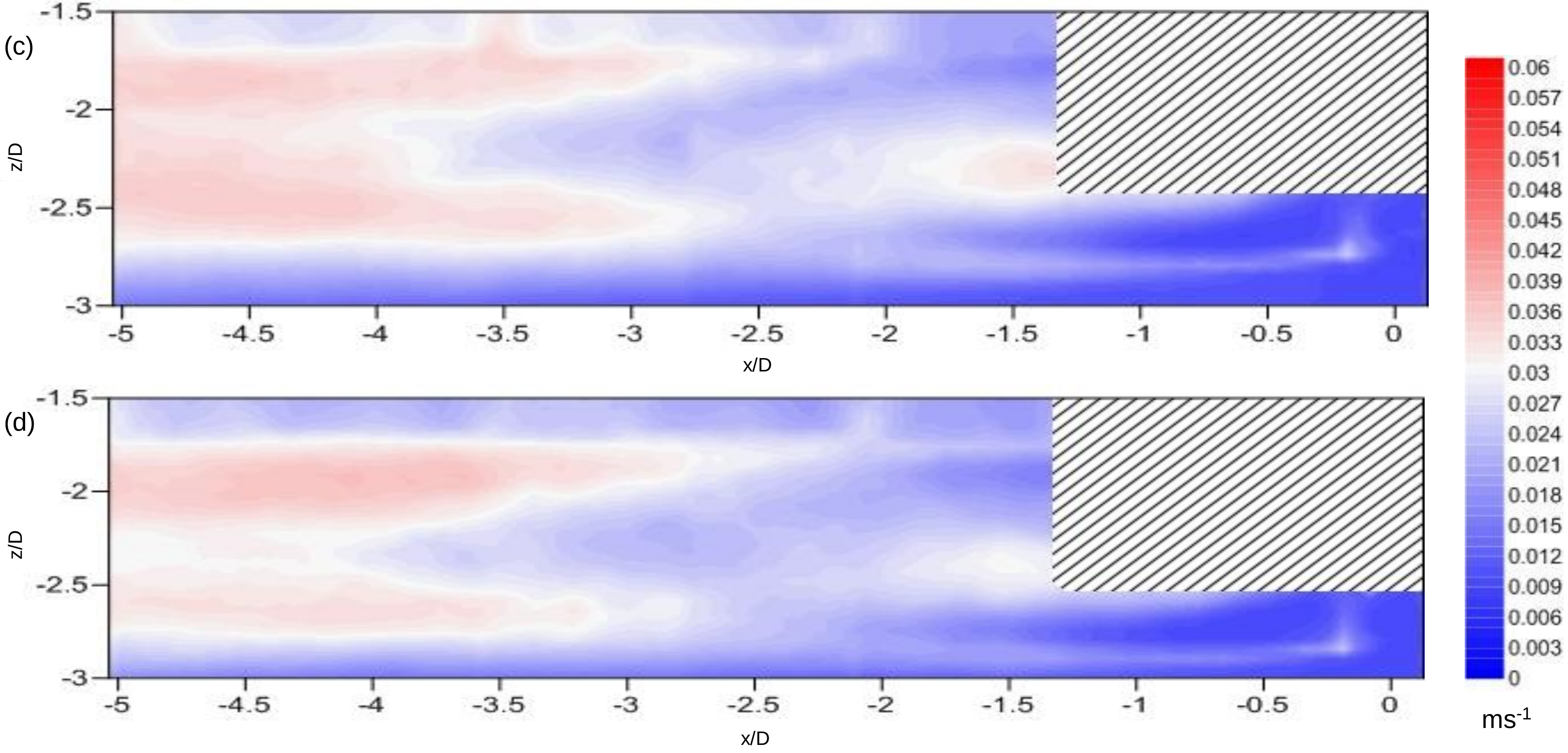

Figure 5.9: Flow structure maps for the standard deviation of the vertical velocity component for the rotor positioned at (c) 180mm above the bed (d) 160mm above the bed. Flow direction is from right to left. Scales on the axes are normalised to rotor diameters (200mm). Areas covered by diagonal shading indicate areas where no data could be collected.

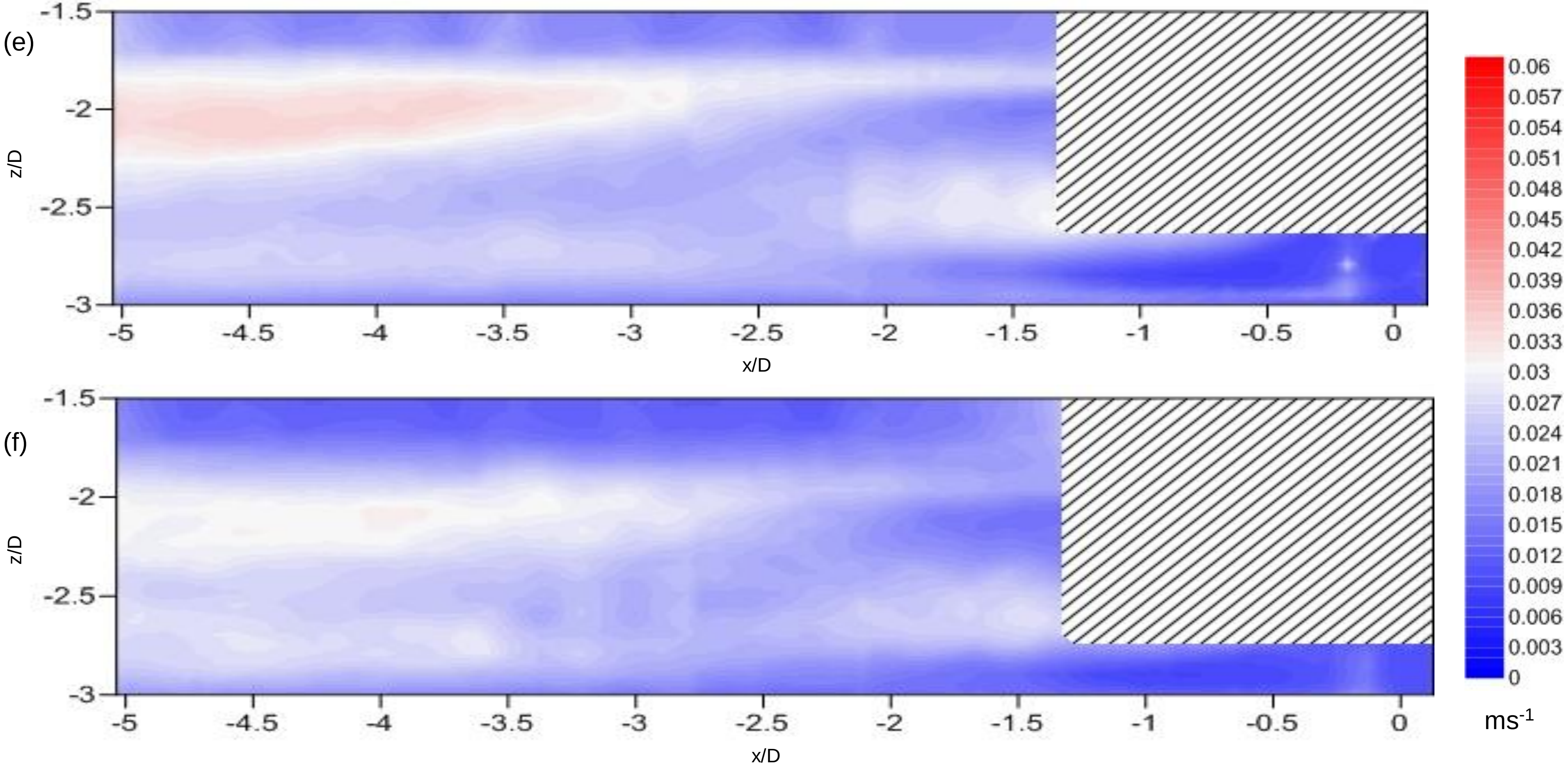

Figure 5.9: Flow structure maps for the standard deviation of the vertical velocity component for the rotor positioned at (e) 140mm above the bed (f) 120mm above the bed. Flow direction is from right to left. Scales on the axes are normalised to rotor diameters (200mm). Areas covered by diagonal shading indicate areas where no data could be collected.

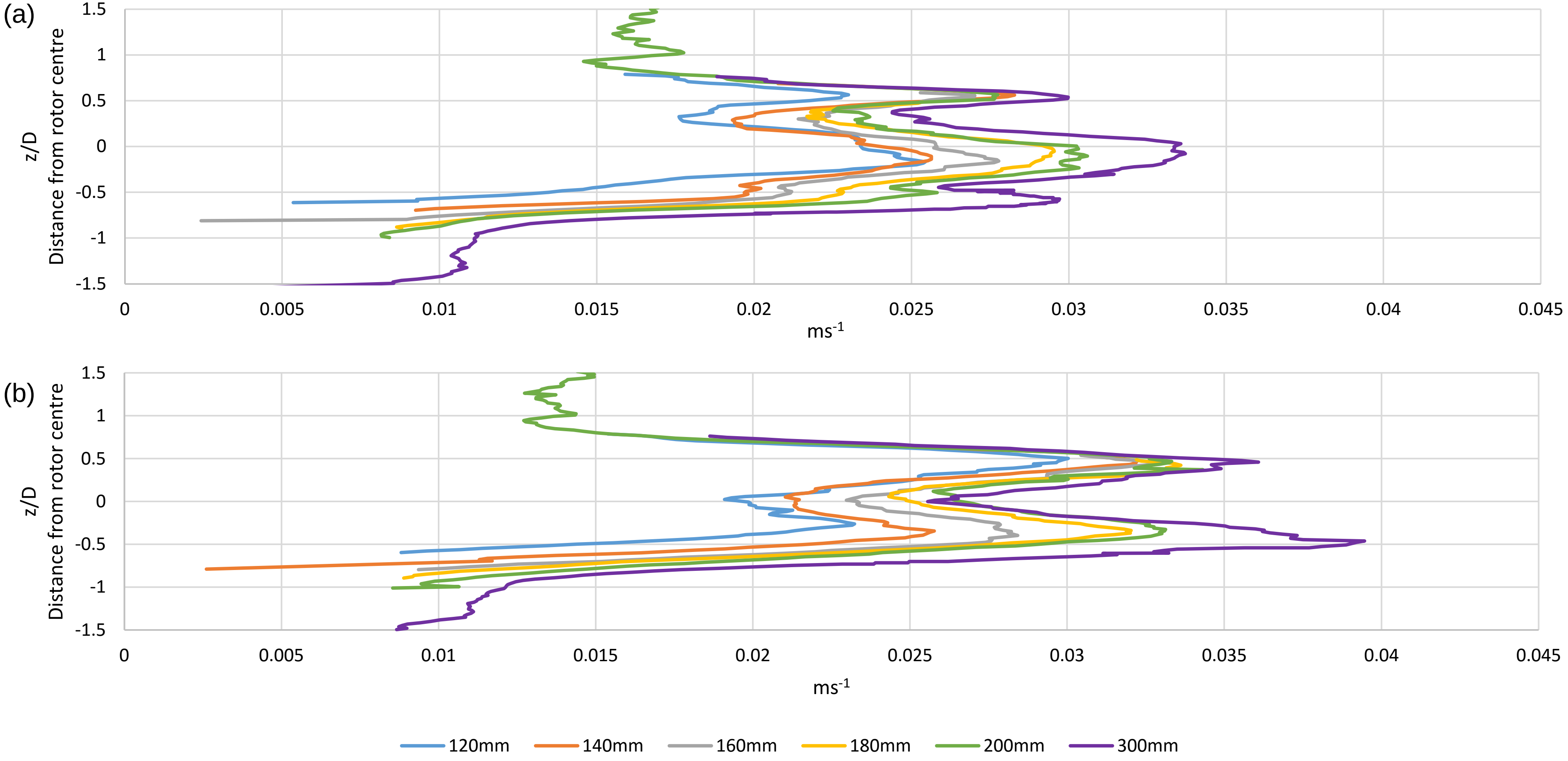

Figure 5.10: Charts showing the vertical profile of the standard deviation of the vertical velocity (w') with the rotor positioned at 120mm, 140mm, 160mm, 180mm, 200mm and 300mm above the channel bed at (a) 2 rotor diameter (b) 3 rotor diameters downstream from the turbine. Scales on the y-axes are normalised to rotor diameters (200mm).

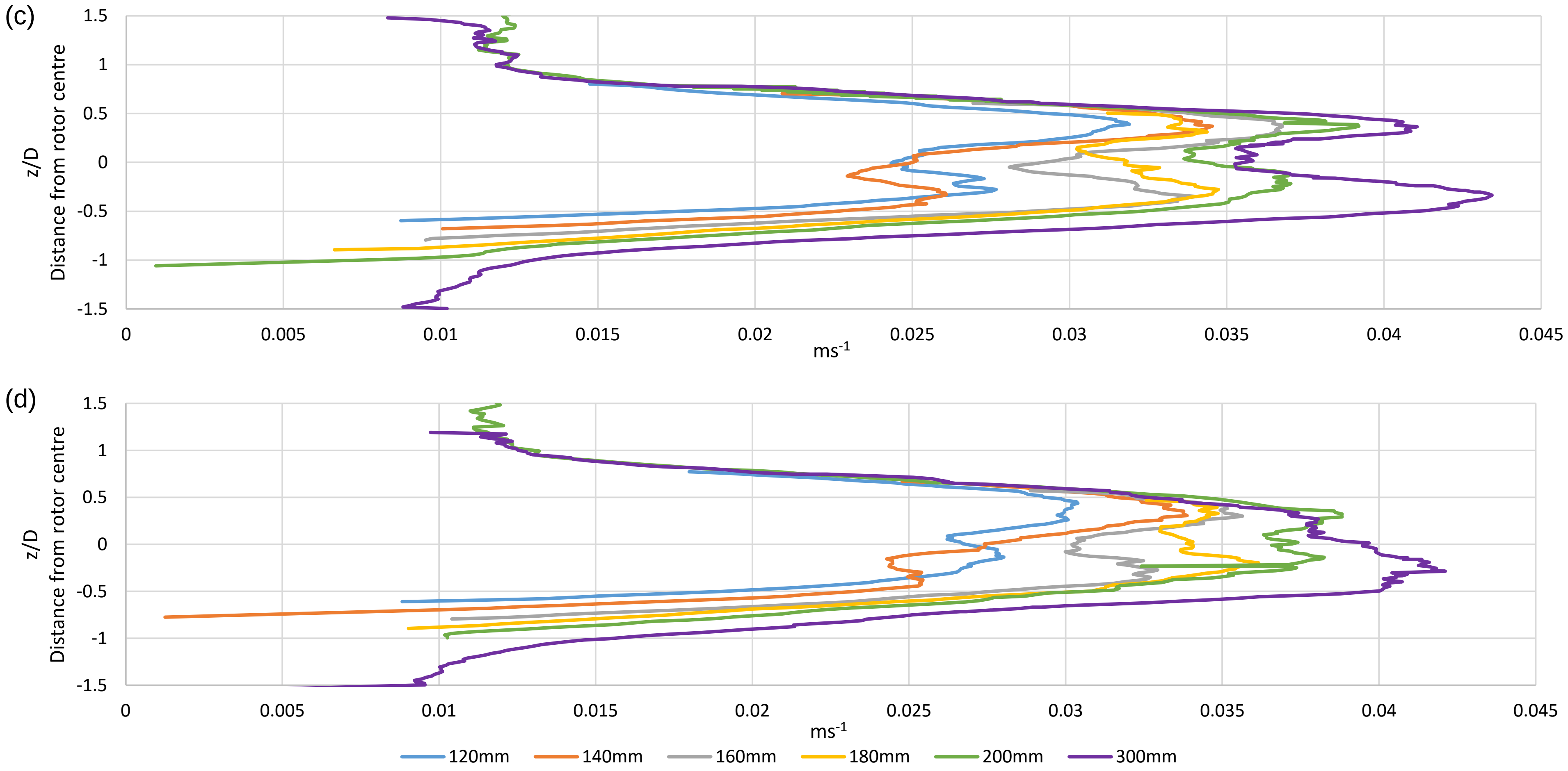

Figure 5.10: Charts showing the vertical profile of the standard deviation of the vertical velocity (w') with the rotor positioned at 120mm, 140mm, 160mm, 180mm, 200mm and 300mm above the channel bed at (c) 4 rotor diameters and (d) 5 rotor diameters downstream from the turbine. Scales on the y-axes are normalised to rotor diameters (200mm).

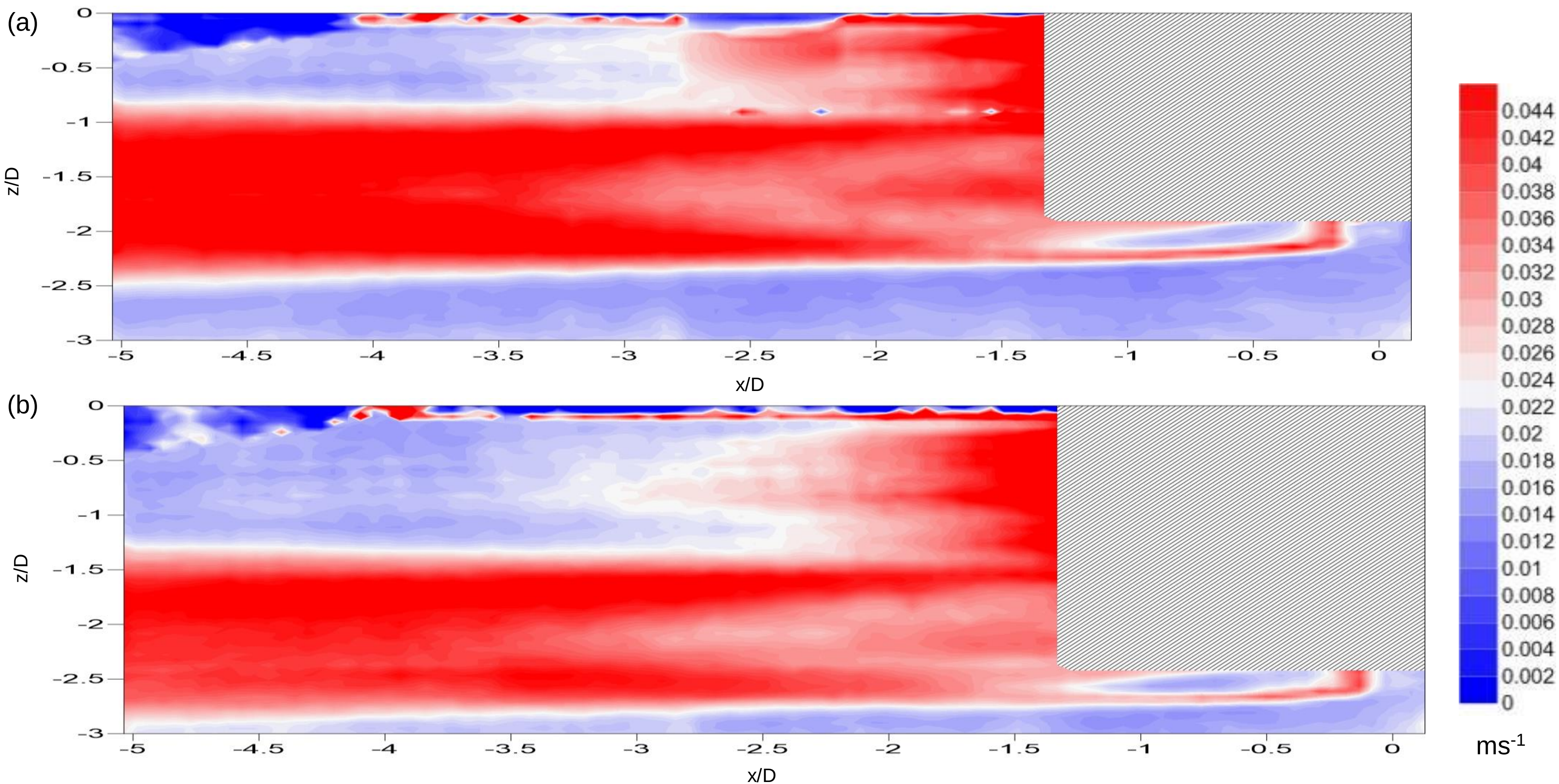

Figure 5.11: Flow structure maps for the standard deviation of the cross-stream velocity component for the rotor positioned at (a) 300mm above the bed (b) 200mm above the bed. Flow direction is from right to left. Scales on the axes are normalised to rotor diameters (200mm). Areas covered by diagonal shading indicate areas where no data could be collected.

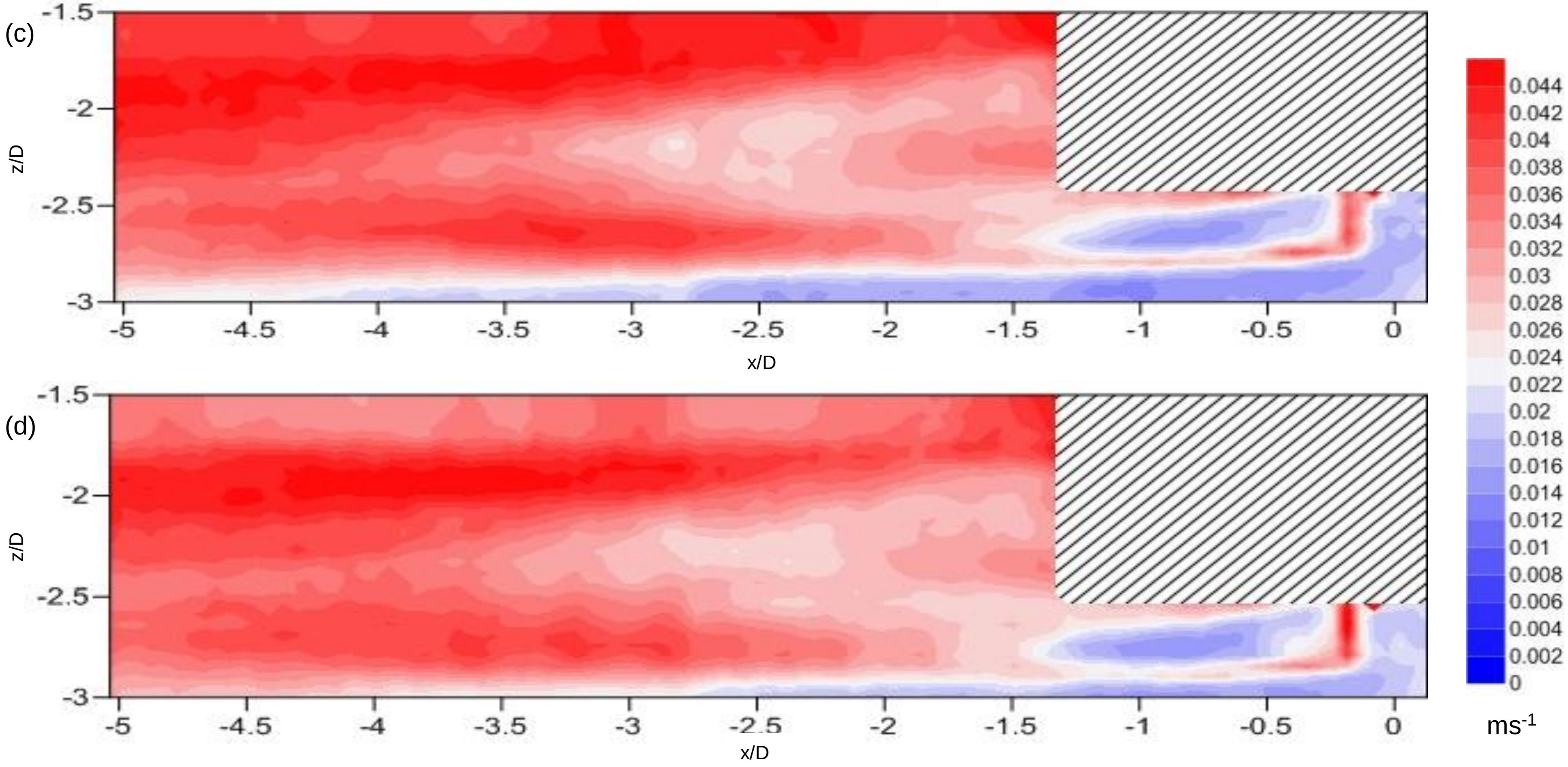

Figure 5.11: Flow structure maps for the standard deviation of the cross-stream velocity component for the rotor positioned at (c) 180mm above the bed (d) 160mm above the bed. Flow direction is from right to left. Scales on the axes are normalised to rotor diameters (200mm). Areas covered by diagonal shading indicate areas where no data could be collected.

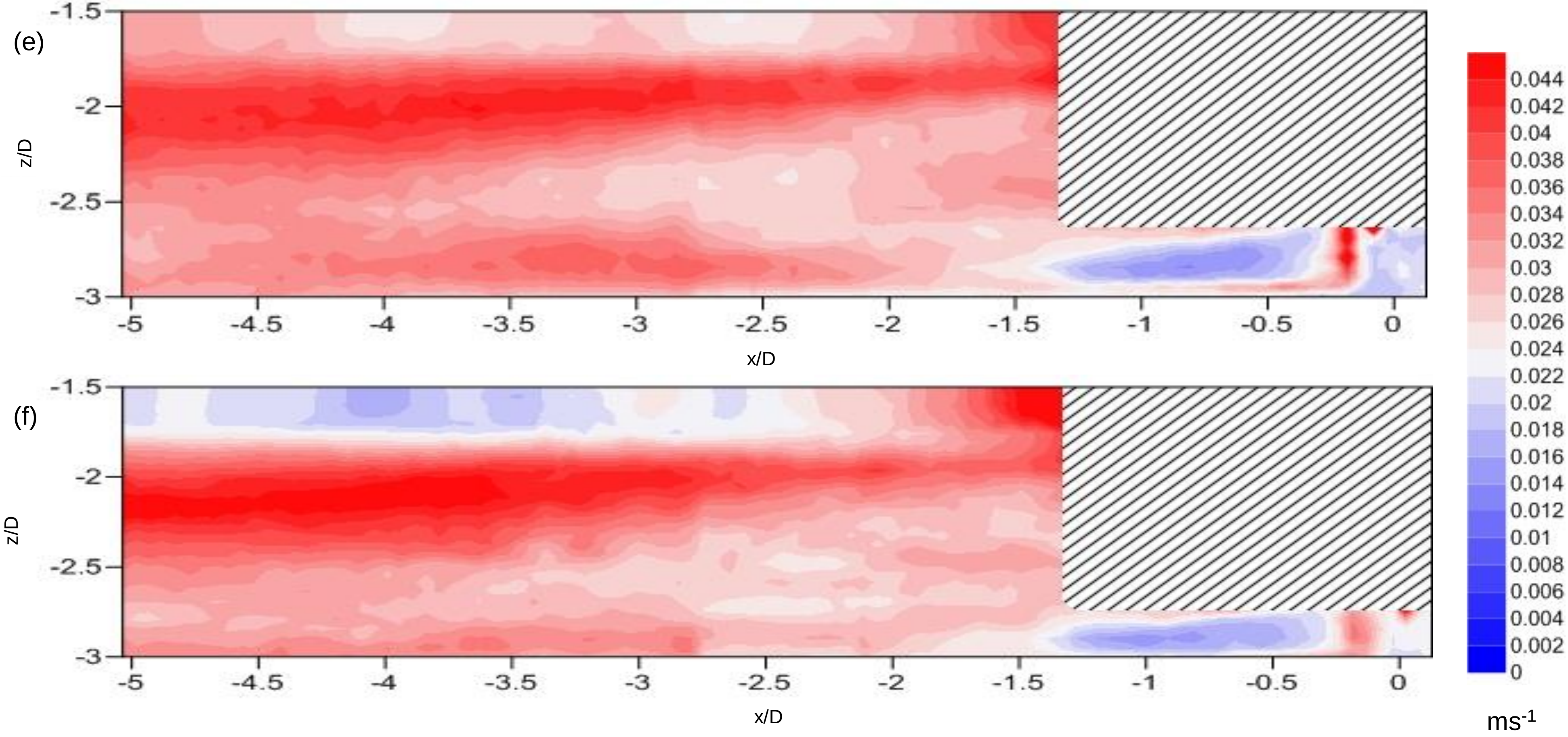

Figure 5.11: Flow structure maps for the standard deviation of the cross-stream velocity component for the rotor positioned at (e) 140mm above the bed (f) 120mm above the bed. Flow direction is from right to left. Scales on the axes are normalised to rotor diameters (200mm). Areas covered by diagonal shading indicate areas where no data could be collected.

There is a noticeable increase in the turbulent kinetic energy (*k*) immediately downstream from the rotor, particularly in line with the blade tips (0.5D above and below the rotor centreline), as shown in figures 5.12 (a) to 5.12 (f) and figures 5.13 (a) to 5.13 (d). The turbulent kinetic energy is greatest when the rotor is at 300mm from the bed. At this rotor height, there are two symmetrical separate regions of increased magnitude of *k* which develop at ~2 rotor diameters downstream. The turbulent kinetic energy is greatest at 3 rotor diameters downstream from the turbine. At this location, the turbulent kinetic energy at the blade tips when the rotor was positioned at 300mm was ~59% greater than *k* at the centre of the turbine. These narrow regions of increased *k* grow in extent as distance downstream increases. The regions appear to merge at ~3.75 rotor diameters downstream from the turbine. As the rotor is lowered closer to the bed, the turbulent kinetic energy becomes more asymmetric and the lower of the two regions has a smaller increase in *k* compared to the upper region.

Immediately above the bed in the area upstream of the rotor, *k* decreases with increasing proximity to the rotor. There is a noticeable decrease in *k* in the immediate vicinity of the rotor, and then a noticeable increase downstream of the rotor. The turbulent kinetic energy continues to increase downstream. This pattern is true for all of the rotor heights. However, the greatest increase in *k* occurs when the rotor is closest to the bed (120mm) (figure 5.14).

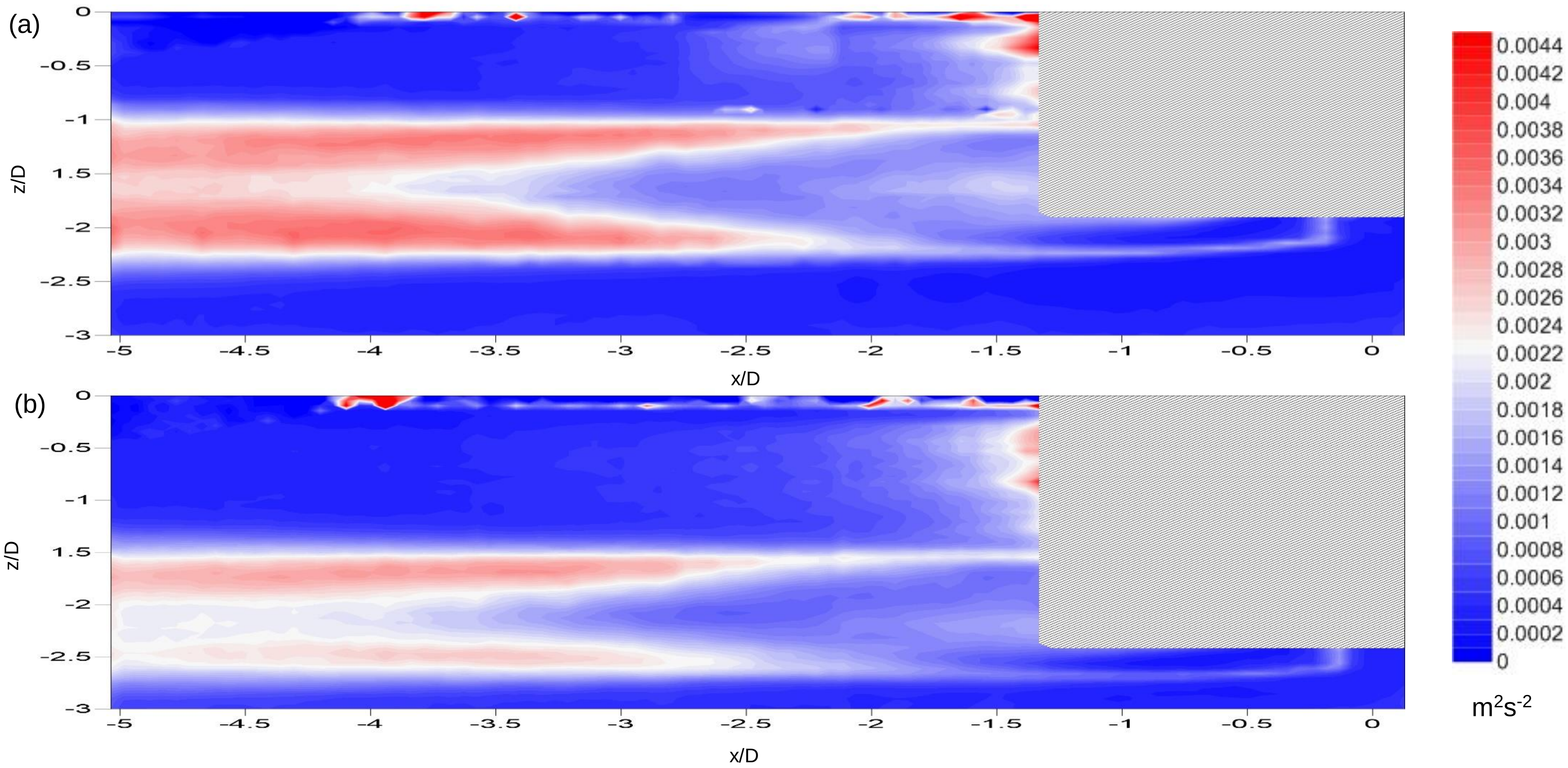

Figure 5.12: Flow structure maps for the turbulent kinetic energy (k) for the rotor positioned at (a) 300mm above the bed and (b) 200mm above the bed. Flow direction is from right to left. Scales on the axes are normalised to rotor diameters (200mm). Areas covered by diagonal shading indicate areas where no data could be collected.

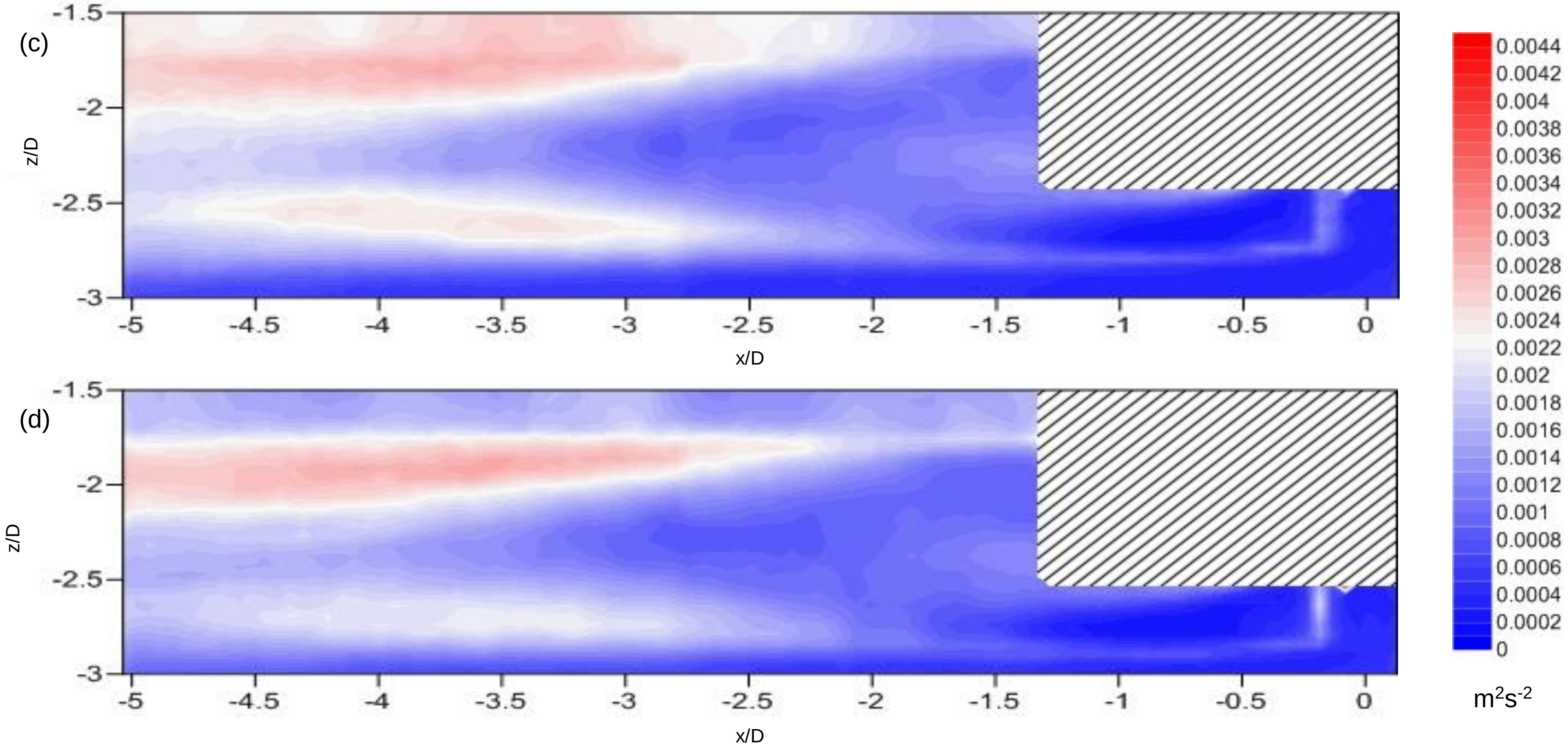

Figure 5.12: Flow structure maps for the turbulent kinetic energy (k) for the rotor positioned at (c) 180mm above the bed (d) 160mm above the bed. Flow direction is from right to left. Scales on the axes are normalised to rotor diameters (200mm). Areas covered by diagonal shading indicate areas where no data could be collected.

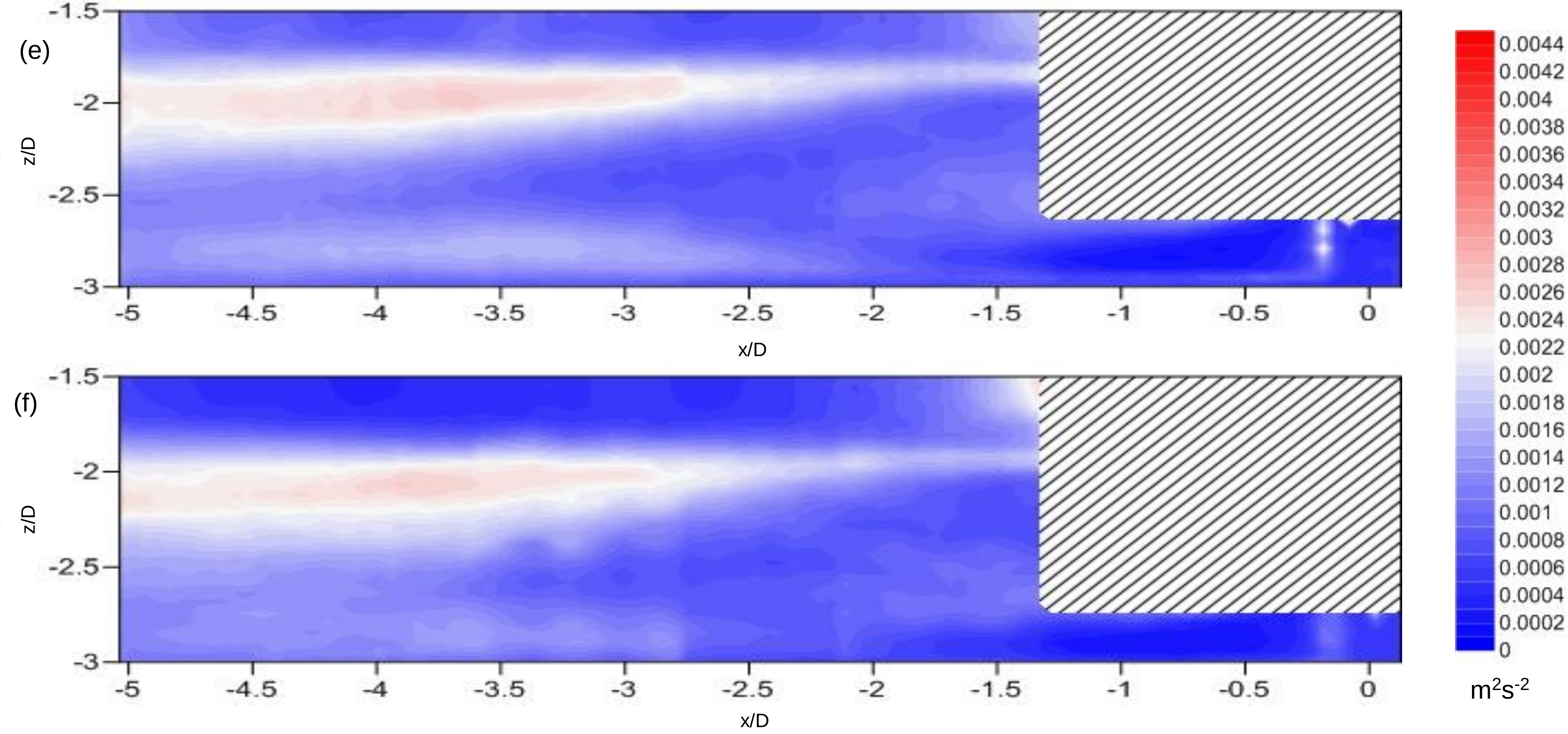

Figure 5.12: Flow structure maps for the turbulent kinetic energy (k) for the rotor positioned at (e) 140mm above the bed (f) 120mm above the bed. Flow direction is from right to left. Scales on the axes are normalised to rotor diameters (200mm). Areas covered by diagonal shading indicate areas where no data could be collected.

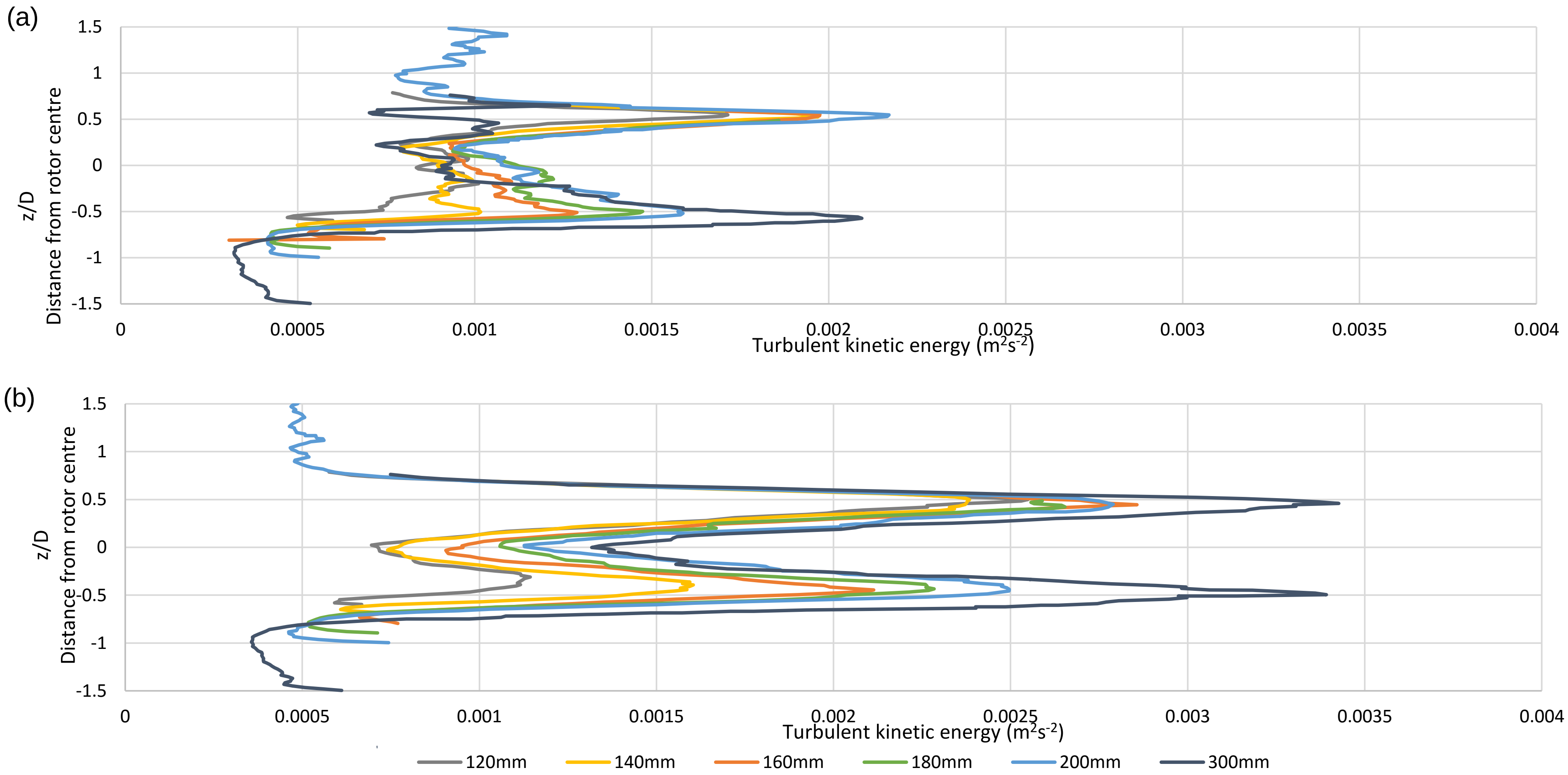

Figure 5.13: Charts showing the vertical profile of the turbulent kinetic energy (k) with the rotor positioned at 120mm, 140mm, 160mm, 180mm, 200mm and 300mm above the channel bed at (a) 2 rotor diameter downstream from the turbine (b) 3 rotor diameters downstream from the turbine. Scales on the y-axes are normalised to rotor diameters (200mm).

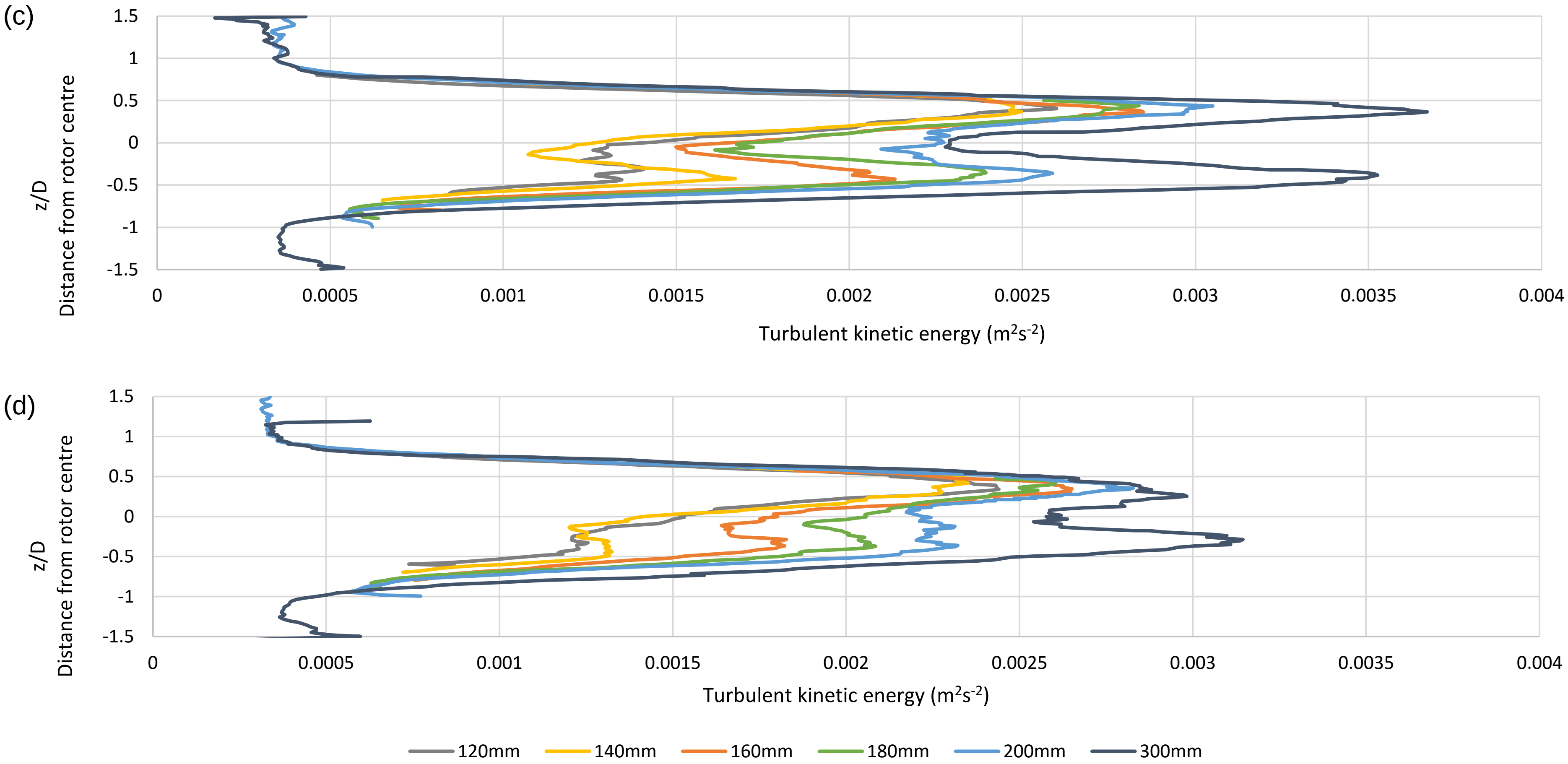

Figure 5.13: Charts showing the vertical profile of the turbulent kinetic energy (k) with the rotor positioned at 120mm, 140mm, 160mm, 180mm, 200mm and 300mm above the channel bed at (c) 4 rotor diameters downstream from the turbine and (d) 5 rotor diameters downstream from the turbine. Scales on the y-axes are normalised to rotor diameters (200mm).

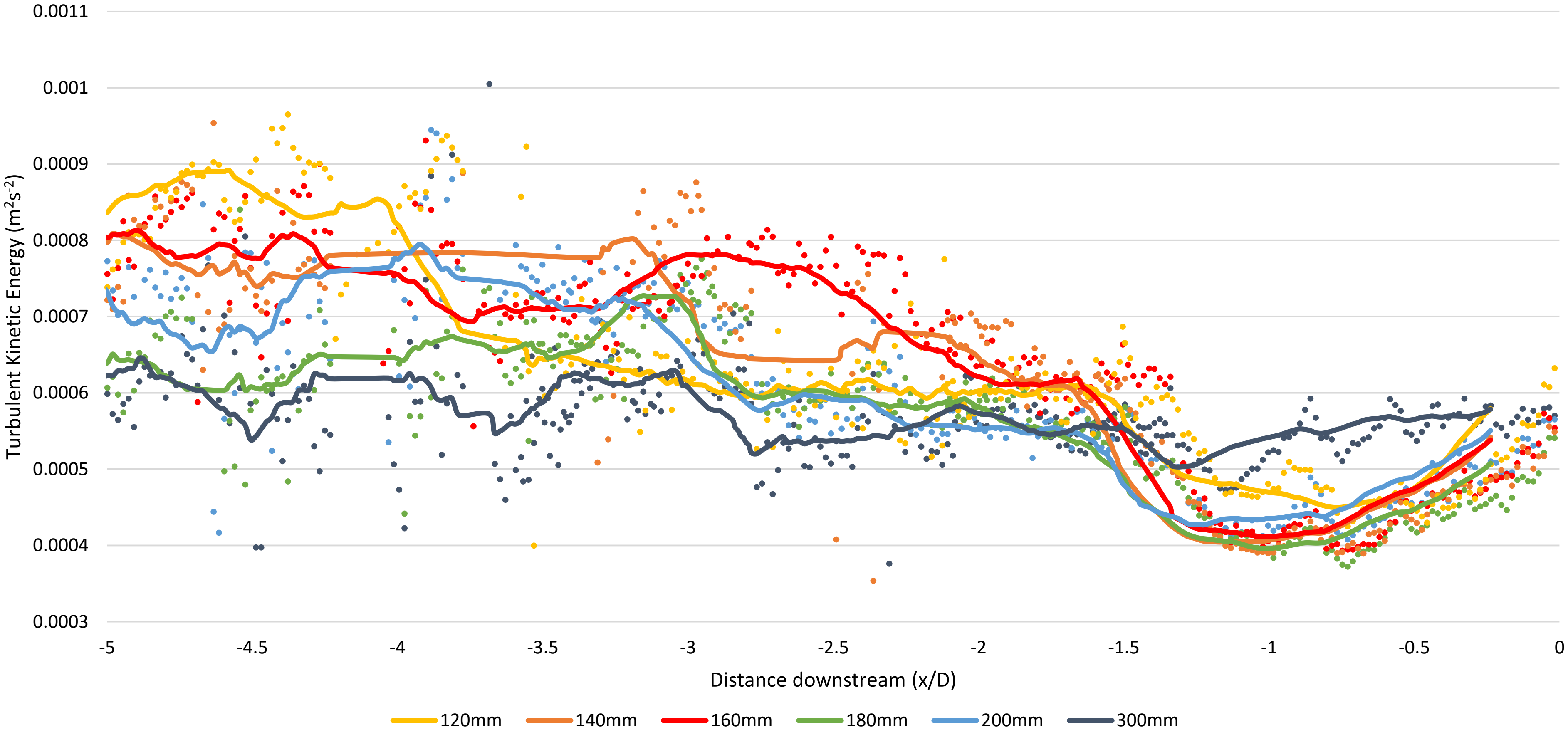

Figure 5.14: Turbulent kinetic energy (k) for rotor heights of 120mm, 140mm, 160mm, 180mm, 200mm and 300mm. Point: Original data points. Solid line: Moving average trend line. Flow direction is from right to left. Scale on the horizontal axis is normalised to rotor diameters (200mm). Rotor is positioned immediately upstream of x=0. The turbulent kinetic energy is measured in the closest measurement cell to the channel bed.

The general patterns seen in the Reynolds shear stress (u'w') flow maps (figures 5.15 (a) to (f)) and vertical profiles (figures 5.16 (a) to (d)) are similar to those in the TKE profiles (figures 5.12 (a) to 5.12(f) and figures 5.13 (a) to 5.13(d)). When the rotor is positioned at 300mm above the bed, the Reynolds shear stress is greatest in line with the rotor tips (figure 5.15 (a)). These zones of increased Reynolds shear stress become larger and they begin to merge further downstream, as shown in figure 5.15 (a) and figures 5.16 (b) to 5.16 (d). The point at which the zones of increased Reynolds shear stress merge downstream is at the same point where the zones of increased TKE merge. The greatest Reynolds shear stress occurs at 4 rotor diameters downstream when the turbine is located at 300mm above the channel bed. At this location, the Reynolds shear stress at the blade tips was ~74% greater than the Reynolds shear stress at the centre of the turbine. When the rotor is lowered to 200mm above the bed, the Reynolds shear stress is greatest in line with the upper blade tip, and significantly lower in line with the lower blade tip. This disparity increases as the rotor gets closer to the bed and this region of increased Reynolds shear stress in line with the lower blade tip diminishes significantly, particularly from ~2 rotor diameters downstream from the TST.

The exact entrainment and shear velocity threshold were not directly measured in the experiments described herein (as detailed in section 3.2). However, it is known that this threshold was not reached under plain channel conditions. Therefore, the plain channel conditions are used to normalise the shear velocity and represent a threshold that can be exceeded due to the presence of the tidal steam turbine. The normalised shear velocity of the plain channel is 1 (indicated by the dashed black line on figure 5.17). There is a significant effect on the normalised shear velocity due to the presence of the rotor. Immediately downstream of the rotor, the normalised shear velocity is increased, with the greatest increase occurring when the rotor is positioned at 120mm above the bed. However, further downstream, the normalised shear velocity is reduced compared to when the rotor is further from the channel bed (figure 5.17).

The normalised shear velocity of the plain channel is exceeded at all rotor heights up to ~2.5 rotor diameters downstream. Further downstream, the normalised shear velocity does not exceed 1 when the rotor is positioned at 120mm and 140mm above the channel bed. At rotor heights between 160mm and 300mm, the normalised shear velocity exceeds 1 until approximately 3.75 rotor diameters downstream.

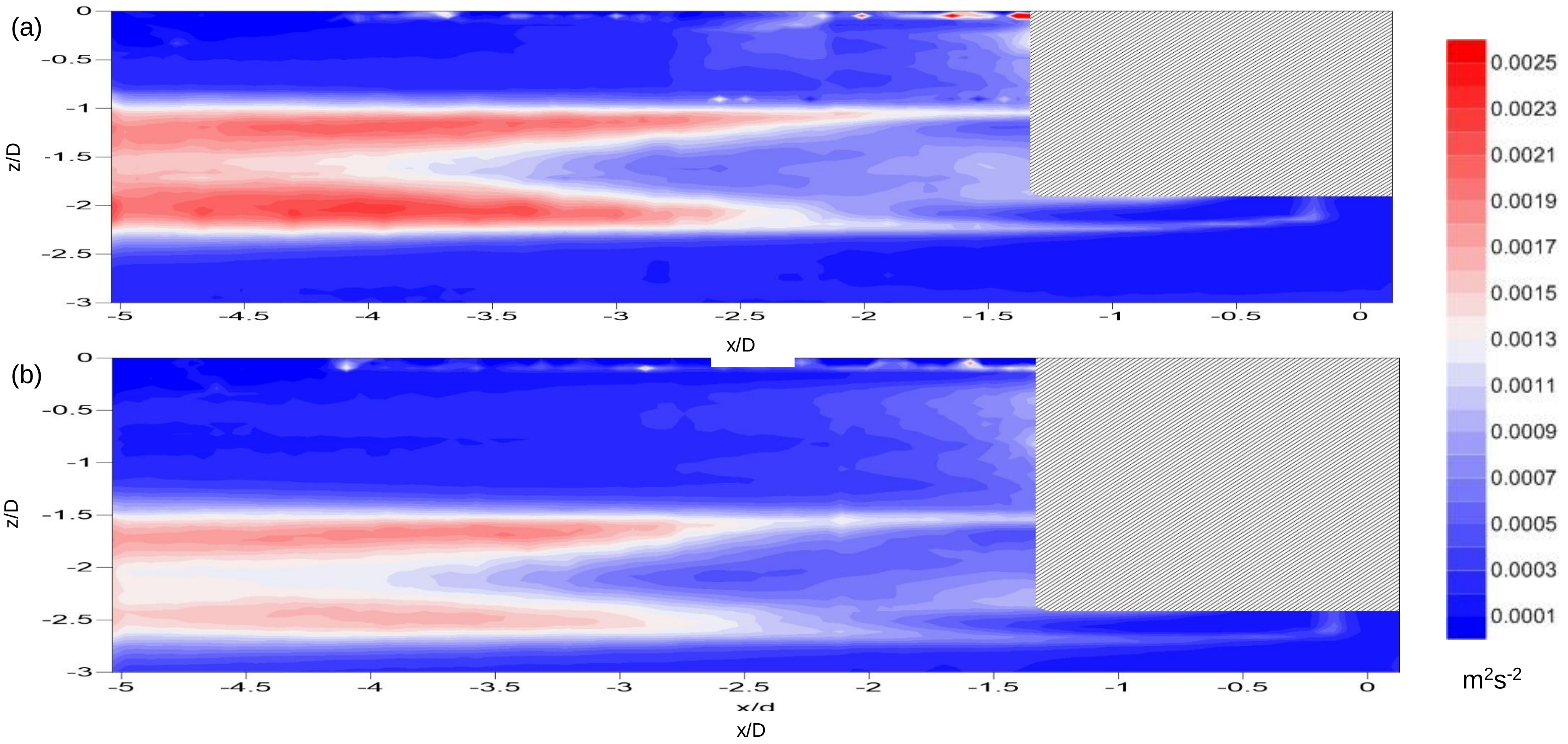

Figure 5.15: Flow structure maps for the Reynolds shear stress (u'w') for the rotor positioned at (a) 300mm above the bed and (b) 200mm above the bed. Flow direction is from right to left. Scales on the axes are normalised to rotor diameters (200mm). Areas covered by diagonal shading indicate areas where no data could be collected.

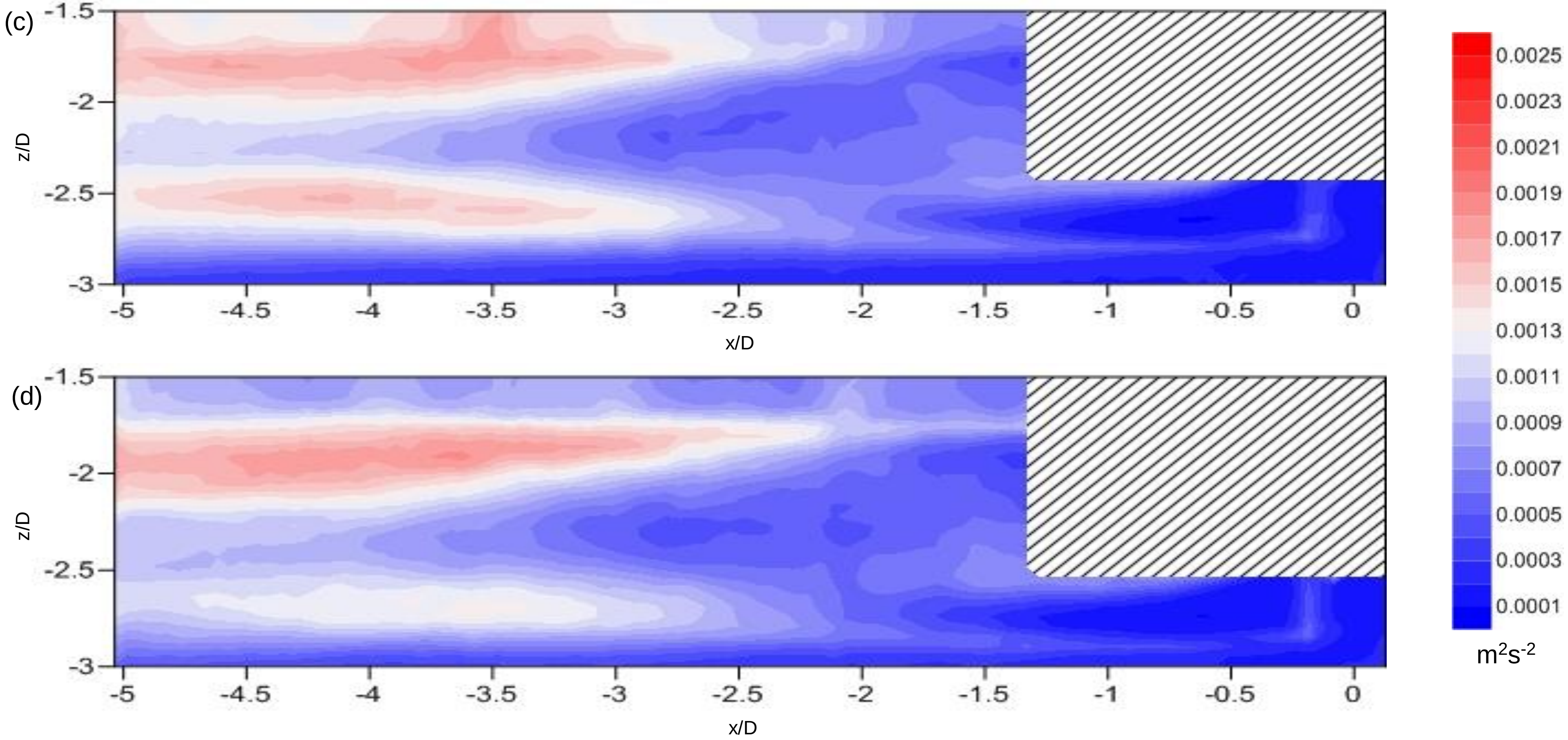

Figure 5.15: Flow structure maps for the Reynolds shear stress (u'w') for the rotor positioned at (c) 180mm above the bed (d) 160mm above the bed. Flow direction is from right to left. Scales on the axes are normalised to rotor diameters (200mm). Areas covered by diagonal shading indicate areas where no data could be collected.

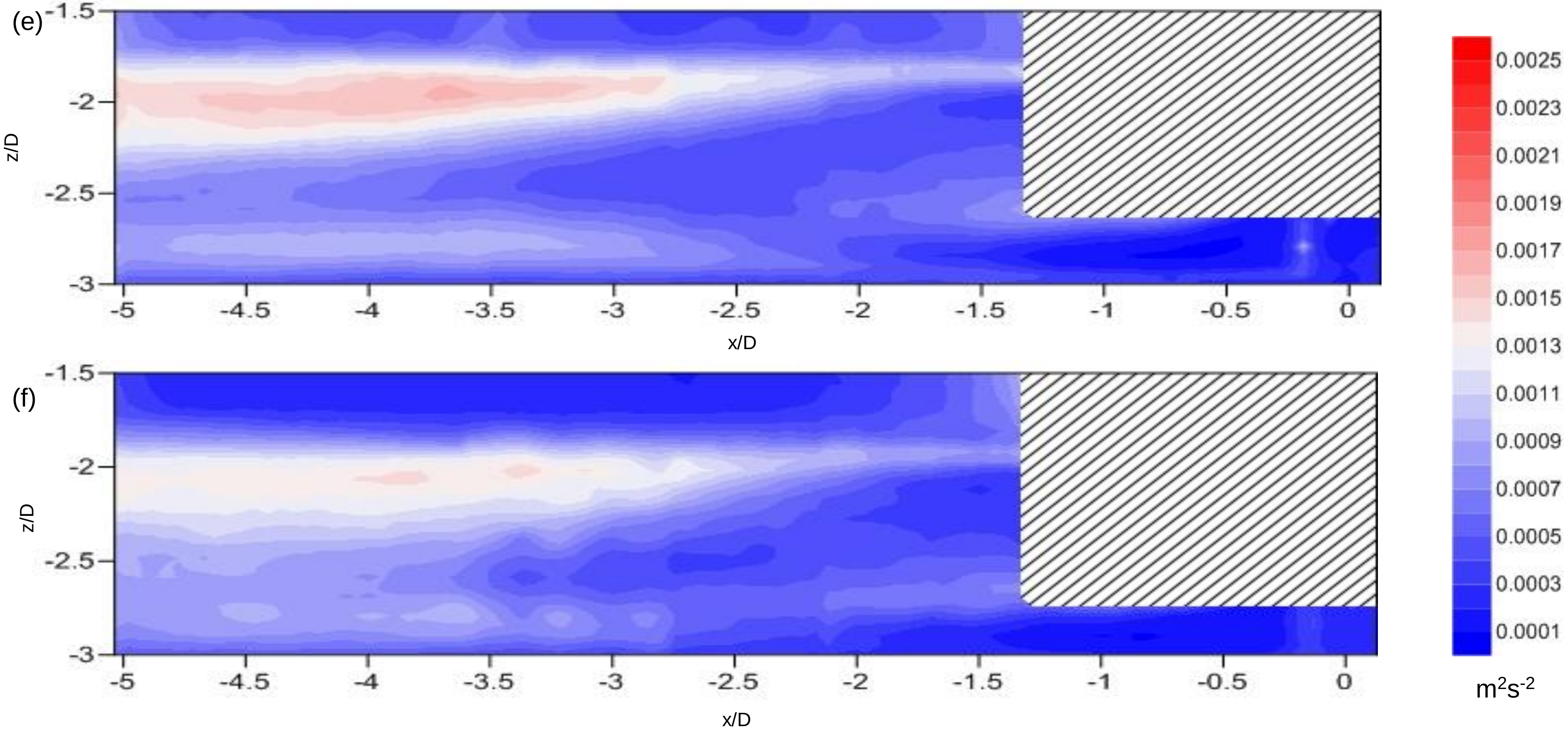

Figure 5.15: Flow structure maps for the Reynolds shear stress (u'w') for the rotor positioned at (e) 140mm above the bed (f) 120mm above the bed. Flow direction is from right to left. Scales on the axes are normalised to rotor diameters (200mm). Areas covered by diagonal shading indicate areas where no data could be collected.

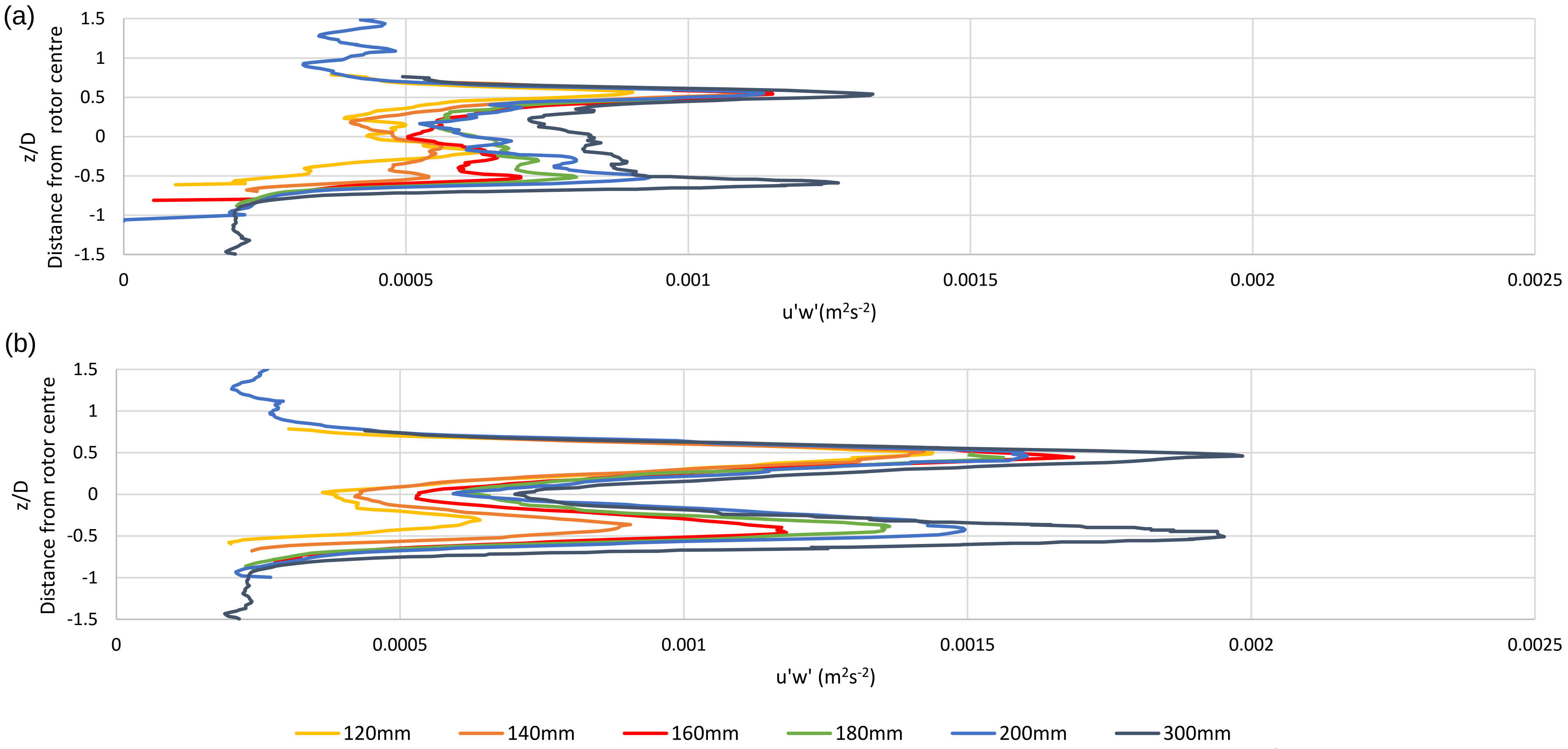

Figure 5.16: Charts showing the vertical profile of the Reynolds shear stress (u'w') with the rotor positioned at 120mm, 140mm, 160mm, 180mm, 200mm and 300mm above the channel bed at (a) 2 rotor diameter downstream from the turbine (b) 3 rotor diameters downstream from the turbine. Scales on the y-axes are normalised to rotor diameters (200mm).

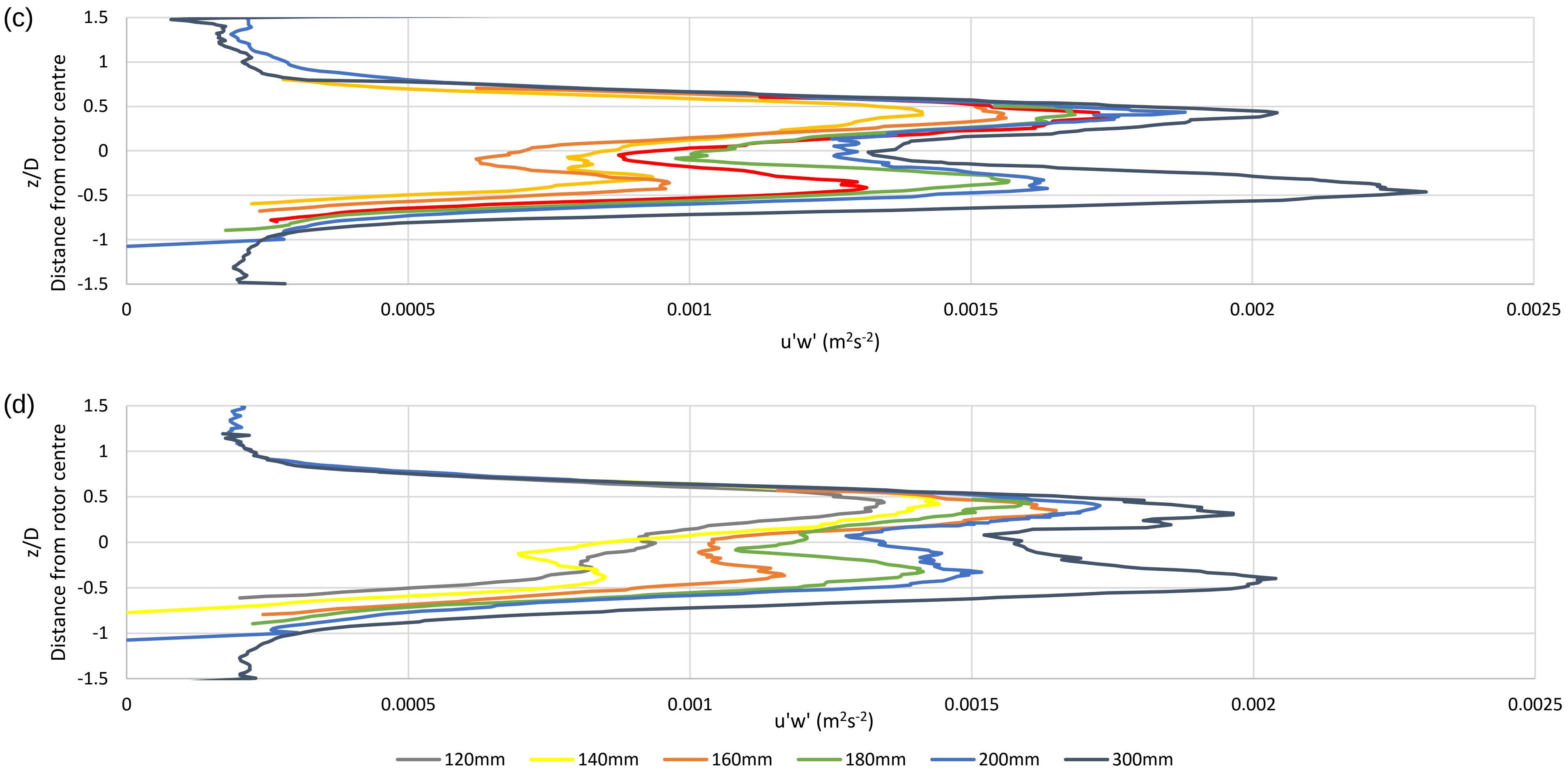

Figure 5.16: Charts showing the vertical profile of the Reynolds shear stress (u'w') with the rotor positioned at 120mm, 140mm, 160mm, 180mm, 200mm and 300mm above the channel bed at (c) 4 rotor diameters downstream from the turbine and (d) 5 rotor diameters downstream from the turbine. Scales on the y-axes are normalised to rotor diameters (200mm).

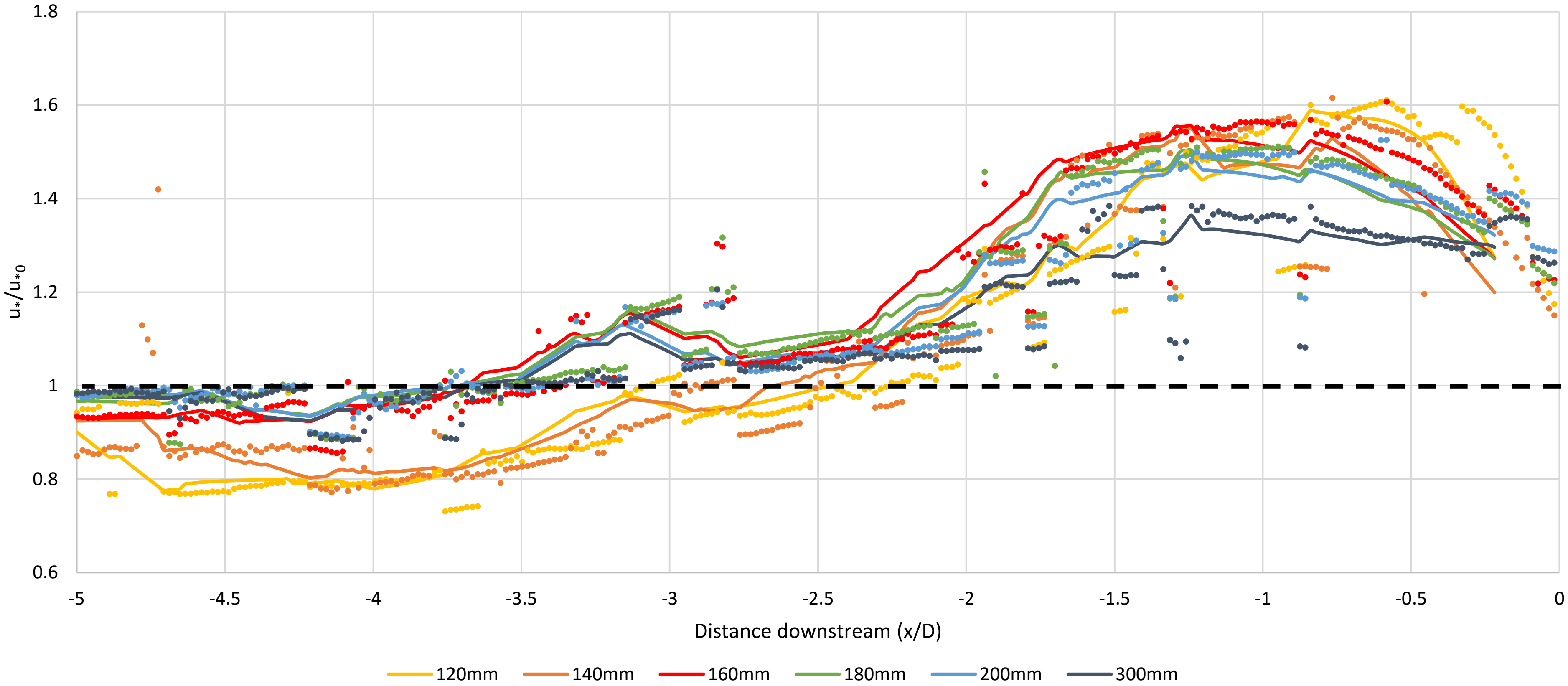

Figure 5.17: Normalised shear velocity (u_*/u_{*0}) *for rotor heights of 120mm, 140mm, 160mm, 180mm, 200mm and 300mm.* $u_{*0} = 0.0541$. *Coloured points: Original data points. Solid coloured line: Moving average trend line. Dashed black line: incoming flow normalised shear velocity. Flow direction is from right to left. Scale on the horizontal axis is normalised to rotor diameters (200mm). Rotor is positioned immediately upstream of x=0. The shear velocity is measured in the measurement cell closest to the channel bed.*

5.4 Discussion

Significant differences can be seen in the flow in the wake of a TST and within the Reynolds shear stress, bed shear stress and turbulence patterns downstream from a TST as a result of changing the proximity of the TST to the channel bed. As the rotor is lowered closer to the bed, the vertical expansion of the wake is restricted. Lowering the rotor leads to an increase in the wake length, as shown in figures 5.2 (a) to 5.2 (f), and therefore a prolonged effect on the mean flow field and turbulence structure downstream from the rotor. The longer wake length is linked to a decrease in downwelling when the rotor is closer to the bed, as shown in figures 5.5 (a) to 5.5 (f). The flow around the wake is more restricted as there is less free-stream flow beneath the wake, and therefore less free-stream flow is brought into the wake to aid with wake recovery.

Previous research in the field identified similar results to those observed herein. Myers and Bahaj (2010) observed a greater wake velocity deficit when the device was closer to the bed, with a greater wake length as a result of slower wake recovery. This change in flow recovery rate is linked to a decrease in shear stress and an increase in free-stream velocity further from the channel bed (Bahaj *et al.* 2007c), as seen in the plain channel profile in figure 3.6. The results in Myers and Bahaj (2010) agree that as distance from the bed increases, the turbulent kinetic energy in the wake area is greater than the free-stream levels, which aids with mixing the free-stream fluid into the wake, and therefore aiding wake recovery by reducing the velocity deficit within the wake. When the rotor is closer to the bed, the increased turbulence in the upper half of the wake does allow wake recovery to occur due to a higher energy influx from the top of the wake, albeit at a slower rate than if it was occurring at equal rates both above and below the wake, as is the case when the rotor is further from the channel bed (Chamorro *et al.*, 2013). The increased turbulence intensity when the rotor is further from the channel bed aids with wake recovery by increasing mixing of the faster moving free-stream fluid with the slower moving flow in the wake. The maximum turbulence intensity is observed at two rotor diameters downstream from the turbine, which is similar to the results presented by Stallard *et al.* (2015), as shown in figure 5.18. The wake width can be defined by the maximum turbulence intensity. Therefore, as seen in figures 5.8 (a) to 5.8 (d), the wake width is approximately one rotor diameter in the experiments described herein.

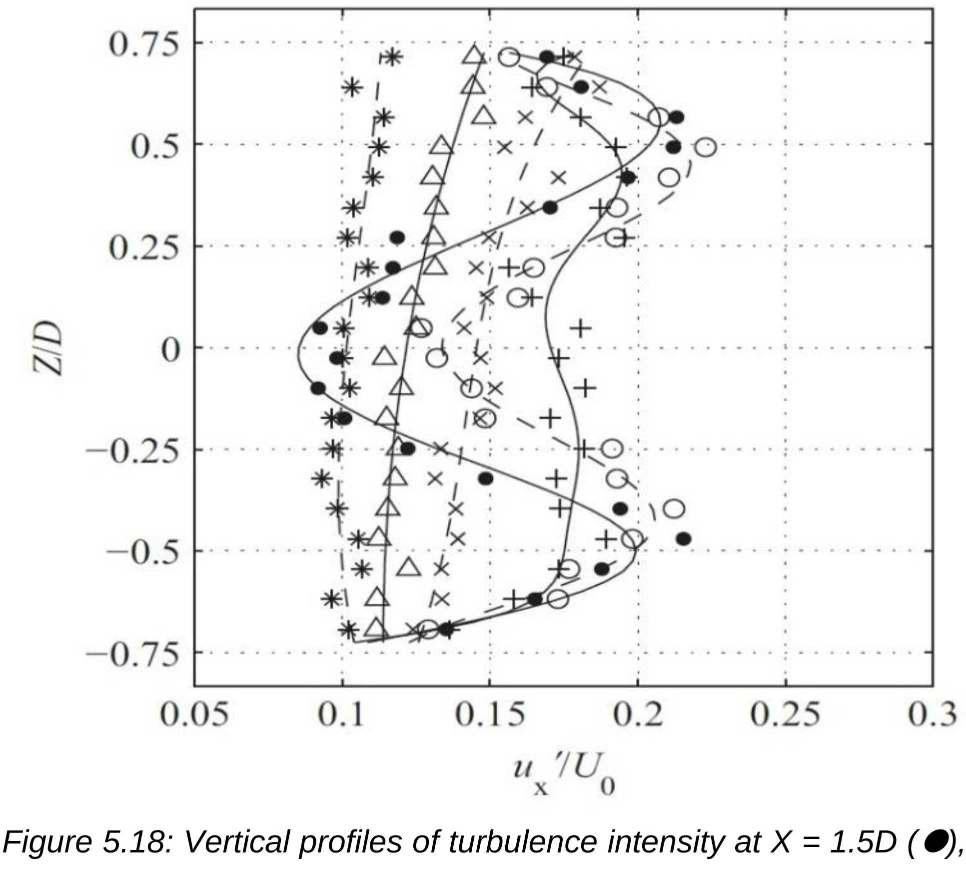

Figure 5.18: Vertical profiles of turbulence intensity at X = 1.5D (●), 2D (○), 4D (+), 6D (x), 8D (Δ) and 12D (✳). Curves indicate trend only (Stallard et al., 2015, pp. 245).

There is a noticeable and enhanced asymmetry of the TST wake as a result of moving the rotor closer to the channel bed. This vertical asymmetry starts to become apparent when the rotor is positioned at 140mm above the channel bed (asymmetry measure of ~1.4), but becomes much more noticeable when the rotor is lowered to 120mm above the bed. When the rotor is at 120mm above the channel bed, the wake has a greater stream-wise velocity in the lower half of the wake close to the rotor (asymmetry measure of ~0.8), but further downstream the wake becomes more asymmetric with a greater velocity deficit close to the bed (asymmetry measure of ~1.7), and therefore a greater stream-wise velocity in the upper half of the wake. The asymmetry leads to a greater interaction between the wake and the channel bed, which has an impact upon the interactions between the rotor and the bed sediment. The asymmetry seen at these rotor heights can be explained by the close proximity of the rotor to the bounding surface of the channel bed. The close proximity leads to disproportionate amounts of flow passing above and below the rotor, with more flow passing above the rotor than below (Bahaj *et al.,* 2007c; Myers and Bahaj, 2010, Stallard *et al.*, 2013).

The wake asymmetry could also be attributed to the turbulent mixing, as indicated by the turbulent kinetic energy, Reynolds shear stress and turbulence intensity. When the rotor is far from the bed, turbulent mixing is greater, and equal both at the top and bottom of the wake area. When the rotor is positioned closer to the bed, the turbulent mixing is greatest in the top of the wake area. This reduction in turbulent mixing in the lower half of the wake slows down wake recovery, and therefore leads to an asymmetric wake, where the velocities are slower in the area of the wake that is closest to the channel bed. The turbulence appears to be related to the high levels of standard deviation of the cross-stream flow. Previous research in the field which used mesh actuator disks to simulate a tidal stream turbine identified similar wake characteristics as those observed in the results presented herein, and determined that the actuator disk acted as a submerged flow obstruction when located close to the channel bed (Bahaj *et al.*, 2007c; Myers and Bahaj, 2010). Churchfield *et al.* (2013). They attributed the vertical asymmetry in the turbine wake to the vertical shear in the mean flow. Research by Stallard *et al.* (2013) indicated that a rotor placed at mid-depth leads to asymmetry immediately downstream of the rotor, with the wake becoming more symmetric further downstream. A similar observation can be seen in figure 5.3 (a) which shows a slight initial asymmetry when the rotor is positioned at 300mm above the bed. This asymmetry is not present at 5D downstream (figure 5.3 (d)).

Studies have indicated that rotors can increase the shear stress on the sea bed, as well as generate sea bed erosion and scour (e.g. Vybulkova *et al.*, 2013; Hill *et al.,* 2014; Möller *et al.,* 2016). Möller *et al.* (2016) carried out experiments in order to quantify the bed shear stress changes as a result of moving the rotor closer towards the bounding surface. It was identified that there was a 22% increase in bed shear stress compared to the free-stream when the rotor was positioned at 0.65D above the channel bed compared to at 1D above the channel bed (figure 5.19). In the case of the study described herein, this would correspond to rotor heights of 200mm and 130mm above the channel bed.

The results observed by Möller *et al.* (2016) can be compared to the results presented in figure 5.17 at rotor heights of 200mm and 120mm above the channel bed. Möller *et al.* (2016) observed a significant increase in the normalised friction velocity in the immediate vicinity of the rotor when the rotor was positioned close to the channel bed, but not when the rotor was positioned further from the bed. In the results presented herein, the increase in the normalised friction velocity in the immediate vicinity of the rotor was observed. However, it was observed for all rotor heights, rather than just one. The decrease in the normalised friction velocity further downstream, as observed by Möller *et al.* (2016), was also observed in the results presented herein. Whilst there are similarities in the results presented herein to those in Möller *et al.* (2016), there are also significant differences. For example, Möller *et al.* (2016) observed that the normalised shear velocity for the lower of the two rotor heights was significantly greater than the normalised shear velocity of the higher rotor height to approximately 4.5 rotor diameters downstream. However, in the results presented herein, after 2 rotor diameters downstream from the turbine, the normalised shear velocity is greatest when the rotor is positioned further from the channel bed (160mm-300mm). In the results presented herein, it was observed that the normalised shear velocity was lower than that of the plain channel (where the normalised shear velocity of the channel is 1) when the rotor was positioned at 120mm and 140mm above the channel bed.

The results presented herein show that whilst the rotor height above the channel bed does impact the wake, it is not necessarily the case that lowering the rotor leads to an increase in shear velocity and bed shear stress. The turbulence is therefore more important for understanding wake recovery and vertical asymmetry than shear velocity.

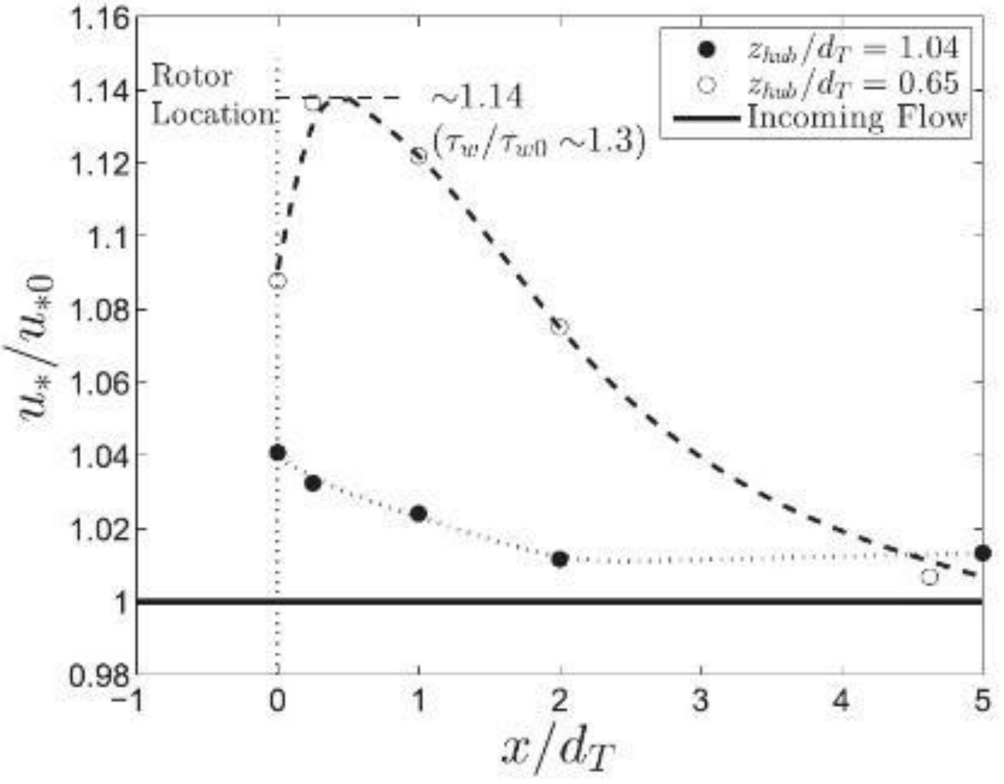

Figure 5.19: Normalized shear velocity (u_*/u_{*0}) *) along the turbine axis at* z_{hub}*=1.04 and* z_{hub}*=0.65 (Moller et al., 2016, pp. 528).*

The bed shear stress is still an important observation as it is linked with bed scour and sediment transport. When the TST was placed within close proximity to the channel bed (120mm), bed shear increased and bed scour and sediment transport were observed downstream from the rotor, as shown in figure 5.20. The scour was most prominent from approximately 2 rotor diameters downstream from the turbine, and continued to the extent of the area of mobile bed over which sediment transport could be observed. This corresponds to the increase in turbulent kinetic energy from ~1.5 rotor diameters downstream (figure 5.14). This also corresponds with the normalised shear velocity, which decreases beyond ~1.5 rotor diameters downstream (figure 5.14). This indicates that turbulent kinetic energy, which takes into account the velocity fluctuations in all three directions (stream-wise, cross-stream and vertical) provides a more accurate indicator of increased shear stress resulting in scour in the results presented herein, compared to the normalised shear velocity. The general trends in the scour presented herein are in agreement with the findings of Hill *et al.* (2014), who observed scour beneath and downstream from a tidal stream turbine, as shown in figure 5.21. Scour and sediment transport were not observed when the rotor was placed further away from the channel bed. It is important to understand the possible scour which may occur as scour of the bed can adversely impact the environment, including affecting benthic communities and increasing the water turbidity (OSPAR Commission, 2008). The scour and resulting deposition can occur at a considerable distance from the tidal stream turbine (Roberts *et al.*, 2016), so the environmental impact is not necessarily limited to the immediate vicinity of the tidal turbine.

Figure 5.20: Image of scour in the mobile bed inset when the rotor was at 120mm above the bed. The actual extent and degree of the scour and sediment transport were not quantified. Blue arrow shows flow direction.

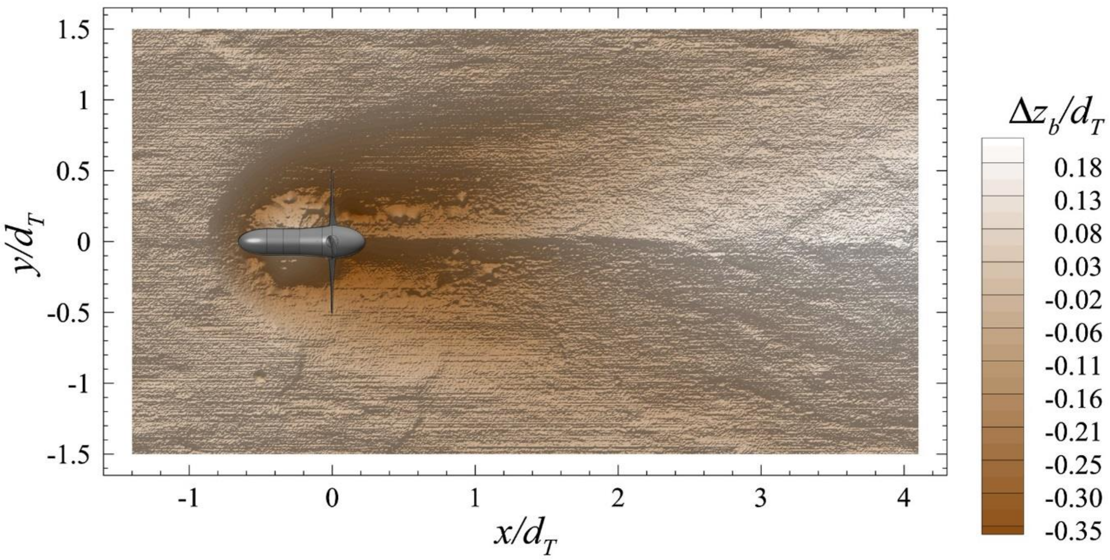

Figure 5.21: End topography from large-scale clear water experiments with the fully operational turbine; flow is left to right (Hill et al., 2014, pp. 4).

5.5 Conclusions

Detailed flow maps of the stream-wise, vertical and cross-stream velocity components, as well as the standard deviation of those velocity components have been presented for 6 different rotor heights above the bed. The TKE (*k*), an estimate of shear stress, turbulence intensity, normalised shear velocity and the Reynolds shear stress (u'w') have also been presented. The results show that the wake of the TST is significantly affected, in terms of velocity deficit, turbulence and vertical wake symmetry, as a result of lowering the TST closer to the channel bed.

The near bed turbulence increases significantly when the rotor is moved closer to the bed, although the overall wake turbulence develops significant asymmetry in the lower half of the wake. When the rotor is positioned at 120mm above the channel bed, the near bed turbulent kinetic energy is 50% less than the initial turbulent kinetic energy by 1 rotor diameter downstream compared to immediately downstream from the turbine. By 4 rotor diameters downstream, the near bed turbulent kinetic energy is 50% greater than immediately downstream from the turbine. However, when the rotor is positioned at 300mm above the channel bed, the turbulent kinetic energy near the bed remains relatively constant downstream.

The opposite pattern is true for the normalised shear velocity. Immediately downstream of the rotor, there is a significant increase in the normalised shear velocity. However, beyond 1.5 rotor diameters downstream, the normalised shear velocity starts to decrease. The normalised shear velocity decreases below that of the plain channel beyond 2.5 rotor diameters downstream. The extent to which it decreases is greatest when the rotor is closer to the channel bed.

The results presented indicate the importance of the vertical positioning of the rotor within a tidal channel, and the impact that the vertical location of the TST can have on the bed shear stress and seabed scouring. Due to tidal stream turbines still being a relatively new technology, there is no standard agreed vertical positioning of the turbine. Therefore, further research needs to be undertaken to fully quantify the impacts of lowering the rotor on both the wake downstream from the rotor, as well as near bed impacts, for developers to be able to make an informed decision regarding the vertical positioning of tidal stream turbines.

Chapter 6

Wake Modification by Waves

How is the wake of a tidal stream turbine modified by waves?

This chapter presents the results of an experimental investigation to evaluate how the presence of combined wave and current flow affects the development of the flow field downstream from a tidal stream turbine (TST).

6.1 Introduction

Tidally-driven currents are often combined with waves, with significant temporal and spatial variability in the flow forcings (Dalrymple and Choi, 2007). To determine the potential impacts of waves on tidal stream turbines, it is important to understand wave motion and linear wave theory.

6.1.1 Basic wave motion and theory

Ocean waves occur when the free surface of the water is disturbed by an external force, most commonly wind. These waves then propagate due to the fluid nature of water. The simplest form is that of a sinusoidal wave, as shown in figure 6.1, and is used to define basic wave properties.

MWL denotes the mean water level. This can also be referred to as the still water level (SWL), and is the average height of the water surface over a long period of time. The tops of the waves are known as crests, conversely the low points are known as troughs. The total vertical distance between a crest and subsequent trough is known as the wave height (H). The amplitude (a) represents the vertical height of the crest above the MWL. The water surface elevation (η) is the vertical distance between a point on a single wave and the

MWL. The wavelength (*L*) is the horizontal distance from any point on one wave and the equivalent point on the next wave, for example, between two crests. The wave period (*T*), is the length of time between consecutive wave crests as they pass a fixed point, the inverse represents the wave frequency (*f*). The waves propagate with a velocity, also known as celerity (*C*). Finally, the water depth between the bed and the MWL is denoted by *d* (Williams, 2015).

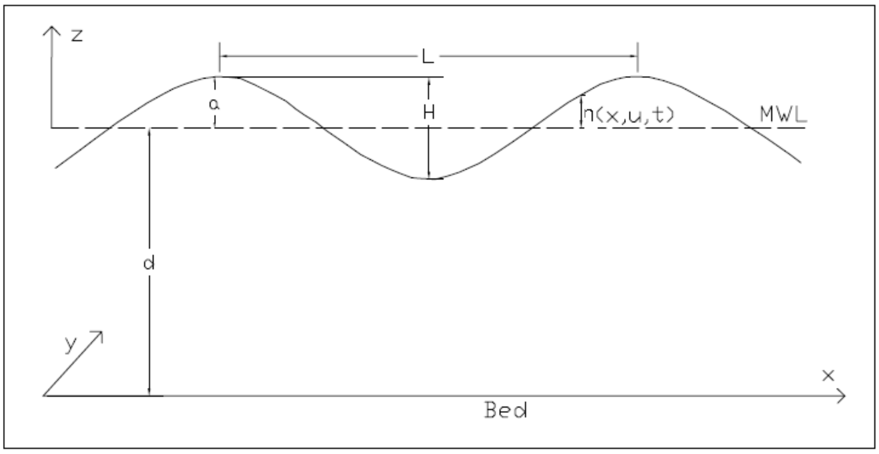

Figure 6.1. Wave definition sketch based on a sinusoidal wave (Williams, 2015, pg. 8).

When the wave height is small in comparison to both the wavelength and the water depth, small amplitude wave theory (Airy, 1845) can be used to describe this behaviour, assuming the following requirements are met: constant depth; water is incompressible; water is inviscid; irrotational motion; and two dimensional motion (Williams, 2015).

The theory is based on the linear theory for the propagation of waves on the surface of a potential flow over a horizontal bottom. The surface elevation of the waves can be described by a sinusoidal curve, and is a function of the horizontal position (*x*) and of the time (*t*). This results in the surface elevation (*η*) being expressed as:

$$\eta = (x, t) = a\cos(k_w x - \omega t) \qquad \text{Equation 16}$$

where k_w is the wave number, defined as the measurements of repeating units of a propagating wave, and is related to the wave length (L) by $k_w = 2\pi/L$. ω is the angular frequency, and relates to the wave frequency (f) by $\omega = 2\pi f$.

The relationship between k_w and ω is represented by the dispersion relation:

$$\omega^2 = gk_w \tanh(k_w d) \qquad \text{Equation 17}$$

When considering a wave field in the presence of a uniform stream-wise flow velocity (*U*) representative of a tidal current flow, the time and length scales are much larger for the current than those of the wave period and wavelength. This allows kinematic properties of plane waves to be applied on uniform currents (Williams, 2015). By applying a depth uniform current (*U*) and using a reference frame moving with the current then:

$$\omega_r{}^2 = (\omega^2 - kU) = gk_w \tanh(k_w d) \qquad \text{Equation 18}$$

where ω_r is the relative frequency composed of the angular frequency and the Doppler shift that the wave experiences on a mean flow. By applying this method, the same value of k is generated as for no current.

6.1.2 Tidal stream turbines with wave-current flow

It has already been determined that the wake of a TST can be affected by the flow speed and direction (Bahaj *et al.,* 2007c; Umeyama *et al.*, 2010) and therefore the presence of waves in combination with a tidal current will most likely impact the shape and extent of the wake. Wave-current interactions have been studied to some extent (e.g. Wolf and Prandle, 1999; Umeyama *et al.,* 2010), and the impact of wave-current interactions on turbine performance, including parameters such as power and thrust have also been previously studied (e.g. Gaurier *et al.*, 2013; Jesus Henriques *et al.*, 2015). However, there has been limited physical modelling conducted to investigate in detail and in a controlled manner, the impact of wave-current interactions on the flow field around, and the downstream wake of, TST devices.

This chapter will examine the shape and length of a TST wake and explore how the wake and flow recovery zone varies in the near field (up to 5 rotor diameters downstream from the rotor tip) as the TST is subjected to waves and combined wave and current flow. There is a lack of studies to date that assess the impact of different flows using scaled rotors rather than actuator disks. As previously mentioned, actuator disks fail in fully replicating the vortex shedding from the blade tips or the swirl as a result of turbine rotation, which are particularly important in the near wake (Batten *et al.,* 2013). There is therefore a need to experimentally investigate the impact of these various flow conditions using scaled tidal stream turbines and to determine the implications for full scale, operational turbines. The results and research presented within this chapter will build upon those from Chapter 4 and Chapter 5 which examined wake development and the interaction of the wake with the channel bed.

6.2 Methodology

This chapter will use experimental data collected during a series of experiments in which a 0.2m diameter TST was subjected to various flow and wave conditions, as described in chapter 3. The flow conditions which will be studied in this chapter are: ii) 1Hz, 6cm waves with a unidirectional current, ii) 1Hz, 10cm waves with unidirectional current, iii) 1.5Hz, 10cm waves with unidirectional current, and iv) unidirectional current-only (U_0=0.32m/s). In order to allow comparison with other studies and research, the relative depth, steepness and wavelength for each of the various flow conditions needs to be determined. The relative depth is defined as d/λ, and the steepness is H/λ where d is water depth, H is wave height and λ is wavelength. For 1Hz, 6cm waves with current, there was a relative depth condition of 0.241, a steepness of 0.024 and a wavelength of 1.56m. For 1Hz, 10cm waves with current, there was a relative depth condition of 0.38, a steepness of 0.064 and a wavelength of 1.56m. For 1.5Hz, 10cm waves with current, there was a relative depth condition of 0.19, a steepness of 0.03 and a wavelength of 0.7m.

Results are presented for the wave gauges to show the variation in wave height. Results are also presented for the stream-wise (u), vertical (w) and cross-stream (v) velocity components for the wave crest and wave troughs of three different wave-current scenarios: 1Hz, 6cm, 1Hz, 10cm and 1.5Hz, 10cm. The wave crests and wave troughs are extracted from the overall PIV data using conditional sampling, as detailed in sections 3.5.2.3 and 3.6.2, such that the flow map represents the majority of the flow field being under a wave crest or trough, rather than when the wave crest or trough was at a single location.

Results are also presented for the ensemble average of these scenarios, as well as the current only flow case. The ensemble average refers to the flow field averaged across the entire measurement area and time (9 measurements positions, with data collected for 107 seconds in each position), and includes entire wave cycles, including wave troughs and crests. The shear stress is represented using the turbulent kinetic energy (TKE) of the flow (see equation 11) and the Reynolds stress (see equation 9), which can be used as methods of estimating shear stress (Biron *et al.,* 2004; Pope *et al.*, 2006). The turbulent kinetic energy and Reynolds stress, as well as the turbulence intensity (u'/U_0)

and normalised shear velocity are presented for the ensemble average and the wave crests and wave troughs. Under wave-current flow conditions they will include wave induced kinematics, and are therefore expected to differ from that of the current only flow.

The stream-wise velocity will be used to identify the wake extent and asymmetry based on the velocity deficit. Cross-stream and vertical velocities will be used to understand wake interaction with the surrounding flow and the internal wake structure. The estimators of shear stress (turbulent kinetic energy and Reynolds stress) will be used to identify the turbulent structures and to understand wake recovery.

6.3 Results

Wave data were recorded on wave gauges situated at various stream-wise locations within the channel (as described in Chapter 3). A subsample of the data from two of these wave gauges are shown in figures 6.2 (a) to (c). Upstream of the rotor, the waves are generated at regular intervals, and maintain a relatively consistent wave height. Downstream of the rotor, the waves are still regular, but their steadiness and height is affected by the presence of the rotor.

Figures 6.3 (a) to (d) show the variation in the tidal stream turbine tip speed ratio under the previously specified flow conditions. In all cases, the average tip speed ratio is 5.12. However, there is greater variation in tip speed ratio under wave-current flow conditions (figures 6.3 (b) to (d)) than under current only flow conditions (figure 6.3 (a)). This variation in tip speed ratio is greatest under 1Hz, 10cm waves with current, where the variation led to the tip speed ratio nearly doubling, but also led to the rotor stalling, as shown in figure 6.3 (c)). However, the stalling only accounted for 0.1% of the rotor revolutions. The greater range in tip speed ratio occurring under a wave cycle for wave-current flow will result in a greater range of thrust coefficient. As a result, the average thrust, and therefore power generation, will differ compared to the steady flow (current only) cases presented in chapters 4 and 5.

There is a clear difference in the stream-wise velocity (*u*) and the wake length between the current-only flow regime (figure 6.4 (a)) and the simultaneous wave and current conditions (figure 6.4 (b) to figure 6.4 (d)), although the vertical extent (approximately 1 rotor diameter) remains similar in all flow cases. At 2 rotor diameters downstream from the turbine (figure 6.5 (a)), the velocity at the vertical centre of the wake (in line with the centre of the rotor at y=~-2.15D) is similar in all flow cases, and is approximately 20-30% of the free-stream velocity. Between 3 and 4 rotor diameters downstream (figures 6.5 (b) and 6.5 (c)), the flow recovery rate is significantly greater in the wave-current flow conditions compared to the current only flow conditions. At 5 rotor diameters downstream (figure 6.5 (d)), under wave-current flow conditions, the flow in the vertical centre of the wake has mostly recovered, to approximately 85% of the free-stream velocity. However, under current only flow conditions, there is still a significant velocity deficit of approximately 60% of the free-stream velocity.

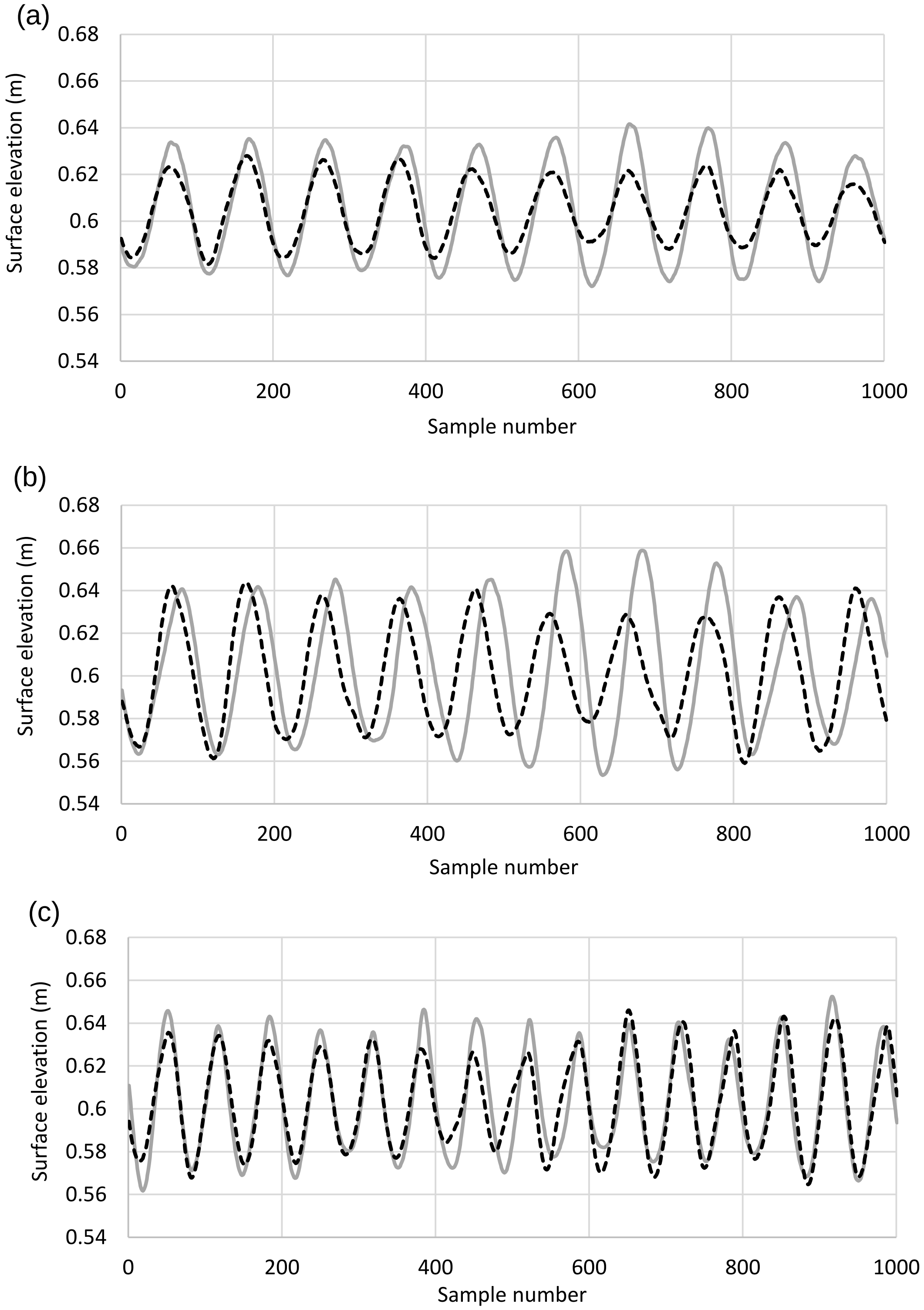

Figure 6.2: Subsample of the wave gauge data showing the recorded wave height for (a) 1Hz, 6cm waves with current (b) 1Hz, 10cm waves with current (c) 1.5Hz, 10cm waves with current. Solid line shows wave gauge data from ~3.5m upstream of rotor. Dashed line shows wave gauge data from ~1.1m downstream from rotor.

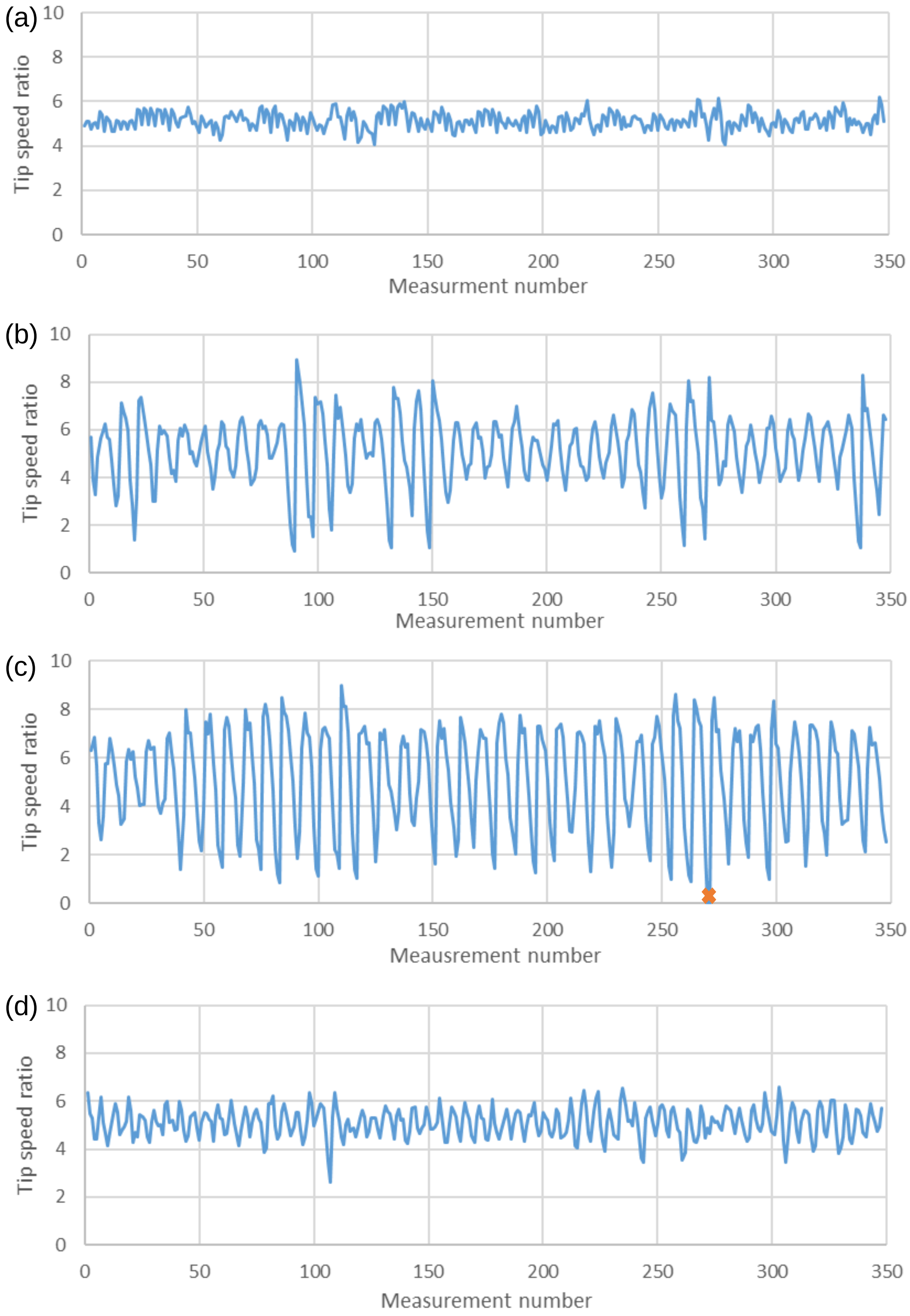

Figure 6.3: Subsample of the rotor data showing the recorded tip speed ratio of the rotor for (a) current-only flow (b) 1Hz, 6cm waves with current (c) 1Hz, 10cm waves with current (d) 1.5Hz, 10cm waves with current. The cross (X) indicates rotor stalling.

For the ensemble average of the stream-wise (*u*) velocity component for the wave and current flow conditions, the wake length is shorter under all wave heights and frequencies than under current only flow conditions (figures 6.4 (a) to (d)). The velocity deficit is substantially lower under wave-current flow conditions than current only conditions (figures 6.5 (a) to (d)).

Under the wave crest, the wake length is similar under 1Hz, 6cm waves with current and 1.5Hz, 10cm waves with current. However, under 1Hz, 10cm waves with current, the wake is longer (figures 6.6 (a) to (c)). The velocity within the wake is similar under 1Hz, 6cm waves with current and 1.5Hz, 10cm waves with current up to 4 rotor diameters downstream. The velocity within the wake under these two wave conditions is substantially lower than the velocity within the wake under 1Hz, 10cm waves with current (figures 6.7 (a) to (d)).

Under the wave trough, the wake length is shorter under 1.5Hz, 10cm waves with current compared to 1Hz, 6cm waves with current and 1Hz, 10cm waves with current, where the wake length is similar under both flow conditions (figures 6.8 (a) to (c)). Up to 4 rotor diameters downstream, the velocity within the wake is lowest under 1Hz, 10cm waves with current, and greatest under 1Hz, 6cm waves with current. However, by 5 rotor diameters downstream, the velocity within the wake is lowest under 1Hz, 6cm waves with current and greatest under 1Hz, 10cm waves with current (figures 6.9 (a) to (d)).

In all cases, there is an area of downwelling immediately beneath the rotor, and upwelling further downstream below the turbine wake. Under current only conditions (figure 6.10 (a)), above the wake is predominantly downwelling, with areas of upwelling close to the turbine support structure. Under wave-current flow conditions (figures 6.10 (b) to (d)), zone above the wake are predominantly upwelling, with an area of downwelling in line with the rotor hub. However, when the wave size is increased to 10cm (figure 6.10 (c)), the area of upwelling above the wake significantly increases by extending further downstream. Increasing the frequency of the waves to 1.5Hz (figure 6.10 (d)) further increases the size of this area of upwelling, and there is very little downwelling present other than directly beneath the rotor.

Under current only flow conditions (figure 6.11 (a)), there is a significant area of strong positive cross-stream flow immediately beneath the rotor, which extends beyond 3D downstream, and approximately 0.3D vertically. There is an area of negative cross-stream flow immediately behind the rotor hub. Under wave-current flow conditions (figures 6.11 (b) to (d)), the area of positive cross-stream flow immediately beneath the tidal stream turbine is significantly smaller, extending less than 0.5D downstream, and 0.1D vertically.

There is stronger negative cross-stream flow in this region immediately beneath the turbine. Immediately downstream of the turbine, an area of negative cross-stream flow, seen in the current only flow conditions, is not present under the wave-current flow conditions. Further downstream there is a similar pattern to the cross-stream flow under all the wave-current flow conditions. Beneath the wake, there is strong negative cross-stream flow and above the wake, there is strong positive cross-streamflow. There appears to be little change in the magnitude of the cross-stream velocities as either the wave height or wave frequency increase.

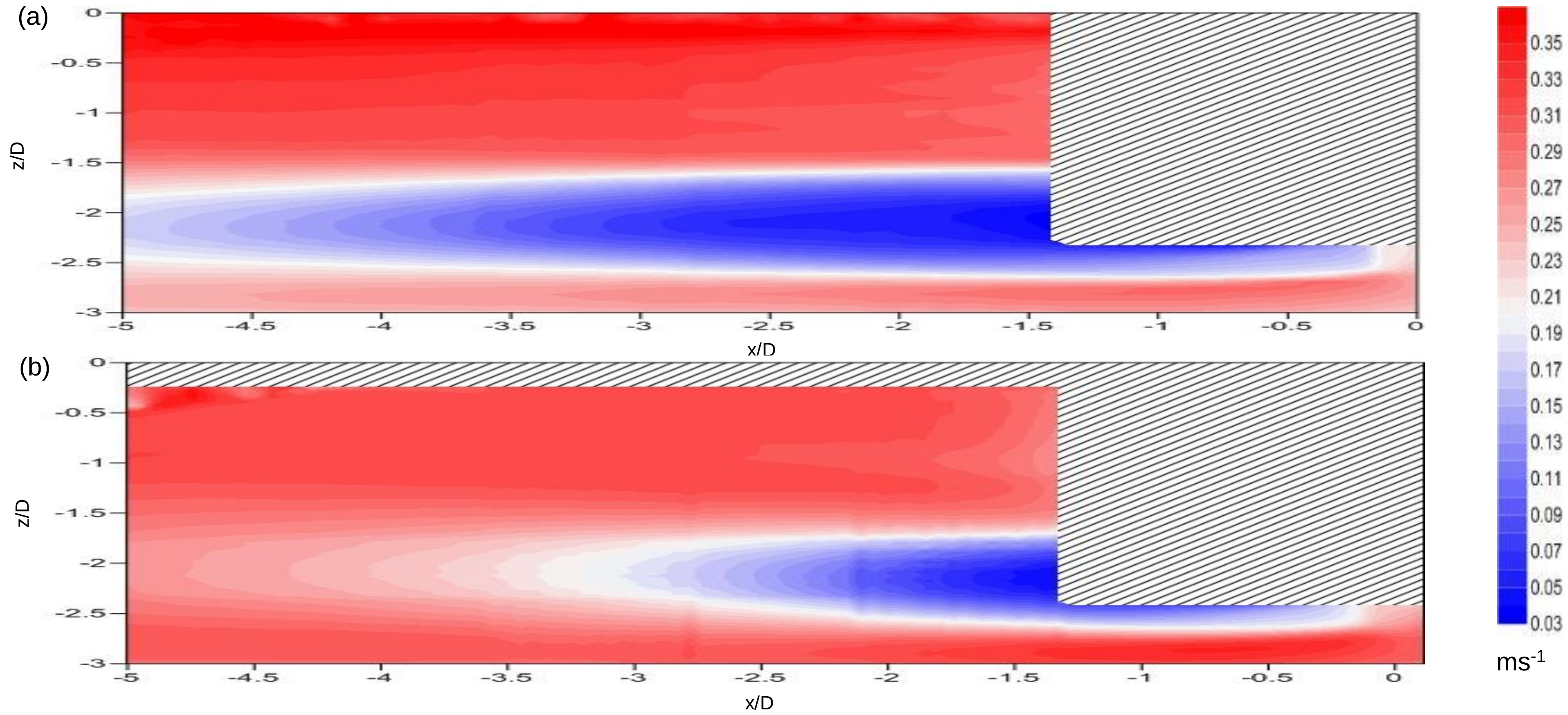

Figure 6.4: Flow structure maps for the stream-wise velocity component for (a) current-only conditions (b) 1Hz, 6cm waves with current (ensemble average) Flow direction is from right to left. Scales on the axes are normalised to rotor diameters (200mm). Areas covered by diagonal shading indicate areas where no data could be collected.

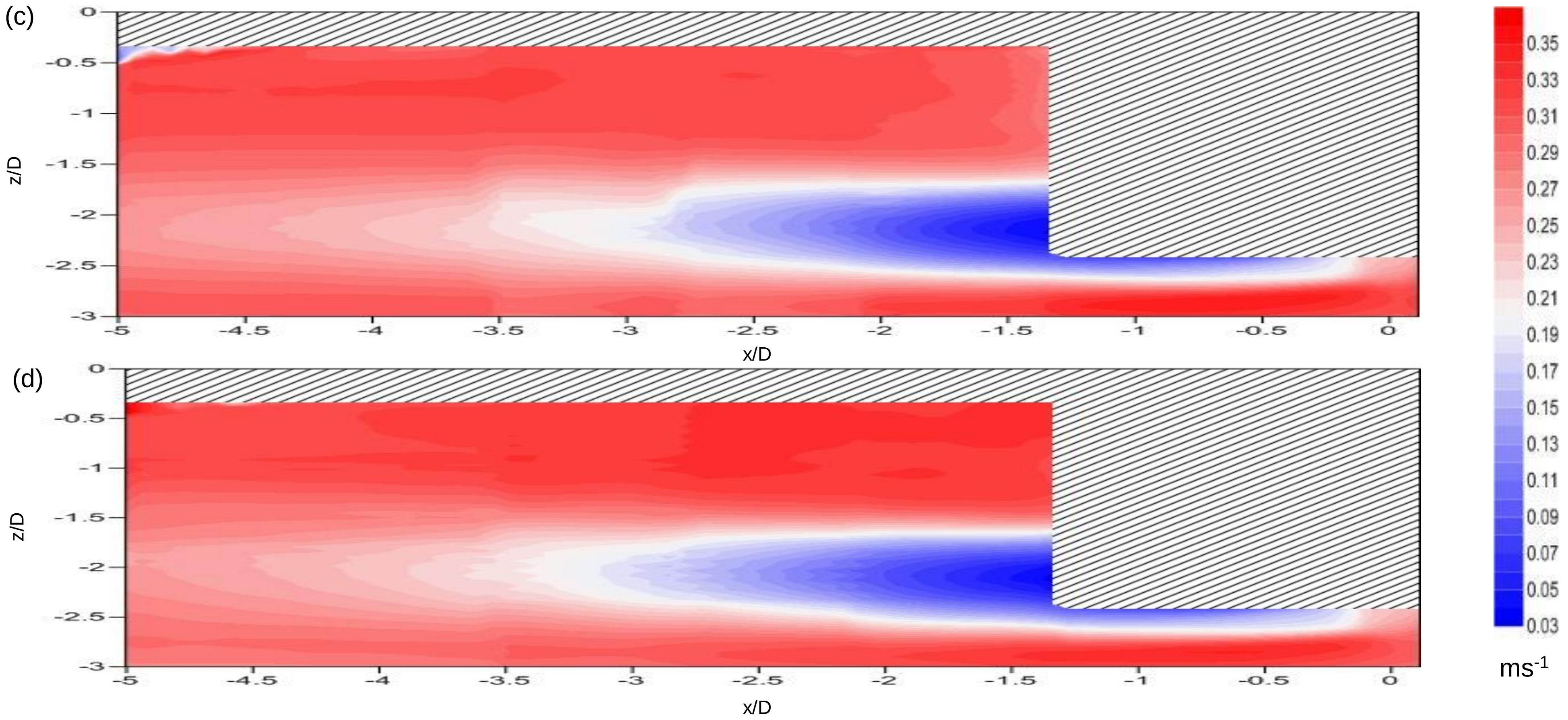

Figure 6.4: Flow structure maps for the stream-wise velocity component for (c) 1Hz, 10cm waves with current (ensemble average) (d) 1.5Hz, 10cm waves with current (ensemble average). Flow direction is from right to left. Scales on the axes are normalised to rotor diameters (200mm). Areas covered by diagonal shading indicate areas where no data could be collected.

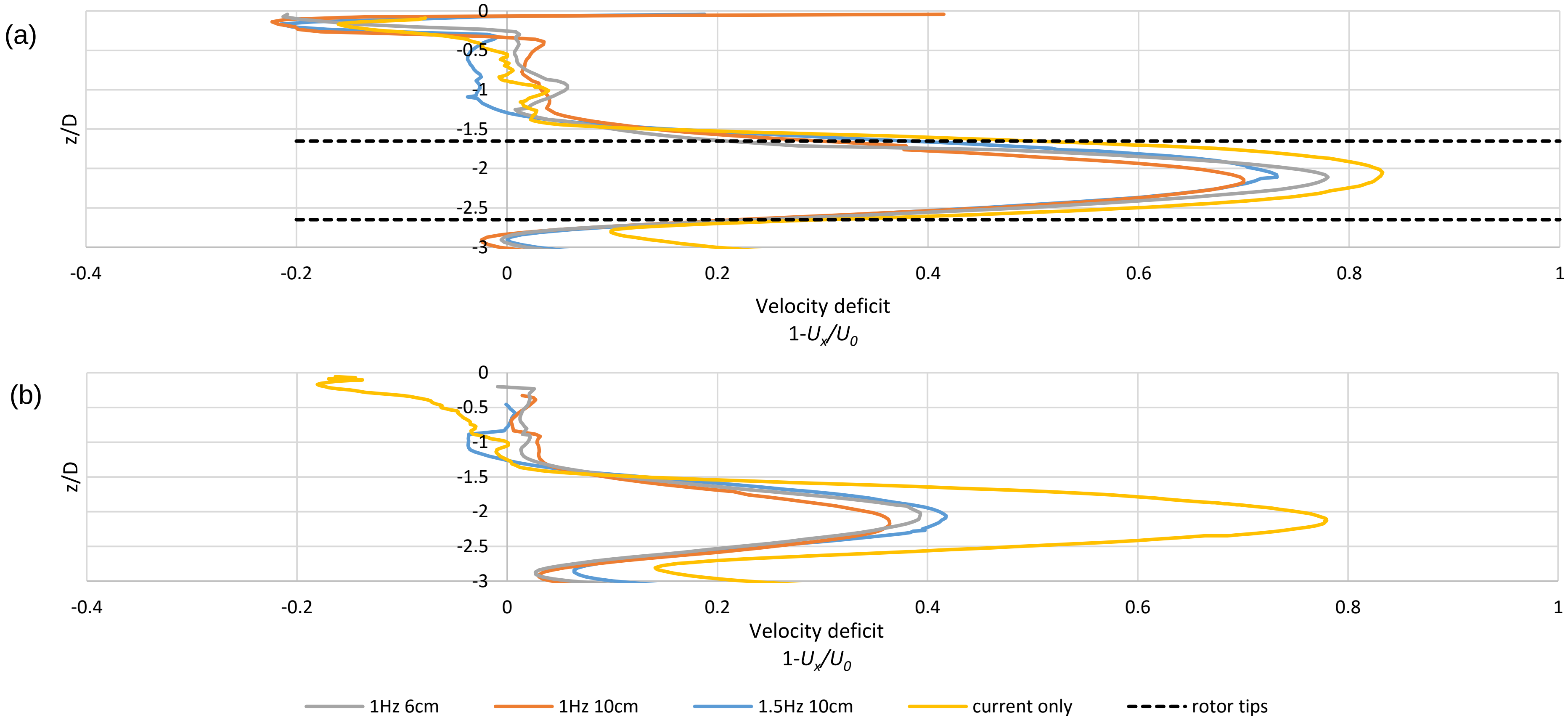

Figure 6.5: Velocity deficit profiles under 1Hz, 6cm waves with current, 1Hz, 10cm waves with current, 1.5Hz, 10cm waves with current and current only flow conditions at (a) 2 rotor diameters downstream from the turbine (b) 3 rotor diameters downstream from the turbine. Scales on the y-axes are normalised to rotor diameters (200mm).

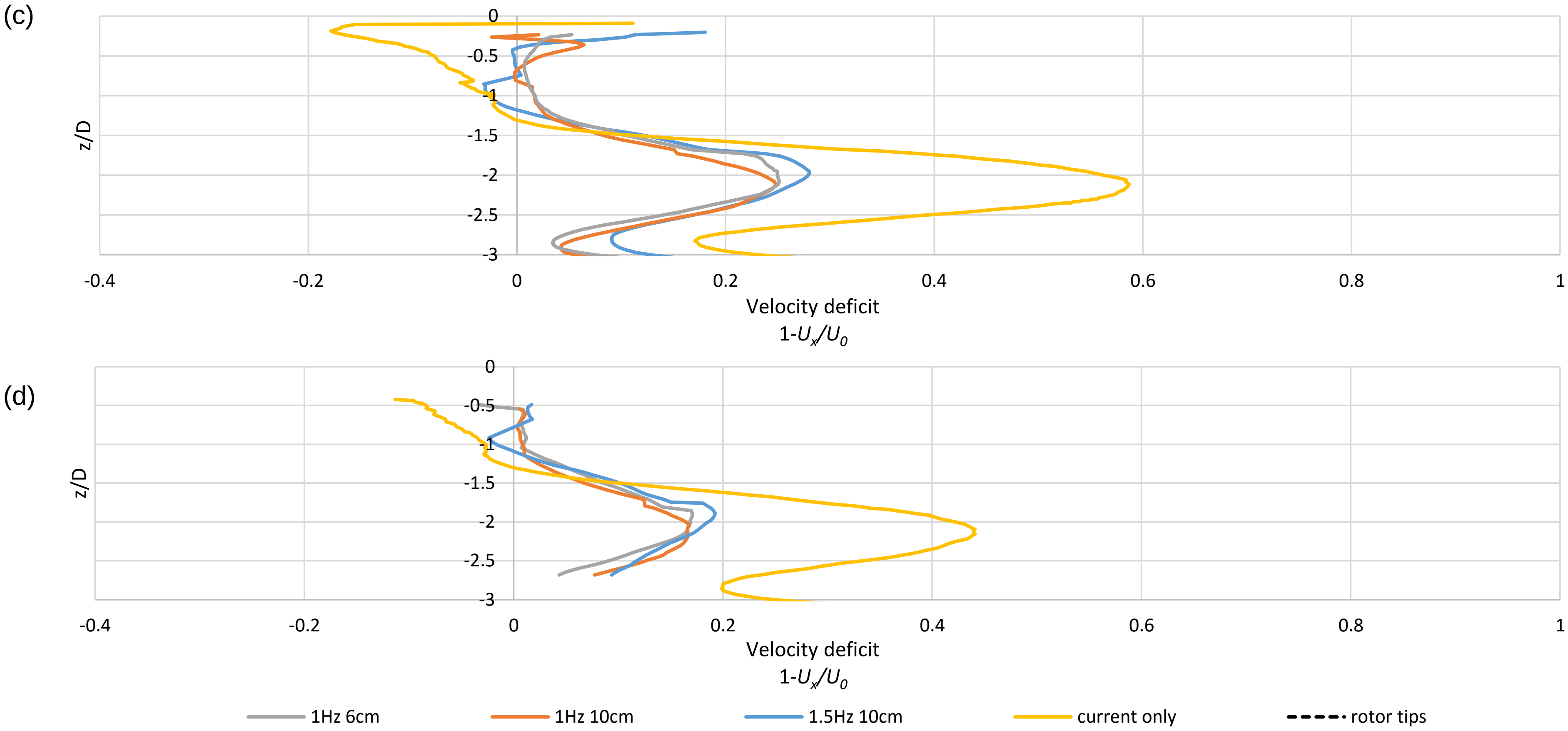

Figure 6.5: Velocity deficit profiles under 1Hz, 6cm waves with current, 1Hz, 10cm waves with current, 1.5Hz, 10cm waves with current and current only flow conditions at (c) 4 rotor diameters downstream from the turbine and (d) 5 rotor diameters downstream from the turbine. Scales on the y-axes are normalised to rotor diameters (200mm).

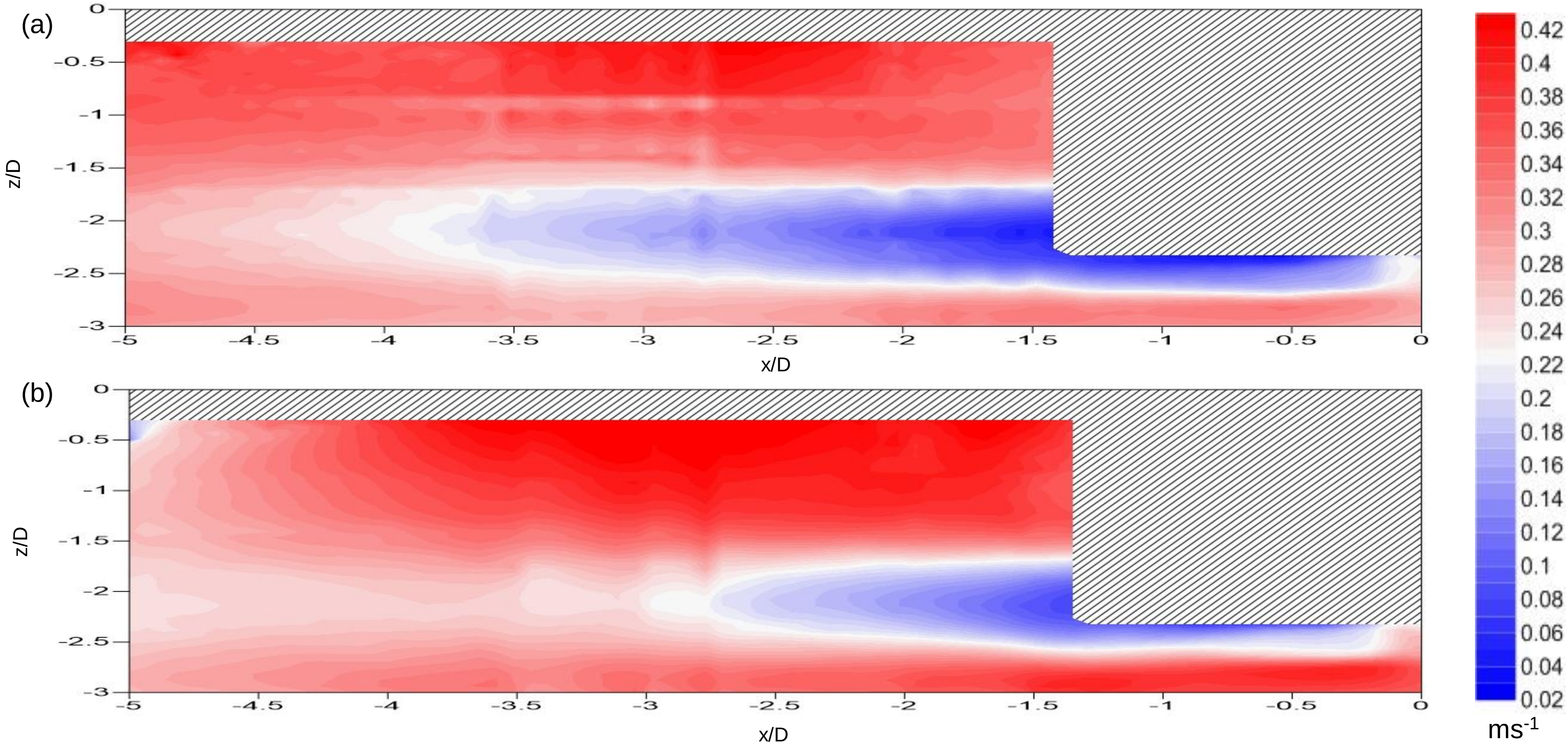

Figure 6.6: Flow structure maps for the stream-wise velocity component for the crest only of (a) 1Hz, 6cm waves with current (b) 1Hz, 10cm waves with current. Flow direction is from right to left. Scales on the axes are normalised to rotor diameters (200mm). Areas covered by diagonal shading indicate areas where no data could be collected.

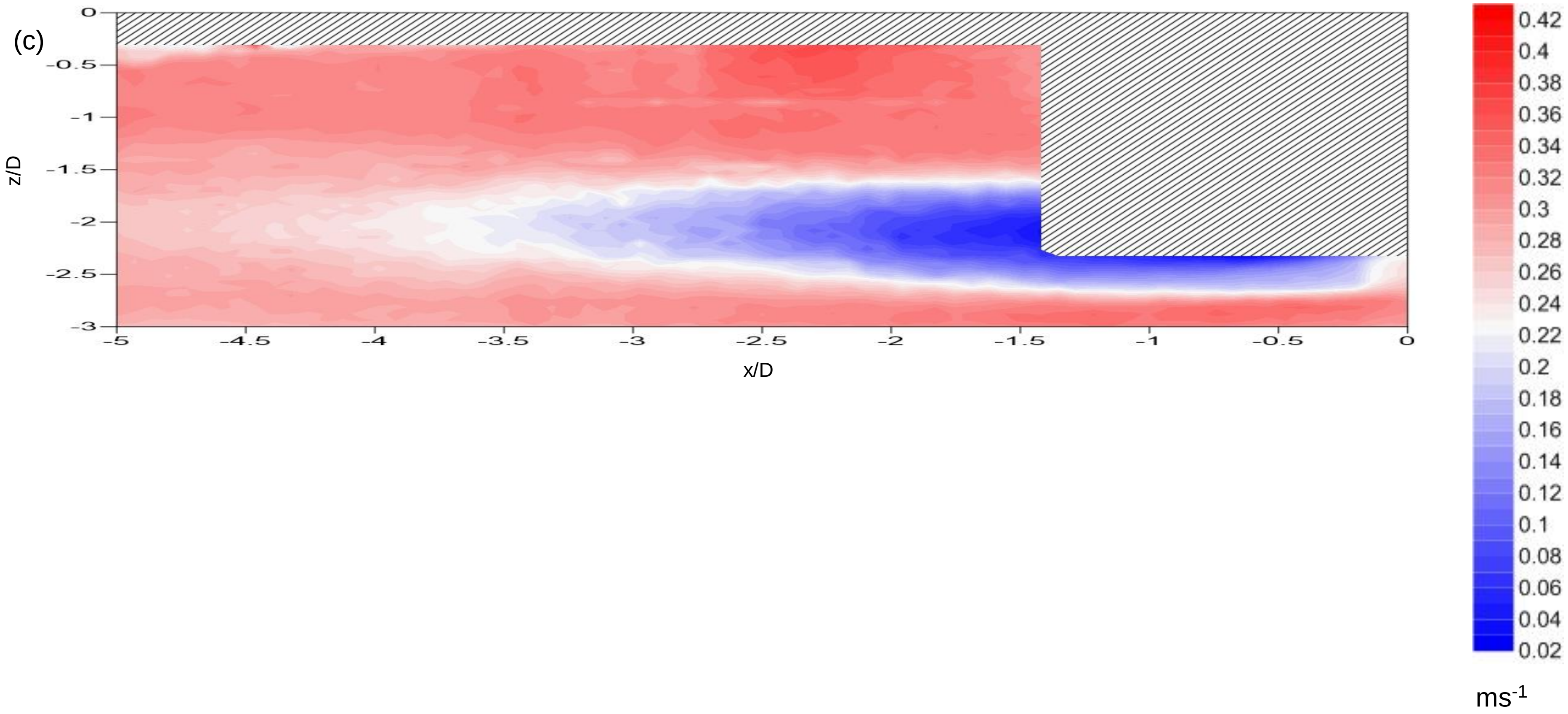

Figure 6.6: Flow structure maps for the stream-wise velocity component for the crest only of (c) 1.5Hz, 10cm waves with current. Flow direction is from right to left. Scales on the axes are normalised to rotor diameters (200mm). Areas covered by diagonal shading indicate areas where no data could be collected.

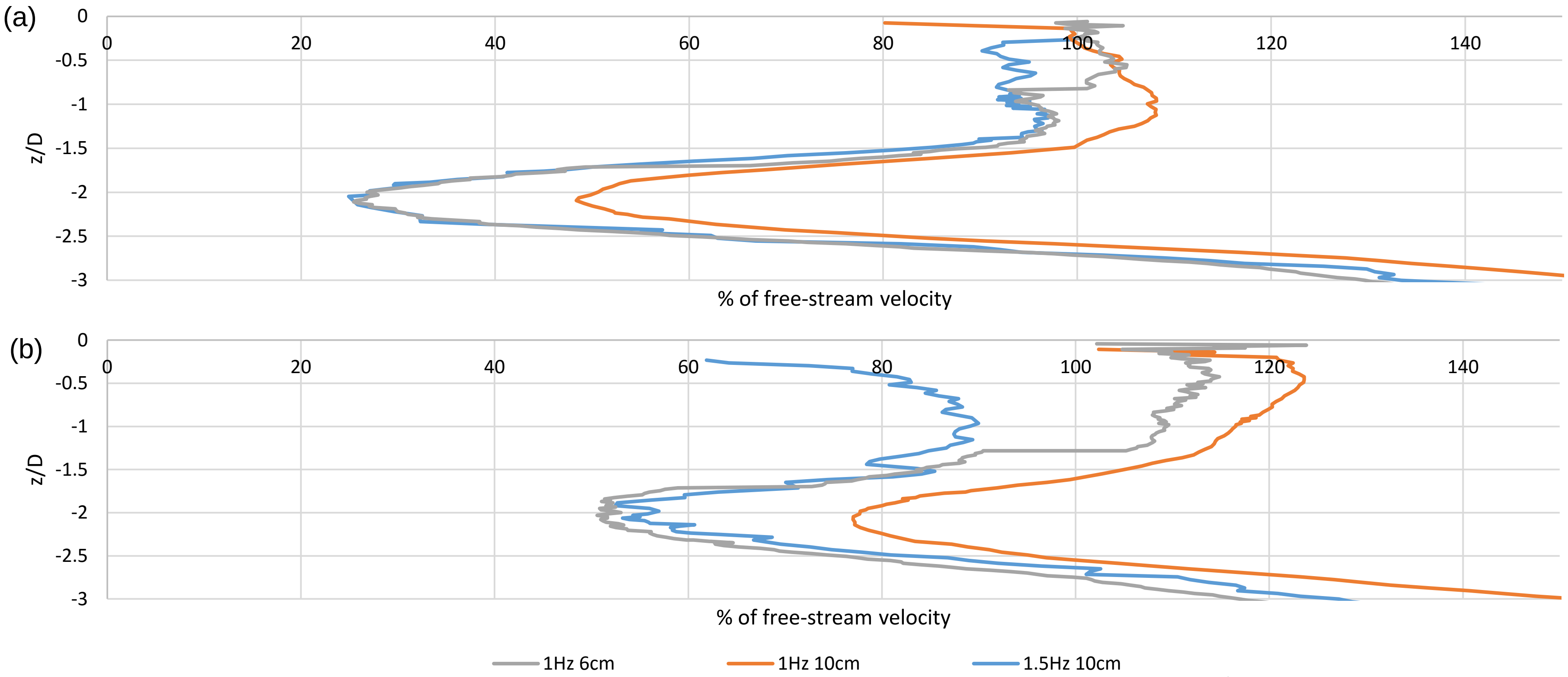

Figure 6.7: Wake deficit charts showing the velocity in the turbine wake under wave crests as a percentage of the free-stream velocity under 1Hz, 6cm waves with current, 1Hz, 10cm waves with current and 1.5Hz, 10cm waves with current at (a) 2 rotor diameters downstream from the turbine (b) 3 rotor diameters downstream from the turbine. Scales on the y-axes are normalised to rotor diameters (200mm).

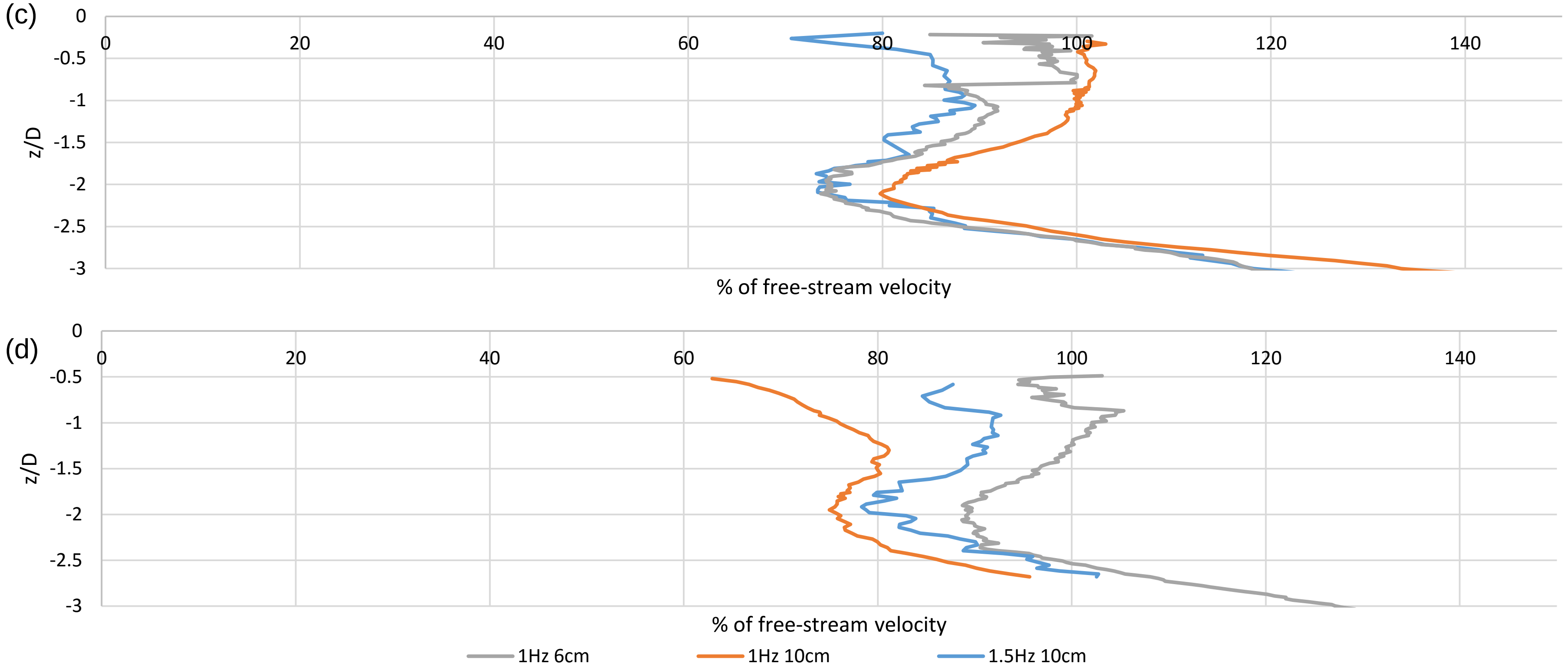

Figure 6.7: Wake deficit charts showing the velocity in the turbine wake under wave crests as a percentage of the free-stream velocity under 1Hz, 6cm waves with current, 1Hz, 10cm waves with current and 1.5Hz, 10cm waves with current at (c) 4 rotor diameters downstream from the turbine and (d) 5 rotor diameters downstream from the turbine. Scales on the y-axes are normalised to rotor diameters (200mm).

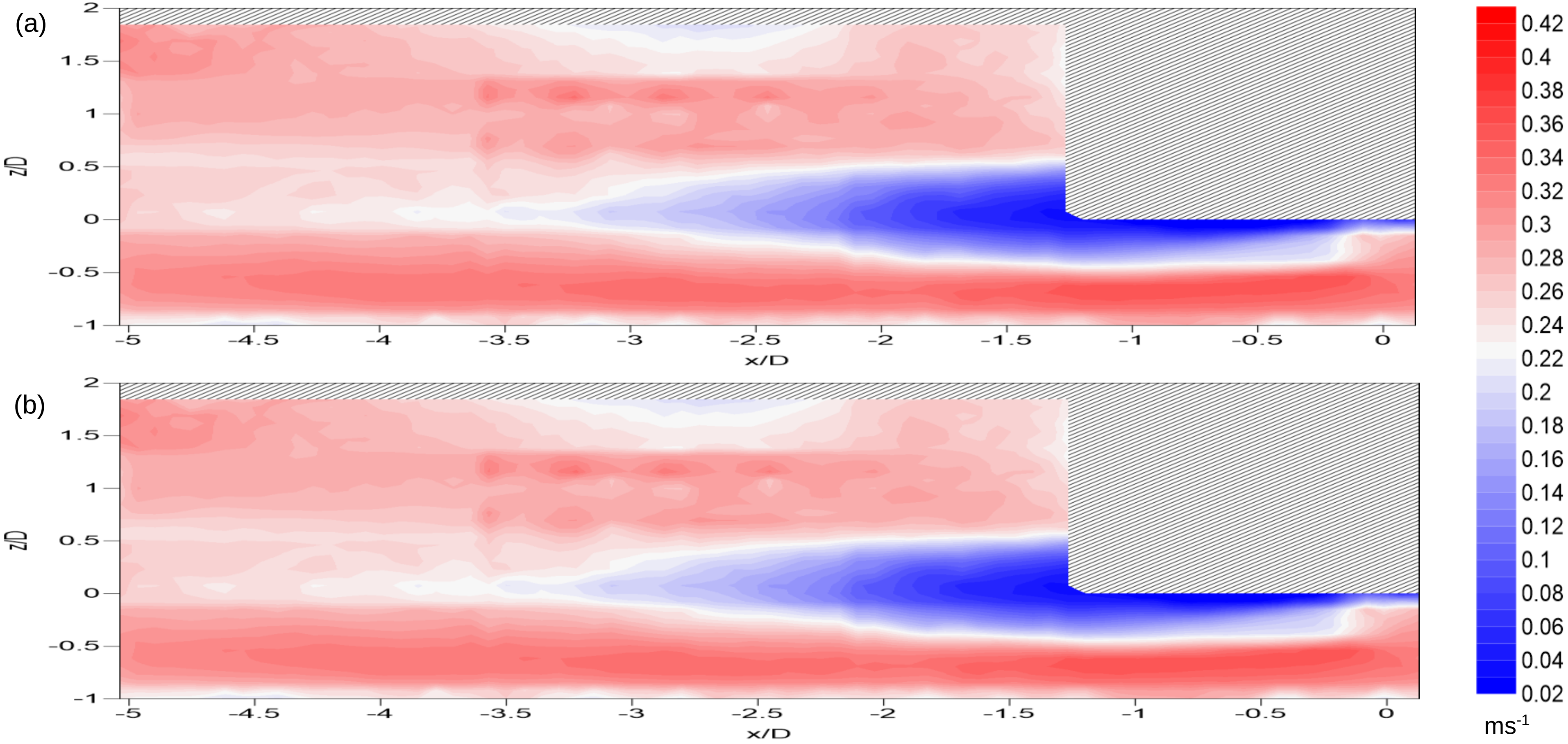

Figure 6.8: Flow structure maps for the stream-wise velocity component for the trough only of (a) 1Hz, 6cm waves with current (b) 1Hz, 10cm waves with current. Flow direction is from right to left. Scales on the axes are normalised to rotor diameters (200mm). Areas covered by diagonal shading indicate areas where no data could be collected.

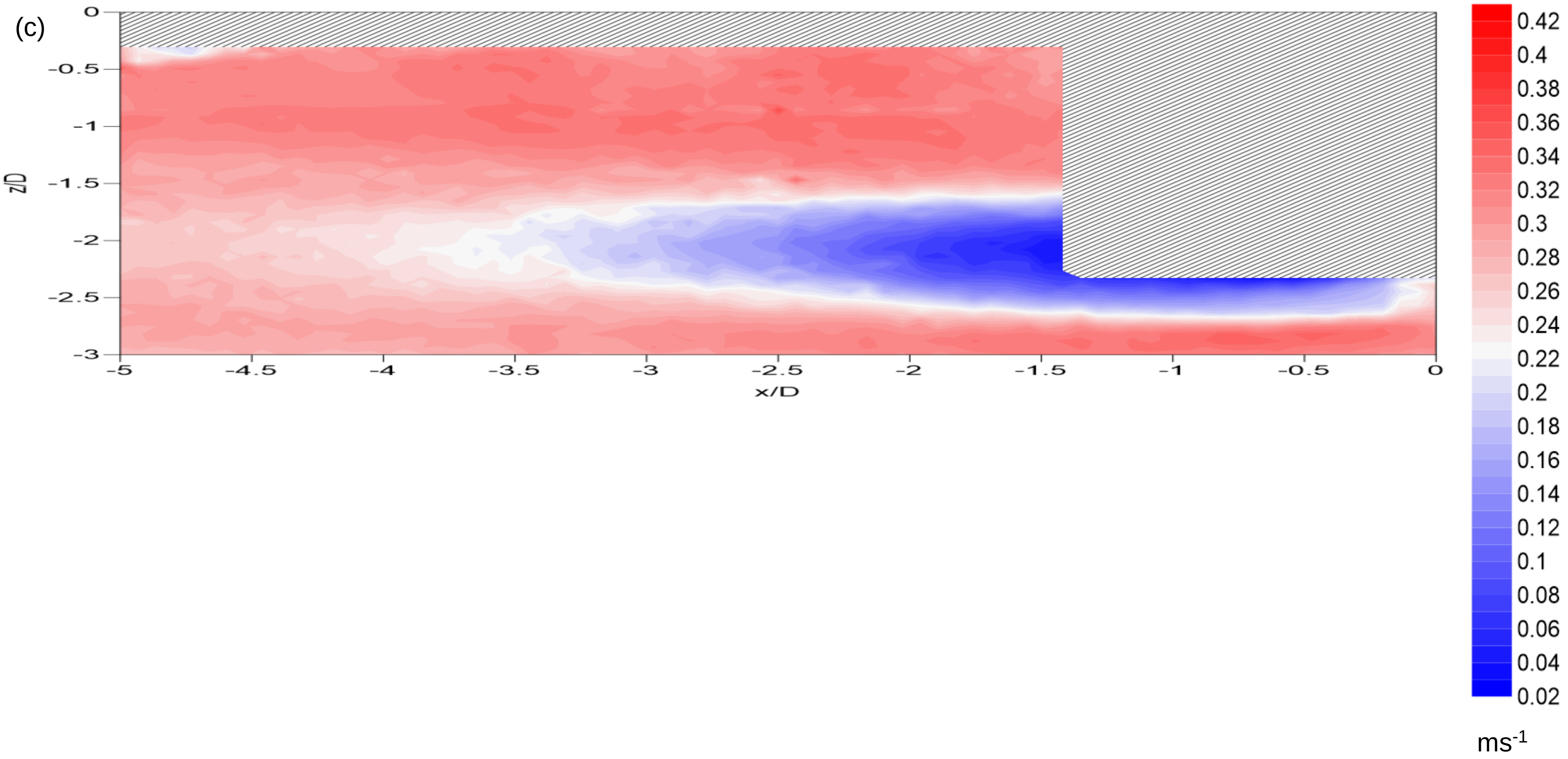

Figure 6.8: Flow structure maps for the stream-wise velocity component for the trough only of (c) 1.5Hz, 10cm waves with current. Flow direction is from right to left. Scales on the axes are normalised to rotor diameters (200mm). Areas covered by diagonal shading indicate areas where no data could be collected.

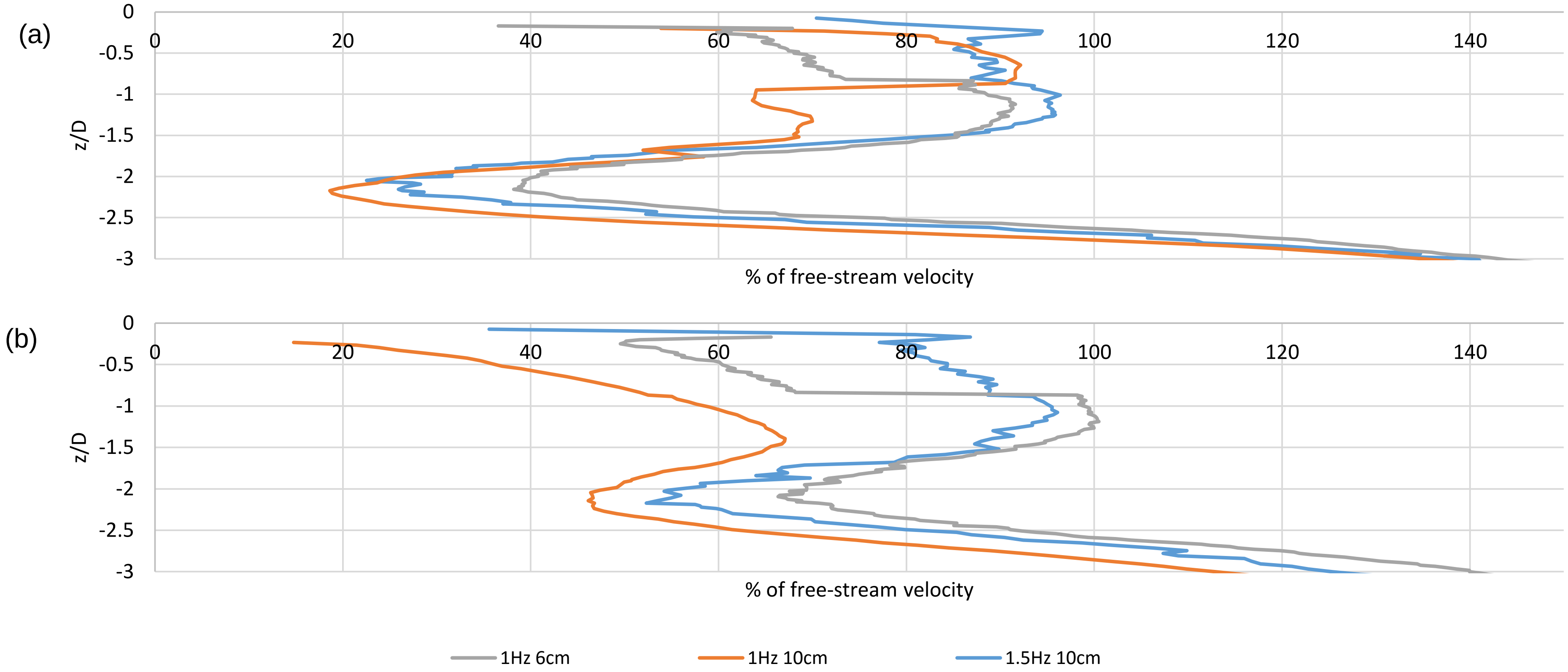

Figure 6.9: Wake deficit charts showing the velocity in the turbine wake under wave troughs as a percentage of the free-stream velocity under 1Hz, 6cm waves with current, 1Hz, 10cm waves with current and 1.5Hz, 10cm waves with current at (a) 2 rotor diameters downstream from the turbine (b) 3 rotor diameters downstream from the turbine. Scales on the y-axes are normalised to rotor diameters (200mm).

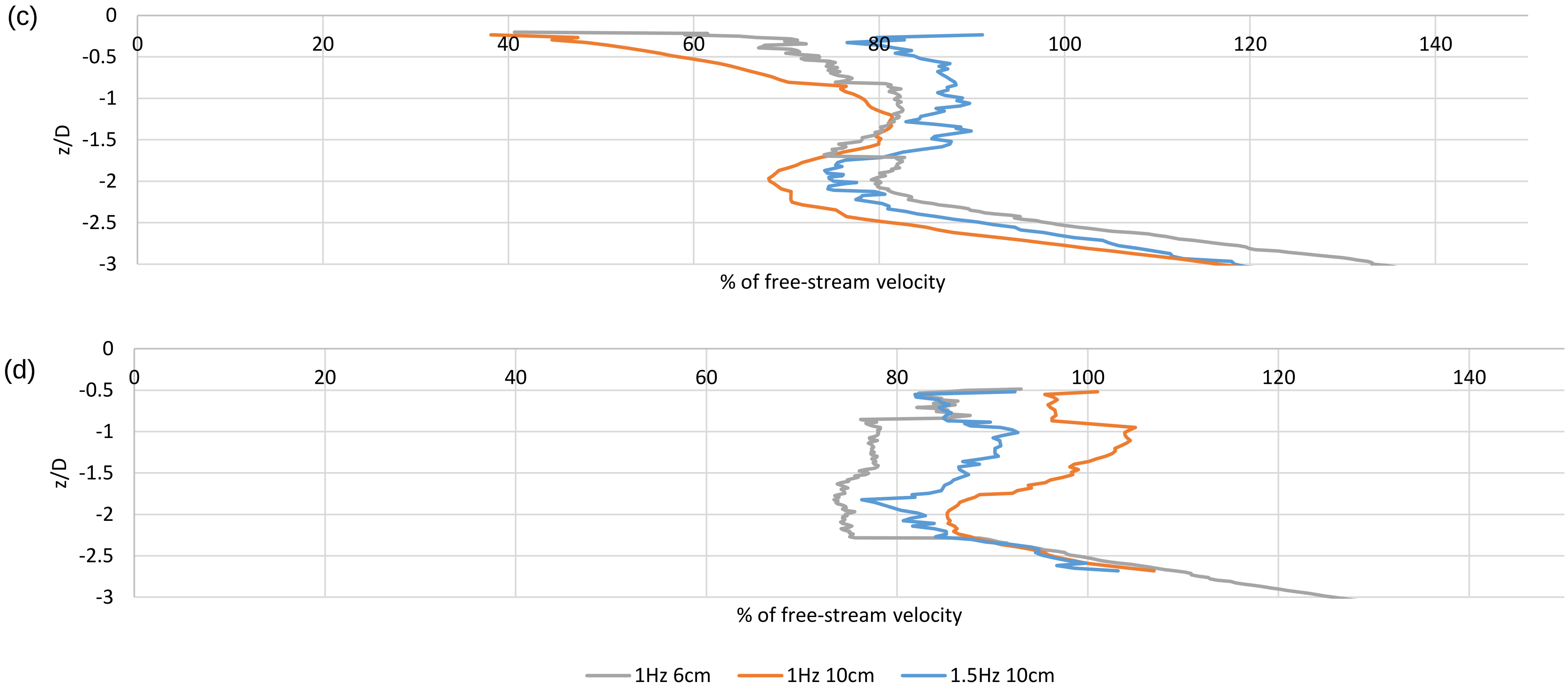

Figure 6.9: Wake deficit charts showing the velocity in the turbine wake under wave troughs as a percentage of the free-stream velocity under 1Hz, 6cm waves with current, 1Hz, 10cm waves with current and 1.5Hz, 10cm waves with current at (c) 4 rotor diameters downstream from the turbine and (d) 5 rotor diameters downstream from the turbine. Scales on the y-axes are normalised to rotor diameters (200mm).

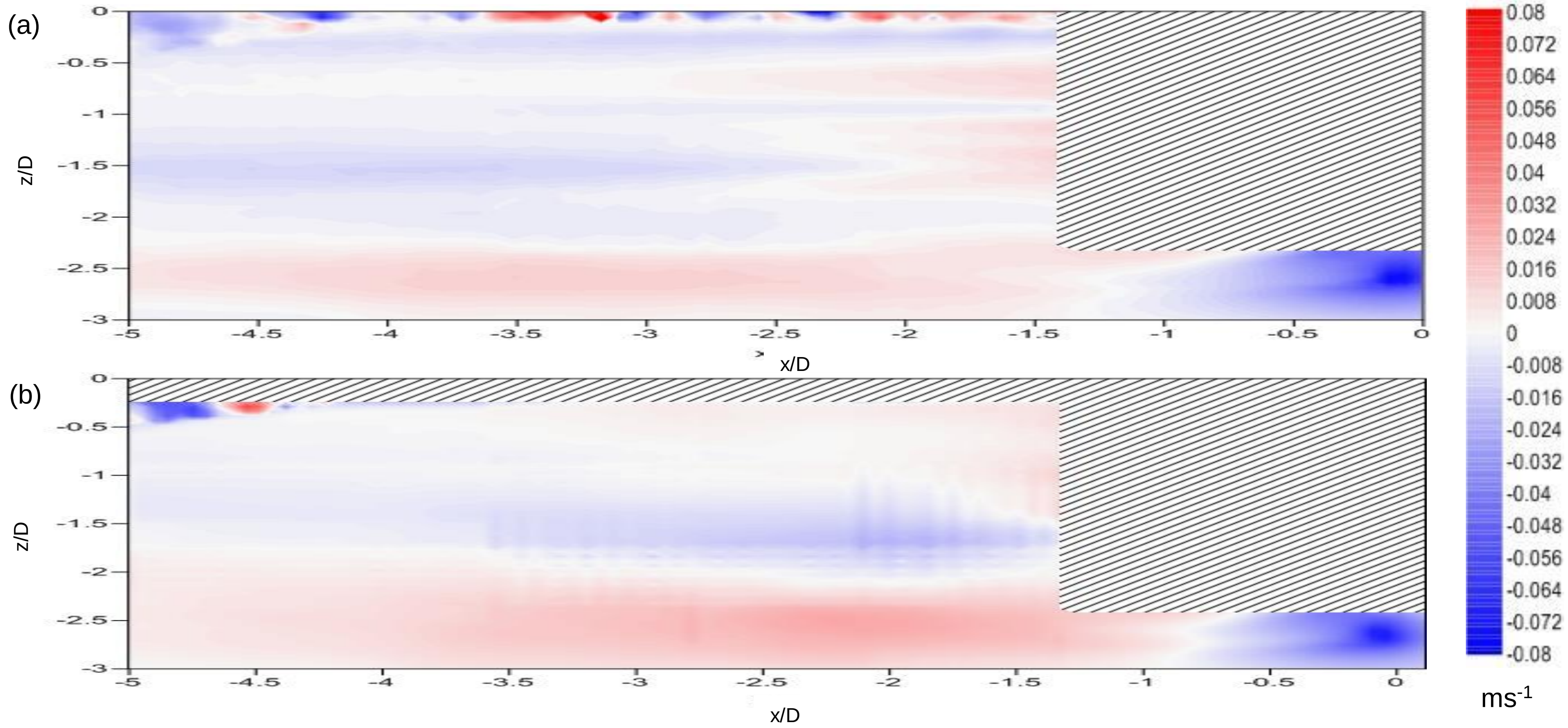

Figure 6.10: Flow structure maps for the vertical velocity component for (a) current-only conditions (b) 1Hz, 6cm waves with current (ensemble average). Flow direction is from right to left. Scales on the axes are normalised to rotor diameters (200mm). Areas covered by diagonal shading indicate areas where no data could be collected.

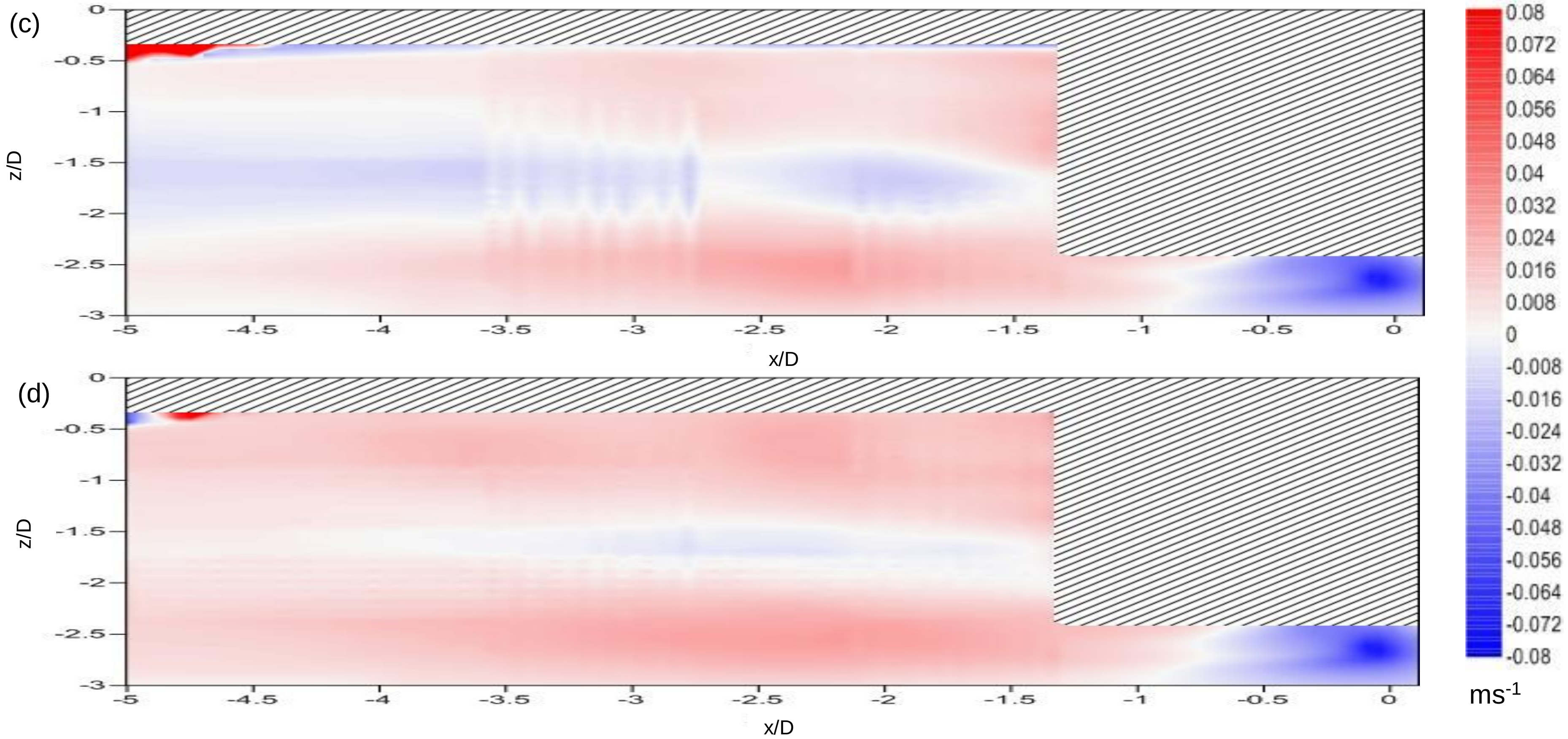

Figure 6.10: Flow structure maps for the vertical velocity component for (c) 1Hz, 10cm waves with current (ensemble average) (d) 1.5Hz, 10cm waves with current (ensemble average). Flow direction is from right to left. Scales on the axes are normalised to rotor diameters (200mm). Areas covered by diagonal shading indicate areas where no data could be collected.

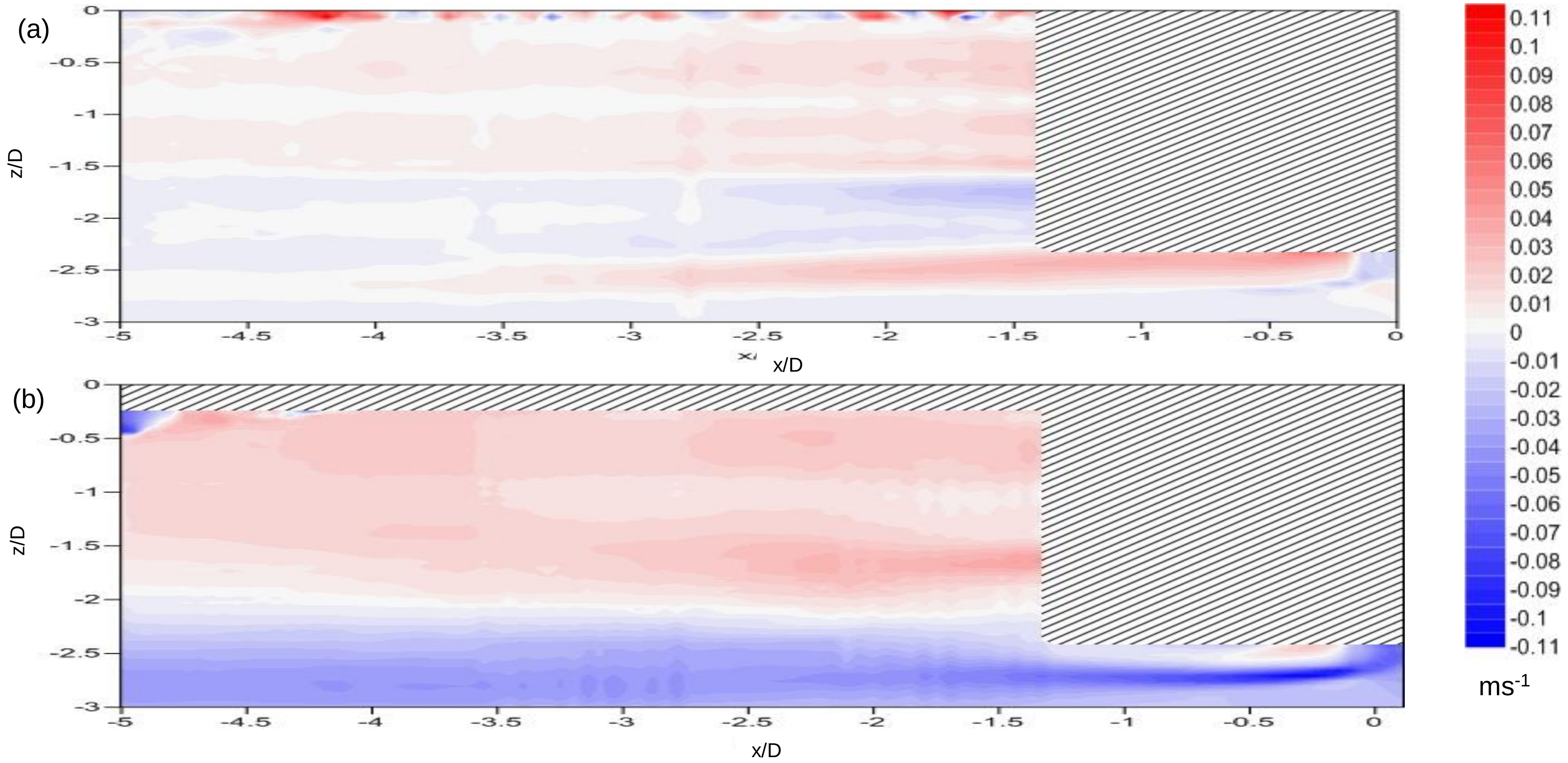

Figure 6.11: Flow structure maps for the cross-stream velocity component for (a) current-only conditions (b) 1Hz, 6cm waves with current (ensemble average). Flow direction is from right to left. Scales on the axes are normalised to rotor diameters (200mm). Areas covered by diagonal shading indicate areas where no data could be collected.

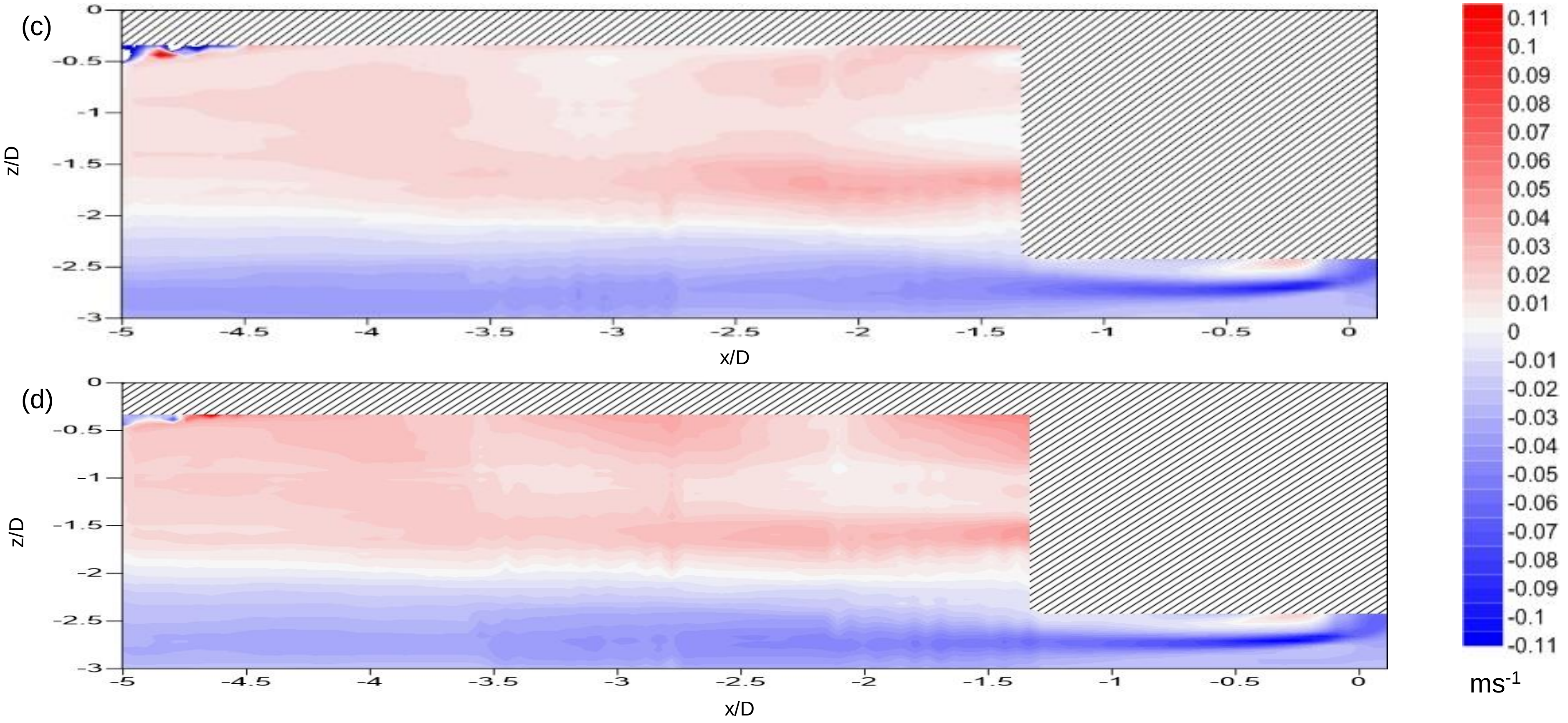

Figure 6.11: Flow structure maps for the cross-stream velocity component for (c) 1Hz, 10cm waves with current (ensemble average) (d) 1.5Hz, 10cm waves with current (ensemble average). Flow direction is from right to left. Scales on the axes are normalised to rotor diameters (200mm). Areas covered by diagonal shading indicate areas where no data could be collected.

Under all flow conditions, there is a significant increase in the turbulent kinetic energy (*k)* and Reynolds stress (*u'w'*) in the wake of the TST. For the ensemble average of the flow conditions, the magnitude of the turbulent kinetic energy and Reynolds stress are greatest under 1Hz, 10cm waves with current when compared to current-only flow conditions, the 1Hz, 6cm waves with current conditions and 1.5Hz, 10cm waves with current conditions (figures 6.12 (a) to (d), 6.13 and 6.14 (a) to (d)). However, when the crest and trough are separated, the turbulent kinetic energy under 1Hz, 10cm waves with current is lower than the turbulent kinetic energy for the 1Hz, 6cm waves with current and 1.5Hz, 10cm waves with current (figure 6.15). Overall, the turbulent kinetic energy is greatest under wave crests than wave troughs. A large portion of the increase in turbulent kinetic energy seen under the waves with current flow conditions can be attributed to the presence of the waves, and the wave induced kinematics.

Under current-only flow conditions, the increase in the magnitude of the turbulent kinetic energy and the Reynolds stress is concentrated around the wake circumference, in-line with the rotor blade tips. Under wave-current flow conditions, the entire flow area has a significant increase in turbulent kinetic energy and Reynolds stress. When looking at the ensemble average of the flow conditions, the greatest increase in the turbulent kinetic energy occurs at around 2 rotor diameters downstream from the tidal turbine (figure 6.13). The greatest increases in the turbulent kinetic energy and Reynolds stress occur in the upper area of the flow close to the water surface (figures 6.12 (a) to (d)). The increase in the magnitude of the turbulent kinetic energy close to the water surface is greatest under 1Hz, 10cm waves with current (figure

6.12 (c)). The increase in the magnitude of the Reynolds stress close to the water surface is greatest under 1Hz, 10cm waves with current (figure 6.14 (c)) and 1.5Hz, 10cm waves with current (figure 6.14 (d)).

Comparing the turbulent kinetic energy and Reynolds stress for all of the wave-current flow conditions shows that increasing the frequency (figures 6.12 (d) and 6.14 (d)) leads to a lesser increase in the magnitude of the turbulent kinetic energy downstream from the rotor compared to the lower frequency waves (figures 6.12 (b), 6.12 (c), 6.14 (b) and 6.14 (c)).

The turbulence intensity (u'/U_0) for the previously specified flow conditions is shown in figures 6.16 (a) to 6.16 (d). Overall, the turbulence intensity is higher under wave-current flow conditions than under current-only flow conditions, particularly just downstream from the rotor. At 2 rotor diameters downstream (figure 6.16 (a)), there are two distinct areas of increased turbulence intensity downstream of the rotor that are aligned with the tips of the rotor blades under all flow conditions. Further downstream, these areas of increased turbulence intensity are still present, but are much less pronounced. Beyond 4 rotor diameters downstream (figure 6.16 (c)), the difference in turbulence intensity between wave-current flow conditions and current-only flow conditions lessens. At all locations downstream, the turbulence intensity is greatest under 1Hz, 10cm waves with current.

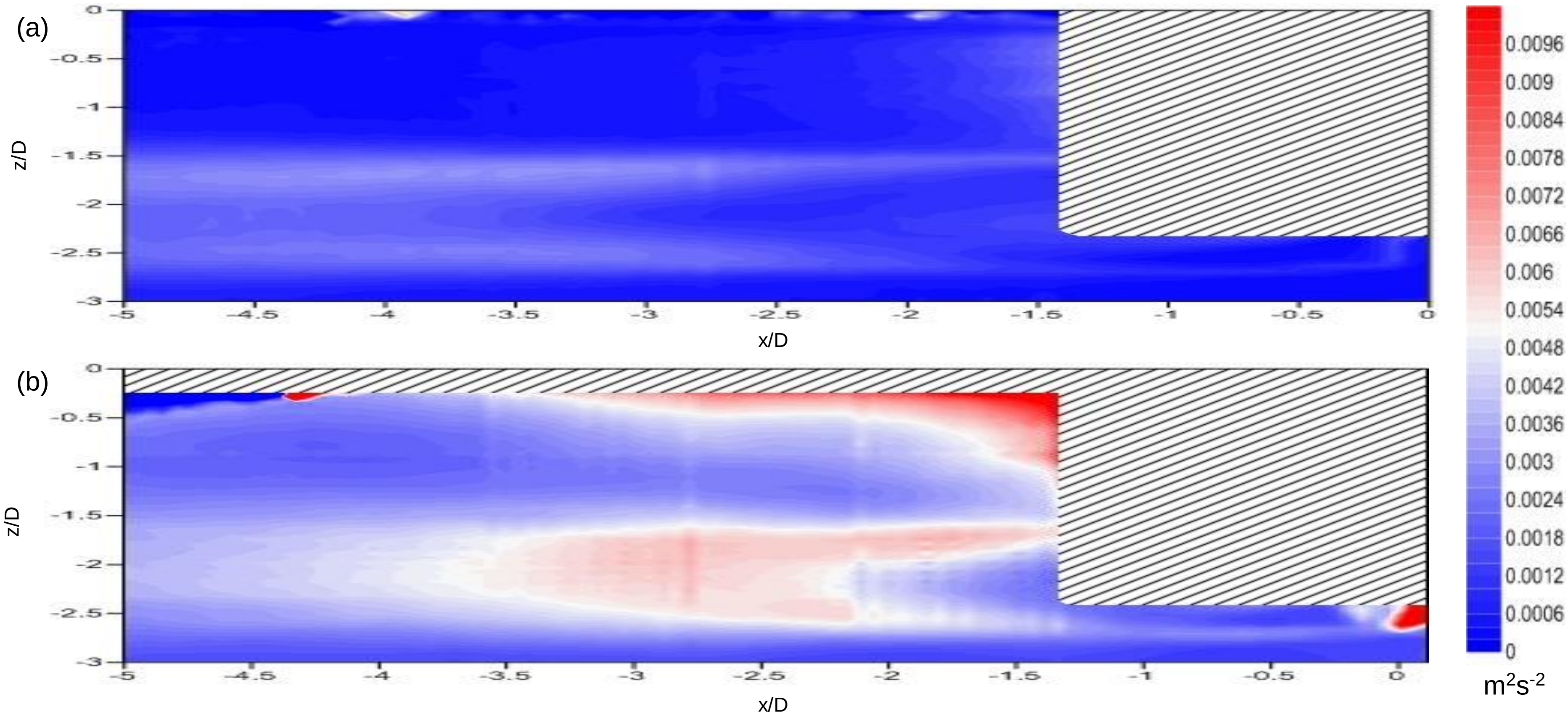

Figure 6.12: Flow structure maps for the turbulent kinetic energy for (a) current-only conditions (b) 1Hz, 6cm waves with current (ensemble average). Flow direction is from right to left. Scales on the axes are normalised to rotor diameters (200mm). Areas covered by diagonal shading indicate areas where no data could be collected.

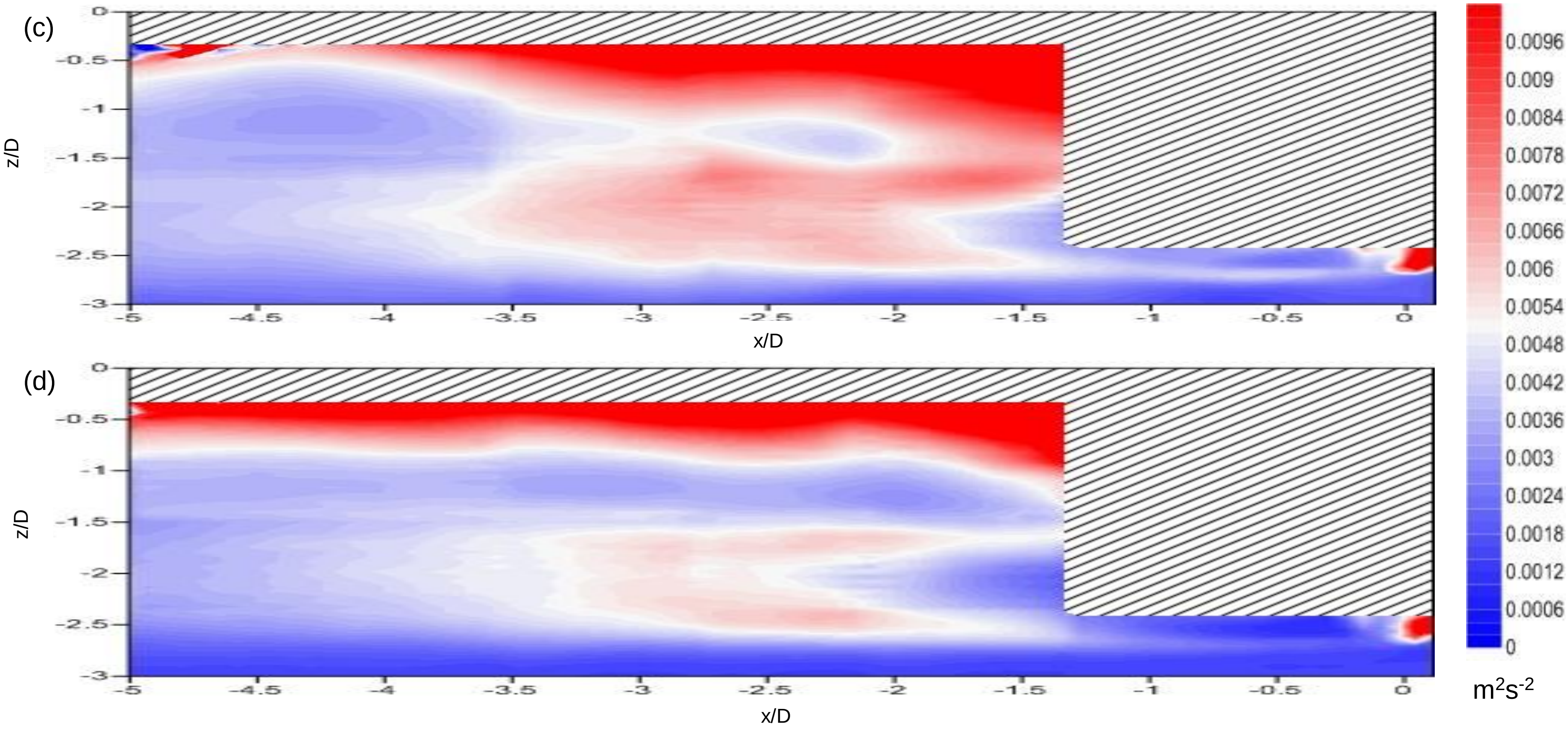

Figure 6.12: Flow structure maps for the turbulent kinetic energy for (c) 1Hz, 10cm waves with current (ensemble average) (d) 1.5Hz, 10cm waves with current (ensemble average). Flow direction is from right to left. Scales on the axes are normalised to rotor diameters (200mm). Areas covered by diagonal shading indicate areas where no data could be collected.

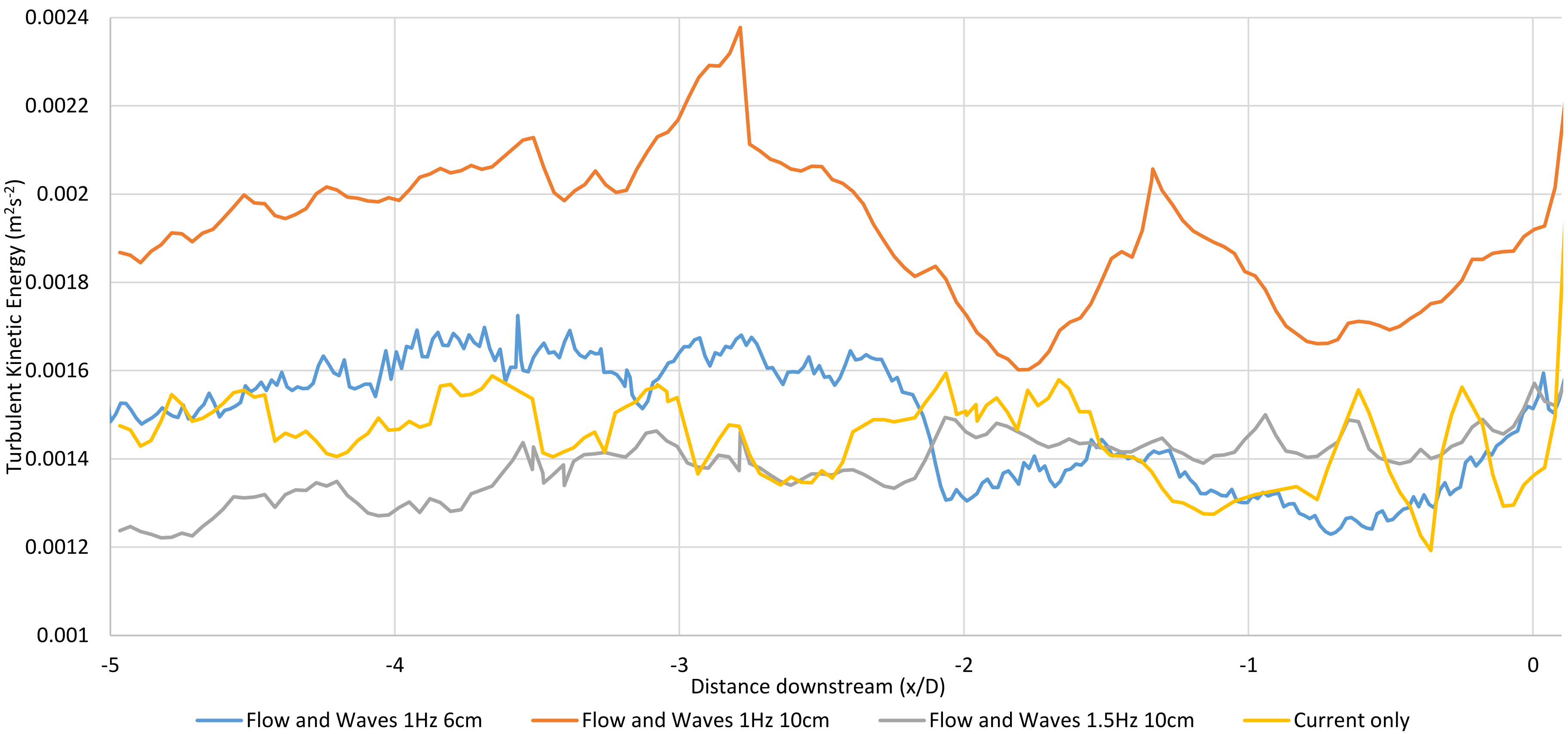

Figure 6.13: Turbulent kinetic energy along the channel bed for current only conditions, 1Hz, 6cm waves with current (ensemble average), 1Hz, 10cm waves with current (ensemble average) and 1.5Hz, 10cm waves with current (ensemble average). Flow direction is from right to left. Scale on the horizontal axis is normalised to rotor diameters (200mm). The turbulent kinetic energy is measured directly above the channel bed.

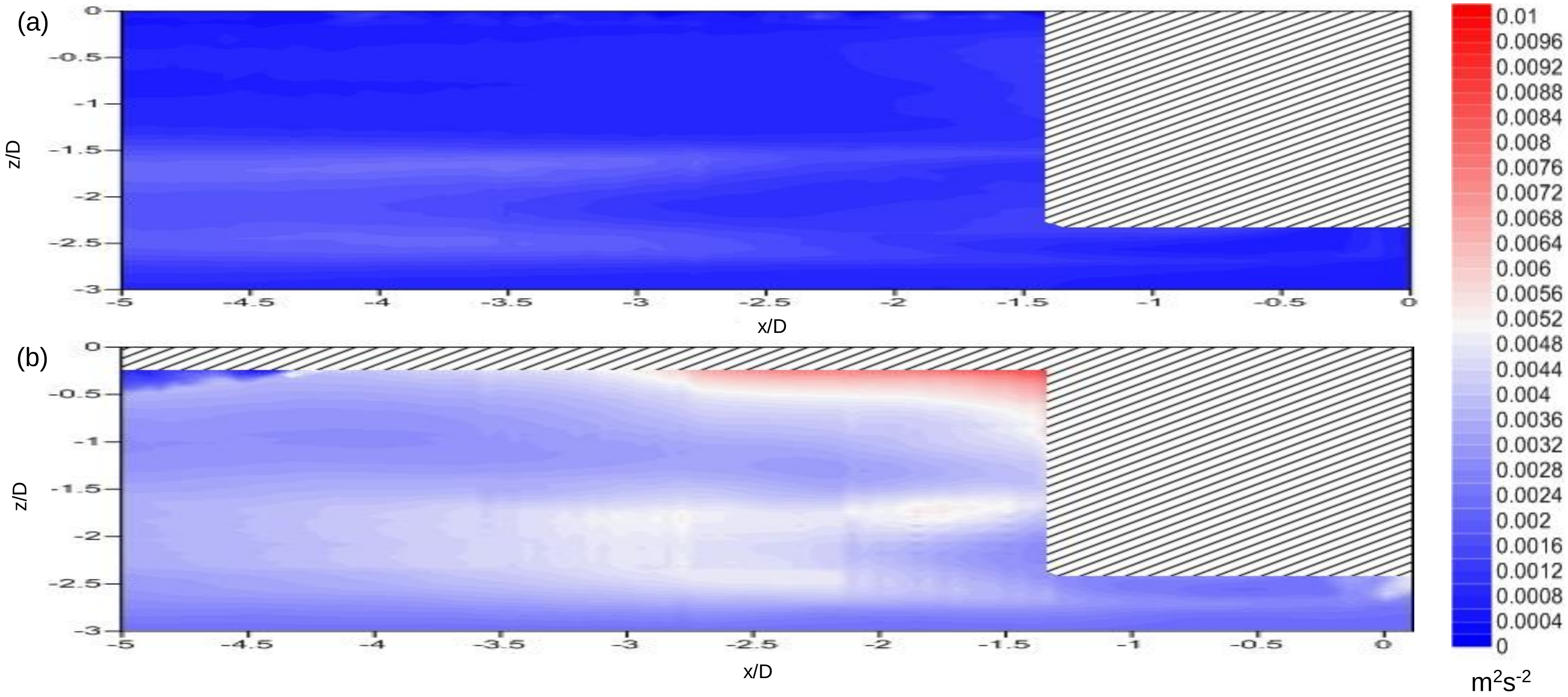

Figure 6.14: Flow structure maps for the Reynolds stress (u'w') (a) current-only conditions (b) 1Hz, 6cm waves with current (ensemble average). Flow direction is from right to left. Scales on the axes are normalised to rotor diameters (200mm). Areas covered by diagonal shading indicate areas where no data could be collected.

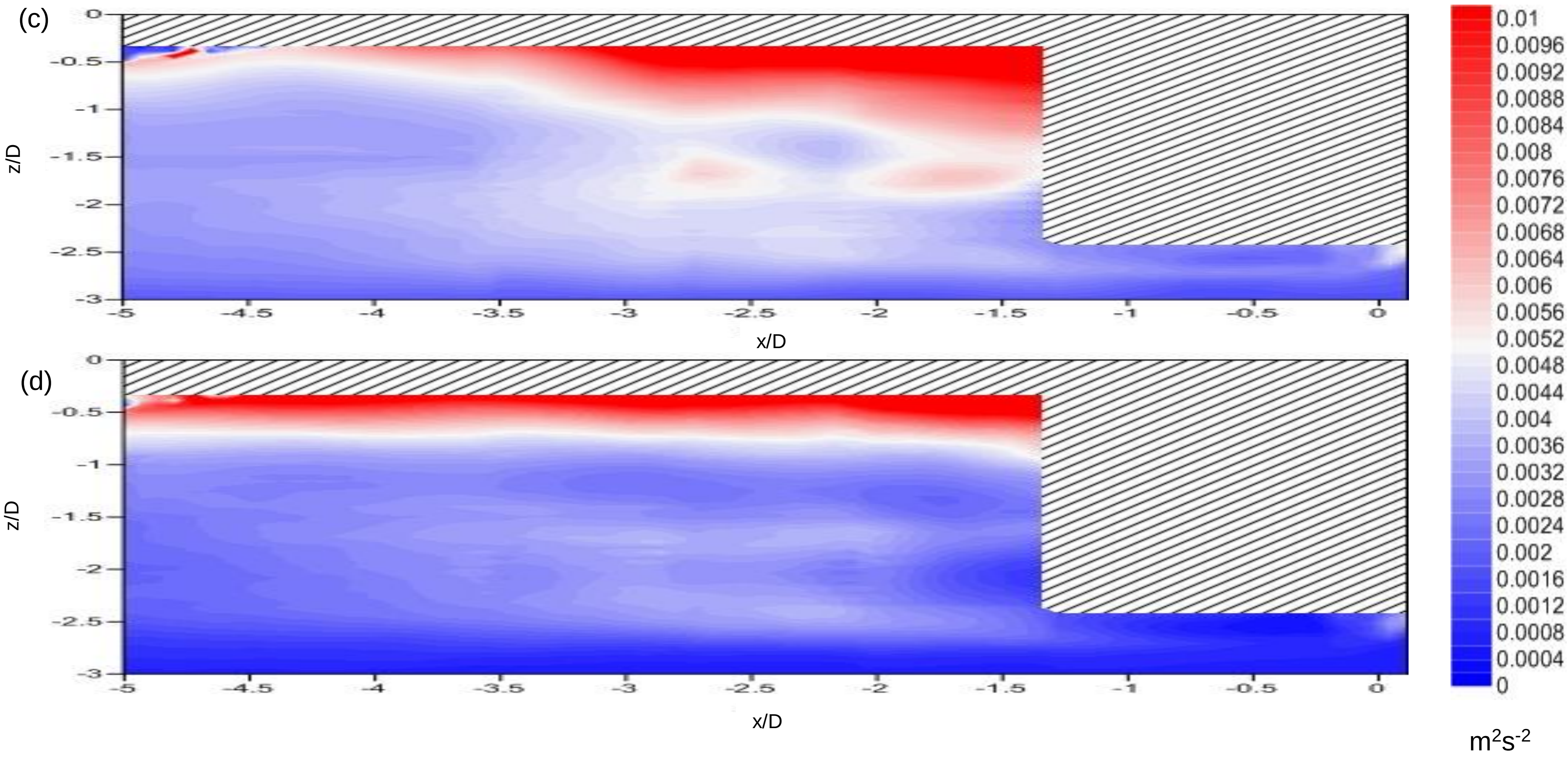

Figure 6.14: Flow structure maps for the Reynolds stress (u'w') (c) 1Hz, 10cm waves with current (ensemble average) (d) 1.5Hz, 10cm waves with current (ensemble average). Flow direction is from right to left. Scales on the axes are normalised to rotor diameters (200mm). Areas covered by diagonal shading indicate areas where no data could be collected.

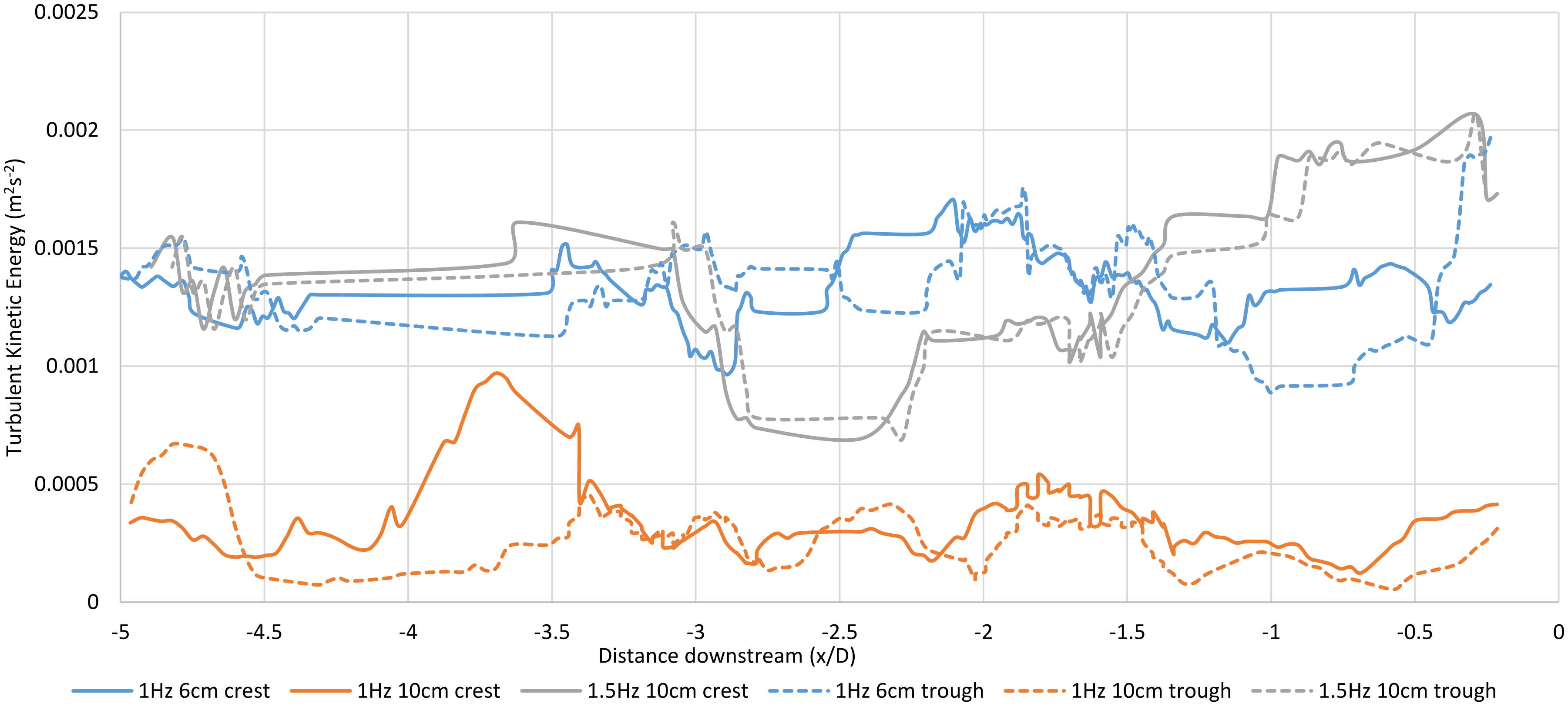

Figure 6.15: Turbulent kinetic energy along the channel bed for wave crest (solid line) and wave trough (dashed line) of 1Hz, 6cm waves with current, 1Hz, 10cm waves with current and 1.5Hz, 10cm waves with current. Flow direction is from right to left. Scale on the horizontal axis is normalised to rotor diameters (200mm). The turbulent kinetic energy is measured directly above the channel bed.

The normalised shear velocity is presented in figures 6.17 and 6.18. Overall, there is an increase in the normalised shear velocity immediately downstream of the tidal stream turbine, with the greatest increase under current only flow conditions compared to the ensemble average for the wave-current flow conditions (figure 6.17). The normalised shear velocity for the ensemble average flow conditions reduces further downstream (figure 6.17).

Overall, the normalised shear velocity under the wave crests and wave troughs increases immediately downstream from the tidal stream turbine, and reduces further downstream (figure 6.18), as seen in the ensemble average of the wave-current flow conditions and current only flow conditions (figure 6.17). The normalised shear velocity is greatest under the wave crest than the wave trough immediately downstream from the rotor, except under 1Hz, 6cm waves with current (figure 6.18). There is a greater fluctuation in the normalised shear velocity under the wave crests and wave troughs than in the ensemble average of the wave-current flow conditions. However, this could be a function of the analysis method which separates the wave crests and wave troughs, and therefore differs from the ensemble average as wave crests and wave troughs only take into account a subset of the collected PIV data.

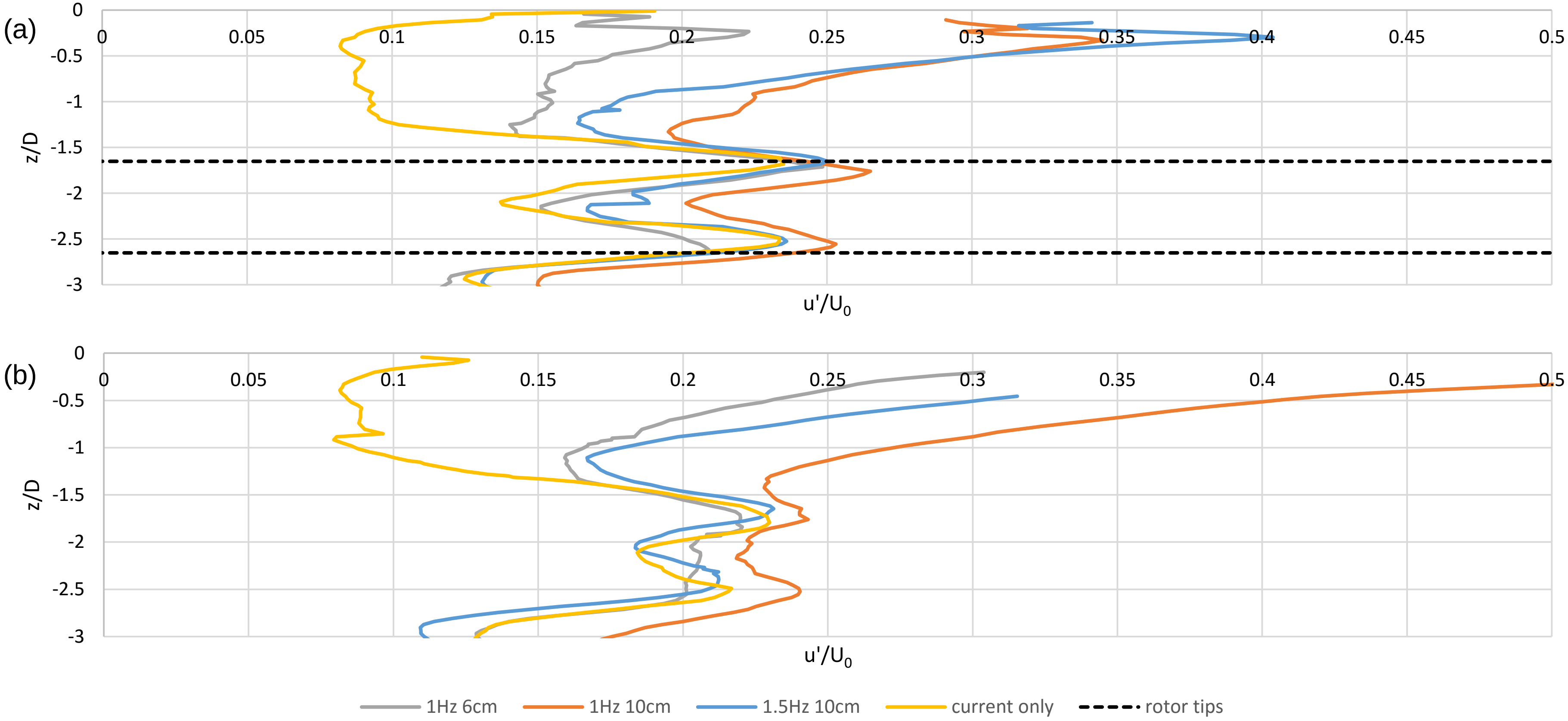

Figure 6.16: Charts showing the vertical profile of the turbulence intensity (u'/U_0) under current only, 1Hz, 6cm waves with current, 1Hz, 10cm waves with current and 1.5Hz, 10cm waves with current at (a) 2 rotor diameters downstream from the turbine (b) 3 rotor diameters downstream from the turbine. Scales on the y-axes are normalised to rotor diameters (200mm).

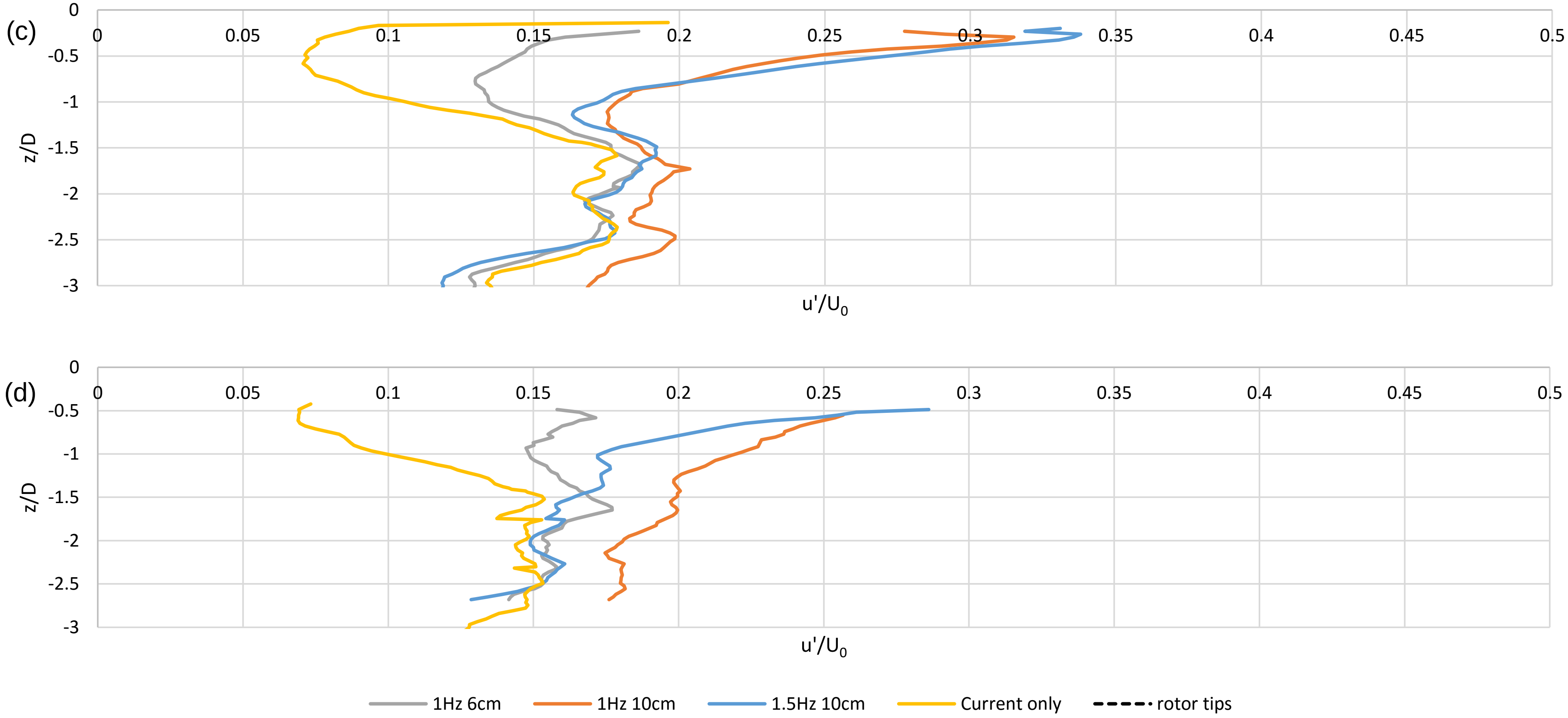

Figure 6.16: Charts showing the vertical profile of the turbulence intensity (u'/U_0) under current only, 1Hz, 6cm waves with current, 1Hz, 10cm waves with current and 1.5Hz, 10cm waves with current at (c) 4 rotor diameters downstream from the turbine and (d) 5 rotor diameters downstream from the turbine. Scales on the y-axes are normalised to rotor diameters (200mm).

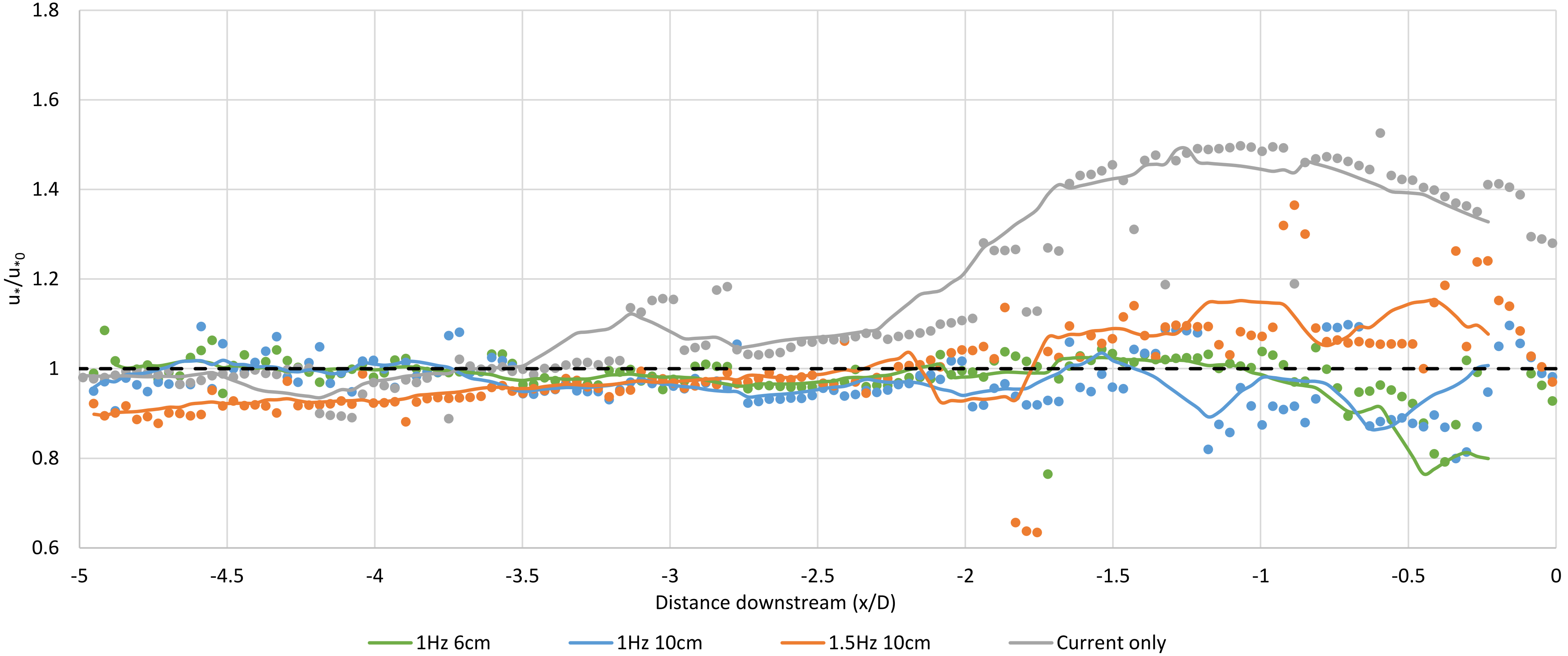

Figure 6.17: Normalised shear velocity (u_*/u_{*0}) *for current only flow, and the ensemble average of 1Hz, 6cm waves with current, 1Hz, 10cm waves with current and 1.5Hz, 10cm waves with current. Coloured points: Original data points. Solid coloured line: Moving average trend line. Dashed black line: incoming flow normalised shear velocity. Flow direction is from right to left. Scale on the horizontal axis is normalised to rotor diameters (200mm). Rotor is positioned immediately upstream of x=0. The shear velocity is measured in the measurement cell closest to the channel bed.*

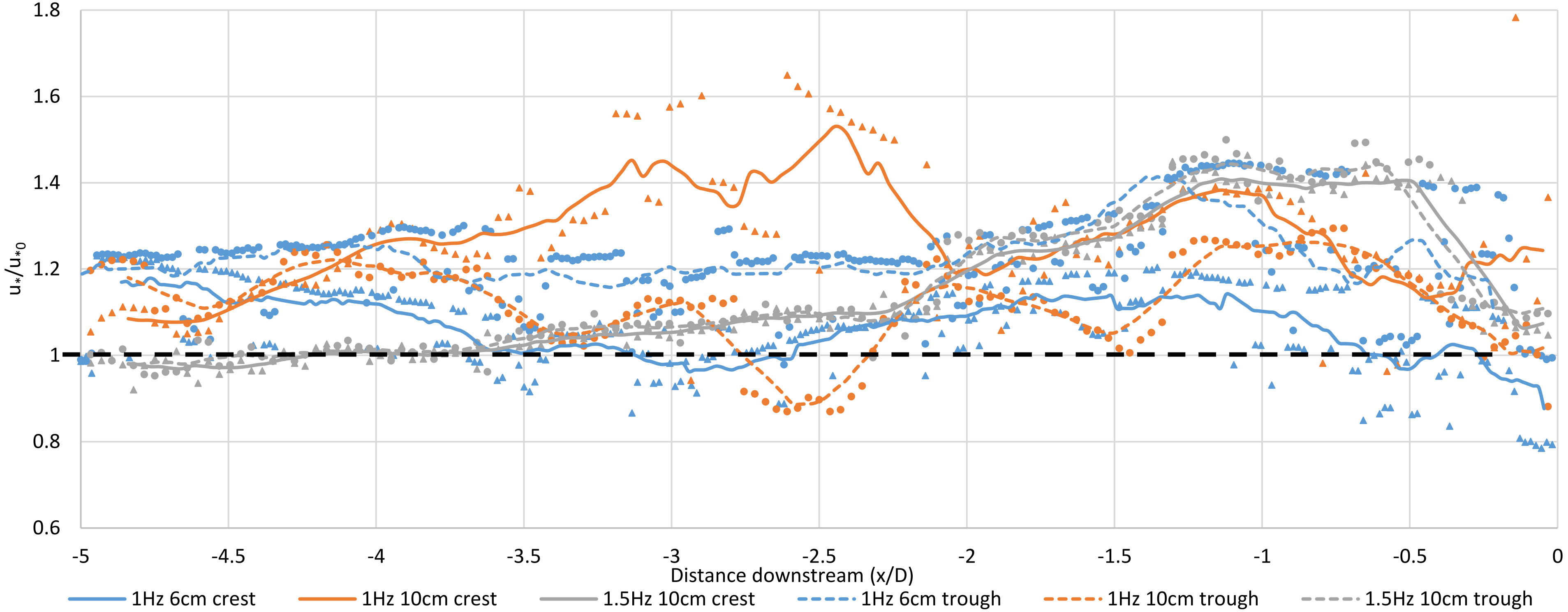

Figure 6.18: Normalised shear velocity (u_*/u_{*0}) *for the wave crests and wave troughs of 1Hz, 6cm waves with current, 1Hz, 10cm waves with current and 1.5Hz, 10cm waves with current. Triangle points: Original data points for wave crests. Solid coloured line: Moving average trend line for wave crests. Coloured circles: Original data points for wave troughs. Dashed coloured line: Moving average trend line for wave troughs. Dashed black line: incoming flow normalised shear velocity. Flow direction is from right to left. Scale on the horizontal axis is normalised to rotor diameters (200mm). Rotor is positioned immediately upstream of x=0. The shear velocity is measured in the measurement cell closest to the channel bed.*

6.4 Discussion

The results above highlight significant differences in the wake structure and dynamics, the bed shear stress and turbulence flow properties in the lee of a TST between current only flow conditions and wave-current flow conditions. The overall wake structure seen in the results of this research are consistent with those presented in previous research. The velocity deficit is greatest closest to the tidal stream turbine in all flow conditions, and reduces downstream, but the deficit is much greater under current only flow conditions compared to the wave-current flow conditions. The results presented by Stallard *et al.* (2013) and Stallard *et al.* (2015) (figure 6.19) also show that the greatest velocity deficit occurs close to the TST, and the velocity deficit reduces as the wake downstream expands. Full flow recovery does not occur in the measurement area of the results presented herein. This is consistent with previous work that has shown that full flow recovery is expected to occur beyond 20 rotor diameters downstream (Stallard *et al.*, 2013).

Previous research examining the effect of wave-current interactions on the near wake of tidal stream turbines (e.g. Stallard *et al.*, 2013; Jesus Henriques *et al.*, 2015) produced results which are in agreement with those presented in this paper. Jesus Henriques *et al.* (2015) identified that there is a significantly lower stream-wise velocity deficit under wave-current flow than under current-only flow conditions. Jesus Henriques *et al.* (2015) also determined that the wave-induced velocities in the wave-current flow conditions enhance the mixing between the flow in the turbine wake and the free-stream flow. This increases the downstream velocity recovery, and therefore shortens the wake under wave-current conditions compared to current only flow conditions. This is in agreement with the findings of the research presented herein. The ensemble average results for the wave-current flow conditions (figures 6.4(a) to (d)) show that the wake length is significantly shorter under wave-current flow than current only flow conditions.

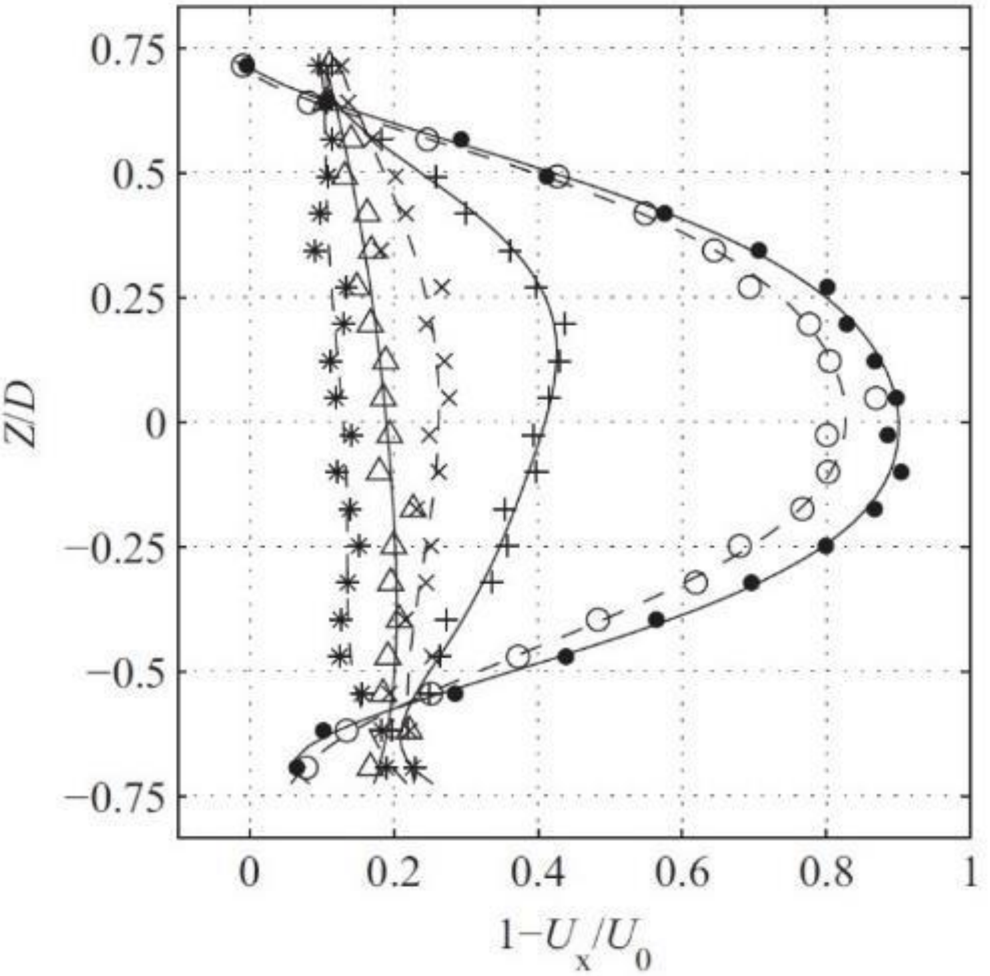

Figure 6.19: Vertical profiles of velocity deficit at X = 1.5D (●), *2D* (○), *4D* (+), *6D* (x), *8D* (Δ) *and 12D* (✳). *Curves indicate trend only (Stallard et al., 2015, pp. 245).*

Across the conditions examined, the results indicate a number of differences in the stream-wise and cross-stream velocities because of altering the wave height or frequency. Vertical velocities become more positive, and there is therefore greater upwelling, as the size and frequency of the waves are increased. Additionally, the vertical velocities are dissipated faster under current-only flow compared to wave-current flow. By 3 rotor diameters downstream from the turbine, the area of upwelling has dissipated and become downwelling under current only flow. Under 1Hz, 6cm waves with current, the area of upwelling has mostly dissipated by 3 rotor diameters downstream. However, under 1Hz, 10cm waves with current and 1.5Hz, 10cm waves with current, the area of upwelling above the wake is still present up to 5 rotor diameters downstream. This is in contrast with the results presented by Jesus Henriques *et al.* (2015). The results by Jesus Henriques *et al.* (2015) showed that both negative and positive vertical velocities dissipated faster under wave-current flow conditions compared to current-only flow conditions. The significant differences seen in the vertical velocity component in the results presented herein are related to the presence of waves, which increases the vertical movement of the flow as the waves move between wave crests and wave troughs. The increased vertical velocities under wave-current flow increase flow mixing and therefore aid in wake recovery.

There is little research to date studying the effects of waves on the flow within the wake. However, Barltrop *et al.* (2006) studied the effect of wave height on turbine performance, and the torque of the rotor is sensitive to the wave height, in particular that of longer waves. Jesus Henriques *et al.* (2014) and Jesus Henriques *et al.* (2015) noted that fluctuations occurred in the power and thrust of the tidal turbine when the turbine was subject to wave-current flow, and that these fluctuations occurred at the same frequency as the waves. It is therefore important to understand that a change in wave frequency could impact the turbine power and thrust.

In the research described herein, it was observed that the rotor stalled under large waves. Although this did not occur regularly, and did not appear to affect the turbine wake, it could have significant impacts on the rotor performance. Barltrop *et al.* (2006) observed rotor stalling under some wave-current flow conditions, and noted that it reduced the turbine torque and increased the thrust. In the research described herein, the rotor stalling only accounted for 0.1% of the rotor revolutions under the 1Hz, 10cm waves with current flow conditions, and is therefore unlikely to have had any significant impact on the wake structure.

There are significant differences seen in the turbulence, normalised shear velocity and shear stress (indicated using TKE and Reynolds stress) under the different flow conditions explained herein. Whilst the normalised shear velocity is lower under wave-current flow than current only flow, there is a significant increase in turbulence intensities and shear stresses under wave-current flow compared to current only flow, particularly under 1Hz, 10cm waves. Luznik *et al.* (2013) indicated that increased turbulence and shear stresses are found in the blade tip region in unsteady flow, which is consistent with the findings of the results presented herein. The increase in turbulent kinetic energy under wave-current flow conditions compared to current-only flow conditions will aid wake recovery by mixing the free-stream fluid into the wake, which leads to the faster wake recovery under the wave-current flow conditions (Myers and Bahaj, 2010, Jesus Henriques *et al.*, 2015). The increased turbulence intensity under wave-current flow aids with wake recovery. The maximum turbulence intensity is observed at 2 rotor diameters downstream, which is similar to the results presented by Stallard *et al.* (2015), as shown in figure 6.20. The wake width can be defined by the distance between the maxima of turbulence intensity.

Therefore, as seen in figures 6.16 (a) to (d), the wake width is approximately 0.8 rotor diameters under 1Hz, 10cm waves with current, 1.5Hz, 10cm waves with current flow conditions and current only flow conditions, and approximately one rotor diameter under 1Hz, 6cm waves with current.

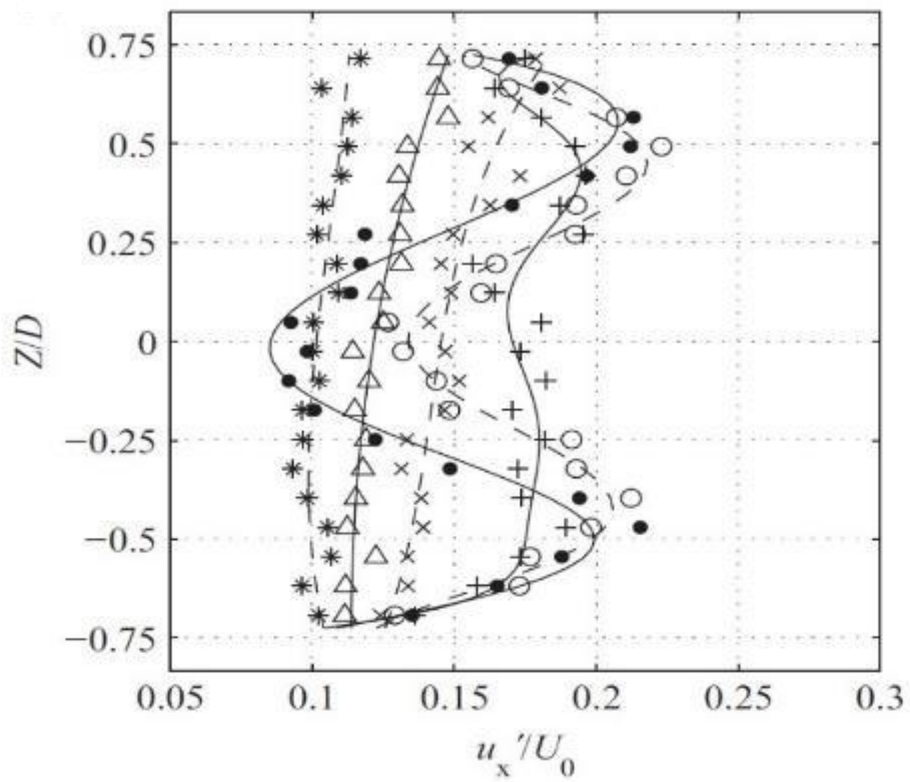

Figure 6.20: Vertical profiles of turbulence intensity at X = 1.5D (●), *2D* (○), *4D* (+), *6D* (x), *8D* (Δ) *and 12D* (✳). *Curves indicate trend only (Stallard et al., 2015, pp. 245).*

The overall wake structure and velocity deficit can have implications, particularly when building tidal turbine farms, as the spacing of the turbines within an array will be affected by wake length and wake recovery (Myers *et al.*, 2010, Jesus Henriques *et al.,* 2015). The increased turbulence and shear stresses may lead to enhanced wake recovery under wave-current flow due to enhanced mixing (Luznik *et al.*, 2013). These factors can therefore have implications for the spacing of turbines in arrays (Myers *et al.*, 2010; Luznik *et al.*, 2013; Jesus Henriques *et al.,* 2015).

There has been limited work undertaken which has attempted to characterise the wake of a tidal stream turbine under wave-current flow, or to compare the wake of a tidal stream turbine under both wave-current flow and current only flow. To the authors' knowledge, no research has been conducted to date which investigates how the wake of a tidal stream turbine differs under the wave crest and the wave trough. Previous research has investigated the impact of wave-current flow on TST performance (e.g. Gaurier *et al.*, 2013; Payne *et al.*, 2015) but these do not focus on the flow dynamics or characteristics downstream from the tidal stream turbine.

The limited research which is available shows that wave-current flow affects both the wake velocity (Jesus Henriques *et al.,* 2015) and also the output and loading of the tidal stream turbine (Jesus Henriques *et al.*, 2014). The impact of wave-current flow on turbine loading was not measured as part of this research. However, a number of studies (e.g. Barltrop *et al.*, 2006; Gaurier *et al.*, 2013; Luznik *et al.*, 2013; Galloway *et al.* 2014) have looked at the effect of wave-current flow on turbine performance. It was identified that surface waves have a significant impact on the power production and blade loading of the turbine (Luznik *et al.*, 2013), and that the main issue surrounding wave-current interaction with tidal stream turbines is not an impact on power output, but the effect that the loading will have on the turbine life (Galloway *et al.*, 2014). Wave-current interactions can cause large additional loading on turbines compared to current only flow, and can therefore lead to accelerated fatigue of the turbine, and must therefore be taken into account when designing tidal stream turbines (Gaurier *et al.,* 2013; Galloway *et al.*, 2014; Payne *et al.,* 2015).

6.5 Conclusions

Detailed flow maps of the stream-wise, vertical and cross-stream velocity components have been presented for the ensemble average of 4 different flow conditions, as well as the stream-wise velocity components for the wave crest and wave trough of the three wave and current flow conditions. The TKE, an estimate of shear stress, and the Reynolds stress (u'w') have also been presented for the ensemble average of the 4 different flow conditions.

The results show that the TST wake is significantly affected in terms of the stream-wise velocity deficit as a result of the wave-current flow compared to the current only flow. The TKE and Reynolds stress downstream from the rotor are significantly increased under wave-current conditions, and this further increases with increasing wave height. The results demonstrate that the effect of wave-current flow on the wake behind a TST is significant and therefore understanding the impact of wave-current flow on tidal turbines and the wake behind a turbine is important, particularly as it may impact turbine placement and turbine design. Moreover, the wake structure dependence on wave height and flow conditions highlights the need to account for wave-current conditions in TST array design in order to maximise array performance across a range of wave-current conditions. As such, there is a need to better examine a range of wave-current conditions across a set of parameter space to better inform and guide TST deployments in various environments.

Chapter 7

Conclusions and Future Work

The research presented herein has investigated the flow field around a small scale tidal stream turbine, and attempted to understand the wake of a tidal stream turbine, and the impact of various flow conditions on the wake flow field, as well as the impact of the turbine on the bed.

The results presented herein show a cross-stream asymmetry and transverse drift in the turbine wake, with a greater velocity deficit on the left hand side of the centreline, compared to the right hand side of the centreline. At 1.5 rotor diameters downstream, the normalised stream-wise velocity is 5% greater on the right hand side of the channel at the vertical centre of the rotor. However, by 4 rotor diameters downstream, the normalised stream-wise velocity is approximately 10% greater on the left hand side of the channel compared to the right hand side of the channel at the vertical centre of the rotor. The cross-stream asymmetry and drift observed in the wake would have implications when determining the lateral spacing of turbines within a channel.

It has been determined that the proximity of the turbine to the channel bed has a significant impact on the wake downstream of the turbine, as well as on the scour of sediment beneath the turbine. Positioning a turbine too close to the channel bed leads to an increase in turbulent kinetic energy and significant sediment scour. The near bed turbulent kinetic energy is approximately 65% greater at 4 rotor diameters downstream, compared to immediately downstream from the rotor when the rotor is positioned close to the channel bed. Conversely, the shear velocity decreases downstream when the rotor is positioned close to the channel bed. The normalised shear velocity beyond 3 rotor diameters downstream is below the observed critical threshold for sediment transport, and is approximately 50% of the normalised shear velocity immediately downstream from the turbine. Positioning a turbine in close proximity to the channel bed leads to a greater velocity deficit within the wake, and a longer wake length. It is therefore necessary to consider the vertical placement of tidal stream turbines within the channel.

It has been shown that the presence of waves significantly affects the wake of a tidal stream turbine, and would have significant impacts on the turbine placement within a channel. Under wave-current flow, the wake length is considerably shorter than under current flow. However, due to the impact of the waves on the flow and turbine, it would be necessary to locate the turbine lower in the tidal channel to minimise these impacts. However, this would then need consideration of the scour that may occur on the bed.

The results presented herein show that the near bed turbulent kinetic energy under the ensemble average of 1Hz, 10cm wave-current flow conditions is approximately 40% greater than the near bed turbulent kinetic energy under the other flow conditions presented in this research. The turbulent kinetic energy is slightly higher under the wave crest compared to the wave trough. However, the near bed turbulent kinetic energy under the wave crest and the wave trough is approximately 3 times lower under 1Hz, 10cm wave-current flow conditions compared to the other flow conditions. The normalised shear velocity is approximately 30% greater under current only flow conditions than wave-current flow conditions up to approximately 1 rotor diameters downstream. Beyond this, the normalised shear velocity for the ensemble average is similar in all flow conditions. The normalised shear velocity is greater under the wave crest than the wave trough for 1Hz, 10cm wave-current flow. Under the remaining flow conditions, the normalised shear velocity is greater under the wave trough than the wave crest.

There are disparities seen in the results presented herein between using the turbulent kinetic energy or the normalised shear velocity as measures of shear stress. The turbulent kinetic energy takes into account the stream-wise, cross-stream and vertical velocities, whereas the normalised shear velocity only takes into account the stream-wise velocity. This may account for some of the discrepancies seen between the two methods. The methods used for estimating shear stress would need to be investigated further to determine the most suitable method for estimating bed shear stress.

The results presented herein show that consideration needs to be given to vertical placement within a channel, both to maximise turbine performance, and to reduce the potential for the turbine to cause bed scour. Figure 7.1 shows an updated version of figure 3.1, which has been modified to present additional information based on the results presented herein. It shows the predicted differences in turbine performance when the rotor is positioned at various heights above the bed under a range of flow conditions. Under all flow conditions, it is expected that the turbine performance increases with distance from both the water surface and the bed.

Near the water surface (s), the wake and turbine performance will be affected by the wave amplitude and the rising and falling tides. In the results presented herein, only one flow depth was used, so it is not possible to fully determine the impact of the rising and falling tides on the turbine wake. However, it was shown that waves affect the turbine wake. Although the turbine was not situated close to the waves in the results presented herein, it is expected that positioning a turbine too high in the channel would lead to the wake and turbine performance being negatively affected by both the change in water depth that occurs with the waves, but also from the motion of the waves themselves. When the turbine was positioned at one-third of the depth, it was determined that the combined current and wave conditions at this turbine height led to a reduced velocity deficit, and 25% greater recovery by 5 rotor diameters downstream, compared to current only conditions. Therefore, the optimal vertical position of a turbine subject to combined wave-current flow would be slightly below mid-depth.

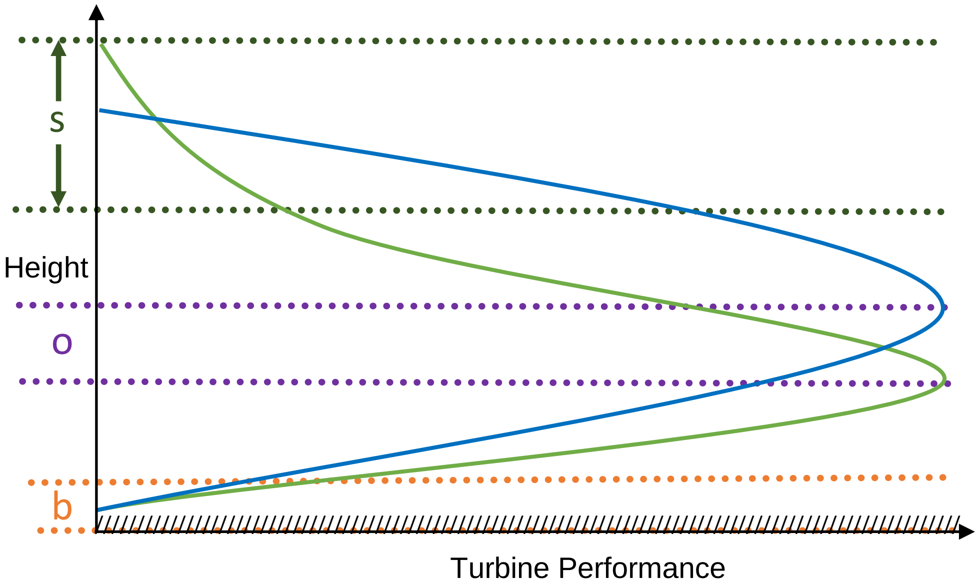

Figure 7.1: Diagram showing the predicted turbine performance under differing flow conditions and turbine heights. Channel bed = //////. Blue line = performance under current only conditions at mean sea level. Green line = performance under combined current and waves. Dashed green line = area affected by water surface. Dashed orange line = area affected by bed proximity. Dashed purple line = optimal placement. Diagram is not to scale and is designed to be a representative estimate only.

Positioning the turbine too close to the channel bed (b) must be avoided, otherwise sediment entrainment can occur, and the wake length and recovery can be negatively affected. In the results presented herein, sediment entrainment occurred when the rotor was positioned at 0.6D from the bed, which was one-fifth of the water depth. Increasing the distance between the turbine and the channel bed reduced any interaction between the wake and the bed. In the results presented herein, the majority of data was collected with the rotor at one-third of the water depth. At this location, the bed effects and surface effects were minimised. However, it would be possible to position a turbine slightly higher than this, as long as the changes in water depth due to the tidal range, and the wave amplitude, are considered.

The optimal vertical placement of the turbine within the channel requires avoiding the water surface (s) and channel bed (b) to minimise the effects of these, and the potential impacts of the wake on the channel bed. The ideal range at which the turbine should be sited (o) needs to take into account the varying flow depth due to the rising and falling tides, the effect of waves, and the effect of bed proximity.

Further data collection with the rotor positioned at various heights under wave-current flow conditions would be required to more fully determine the optimal vertical placement of the turbine subject to wave-current flow conditions. It would also be necessary to collect data with varying flow depths to determine the impact of the varying tidal height. However, based on the results presented herein, positioning a turbine slightly below mid-depth would be optimal under both combined current and wave flow as well as under current only flow whilst allowing for the tidal ebb and flood. It would also minimise blockage from turbine obstruction as flow can pass unrestricted both above and below the turbine.

The work presented in this thesis provides a large dataset of wake measurements which can be used to compare with numerical models. Some of the data presented herein has already been used as a comparison to numerical models. However, further comparison of the experimental data with numerical models would allow for validation of numerical models, and therefore greater accuracy in their modelling abilities.

Data surrounding power and thrust of the turbine were not collected during this work, as a result of the setup and turbine construction. It would be beneficial to collect data for these parameters, and to be able to combine it with the flow data, particularly under combined wave-current flow, where experimental data in that research field is currently limited. This data is of particular importance as rotor stalling was observed under large waves in the research presented herein. Rotor stalling accounted for 0.1% of rotor revolutions in this work. Although this is only a small percentage of the rotor revolutions, it should still be a consideration when determining rotor performance when located in areas subject to waves.

The effect of the tidal stream turbine on the channel bed was considered during the experimental programme. It was determined that the rotor had a significant impact on the bed sediment beneath the turbine, particularly when the rotor was positioned close to the bed. However, it is important to consider different bed structures, including different sediment types, as well as sediment with vegetation, in order for the environmental impact of tidal stream turbines to be better understood.

Due to the experimental design, and significant ethical issues, it was not possible to experimentally measure the impact of the tidal stream turbine on marine fauna. It is of significant interest to the research field to fully understand the potential impacts of tidal stream turbines on all areas of the environment. Future work should attempt to model and understand these impacts.

This thesis has attempted to discuss the possible implications of placing tidal stream turbines in arrays, as is likely to be the case when turbines are implemented at full scale. However, the experimental programme did not collect any data for an array of turbines. Further experiments should be conducted in order to identify the impact of both the turbine wakes upon one another, and also the impact of combined turbine wakes upon the flow and surrounding environment (such as the channel bed). This would expand on the work by other researchers, including Myers *et al.* (2011) who investigated the flow field around turbine arrays with various turbine spacing arrangements. However, as is the case with a large proportion of the research in the field, Myers *et al.* (2011) used porous disks for the research, rather than a model tidal stream turbine, and also did not consider the impact of wave-current flow on the flow field within the array.

References

ABP Marine Environmental Research Limited (2005) *Potential Nature Conservation and Landscape Impacts of Marine Renewable Energy Development in Welsh Territorial Waters.* Countryside Commission for Wales.

ABP Marine Environmental Research Limited (2008) *Atlas of UK Marine Renewable Energy Resources: Atlas Pages: A Strategic Environmental Assessment Report*. Department for Business Enterprise and Regulatory Reform.

Adrian, R. J. (1991) Particle-imaging techniques for experimental fluid mechanics. *Annual Review of Fluid Mechanics,* 23, 261-304.

Adrian, R. J. (1997) Dynamic ranges of velocity and spatial resolution of particle image velocimetry. *Measurement Science and Technology*, 8 (12), 1393-1398.

Adrian, R. J. and Westerweel, J. (2011) *Particle Image Velocimetry.* Cambridge University Press. New York.

Ahmadian, R., Falconer, R. and Bockelmann-Evans, B. (2012) Far-field modelling of the hydro-environmental impact of tidal stream turbines. *Renewable Energy,* 38 (1), 107-116.

Airy, G. B. (1845) *On Tides and Waves: Encyclopaedia Metropolitana, Volume 5.* London: William Clowes and Sons, 241-396.

Amin, I. and Xiao, Q. (2013) Numerical simulation of a horizontal axis tidal turbine with a pre-swirl stator. In: G. Soares and L. Pena, eds., *Developments of Marine Transportation and Exploitation of Sea Resources*. London: Taylor and Francis Group, pp. 863-869.

Bagnold, R. A. (1966) An approach to the sediment transport problem from general physics. *Geological Survey Professional Paper*, 422, 1-37.

Bahaj, A. S. and Myers, L. (2003). Fundamentals applicable to the utilisation of marine current turbines for energy production. *Renewable Energy*, 28 (14), 2205-2211.

Bahaj, A. S., Batten, W. M. J. and McCann, G. (2007a) Experimental verifications of numerical predictions for the hydrodynamic performance of horizontal axis marine current turbines. *Renewable Energy*, 32, 2479-2490.

Bahaj, A. S., Molland, A. F., Chaplin, J. R. and Batten, W. M. J. (2007b) Power and thrust measurements of marine current turbines under various hydrodynamic flow conditions in a cavitation tunnel and a towing tank. *Renewable Energy*, 32, 407-426.

Bahaj, A. S., Myers, L. E., Thomson, M. D. and Jorge, N. (2007c) Characterising the wake of horizontal axis marine current turbines. *Proceedings of the 7th European Wave and Tidal Energy Conference*. Porto, Portugal, 11-13 September.

Bansal, R. K. (2010) *A Textbook of Stregnth of Materials.* Laxmi Publications, New Delhi.

Barber, J. A. (2005) *Naval Shiphandler's Guide*. Naval Institute Press, Maryland.

Barber, R. B. (2014) *Passive Pitch Control in Marine Hydrokinetic Turbine Blades.* Masters of Science in Engineering Thesis, University of Washington.

Barltrop, N., Varyani, K. S., Grant, A., Clelland, D. and Pham, X. (2006) Wave-current interactions in marine current turbines. *Proceedings of the Institution of Mechanical Engineers, Part M: Journal of Engineering for the Maritime Environment*, 220 (4), 195-203.

Bartl, J., Pierella, F. and Sætran, L. (2012) Wake measurements behind an array of two model wind turbines. *Energy Procedia,* 24, 305-312.

Batten, W. M. J., Bahaj, A. S., Molland, A. F. and Chaplin, J. R. (2006) Hydrodynamics of marine current turbines. *Renewable Energy*, 31, 249-256.

Batten, W. M. J., Harrison, M. E. and Bahaj, A. S. (2013) Accuracy of the actuator disc-RANS approach for predicting the performance and wake of tidal turbines. *Philosophical Transactions of the Royal Society A*, 371, 1-14.

Bir, G. S., Lawson, M. J. and Li, Y. (2011) Structural design of a horizontal-axis tidal current turbine composite blade. *ASME 30th International Conference on Ocean, Offshore and Arctic Engineering*, Rotterdam, The Netherlands, June 19-24 2011.

Biron, P. M., Robson, C., Lapointe, M. F. and Gaskin, S. J. (2004) Comparing different methods of bed shear stress estimates in simple and complex flow fields. *Earth Surface Processes and Landforms,* 29, 1403-1415.

Black and Veatch Ltd (2005) *Phase II UK Tidal Stream Energy Resource Assessment.* Middlesex, Black and Veatch Ltd.

Blue Energy Canada (2014) *Technology – method – Vertical axis hydro turbine*. Available online: http://bluenergy.com//vertical-axis-turbine/vaht/ [Accessed 06/08/2014].

Boehlert, G. W. and Gill, A. B. (2010) Environmental and ecological effects of ocean renewable energy development: a current synthesis. *Oceanography*, 23 (2), pp. 68-81.

Boyle, G., Everett, B. and Alexander, G. (2012) Introducing renewable energy. In: G. Boyle, ed., *Renewable Energy: Power for a Sustainable Future*. Oxford: Oxford University Press, 1-20.

Briggs, L. J. (1959) Effect of spin and speed on the lateral deflection (curve) of a baseball; and the Magnus effect of smooth spheres. *American Journal of Physics*, 27 (8), 589-596.

Brossard, C., Monnier, J. C., Barricau, P., Vandernoot, F. X., Le Sant, Y., Champagnat, F. and Le Besnerais, G. (2009) Principles and Applications of Particle Image Velocimetry. *Aerospace Lab Journal*, 1 (3), 1-11.

Buhl, M. L. (2005) *A new empirical relationship between thrust coefficient and induction factor for the turbulent windmill state*. Colorado: National Renewable Energy Laboratory. Available online: https://www.nrel.gov/docs/fy05osti/36834.pdf [Accessed 04/01/2018].

Burrows, R., Yates, N. C., Hedges, T. S., Li, M., Zhou, J. G., Chen, D. Y., Walkington, I. A., Wolf, J. and Procter, R. (2009) Tidal energy potential in UK waters. *Proceedings of the ICE – Maritime Engineering,* vol. 162, 155-164.

Cada, G., Ahlgrimm, J., Bahleda, M., Bigford, T., Stavrakas, S. D., Hall, D., Moursund, R. and Sale, M. (2007) Potential impacts of hydrokinetic and wave energy conversion technologies on aquatic environments. *Fisheries*, 32 (4), 174-181.

Chamorro, L. P., Hill, C., Morton, S., Ellis, C., Arndt, R. E. A. and Sotiropoulos, F. (2013) On the interaction between a turbulent open channel flow and an axial-flow turbine. *Journal of Fluid Mechanics*, 716, 658-670 .

Charlier, R. H. and Justus, J. R. (1993) *Ocean Energies: Environmental, Economic and Technological Aspects of Alternative Power Sources.* Amsterdam: Elsevier.

Chen, L. and Lam, W-H. (2014) Methods of predicting sea bed scour around a marine current turbine. *Renewable and Sustainable Energy Reviews*, 29, 683-692.

Churchfield, M, J., Li, Y. and Moriarty, P. J. (2013) A large-eddy simulation study of wake propagation and power production in an array of tidal-current turbines. *Philosophical Transactions of the Royal Society A*, 371, 1-15.

Clean Current (2014) *Tidal turbines*. Available online: http://cleancurrent.com/tidal-turbines [Accessed 16/05/2014].

Coiro, D. P., Maisto, U., Scherillo, F., Melone, S. and Grasso, F. (2006) Horizontal axis tidal current turbine: numerical and experimental investigations. *Proceedings of Offshore Wind and Other Marine Renewable Energies in Mediterranean and European Seas,* European Seminar, Rome, Italy.

Consul, C. A. (2011) *Hydrodynamic analysis of a tidal cross-flow turbine*. PhD Thesis. University of Oxford.

Cook, J., Oreskes, N., Doran, P. T., Anderegg, W. R. L., Verheggen, B., Maibach, E. W., Carlton, J. S., Lewandowsky, S., Skuce, A. G., Green, S. A., Nuccitelli, D., Jacobs, P., Richardson, M., Winkler, B., Painting, R. and Rice, K. (2016). Consensus on consensus: a synthesis of consensus estimates on human-caused global warming. *Environmental Research Letters*, 11 (4).

Creciun, P. (2013) *The effects of blockage ratio and distance from a free surface on the performance of a hydrokinetic turbine.* MSc Thesis. Lehigh University.

Dalrymple, R. W. and Choi, K. (2007) Morphologic and facies trends through the fluvial-marine transition in tide-dominated depositional systems: A schematic framework for environmental and sequence-stratigraphic interpretation. *Earth-Science Reviews*, 81, 135-174.

Dantec Dynamics (2014a) *Particle image velocimetry.* Available online: http://www.dantecdynamics.com/particle-image-velocimetry/ [Accessed: 22/12/2014].

Dantec Dynamics (2014b) *Measurement Principles of PIV*. Available online: http://www.dantecdynamics.com/measurement-principles-of-piv/ [Accessed: 22/12/2014].

Dantec Dynamics (2014c) *Stereo PIV (2D3D PIV).* Available online: http://www.dantecdynamics.com/stereo-piv-2d3c-piv/ [Accessed: 23/12/2014].

Dantec Dynamics (2016a) *Direct Linear Transform (DLT).* Available online: http://service.dantecdynamics.com/help/dshelp/content/analysis/imaging%20model%20fit/direct%20linear%20transform.htm [Accessed 11/10/2016].

Dantec Dynamics (2016b) *Stereo-PIV*. Available online: http://service.dantecdynamics.com/help/dshelp/content/analysis/stereo%20piv/stereo%20piv.html [Accessed: 11/10/2016].

Dey, S. (2011) Entrainment threshold of loose boundary streams. In Rowiński, P. (ed) *Experimental Methods in Hydraulic Research.* Berlin: Springer, 29-48.

Edmunds, M., Malki, R., Williams, A. J., Masters, I. and Croft, T. N. (2014) Aspects of tidal stream turbine modelling in the natural environment using a coupled BEM-CFD model. *International Journal of Marine Energy*, 7, 20-42.

Ellenrieder, K. D. von and Pothos, S. (2008) PIV measurements of the asymmetric wake of a two dimensional heaving hydrofoil. *Experiments in Fluids*, 44, 733-745.

Elliott, D. (2012) Tidal Power. In: G. Boyle, ed., *Renewable Energy: Power for a Sustainable Future*. Oxford: Oxford University Press, 241-296.

EPSRC (2017) *Interactions of flow, tidal stream turbines and local sediment bed under combined waves and tidal conditions (INSTRON).* Available online: http://gow.epsrc.ac.uk/NGBOViewGrant.aspx?GrantRef=EP/J010359/1 [Accessed 27/06/2017].

Escaler, X., Egusquiza, E., Farhat, M., Avellan, F. and Coussirat, M. (2006) Detection of cavitation in hydraulic turbines. *Mechanical Systems and Signal Processing,* 20, 983-1007.

European Commission (2017) *Renewable energy*. Available at: https://ec.europa.eu/energy/en/topics/renewable-energy [Accessed 24/07/2017].

European Union (2009) *Promotion of the use of energy from renewable sources and* amending and subsequently repealing Directives 2001/77/EC and 2003/30/EC (Directive 2009/28/EC). European Parliament, Council of the European Union.

Faber, Maunsell and Metoc PLC (2007) *Scottish marine renewable strategic environmental assessment environmental report.* Scottish Executive.

Fagherazzi, S., Gabet, E. J. and Furbish, D. J. (2004) The effect of bidirectional flow on tidal channel planforms. *Earth Surface Processes and Landforms*, 29, 295-309.

Farrell, K. M., Harris, W. B., Mallinson, D. J., Culver, S. J., Riggs, S. R., Pierson, J., Self-Trail, J. M. and Lautier, J. C. (2012) Standardizing texture and facies codes for a process-based classification of clastic sediment and rock. *Journal of Sedimentary Research*, 82, 364-378.

Fluid Mechanics Ltd (2014) *Fluid mechanics – transient flow*. Available online: http://www.fluidmechanic.co.uk/transient.htm [Accessed 06/08/2014].

Fraenkel, P. L. (2002) Power from marine currents. *Proceedings of the Institution of Mechanical Engineers, Part A: Journal of Power and Energy*, 216 (1), 1-14.

Fraenkel, P. L. (2006) Tidal current energy technologies. *Ibis*, 148, 145-151.

Franc, J. and Michel, J. (2005) *Fundamentals of Cavitation.* Dordrecht, Kluwer Academic Publishers.

Frid, C., Andonegi, E., Depestele, J., Judd, A., Rihan, D., Rogers, S. I. and Kenchington, E. (2012) The environmental interactions of tidal and wave energy generation devices. *Environmental Impact Assessment Review*, 31 (1), 133-139.

Fujita Research (2000) *Wave and tidal power*. Available online: http://www.fujitaresearch.com/reports/tidalpower.html [Accessed 13/04/2015].

Galloway, P. W., Myers, L. E. and Bahaj, A. S. (2014) Quantifying wave and yaw effects on a scale tidal stream turbine. *Renewable Energy*, 63, 297-307.

Gaurier, B., Davies, P., Deuff, A. and Germain, G. (2013) Flume tank characterisation of marine current turbine blade behaviour under current and wave loading. *Renewable Energy,* 59, 1-12.

Grant, I., Mo, M., Pan, X., Parkin, P., Powell, J., Reinecke, H., Shuang, K., Coton, F. and Lee, D. (2000) An experimental and numerical study of the vortex filaments in the wake of an operation, horizontal-axis, wind turbine. *Journal of Wind Engineering and Industrial Aerodynamics,* 85, 177-189.

Guerin, A. J., Jackson, A. C., Bowyer, P. A. and Youngson, A. F. (2014) *Marine Research Report: Hydrodynamic Models to Understand Salmon Migration in Scotland.* The Crown Estate.

Hammar, L., Andersson, S., Eggertsen, L., Haglund, J., Gullström, M., Ehnberg, J. and Molander, S. (2013) Hydrokinetic turbine effects on fish swimming behaviour. *PloS one*, 8 (12), 1-12.

Hansen, M. O. L., Sørensen, N. N. And Flay, R. G. J. (2000) Effect of placing a diffuser around a wind turbine. *Wind Energy*, 3, 207-213.

Hardisty, J. (2009) *The Analysis of Tidal Stream Power*. Chichester, UK: John Wiley & Sons Ltd.

Hardy, R. J., Lane, S. N., Lawless, M. R., Best, J. L., Elliott, L. and Ingham, D. B. (2005) Development and testing of a numerical code for treatment of complex river channel topography in three-dimensional CFD models with structured grids. *Journal of Hydraulic Research*, 43 (5), 468-480.

Harrison, M. E., Batten, W. M. J., Myers, L. E. and Bahaj, A. S. (2009) A comparison between CFD simulations and experiments for predicting the far wake of horizontal axis tidal turbines. *Proceedings of the 8th European Wave and Tidal Energy Conference,* Uppsala, Sweden, 2009.

Hicks, S. D. (2006) *Understanding tides.* Washington, D. C.: United States Department of Commerce.

Hill, C., Musa, M., Chamorro, L. P., Ellis, C. and Guala, M. (2014) Local scour around a model hydrokinetic turbine in an erodible channel. *Journal of Hydraulic Engineering*, 140 (8), 1-10.

Hill, C., Musa, M. and Guala, M. (2016) Interaction between instream axial flow hydrokinetic turbines and uni-directional flow bedforms. *Renewable Energy*, 86, 409-421.

Huang, H., Dabiri, D. and Gharib, M. (1997) On errors of digital particle image velocimetry. *Measurement Science and Technology,* 8, 1427-1440.

Iglesias, G., Sanchez, M., Ramos, V., Carballo, R. and Greaves, D. (2014) Effects of a tidal farm on the transient and residual circulation of an estuary. *3rd Oxford Tidal Energy Workshop.* Oxford, UK, 7-8 June 2014.

IPCC (2014) Climate change 2014: synthesis report. Available online: http://www.ipcc.ch/pdf/assessment-report/ar5/syr/SYR_AR5_FINAL_full_wcover.pdf [Accessed 27/06/2017].

Jesus Henriques, T. A. de., Hedges, T. S., Owen, I. and Poole, R. J. (2015) The effect of wave-current interaction on the near-wake of horizontal axis tidal stream turbines. *Proceedings of the 11th European Wave and Tidal Energy Conference*, Nantes, France, 6-11 September 2015.

Jesus Henriques, T. A., de., Tedds, S. C., Bostari, A., Najafian, G., Hedges, T. S., Sutcliffe, C. J., Owen, I. and Poole, R. J. (2014) The effects of wave-current interaction on the performance of a model horizontal axis tidal turbine. *International Journal of Marine Energy*, 8, 17-35.

Ji, Z. (2008) *Hydrodynamics and Water Quality: Modelling Rivers, Lakes and Estuaries.* Hoboken, New Jersey, John Wiley and Sons Ltd.

Johansson, T. B., Kelly, H., Reddy, A. K. M. and Williams, R. H. (1993) Renewable fuels and electricity for a growing world economy: defining and achieving the potential. In: T. B. Johansson, H. Kelly, A. K. N. Reddy and R. H. Williams, eds., *Renewable Energy: Sources for Fuels and Electricity.* Washington: Island Press, 1-72.

Johnston, A., Ausden, M., Dodd, A. M., Bradbury, R. B., Chamberlain, D. E., Jiguet, F., Thomas, C. D., Cook, A. S. C. P., Newson, S. E., Ockendon, N., Rehfisch, M. M., Roos, S., Thaxter, C. B., Brown, A., Crick, H. Q. P., Douse, A., CcCall, R. A., Pontier, H., Stroud, D. A., Cadiou, B., Crowe, O., Deceuninck, B., Hornman, M. and Pearce-Higgins, J. W. (2013) Observed and predicted effects of climate change on species abundance in protected areas. *Nature Climate Change*, 3, 1055-1061.

Jordan, L. B., Simmons, S., McLelland, S., Murphy, B., Parsons, D. and Vybulkova, L. (2015) The impact of tidal stream turbines on 3D flow and bed shear stress measured with particle image velocimetry in a laboratory flume. *Proceedings of the 11th European Wave and Tidal Energy Conference*, Nantes, France, 6-11 September 2015.

Keane, R. D. and Adrian, R. J. (1992) Theory of cross-correlation analysis of PIV images. *Applied Scientific Research*, 49, 191-215.

Kerr, D. (2007) Marine energy. *Philosophical Transactions. Series A: Mathematical, Physical and Engineering Sciences.* 365 (1853), 971-992.

Khalid, S. S., Liant, Z. and Shah, N. (2013) Harnessing tidal energy using vertical axis tidal turbine. *Research Journal of Applied Sciences, Engineering and Technology*, 5 (1), 239-252.

Khan, M. J., Bhuyan, G., Iqbal, M. T. and Quaicoe, J. E. (2009) Hydrokinetic energy conversion systems and assessment of horizontal and vertical axis turbines for river and tidal applications: a technology and status review. *Applied Energy*, 86, 1823-1835.

Kim, S. C., Friedrichs, C. T.Maa, J. P. Y, and Wright, L. D. (2000) Estimating bottom stress in tidal boundary layer from acoustic doppler velocimetry data. *Journal of Hydraulic Engineering*, 126 (6), 399-406.

Kregting, L., Elsaesser, B., Kennedy, R., Smyth, D., O'Carroll, J. and Savidge, G. (2016) Do changes in current flow as a result of arrays of tidal turbines have an effect on benthic communities? *PLoS ONE,* 11 (8).

Lebrón, J., Cal, R. B., K., H., Castillo, L. and Meneveau, C. (2009) Interaction between a wind turbine array and a turbulent boundary later. *11th Americas Conference on Wind Engineering*, San Juan, Puerto Rico, 22-26 June 2009.

Li , Y. and Çalişal, S. M. (2010) Numerical analysis of the characteristics of vertical axis tidal current turbines. *Renewable Energy,* 35 (2), 435-442.

Lloyd, T. P., Turnock, S. R. and Humphrey, V. F. (2011) Modelling techniques for underwater noise generated by tidal turbines in shallow waters. *Proceedings of the 30th International Conference on Ocean, Offshore and Arctic Engineering*. Rotterdam, The Netherlands, 19-24 June.

Lohrmann, A., Cabrera, R. and Kraus, N. C. (1994) Acoustic-Doppler Velocimeter (ADV) for laboratory use. *Proceedings of Conference on Fundamentals and Advancements in Hydraulic Measurements and Experimentation.* New York, 1-5 August 1994.

Lu, Y. and Lueck, R. G. (1999) Using a broadband ADCP in a tidal channel. Part I: Mean flow and shear. *Journal of Atmospheric and Oceanic Technology,* 16, 1556-1567.

Lunar Energy (2014a) *Technology*. Available online: http://lunarenergy.co.uk/productOverview.htm [Accessed 16/05/2014].

Lunar Energy (2014b) *Venturi duct*. Available online: http://www.lunarenergy.co.uk/duct.htm [Accessed 31/07/2014].

Luque, R. F. (1974) *Erosion and transport of bed-load sediment*. PhD thesis. Technische Hogeschool Delft. Available online: https://repository.tudelft.nl/islandora/object/uuid:2627433e-275e-4327-8841-ae998a6c525c/datastream/OBJ [Accessed 08/01/2018].

Luznik, L., Benthem, M. Flack, K. A. and Lust, E. E. (2013) Near wake characteristics of a model horizontal axis marine current turbine under steady and unsteady inflow conditions. *IEEE 2013 Oceans*, San Diego, 23-27 September 2013.

Malki, R., Masters, I., Williams, A. J. and Croft, N. T. (2014) Planning tidal stream turbine array layouts using a coupled blade element momentum – computation fluid dynamics model. *Renewable Energy,* 63, 46-54.

Manwell, J. F., McGowan, J. G. and Rogers, A. L. (2003) *Wind Energy Explained: Theory, Design and Application.* Chicester: John Wiley and Sons Ltd.

Marine Current Turbines (2014a) *SeaGen Technology*. Available online: http://marineturbines.com/Seagen-Technology [Accessed 25/07/2014].

Marine Current Turbines (2014b) *Marine Current Turbines kicks off first tidal array for Wales.* Available online: http://www.marinecurrentturbines.com/3/news/article/44/marine_current_turbines_kicks_off_first_tidal_array_for_wales [Accessed 25/07/2014].

Marine Current Turbines (2014c) *Energy Capture*. Available online: http://www.marineturbines.com/SeaGen-Technology/Energy-Capture [Accessed 31/07/2014].

McCall, R., Saunders, A., Shepperd, P. and Beadle, R. (2007) Tidal power in the UK – research report 1 – UK tidal resource assessment. *Sustainable Development Commission,* Consultant Report.

McCombes, T., Johnstone, C. and Grant, A. (2011) Unsteady 3D wake modelling for marine current turbines. *IET Renewable Power Generation,* 5 (4), 299-310.

Met Office (2017) *What is climate change?* Available online: http://www.metoffice.gov.uk/climate-guide/climate-change [Accessed 27/07/2017].

Möller, N. J., Kim, H., Neary, V. S., García, M. H. and Chamorro, L. P. (2016) On the near-wall effects indicted by an axial-flow rotor. *Renewable Energy,* 91, 524-530.

Moshin, S., Tomita, S. and Tajima, Y. (2011) Experimental study on interaction of waves, currents, and dynamic morphology changes. In Burns, S. E., Bhatia, S. K., Avila, C. M. C. and Hunt, B. E.(eds) *Scour and Erosion: Proceedings of the Fifth International Conference on Scour and Erosion.* Virginia: ASCE Publications, 697-706.

Myers, L. E., Bahaj, B., Germain, G. and Giles, J. (2008) Flow boundary interaction effects for marine current energy conversion devices. *10th World Renewable Energy Congress 2008,* Glasgow, Scotland, 19-25 July.

Myers, L. E. and Bahaj, A. S. (2009) Near wake properties of horizontal axis marine current turbines. *Proceedings of the 8th European Wave and Tidal Energy Conference,* Uppsala, Sweden, 2009.

Myers, L. E. and Bahaj, A. S. (2010) Experimental analysis of the flow field around horizontal axis tidal turbines by use of scale mesh disk rotor simulators. *Ocean Engineering,* 37, 218-227.

Myers, L. E., Keogh, B. and Bahaj, A. S. (2011) Experimental investigation of inter-array wake properties in early tidal turbine arrays. *OCEANS 2011,* Waikoloa, HI, USA, 19-22 September 2011.

Myers, L. E. and Bahaj, A. S. (2012) An experimental investigation simulating flow effects in first generation marine current energy converter arrays. *Renewable Energy,* 37, 28-36.

Nash, S., O'Brien, N., Olbert, A. and Hartnett, M. (2014) Modelling the far field hydro-environmental impacts of tidal turbine farms – a focus on tidal regime, inter-tidal zones and flushing. *Computers and Geosciences,* 71, 20-27.

Neary, V. S., Gunawan, B., Hill, C. and Chamorro, L. P. (2013) Near and far field flow disturbances induced by model hydrokinetic turbine: ADV and ADP comparison. *Renewable Energy*, 60, 1-6.

Neill, S. P., Jordan, J. R. and Couch, S. J. (2012) Impact of tidal energy converter (TEC) arrays on the dynamics of headland sand banks. *Renewable Energy,* 37 (1), 387-397.

Neill, S. P., Litt, E. J., Couch, S. J. and Davies, A. G. (2009) The impact of tidal stream turbines on large-scale sediment dynamics. *Renewable Energy*, 37 (1), 387-397.

Nihoul, J. C. and Ronday, F. C. (1975) The influence of the "tidal stress" on the residual circulation. Application to the Southern Bight of the North Sea. *Tellus,* 27 (5), 484-490.

Nortek AS (2017) *Products.* Available online: http://www.nortek-as.com/en/products [Accessed 20/12/2017].

Olczak, A., Sudall, D., Stallard, T. and Stansby, P. (2015) Evaluation of RANS BEM and self-similar wake superposition for tidal stream turbine arrays. *Proceedings of the 11th European Wave and Tidal Energy Conference*, Nantes, France, 6-11 September 2015.

O Rourke, F. Boyle, F. and Reynolds, A. (2010) Tidal energy update 2009. *Applied Energy*, 87 (2), 398-409.

Osborne, P. (1998) *Fujita Research report – wave and tidal power*. Available online: www.fujitaresearch.com/reports/tidalpower.html [Accessed 07/12/2016].

OSPAR Commission (2008) *Assessment of the environmental impact of offshore wind-farms.* London, United Kingdom.

Parker, C. M. and Leftwich, M. C. (2016) The effect of tip speed ratio on a vertical axis wind turbine at high Reynolds numbers. *Experiments in Fluids,* 57, (74), 1-11.

Payne, G. S., Stallard, T. and Martinez, R. (2015) Experimental investigation of tidal rotor loading due to wave, current and impact with sea animals. *Proceedings of the 11th European Wave and Tidal Energy Conference*, Nantes, France, 6-11 September 2015.

Pelc, R. and Fujita, R. M. (2002) Renewable energy from the ocean. *Marine Policy*, 26, 471-479.

Plew, D. R. and Stevens, C. L. (2013) Numerical modelling of the effect of turbines on currents in a tidal channel – Tory Channel, New Zealand. *Renewable Energy,* 57, 269-282.

Polagye, B. L. (2009) *Hydrodynamic Effects of Kinetic Power Extraction by In-Stream Tidal Turbines.* Michigan, ProQuest.

Polagye, B. L., Cleve, B. V., Copping, A. and Kirkendall, K. (2010) Environmental effects of tidal energy development. *Proceedings of a scientific workshop*. U.S. Department of Commerce.

Pope, N. D., Widdows, J. and Brinsley, M. D. (2006) Estimation of bed shear stress using the turbulent kinetic energy approach – a comparison of annular flume and field data. *Continental Shelf Research,* 26, 959-970.

Prasad, A. K. (2000) Particle image velocimetry. *Current Science*, 79 (1), 51-60.

Rambabu, M., Narasimh Rao, S. and Sundar, V. (2003) Current-induced scour around a vertical pile in cohesive soil. *Ocean Engineering*, 30, 893-920.

Ramos, V., Carballo, R., Sanchez, M., Veigas, M. and Iglesias, G. (2014) Tidal stream energy impacts on estuarine circulation. *Energy Conversion and Management*, 80, 137-149.

Rapaport, D. C. and Clementi, E. (1986) Eddy formation in obstructed fluid flow: a molecular-dynamics study. *Physical Review Letters,* 57 (6), 695-698.

Renewable UK (2002) *RenewableUK marine energy database.* Available online: https://maps.espatial.com/maps/pages/map.jsp?geoMap Id=19671&TENANT_ID=115744 [Accessed 05/08/2015].

RenewableUK (2016) *Wave & tidal energy*. Available online: www.renewableuk.com/page/WaveTidalEnergy [Accessed 07/12/2016].

Rijn, L. C. V. (1984) Sediment transport, part II: suspended load transport. *Journal of Hydraulic Engineering.* 110 (11), 1613-1641.

Roberts, A., Thomas, B., Sewell, P., Khan, Z., Balmain, S. and Gillman, J. (2016) Current tidal power technologies and their suitability for applications in coastal and marine areas. *Journal of Ocean Engineering and Marine Energy*, 2 (2), 227-245.

Ryan, K. J., Coletti, F., Elkins, C. J., Dabiri, J. O. and Eaton, J. K. (2016) Three-dimensional flow field around and downstream of a subscale model rotating vertical axis wind turbine. *Experiments in Fluids,* 57 (38).

Shields, M. A., Woolf, D. K., Grist, E. P. M., Kerr, S. A., Jackson, A. C., Harris, R. E., Bell, M. C., Beharie, R., Want, A., Osalusi, E., Gibb, S. W. and Side, J. (2011) Marine renewable energy: the ecological implications of altering the hydrodynamics of the marine environment. *Ocean and Coastal Management*, 54 (1), 2-9.

Sime, L. C., Ferguson, R. I. and Church, M. (2007) Estimating shear stress from moving boat acoustic doppler velocity measurements in a large gravel bed river. *Water Resources Research*, 43 (3).

Sinha, B. and Pingree, R. D. (1997) The principal lunar semidiurnal tide and its harmonics: baseline solutions for M2 and M4 constituents on the North-West European Continental Shelf. *Continental Shelf Research* , 17 (11), 1321-1365.

Sørensen, B. (2004) *Renewable Energy: Its Physics, Engineering, Use, Environmental Impacts, Economy and Planning Aspects.* London: Elsevier Academic Press.

Stacey, M. T., Monismith, S. G. and Burau, J. R. (1999) Measurements of Reynolds stress profiles in unstratified tidal flow. *Journal of Geophysical Research,* 104 (5), 10933-10949.

Stallard, T., Collings, R., Feng, T. and Whelan, J. (2013) Interactions between tidal turbine wakes: experimental study of a group of three-bladed rotors. *Philosophical Transactions of the Royal Society A*, 371, 1-13.

Stallard, T., Feng, T. and Stansby, P. K. (2015) Experimental study of the mean wake of a tidal stream rotor in a shallow turbulent flow. *Journal of Fluids and Structures*, 54, 235-246.

Stapleton, K. R., and Huntley, D. A. (1995) Seabed stress determinations using the intertial dissipation method and the turbulent kinetic energy method. *Earth Surface Processes and Landforms*, 20, 807-815.

Stroeve, J., Holland, M. M., Meier, W., Scambos, T. and Serreze, M. (2007) Arctic sea ice decline: Faster than forecast. *Geophysical Research Letters,* 34.

Sulaiman, M. S., Sinnakaudan, S. K. and Shukor, M. R. (2013) Near bed turbulence measurement with Acoustic Doppler Velocimeter (ADV). *KSCE Journal of Civil Engineering*, 17 (6), 1515-1528.

Sun, X., Chick, J. P. and Bryden, I. G. (2008) Laboratory-scale simulation of energy extraction from tidal currents. *Renewable Energy,* 33 (6), 1267-1274.

Sutherland, J. and Soulsby, R. I. (2010) Guidelines for physical modelling of mobile sediments. *Proceedings of the Third International Conference on the Application of Physical Modelling to Port and Coastal Protection.* Barcelona, 28th September to 1st October 2010.

Tedds, S. C., Owen, I. and Poole, R. J. (2014) Near-wake characteristics of a model horizontal axis tidal stream turbine. *Renewable Energy*, 63, 222-235.

Tescione, G., Ragni, D., He, C., Ferreira, C. J. S. and Bussel, G. J. W. (2014) Near flow wake analysis of a vertical axis wind turbine by stereoscopic particle image velocimetry. *Renewable Energy,* 70, 47-61.

The Scottish Government (2011) *Pentland Firth and Orkney waters marine spatial plan framework and regional locational guidance for marine energy* (March 2011). *Scotland*. Available online: http://www.gov.scot/Resource/Doc/295194/0115355.pdf [Accessed 02/01/2018].

Theunissen, R., Scarano, F. and Riethmuller, M. L. (2007) An adaptive sampling and windowing interrogation method in PIV. *Measurement Science Technology*, vol 18, 275-287.

The World Bank (2017) *World development indicators*. Available online: http://data.worldbank.org/data-catalog/world-development-indicators [Accessed 23/06/2017].

Thomas, F. O. and Liu, X. (2004) An experimental investigation of symmetric and asymmetric turbulent wake development in pressure gradient. *Physics of Fluids*, 16 (5), 1725-1745.

Thompson, C. E. L., Amos, C. L., Jones, T. E. R. and Chaplin, J. (2003) The manifestation of fluid-transmitted bed shear stress in a smooth annular flume - a comparison of methods. *Journal of Coastal Research*, 19 (4), 1094-1103.

Turner, J. A. (1999) A realizable renewable energy future. *Science*, 285, 687-689

Turnock, S. R., Phillips, A. B., Banks, J. and Nicholls-Lee, R. (2011) Modelling tidal current turbine wakes using a coupled RANS-BEMT approach as a tool for anbalysing power capture of arrays of turbines. *Ocean Engineering*, 38 (11-12), 1300-1307.

Umeyama, M., Shintani, T. and Watanabe, S. (2010) Measurements of particle velocities and trajectories in a wave-current motion using particle image velocimetry. *Proceedings of the 32nd International Conference on Coastal Engineering.*

United Nations (1992) *United Nations framework convention on climate change.* Available online: https://unfccc.int/files/essential_background/background_publications_htmlpdf/application/pdf/conveng.pdf [Accessed 27/06/2017]

United States Environmental Protection Agency (2012) *Channel processes: suspended sediment transport*. Available online: http://water.epa.gov/scitech/datait/tools/warsss/suspend.cfm [Accessed 10/04/2015].

U.S. Department of Transportation (2009) *Pilot's Handbook of Aeronautical Knowledge*. U. S. Government Printing Office, Washington.

Vanoni, V. A. (1964) *Measurements of critical shear stress*. Pasadena: California Institute of Technology.

Vermeer, L. J., Sørensen, J. N. and Crespo, A. (2003) Wind turbine wake aerodynamics. *Progress in Aerospace Sciences*, 39 (6-7), 467-510.

Viehman, H. A. (2012) *Fish in a Tidally Dynamic Region in Marine: Hydroacoustic Assessments in Relation to Tidal Power Development.* Master of Science Thesis. University of Maine.

Vybulkova, L. (2013) *A Study of the Wake of an Isolated Tidal Turbine with Application to its Effects on Local Sediment Transport.* PhD Thesis. University of Glasgow. Available online: http://theses.gla.ac.uk/4997/1/2013vybulkovaphd.pdf [Accessed 22/03/2016].

Vybulkova, L., Vezza, M. and Brown, R. (2013) The impact of tidal turbines on small-scale seabed erosion. *Proceedings of the 10th European Wave and Tidal Energy Conference.* Aalborg, Denmark, 2-6 September 2013.

Walker, S. R. J. (2014) *Hydrodynamic interactions of a tidal stream turbine and support structure*. PhD thesis. University of Sheffield.

Walkington, I. and Burrows, R. (2009) Modelling tidal stream power potential. *Applied Ocean Research,* 31, 239-245.

Wang, D., Altar, M. and Sampson, R. (2007) An experimental investigation on cavitation, noise and slipstream characteristics of ocean stream turbines. *Proceedings of the Institution of Mechanical Engineers, Part A: Journal of Power and Energy*, 221 (2), 219-231.

Whelan, J. I., Graham, J. M. R. and Peiro, J. (2009) A free-surface and blockage correction for tidal turbines. *Journal of Fluid Mechanics*, 624, 281-291.

Wieneke, B. and Pfeiffer, K. (2010) Adaptive PIV with variable interrogation window size and shape. *15th International Sympossium on Applications of Laser Techniques to Fluid Mechanics,* Lisbon, Portugal. 5th-8th July 2010.

Willert, C. E. and Gharib, M. (1991) Digital particle image velocimetry. *Experiments in Fluids,* 10, 181-193.

Williams, H. E. (2015) *Uncertainty in the prediciton of overtopping parameters in numerical and physical models due to offshore spectral boundary conditions*. PhD thesis. University of Nottingham. Available online: http://eprints.nottingham.ac.uk/30339/1/WILLIAMSHE_4171939_Thesis_Final.pdf [Accessed 26/02/2018].

Wilson, B., Batty, R. S., Daunt, F. and Carter, C. (2006) *Collision Risks Between Marine Renewable Energy Devices and Mammals, Fish and Diving Birds: Report to the Scottish Executive.* Scottish Association for Marine Science, Oban, Scotland.

Wolf, J. and Prandle, D. (1999) Some observations of wave-current interaction. *Coastal Engineering,* 37, 471-485.

Wu, W., Wang, S. S. Y. and Jia, Y. (2010) Nonuniform sediment transport in alluvial rivers. *Journal of Hydraulic Research*, 38 (6), 427-434.

Xia, J., Falconer, R. A. and Lin, B. (2010) Impact of different tidal renewable energy projects on the hydrodynamic processes in the Severn Estuary, UK. *Ocean Modelling*, 32 (1-2), 86-104.